SOLAR ENERGY CONVERSION IN PLANTS AND BACTERIA STUDIED USING FTIR DIFFERENCE SPECTROSCOPY AND QUANTUM CHEMICAL COMPUTATIONAL METHODOLOGIES

by

SREEJA PARAMESWARAN

Under the Direction of Dr. Gary Hastings

ABSTRACT

This dissertation presents a study of the molecular mechanism underlying the highly efficient solar energy conversion processes that occur in the Photosystem I (PS I) reaction centers in plants and bacteria. The primary electron donor P_{700} is at the heart of solar energy conversion process in PS I and the aim is to obtain a better understanding of the electronic and structural organization of P_{700} in the ground and excited states. Static Fourier Transform Infra-Red (FTIR) difference spectroscopy (DS) in combination with site directed mutagenesis and Density Functional Theory (DFT) based vibrational frequency simulations were used to investigate how protein interactions such as histidine ligation and hydrogen bonding modulate this organization.

(P_{700}^{+}-P_{700}) FTIR DS at 77K were obtained from a series of mutants from the cyanobacterium *Synechocystis* sp. 6803 (*S. 6803*) where the amino acid residues near the C=O groups of the two chlorophylls of P_{700} where specifically changed. (P_{700}^{+}-P_{700}) FTIR DS was also obtained for a set of mutants from *C. reinhardtii* where the axial ligand to A_0, the primary electron acceptor in PS I was modified. The FTIR DS obtained from these mutants provides information on the axial ligands, the hydrogen bonding status as well as the polarity of the environment of specific functional groups that are part of the chlorophyll molecules that constitute P_{700}. Assignment of the FTIR bands to vibrational modes in specific types of environment is very difficult. In order to assist the assignment of the difference bands in experimental spectra DFT based vibrational mode frequency calculations were undertaken for Chl-*a* and Chl-a^{+} model molecular systems under different set of conditions; in the gas phase, in solvents using the Polarizable Continuum Model (PCM), in the presence of explicit solvent molecules using QM/MM methods, and in the presence of axial ligands and hydrogen bonds. DFT methods were also used to calculate the charge, spin and redox properties of Chl-a/Chl-a' dimer models that are representative of P_{700}, the primary electron donor in PS I.

INDEX WORDS: Photosynthesis, Photosystem I (PS I), P_{700}, Fourier transform infrared (FTIR), Synechocystis sp. PCC 6803 (*S. 6803*), *Chlamydomonas reinhardtii* (*C. reinhardtii*), Density Functional Theory (DFT), Chlorophyll *a* (Chl-*a*), Polarizable Continuum Model (PCM), QM/MM

SOLAR ENERGY CONVERSION IN PLANTS AND BACTERIA STUDIED USING FTIR DIFFERENCE SPECTROSCOPY AND QUANTUM CHEMICAL COMPUTATIONAL METHODOLOGIES

by

SREEJA PARAMESWARAN

A Dissertation Submitted in Partial Fulfillment of the Requirements for the Degree of

Doctor of Philosophy

in the College of Arts and Sciences

Georgia State University

2009

SOLAR ENERGY CONVERSION IN PLANTS AND BACTERIA STUDIED USING FTIR DIFFERENCE SPECTROSCOPY AND QUANTUM CHEMICAL COMPUTATIONAL METHODOLOGIES

by

SREEJA PARAMESWARAN

Committee Chair: Dr. Gary Hastings

Committee: Dr. Richard H. Miller
Dr. William H. Nelson
Dr. A. G. Unil Perera
Dr. Brian D. Thoms

Electronic Version Approved:

Office of Graduate Studies
College of Arts and Sciences
Georgia State University
August 2009

ACKNOWLEDGEMENTS

My time at the Department of Physics and Astronomy at Georgia State University as a graduate student has been a great learning experience both as a researcher and as a person, for which I have many to thank.

First of all, my sincere gratitude goes to Dr. Gary Hastings for his invaluable guidance and support in completing this dissertation, for his patience during times when my progress was slow, and for his trust in me. Many in Dr. Hastings research group have contributed to this research. Dr. Ruili Wang, Priyangika B. Jayaweera, Hari Prasad Lamichhane, Nan Zhao, and Jing Guo deserve mention for their support. I must also thank my committee members, Dr. Richard H. Miller, Dr. William H. Nelson, Dr. A. G. Unil Perera, and Dr. Brian D. Thoms for their guidance and support.

This work would not have been possible without the high performance computing facilities at the University Academic Technology Services (UATS) research computing at Georgia State University. I am grateful to Mr. Art Vandenberg, the director of UATS and Mr. Victor Bolet and other staff at the UATS for their immense support for the duration of my PhD program.

I would also like to thank the remarkable teachers at Georgia State University, including, but not limited to, Dr. Nikolaus Dietz, Dr. Gary Hastings, Dr. Steven Manson, Dr. Unil Perera, Dr. Mark Stockman, Dr. Robert Simmons, and Dr. Markus Germann. I would like to thank late Dr. Thomas Netzel for his inspirational teachings in aspects of quantum chemistry.

Thanks are also due to numerous others in the Physics and Astonomy community: Charles Hopper and Peter Walker at the Physics Shop, Duke Widsor, Carola Butler, Yvette

Hilaire and Felicia Watts and all the staff at the Physics and Astronomy office who have helped with administrative dealings.

Financial support for this research came through research grants from United State Department of Agriculture (USDA grant number 2004-35318-14889), and National Science Foundation (NSF grant number DBI: 0352324). The support is gratefully acknowledged.

Most importantly, I thank my husband, Arun, for his unconditional love and support. I would also like to thank my parents and my brothers back home who have been very supportive throughout my life. Finally, I thank all of my family members, friends, and strangers who have knowingly or unknowingly helped me on the way.

TABLE OF CONTENTS

LIST OF TABLES

LIST OF FIGURES

CHAPTER 1

INTRODUCTION

Photosynthesis is the process of conversion of solar energy to chemical energy [1]. Photosynthetic process can be classified into two, oxygenic and anoxygenic photosynthesis. Oxygenic photosynthesis takes place in plants, algae and cyanobacteria where water and atmospheric CO_2 is used to synthesis carbohydrates in the presence of sunlight while releasing oxygen [2-4]. Anoxygenic photosynthetic organisms, for example, purple bacteria, green sulfur bacteria and heliobacteria, uses solar energy to create organic compounds but do not produce oxygen. Oxygenic photosynthesis is carried out in two separate sets of reactions, the light reactions and the dark reactions. The light reactions take place in two protein complexes called Photosystem I (PS I) and Photosystem II (PS II). These protein complexes are bound to the thylakoid membrane in oxygen evolving photosynthetic organisms. Figure 1.1 shows the schematic representation of the protein complexes that engage in photosynthesis situated within the thylakoid membrane.

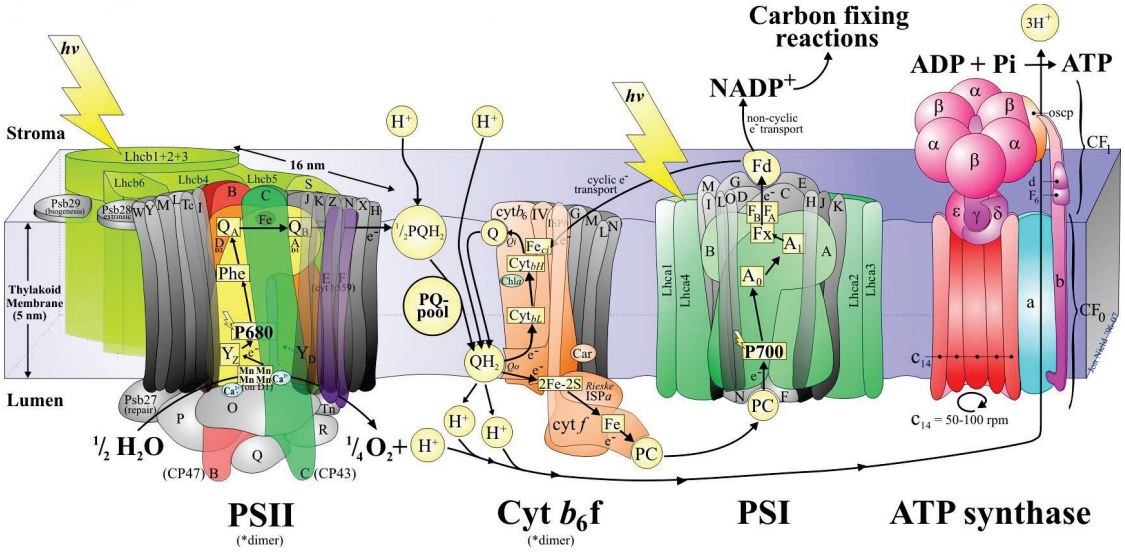

Figure 1.1: Schematic representation of the four protein complexes within the thylakoid membrane.

Solar photons are captured by chlorophyll antenna pigments bound to the periphery of PS II and PS I. The captured energy is rapidly transferred to a special pigment (or group of pigments) in the reaction center (RC) called the primary electron donor. The primary electron donor in PS I/PS II is called P_{700}/P_{680} (Figure 1.1), respectively. Upon excitation of the primary electron donor an electron is transferred via a series of acceptors across the membrane to a terminal acceptor species that is either an iron-sulfur cluster (F_A/F_B in Figure 1.1) or a quinone (Q_B in Figure 1.1). The sequential vectorial electron transfer leads to electrical potential difference across the thylakoid membrane. The energy in the gradient is captured or harnessed by the ATPsynthase and used to generate ATP. The dark reaction uses these molecules to reduce CO_2 to carbohydrates.

1.1 Photosystem I

PS I is a protein pigment complex which catalyses the light induced transfer of electrons across the thylakoid membrane from plastocyanin to ferredoxin. PS I (Figure 1.2), consists of 12 protein subunits 96 chlorophyll *a* (Chl-*a*) molecules, 22 beta-carotenes, two phylloquinones, three Fe_4S_4 clusters (F_x, F_A and F_B), four lipids and a Ca^{2+} ion [5-7]. Subunits *PsaA* and *PsaB* enclose the electron transfer (ET) chain comprising of six chlorophyll molecules, the phylloquinone pair and the three Fe_4S_4 clusters. The rest of the 90 chlorophylls along with 22 carotenoids comprise the antenna system where the light capturing takes place.

The energy collected by the antenna is transferred to the center of the PS I complex where the electron transport chain is located. Charge separation begins by the excitation of $P_{700,}$ a special pair of chlorophyll molecules [8-12]. P_{700}^*, the excited state of the primary electron donor, transfers the electron to A_0 which is a chlorophyll molecule and eventually to the

phylloquinone. The electron passes through the three Fe_4S_4 clusters and is finally used for the reduction of ferredoxin, the final electron acceptor of PS I.

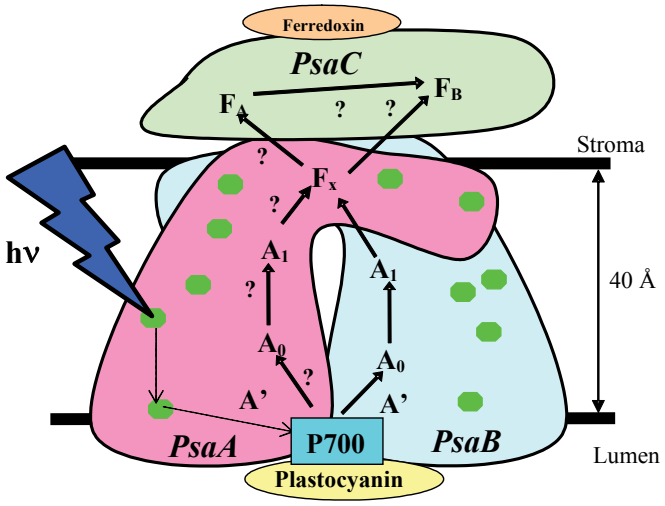

Figure 1.2: Schematic depicting the architecture of the PS I core complex, embedded in the thylakoid membrane. The possible routes for electron transfer are shown with arrows.

The electron transport chain located at the center of the PS I complex is the most important part of system. The structural organization of the ET cofactors and the electron transfer rates (in cyanobacteria) [5] are shown in Figure 1.3.

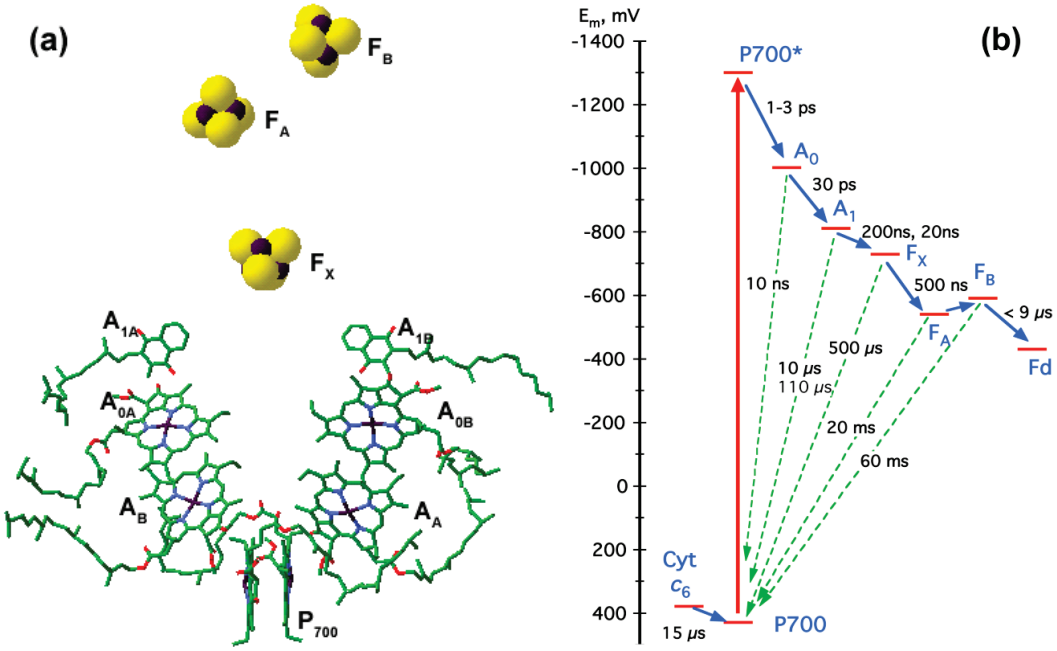

Figure 1.3: (a) Electron transfer chain in PS I [5] (b) RT electron transfer rates in cyanobacterial PS I [13].

The electron transfer pathway consists of P_{700}, a dimer of a chlorophyll *a* (Chl-*a*) and a chlorophyll *a'* (Chl-*a'*) molecule, which is the primary electron donor; two bridging chlorophyll *a* molecules ; the primary electron acceptor, two chlorophyll *a* molecules called A_0, all arranged in a pseudo-C_2 symmetry. Two phylloquinone molecules, named as A_1, function as the secondary electron acceptors. F_x, a 4Fe-4S cluster accepts the electron from one or both of the phylloquinones and transfer it to the terminal acceptors, F_A and F_B, where both these acceptors are 4Fe-4S clusters[5]. The cofactors of electron transfer chain form two branches; the cofactors of the A-branch are coordinated by *PsaA* protein, whereas the cofactors of the B-branch are coordinated mainly by *PsaB* protein of PS I and it is unclear if electron transfer occurs down one or both of these symmetrical branches [13-20].

A wide range of techniques has been used to study ET in PS I, including time resolved optical and EPR spectroscopy, in combination with site-directed mutagenesis (SDM). These studies provide evidence for two kinetic phases of ET in PS I from cyanobacteria [21-23]. The fast phase observed with a lifetime of ~10-20 ns has been attributed to ET along the B branch while the slow phase with lifetime of ~200-300 ns was attributed to ET along the A branch.

Site-specific mutations of amino acids close to the A_1 and A_0 pigments has been constructed , (in green algae, *C. reinhardtii* as well as in cyanobacterium, *Synechocystis* sp. PCC 6803) to alter the environment of these ET cofactors on the A and B branches separately [24]. Studies of these various mutants provide evidence for both branches being active, but to different extent in different species. Site-directed mutations in *C. reinhardtii* provide evidence for forward ET being more or less equal along both branches [24-26]. In cyanobacteria, however, forward ET seems to be predominantly along the A branch, and is associated with the slow phase of ET [13, 20, 22, 23, 27].

Figure 1.3(b) shows an outline of the overall light induced energetics of ET in PS I. The left side axis gives the redox potential for each radical pair [11]. P_{700} has some very unique redox properties. The lowest excited singlet state of P_{700} (P_{700}*) has a negative redox potential of ~-1300 mV. This is unprecedented for any molecular species in nature. In addition, the redox potential for P_{700} is about +400 mV which is surprisingly low given that isolated Chl-*a* molecules have redox potentials near 800 mV. One of the goals of this dissertational research is to help establish what factors determine the unique redox properties of P_{700}.

Following light excitation of P_{700} an electron is transferred to A_0 in ~1-3 ps followed by the transfer of electron from A_0^- to A_1 in about 30ps [10, 11]. The energy transfer processes that lead to the excitation of P_{700} also occur in about 30 ps. This makes direct observation of A_0^- formation/decay, and A_1^- formation, very difficult [28].

Forward ET from A_1^- to F_X is the first reaction that can be observed spectroscopically without complications associated with antenna energy transfer processes. Forward ET from A_1^- to F_X is characterized by two time constants of 20 ns (fast) and 200ns (slow) [21]. It has been shown in cyanobacteria that the fast phase is temperature independent, while the slow phase slows even more as the temperature is decreased [29-31].

If the forward electron transfer from A_0^- to A_1 is blocked, by removal or pre-reduction of A_1, $P_{700}^+A_0^-$ decays by charge recombination with a half-life of ~30ns to form the triplet state, $^3P_{700}$ [10]. The triplet state then decays to the ground state on the micro to millisecond timescale [10]. Similarly, charge recombination of the secondary radical pair state, $P_{700}^+A_1^-$, occurs when F_X, F_A and F_B are either removed or pre-reduced [10]. Finally, if none of the acceptors are modified, the recombination lifetime of the terminal radical pair state, $P_{700}^+/F_{A/B}^-$, is about 80 ms

[10]. With such a long lifetime it is straightforward to photo-accumulate a substantial population of the $P_{700}^{+}F_{A/B}^{-}$ state and makes the generation of (P_{700}^{+}-P_{700}) FTIR difference spectra feasible.

1.2 P_{700}, The Primary Electron Donor in PS I

1.2.1 A Brief Historical Review

The primary electron donor in PS I was named P_{700} by Kok, B. in 1956 (P for 'pigment' and '700' because he observed a light induced absorption change in spinach chloroplast around 700 nm) [32].

Early research on the structure and properties of the primary electron donor were mainly based on optical and EPR studies in comparison with Chl-*a* [33]. The first EPR signal from the P_{700}^{+} was obtained by Commoner in 1956 [34]. Later EPR signals associated with P_{700}^{+} and their kinetics, as well as the kinetics of optical signals were also obtained and correlated quantitatively [33, 35-37]. These early studies established P_{700} as one or more Chl-*a* molecule(s).

In 1971, Norris and co-workers noticed that the line width of the P_{700}^{+} EPR spectrum is narrower than that of Chl-*a* monomers and is consistent with an unpaired spin delocalization over an entity containing two chlorophyll molecules. This led to the conclusion that P_{700} is a Chl-*a* dimer [38]. This proposal was also supported by optical spectroscopy studies. P_{700} absorbs at 700 nm which is 30 nm further to the red than that of Chl-*a* in solution and such a shift suggests a multimeric nature to P_{700}. Also, the light-minus-dark difference circular dichroism (CD) spectrum of PS I particles shows two approximately equal bands at 696.5(+) and 688(-) nm [33, 39] which was again an indication of a dimeric structure. FTIR difference spectra obtained from PS I particles show a broad positive difference band centered near 3200 cm^{-1}, which is characteristic of the electronic transition of a dimeric species. Also two difference bands are

observed for P_{700} FTIR DS in the region of the ester absorption for Chl-*a* in solution, which also indicate that two different pigments contribute to the spectra.

1.2.2 X-Ray Crystallography of P_{700}

The first X-ray crystal structural model of PS I at 6Å resolution was isolated from Synechococcus sp. (now named *Thermo-synechococcus elongatus*) in 1987 [40]. Detailed structure at 4Å followed soon and a dimeric nature for P_{700} was proposed based on these X-ray crystallographic studies. A more complete structure of PS I at 2.5Å came out in 2001 [6, 7, 41-45], in which the two chlorophylls of P_{700} were clearly resolved and it became evident that P_{700} was a hetrodimer of a Chl-*a* and Chl-*a'* molecule (which is an epimer at the C_{13} position of the chlorin ring system), located on *PsaB* (P_B) and *PsaA* (P_A) respectively. The resolution of the crystal structure was also sufficient to analyze the protein-cofactor interactions and shows that P_{700} is an asymmetric dimer with the two chlorophyll molecules having different extent of interactions with the protein environment.

1.2.3 Structure of Chlorophyll-*a*

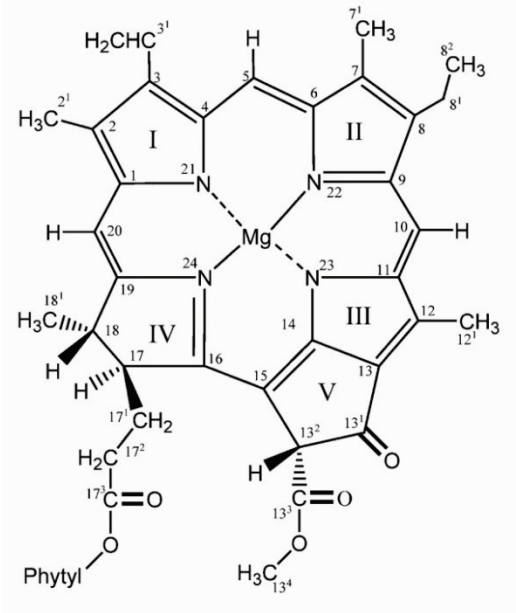

Figure 1.4: Molecular structure and IUPAC numbering scheme for chlorophyll-*a*.

The molecular structure and IUPAC numbering scheme for Chl-*a* is shown in Figure 1.4. Chl-*a* consists of a penta-pyrrolic porphyrin body with a long phytyl tail attached at the 17 position. Chl-*a* is a magnesium containing porphyrin, with the magnesium coordinated by four nitrogen atoms and characteristically contains a vinyl group at position 3. The four pyrrol rings are joined by methelene bridges and the system of double bonds forms a closed, conjugated macrocyclic loop [46, 47].

1.2.4 The Structure of P_{700}

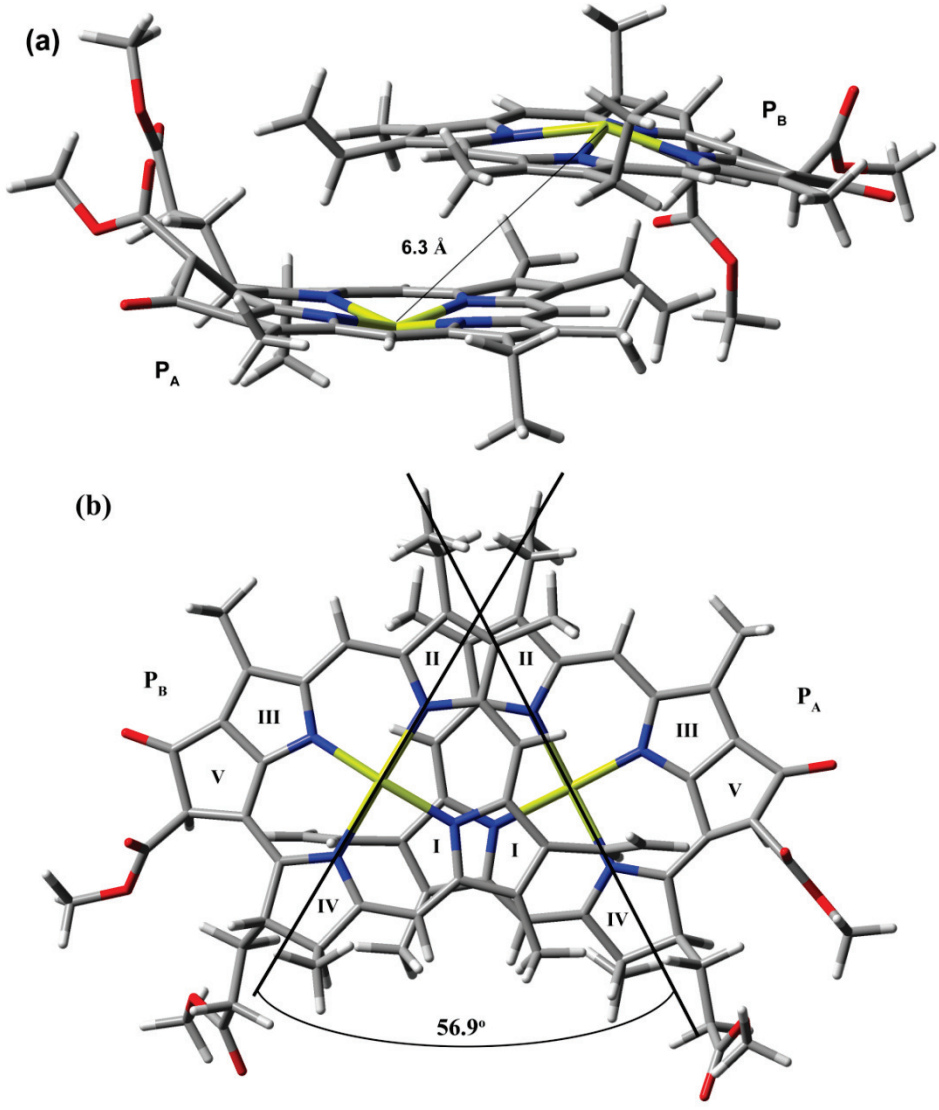

Figure 1.5: (a) Structure of P_{700} showing the Mg-Mg distance (b) The angle between the lines formed by the Mg-N4 bonds on either pigment is 56.9º.

The primary electron donor P_{700}, is a heterodimer consisting of a Chl-*a* (P_B) and a Chl-*a'*(P_A) molecule. Chl-*a'* is an epimer of Chl-*a* at the C_{13} position of the chlorin ring system (Figure 1.4). The macrocycles of two chlorophylls of P_{700} are parallel and is separated by 3.6 Å. Pyrole rings I and II of P_A and P_B overlap, and the Mg^{2+} ions are separated by 6.3 Å and the $N4_A$-Mg_A-Mg_B-$N4_B$ dihedral angle is ~57° (Figure 1.5).

1.2.5 The Protein Environment of P_{700}

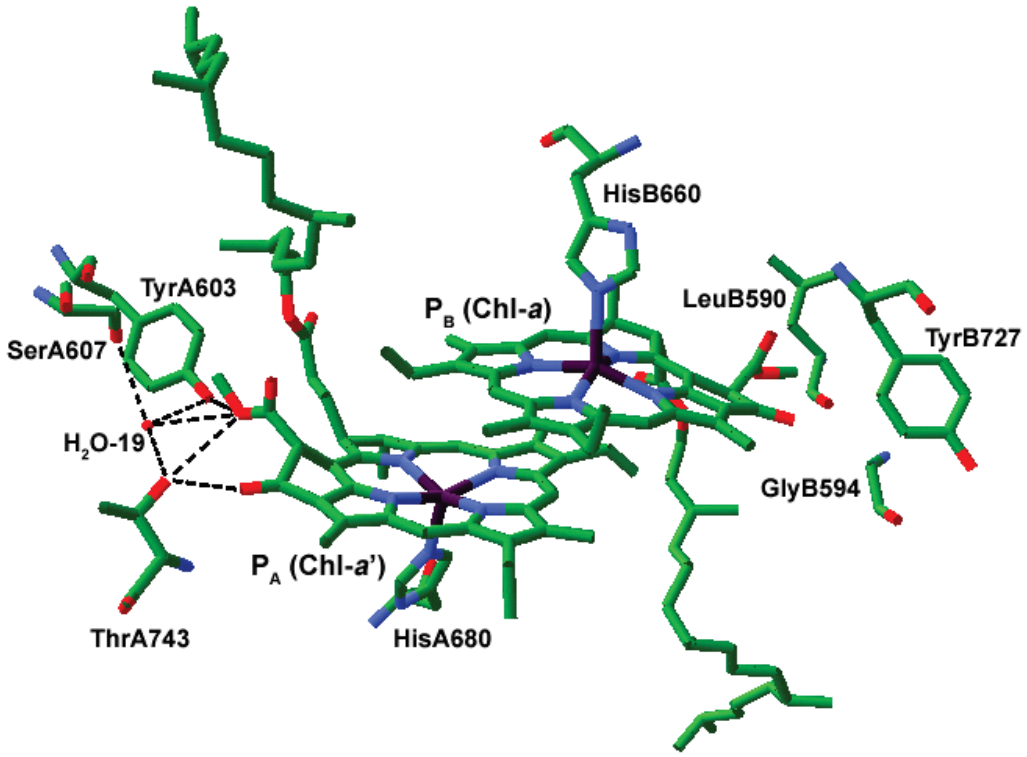

Figure 1.6: Structure of P_{700} obtained from the X-ray crystallographic structure analysis at 2.5Å resolutions.

The Chl-*a* and Chl-*a*' molecules of P_{700} are bound to *PsaA* and *PsaB* and the amino acid environment around these molecules is decidedly asymmetric (Figure 1.6). Both the chlorophylls of P_{700} are axially ligated to histidine residues symmetrically (HisA680 and HisB660 in *Thermo-synechococcus elongatus* sequence numbering scheme) but their hydrogen bonding interaction with the protein back bone is asymmetric.

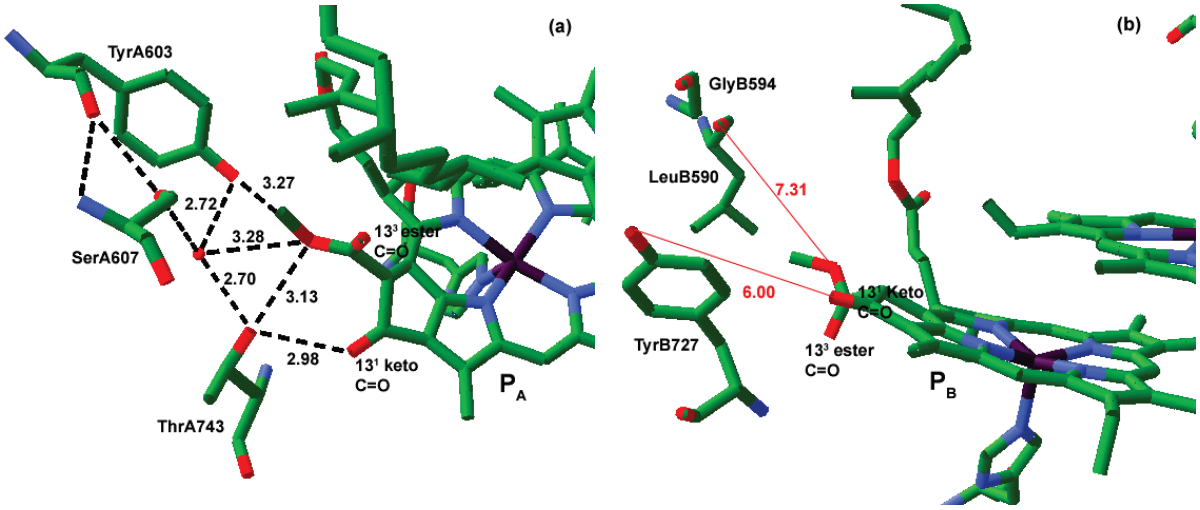

Figure 1.7: (a) View of ring V of P_A showing possible H-bond interactions to the 13^1 keto and 13^3 ester C=O groups. (b) View of ring V of P_B showing the nearby amino acids. These residues does not provide any H-bond to P_B.

Figure 1.7(a) shows that the hydroxyl oxygen of ThrA743 (The amino acid numbering is according to the sequence of the cyanobacterium *Thermo-synechococcus elongates,* for *Synechocystis* sp. PCC 6803, and *C. reinhardtii* sequence numbering see Table 1.1) is 2.98 Å from the 13^1 keto carbonyl (C=O) oxygen of P_A and is suitably positioned to form a hydrogen bond. In addition, the ThrA743 hydroxyl oxygen is 2.7 Å from the oxygen atom of a water molecule (H_2O-19). The oxygen atom of H_2O-19 water molecule is 3.28 Å away from the methoxy oxygen of the 13^3 ester C=O of P_A, and is also within hydrogen bonding distance to TyrA603 and SerA607.The C=O groups of P_B on the other hand is free of any hydrogen bonding interactions (Figure 1.7(b)).

Table 1.1: Sequence numbering of some *PsaA* and *PsaB* aminoacids in close proximity of P_{700} in *Thermo-synechococcus elongates*, *Synechocystis* sp. PCC 6803, and *Chlamydomonas reinhardtii*.

	S. elongatus	Synechocystis	C. reinhardtii
Axial ligands to P_{700}	HisA680 HisB660	HisA676 HisB651	HisA676 HisB656
Vicinity of 13^1 keto C=O of P_{700}	ThrA743 TyrB727	ThrA739 TyrB718	ThrA739 TyrB722
Vicinity of 13^3 ester C=O of P_{700}	SerA607, TyrA603 GlyB594, LeuB590	SerA603, TyrA599 GlyB585,LeuB581	SerA604,TyrA600 GlyB589,LeuB585
Vicinity of 17^3 ester C=O of P_{700}	TyrA735 PheB710	TyrA729 PheB710	TyrA731 PheB714

1.3 Structure of the Bridging or Accessory Chlorophylls

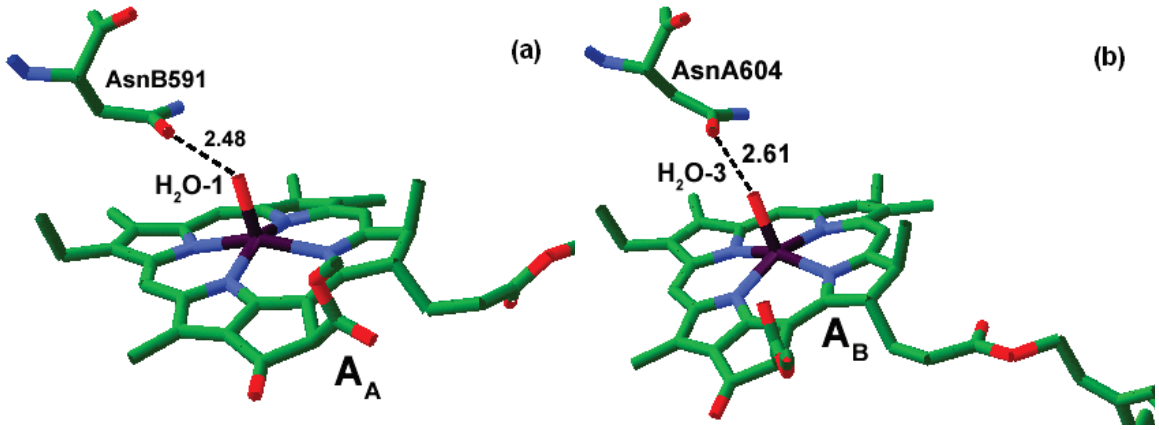

Figure 1.8: The bridging accessory chlorophylls in PS I showing their axial ligands and the asparagine residue that provides hydrogen bond to the water molecule that provides the axial ligand (a) A_A, the chlorophyll pigment in the A-branch and (b) A_B, the chlorophyll pigment in the B-branch.

The second pair of the chlorophylls in the electron transfer pathway in PS I, termed A_A and A_B (Figure 1.3), are in close proximity (8-12 Å) to the P_{700} chlorophylls and the A_0 chlorophylls. Unlike the asymmetry noted above for the chlorophylls of P_{700}, there are no significant differences in the environments of A_A and A_B. Axial ligands to A_A/A_B are provided by water molecules that are hydrogen bonded to AsnB591/AsnA604, respectively (Figure 1.8) (*Thermo-synechococcus elongatus* sequence numbering scheme). Interestingly, the *PsaB* subunit provides the axial ligand to the bridging chlorophyll in the A-branch of electron transfer while *PsaA* provides a ligand to chlorophyll on the B-branch. There are no hydrogen bonds to substituent groups of A_A/A_B.

1.4 A_0, The Primary Electron Acceptor in PS I

The Chl-*a* molecules designated A_{0A} and A_{0B} in Figure 1.3 are thought to be the primary electron accepting pigments from the excited state of P_{700}. Axial ligands to A_{0A}/A_{0B} are provided by the sulfur atom of MetA688/MetB668, respectively (*Thermo-synechococcus elongatus* sequence numbering scheme). The 13^1 keto carbonyl oxygen of ring V of A_{0A}/A_{0B} are hydrogen bonded to the hydroxyl group of TyrA696/TyrB676, respectively (see Figure 1.9).

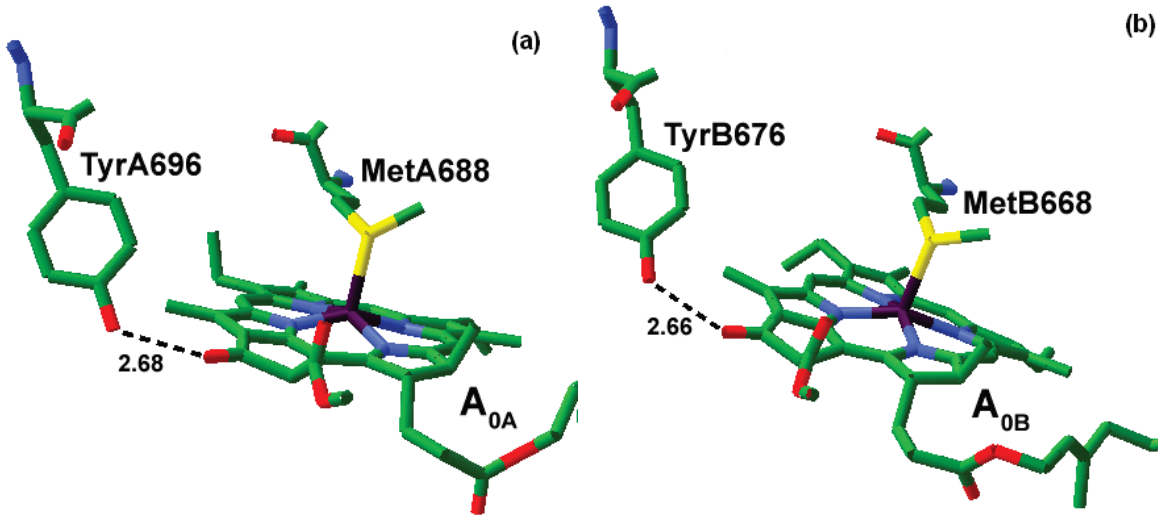

Figure 1.9: The primary electron acceptor in PS I. (a) A_{0A} pigment along with the MetA688 residue that provides the axial ligand and TyrA696 residue that provides hydrogen bond to the 13^1 keto C=O group. (b) A_{0B} pigment along with the MetB668 residue that provides the axial ligand and TyrB676 residue that provides hydrogen bond to the 13^1 keto C=O group.

The primary charge separation in PS I leads to the reduction of the primary electron acceptor, A_{0A}, A_{0B}, or both, creating the radical pair $P_{700}^{+}A_0^{-}$ in ~ 1-3 ps. The unpaired electron is transferred to the phylloquinone secondary acceptor A_1 then to the iron sulfur clusters, F_X, F_A and F_B.

A_0 is the first spectroscopically resolved electron acceptor in PS I and numerous studies have been performed using PS I particles from cyanobacteria as well as algae and the electron transfer capabilities of the two possible pathways, the A and B-branches, is still under debate. Site-directed mutations of the Met residue that serves as the axial ligand to each A_0 has been made in *Synechocystis* and *C. reinhardtii* in order to probe the direction of electron transfer in these species [13, 20, 24, 26, 27, 48-50]. Ultrafast pump probe measurements [24, 26] and EPR measurements [49, 51] from the *C. reinhardtii* mutants indicate a slowing of electron transfer from the affected A_0 chlorophylls in the mutants of both MetA688 and MetB668, implying that both branches of electron transfer are active. In contrast, studies on *Synechocystis* mutants shows that electron transfer is strongly biased toward the A-branch. Mutaion of the axial ligand to A_0

on the A-branch altered the spin polarization patters of the $P_{700}^{-}A_1^{-}$ and $P_{700}^{+}F_x^{-}$ radical pairs observed in transient EPR measurements indicating an increase in the lifetime of the $P_{700}^{+}A_0^{-}$ radical pair and a significant population of the $^3P_{700}$ formed by radical pair recombination. Mutation of MetB668 on the other hand had no discernable effect on the transient EPR signals [13, 27]. Ultrafast pump probe measurements also showed that the forward electron transfer from A_0 was slowed when Met688 was altered, but not when MetB668 was altered [20].

Mutations have also been made for the tyrosine residues, TyrA696 and TyrB676, that donate a hydrogen bond to the 13^1 keto oxygen of the A_0 chlorophylls. Transient optical absorption spectroscopy performed *in vivo* and transient EPR measurements from thylakoid membranes in these mutants showed that the mutations affect the relative amplitudes, but not the lifetimes, of the ~20 ns and 200 ns components, which have been proposed to represent the forward electron transfer from A_{1B} and A_{1A}, respectively. The mutation of TyrA696 increases the fraction of the faster component at the expense of the slower component, with the opposite effect seen in the TyrB676 mutant. This result was interpreted as a decrease in the relative use of the targeted branch thus supporting the bi-directional electron transfer mechanism in *C. reinhardtii*.

The effect of the mutation of the axial ligand of A_0 on the (P_{700}^{+}-P_{700}) FTIR difference spectra has been investigated in detail and the results are presented in Chapter 4 of this dissertation.

1.5 Fourier Transform Infra-Red (FTIR) Difference Spectroscopy (DS)

1.5.1 Infrared Absorbance Spectra

Infrared (IR) spectroscopy is used to probe/monitor vibrations in molecules exploiting the fact that molecules have specific frequencies at which they rotate or vibrate corresponding to discrete energy levels (vibrational modes). An IR spectrum is a plot of the incident IR radiation

passing through a sample versus wavenumber (or wavelength). Thus specific absorption bands in an IR spectrum relate to specific vibrational modes of specific molecular bonds.

The set of vibrational modes in a molecular sample is completely dependent on the molecular bonding geometry of the sample. This geometry is different for different samples. Therefore, IR spectroscopy is a tool that can be used to establish a unique fingerprint or signature for a given molecular sample.

1.5.2 Normal Modes

A normal mode of a molecule is defined as a vibration during which all of the atoms in the molecule move with the same frequency and phase. The frequency of this periodic motion is known as vibration frequency. A molecular vibration is excited when the molecule absorbs a quantum of energy, E, corresponding to the vibration's frequency, ν (in wavenumber), according to the relation

$$E = h\nu \qquad (1.1)$$

where *h* is Planck's constant. The set of normal modes of a pure chemical compound in a given environment is unique. For this reason the IR spectrum, which is representative of the normal mode structure of a molecule, is a unique identifier of a specific molecule in a specific environment and provides a “fingerprint” of the molecule(s).

To a first approximation, the motion in a normal vibration can be described as a kind of simple harmonic motion and the frequency of the vibration can be calculated using the equation

$$\nu = \frac{1}{2\pi c}\sqrt{\frac{k}{\mu}} \qquad (1.2)$$

where, k is the force constant (spring constant) and μ is the reduced mass. The reduced mass is given by

$$\mu = \frac{m_1 m_2}{m_1 + m_2} \qquad (1.3)$$

where m_1 and m_2 are the component masses of the two atoms forming the chemical bond.

Equation 1.2 gives the simple link relating the frequency of light that a molecule will absorb to the reduced mass of the interacting atoms and the strength of the covalent bond between the two atoms.

1.5.3 Mass and Electronic Effects

Equation 1.2 indicates that when the force constant (k) increases, vibrational mode frequency increases or up-shift, and vice versa. The force constant is related to the distribution of electron density within the chemical bond between the atoms. Hence the vibrational frequency of a functional group also depends on the electronic structure of a molecule. The higher the electron density in a bond the shorter the bond length, which in turn increases the force constant so that the vibrational frequency increases. Anion and cation formation of a molecule will cause changes in molecular electronic structure. Such frequency shifts are easily observed in IR spectra. Frequency shifts caused by changes in electronic structure of molecules (changes in force constant) is called an electronic effect.

The frequency of the vibrational mode also depends on the reduced mass of the vibrating pair of atoms (equation 1.2). Increasing the reduced mass (using isotope labeled atoms) will cause the vibrational frequency to decrease or down-shift, and vice versa. This type of isotope induced frequency alteration is called a mass effect.

1.5.4 Group Frequencies

Functional groups are specific groups of atoms within molecules that absorb infrared radiation in the same frequency range regardless of the size of the molecule it is a part of. Group frequency is defined as a diagnostic infrared band position for a particular chemical functional

group. For example, C-H stretching vibrations occur in the 2800-3000 cm^{-1} range no matter what type of molecule the functional group is part off. In the IR absorption spectrum of a molecular sample, strong bands in the 2800-3000 cm^{-1} range indicate that the molecule under study contains C-H groups.

With a knowledge of group frequencies associated with a variety of functional groups, IR band positions (frequencies) can indicate if a specific functional group is present or absent in a sample. This correlation between group frequencies and molecular structure is one of the reasons that infrared spectroscopy is such a useful tool.

1.5.5 Peak Intensities and Peak Width

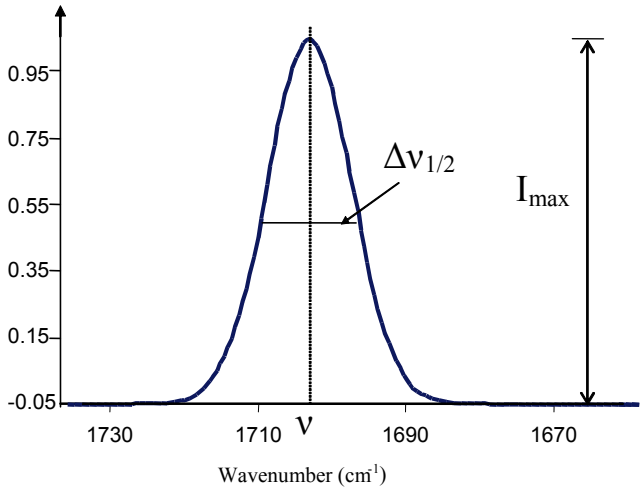

Figure 1.10: Information available in an IR absorption band.

An infrared absorption band is characterized by its peak frequency, its intensity and its width, as shown in the Figure 1.10. Band intensity is often measured simply as the maximum peak height and often allows one to distinguish which bands are due to which functional groups.

An absorption band can be described quantitatively by the Beer-Lambert law:

$$A = \log(\frac{I_0}{I}) = \varepsilon c l \qquad (1.4)$$

where A is absorbance; I_0 is the intensity of incident radiation; I is the intensity after passing through the sample; ε is the molar extinction coefficient or absorptivity; c is the concentration; and l is the path length.

The molar extinction coefficient ε depends on the square of the change in dipole moment, of the chemical bond and also on the wavelength. For a given concentration and path length, the absolute intensity of the absorption is determined by the change in dipole moment. In other words, vibrations from different chemical functional groups in the molecule give rise to infrared bands of different intensities due to difference in the change in dipole moment upon light excitation or absorptivity ε.

Carbonyl C=O groups have a large dipole moment; the change in dipole moment is also large during vibration. Therefore, C=O groups give intense IR bands, and is quite easy to identify. Chl-*a* molecule contains three C=O groups (Figure 1.4). P_{700} consists of two Chl-*a* molecules, and therefore contains six C=O groups. These C=O groups of P_{700} give rise to intense bands in IR spectra, that can be used to probe the molecular electronic structure of P_{700}.

The width of an infrared band mainly depends on the chemical environment of the vibrating molecule. When the density of a sample is high, such as samples in the liquid and solid phase, neighboring molecules will interact electrostatically (with each other and the solvent molecules) causing changes in the electronic organization of individual molecules. Thus, individual molecules will vibrate at slightly different frequencies. This leads to band broadening for the sample as a whole, as each individual molecule can be in a range of slightly different environments. The width of a band therefore provides information about the strength and nature of molecular interaction. Hydrogen bonding causes considerable band broadening [52]. For the same reason polar molecules generally exhibit broader infrared bands than non-polar molecules.

1.5.6 Difference Spectra

Figure 1.11 shows an infrared absorption spectrum for a suspension of PS I particles from cyanobacterium *S.6803*. The prominent bands of the spectrum can be identified based on the idea of functional group frequencies. The intensity of an absorption band depends on the concentration of the absorbing chromophore and the path length of the sample. In the PS I protein sample there are many thousands of functional groups contributing to each bands in the absorption spectrum. Given the very complex nature of the sample, the bands in the spectrum are very broad and specific molecular bond information cannot be extracted from this absorption spectrum. To obtain specific molecular level information from such a complicated sample difference techniques must be used.

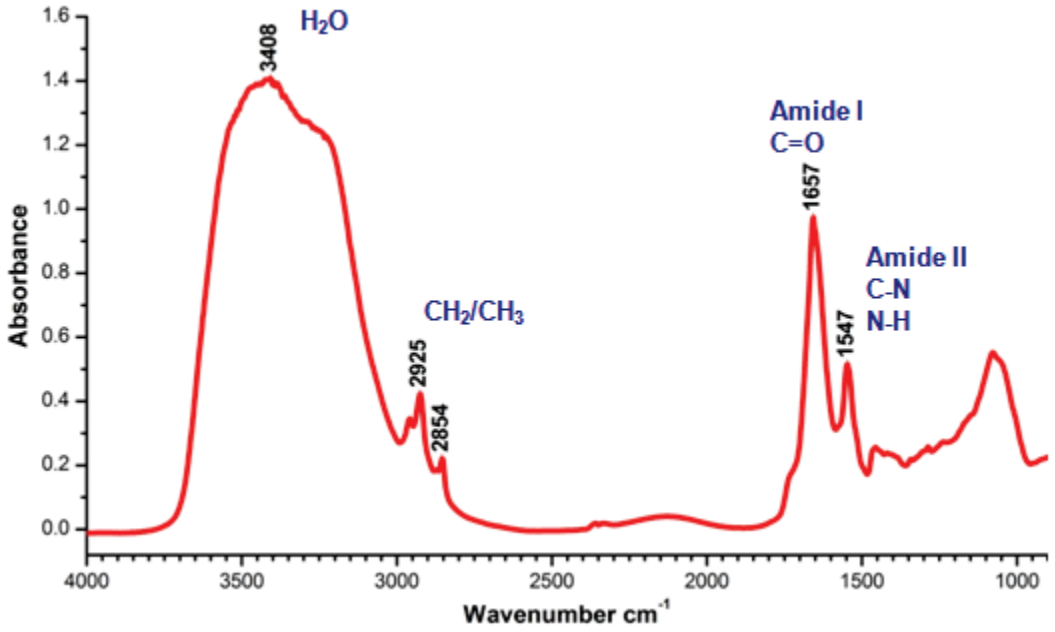

Figure 1.11: Infrared absorption spectrum of PS I particles from cyanobacterium *S. 6803*.

A difference spectrum is constructed by subtracting one absorbance spectrum from another that has been changed slightly due to some perturbation. Figure 1.12 shows a hypothetical absorption band of a molecular group. If the molecule is perturbed, for example, by the absorption of a visible photon (leading to the formation of a cation radical) there will be a

change in electron density of the molecule. This will modify the molecular bonds in the molecule, leading to frequency shifts of the molecular bonds (see section 1.5.3 for details). Figure 1.12 shows an absorption band that up-shift upon excited state formation. The absorption spectrum of excited state minus ground state gives the difference spectrum also shown in Figure 1.12. In the difference spectrum the negative band is due to a molecular mode with the absorbing pigment in the ground state, while the positive band is due to the same molecular mode of the pigment in the excited state. Only the vibrational modes that change in intensity or frequency between the two different states show up in the difference spectrum, all unchanged molecular modes are subtracted out.

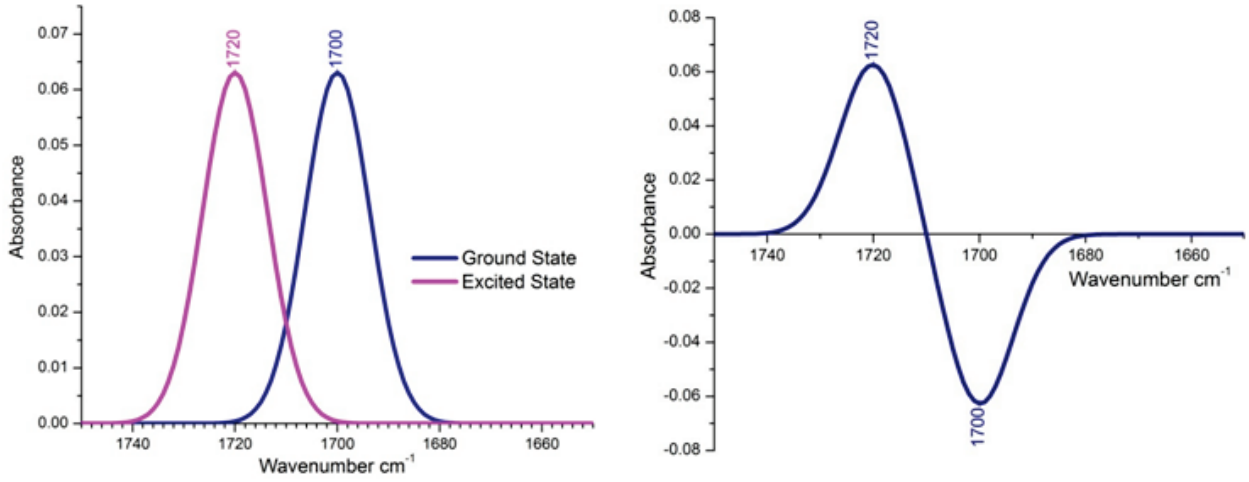

Figure 1.12: Schematic showing the construction of an IR difference band. The absorption spectrum of excited state minus ground state gives the difference spectrum shown on the right.

In a large pigment protein complex such as PS I, light excitation causes the formation of a Chl-*a* cation radical. Only molecular modes in the vicinity of this radical will be perturbed and show up in a difference spectrum. All modes associated with the protein, the solvent and other pigments will cancel out and the bands associated with single molecular bonds in PS I can be resolved using difference techniques.

The intensity of a difference band depends on the shift induced upon excited state formation, the smaller the shift, the lower the intensity of the difference band. The magnitude of

a difference band shift gives a measure of the change in electron density distributed in the molecular bond. The intensity of a difference band therefore gives a crude measure of how electron density within a bond is modified by the perturbation.

By subtracting one difference spectrum from another a double difference spectrum (DDS) can be generated, and provides information on how complete difference bands change upon isotope labeling or site directed mutagenesis of PS I particles. Figures 1.13 and 1.14 shows simulated double difference spectrum generated from two shifted difference bands.

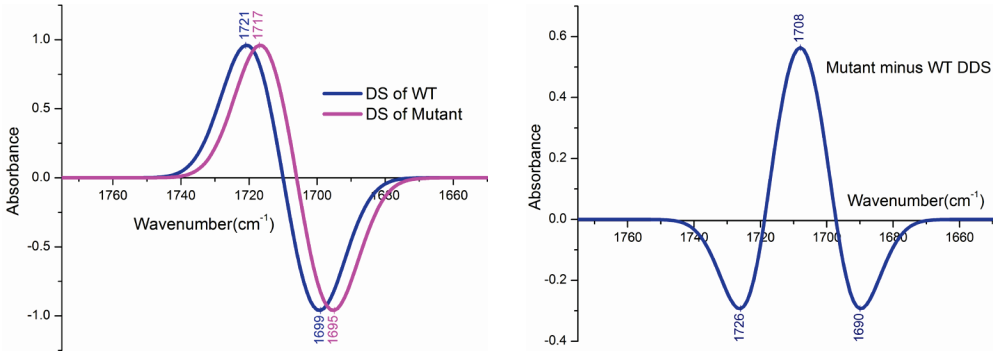

Figure 1.13: Double difference band formation. A complete difference band is down shifted 4cm^{-1}. For production of the difference spectrum of wild type (WT), a vibrational mode giving rise to a Gaussian band at 1699 cm^{-1}, with a width of 8 cm^{-1} and intensity 1.0, was assumed to up-shift to 1721 cm^{-1} upon cation formation.

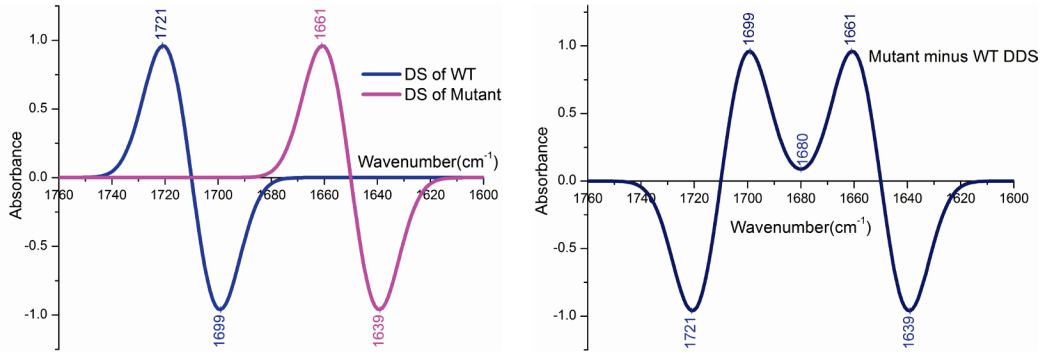

Figure 1.14: Double difference band formation. A complete difference band is down shifted 60cm^{-1}. For production of the difference spectrum of wild type (WT), a vibrational mode giving rise to a Gaussian band at 1699 cm^{-1}, with a width of 8 cm^{-1} and intensity 1.0, was assumed to up-shift to 1721 cm^{-1} upon cation formation.

In Figure 1.13 difference band 1721(+)/1699(-) cm^{-1} in the WT sample was assumed to down-shift due to mutation or isotope labeling. Such a down-shifting difference band gives a -/+/- feature in the DDS. On the other hand an up-shifting difference band would give a +/-/+

feature in a DDS. The widths and intensities of the band in the DDS spectrum are sensitive to the band shift of a complete difference band. The larger the difference band shifts the higher the intensity of the features in the DDS. If the difference band shift is large enough, four features are expected in the DDS, as shown in Figure 1.14. If there is no change for a given difference band the DDS will be featureless. Thus, DDS simplify the analysis of changes in (P_{700}^{+}-P_{700}) FTIR DS that arise due to mutation or isotope labeling.

1.6 FTIR Spectroscopy of P_{700}

P_{700} is at the heart of the photochemistry in PS I and has been the subject of sustained interest over the last two decades. Despite this, its molecular composition, its electronic structure in the ground (P_{700} neutral), cationic (P_{700}^{+}) and triplet ($^{3}P_{700}$) state are still poorly understood. Given the importance of P_{700}, and the many unresolved questions surrounding its electronic and structural organization, FTIR difference spectroscopy in combination with quantum chemical computational methodologies were used to study the molecular details of both P_{700} and P_{700}^{+}. (P_{700}^{+}-P_{700}) FTIR DS have been collected under many sets of conditions: from PS I particles from different strains, to particles with site directed mutations near the P_{700} and A_0 Chl's, to specifically isotope labeled PS I particles. Unambiguous assignment of the bands in these (P_{700}^{+}-P_{700}) FTIR DS is difficult but critical, and it is to this task that virtually most of this dissertation is devoted.

1.6.1 Light-Induced (P_{700}^{+}-P_{700}) FTIR Difference Spectra

Figure 1.15 shows a light-induced (P_{700}^{+}-P_{700}) FTIR DS obtained at 77K using PS I particles from *S.6803*, in the 5000-1200 cm^{-1} spectral region. The FTIR DS shows a broad, positive difference band centered at ~3300 cm^{-1} which has roughly twice the intensity of the positive band at 1754 cm^{-1}. This band is also observed in the FTIR DS obtained using many

other types of photosystems from many species, such as PS I from *S.7002* (unpublished data), PS I from *Acaryochloris marina* [53, 54], PS I from *C. reinhardtii* [54], PS I from green sulfur bacteria [55, 56], PS I from purple bacteria, [55, 57, 58] and PS I from heliobacteria [58, 59].

This broad positive band is generally considered as being due to a low frequency electronic transition that is associated with the dimeric nature of the primary electron donor [57, 60]. The band therefore gives indication that the species under study consists of at least two chlorophyll molecules.

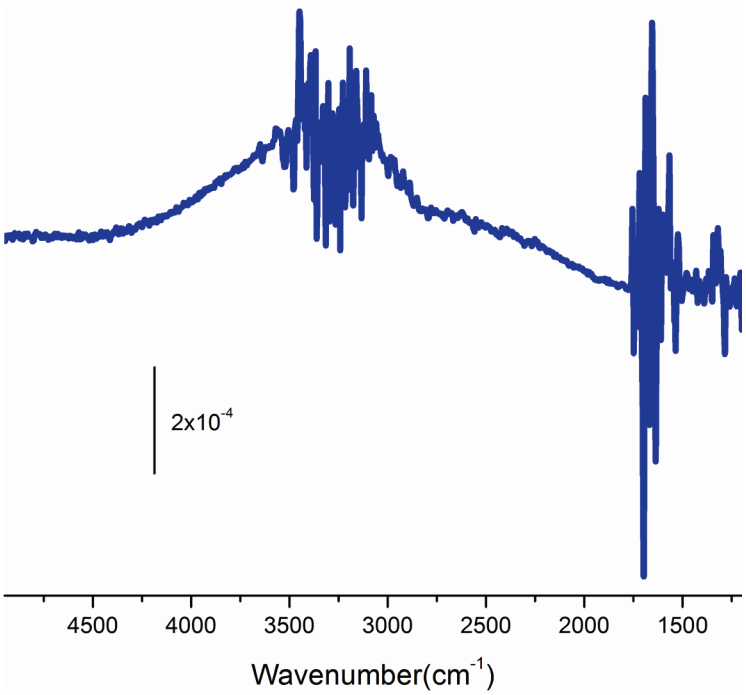

Figure 1.15: FTIR difference spectrum in the 5000-1200 cm^{-1} spectral region, obtained following light excitation of PS I particles from *S.6803* at 77K.

Figure 1.16 shows a highly resolved light induced (P_{700}^{+}-P_{700}) FTIR DS in the frequency region 1800-1200 cm^{-1} obtained from PS I particles of *S. 6803* at 77K. The frequency of each band provides information on the functional group that could cause it. Negative bands are due to the ground state (P_{700}) while positive bands are due to the excited state (P_{700}^{+}). Since different bands of P_{700} provide information on the electronic structure of a particular molecular group, if many difference bands associated with several vibrational groups of the Chls of P_{700} can be

identified then the electronic structure at several position of the Chl macrocycle can be estimated. In this way the structural and electronic organization of P_{700} and P_{700}^{+} can be elucidated.

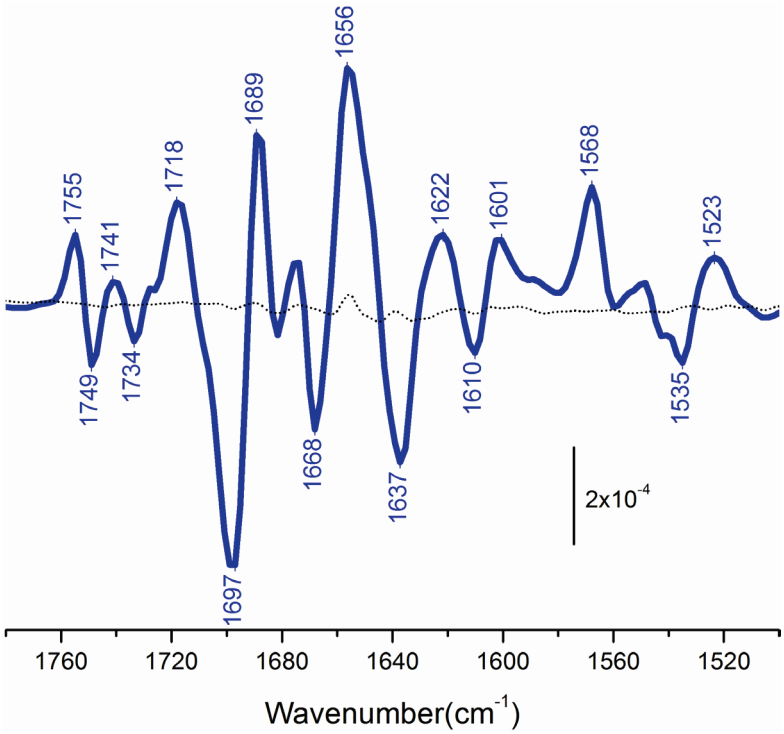

Figure 1.16: FTIR difference spectra obtained following light excitation of PS I particles from *S. 6803* at 77K, in the 1800-1500 cm^{-1} region. The dotted line shows the dark minus dark difference spectra, which actually give an estimate of the noise level in the experiment.

1.6.2 Identification of the Carbonyl Modes of P_{700}

Tavitian et al. obtained the first room temperature light-induced FTIR difference spectra of P_{700} photooxidation from PS I particles isolated from pea in 1986 [61]. From these measurements the largest negative band at ~1700 cm^{-1} in the FTIR DS (Figure 1.14) was proposed to be due to the 13^1 keto C=O group of Chl-*a* molecule(s) that constitute P_{700}. This band was supposed to up-shift to 1718 cm^{-1} upon cation formation. The difference bands at 1755(+)/1749(-) and 1741(+)/1734(-) were proposed to be due to the 17^3 and 13^3 ester C=O groups, respectively, that up-shifts upon cation formation. These band assignments were very

tentative and based on the band frequencies and comparison to neutral Chl-*a* IR absorption spectra.

Cation minus neutral FTIR difference spectra of Chl-*a* and pyroChl-*a* (Chl-*a* lacking the 13^3 ester C=O group) in tetrahydrofuran (THF) were generated by Mäntele et al. in 1988 [62] to assist the assignment of the IR difference bands in the (P_{700}^+-P_{700}) spectra. In (Chl-a^+-Chl-*a*) FTIR DS two clear difference bands are observed at 1751(+)/1738(-) and 1718(+)/1693(-) cm^{-1}. The 1751(+)/1738(-) cm^{-1} band is absent in (pyroChl-a^+-pyroChl-*a*) FTIR DS. The disappearance of this band in the pyroChl-*a* spectrum lead to the assignment of the band to the 13^3 ester C=O group. Notably, the 17^3 ester band did not contribute to the (Chl-a^+-Chl-*a*) and (pyroChl-a^+-pyroChl-*a*) FTIR DS. The 1718(+)/1693(-) cm^{-1} band [1712(+)/1686(-) cm^{-1} in (pyroChl-a^+-pyroChl-*a*) FTIR DS] observed in both (Chl-a^+-Chl-*a*) and (pyroChl-a^+-pyroChl-*a*) FTIR DS was assigned to the 13^1 keto C=O group of Chl-*a*. Based on these observations, the difference band at 1718(+)/1697(-) cm^{-1} in the light-induced (P_{700}^+-P_{700}) FTIR DS (Figure 1.16) was assigned to the 13^1 keto C=O group of Chl-*a*. The two difference bands observed at 1755(+)/1749(-) and 1741(+)/1734(-) cm^{-1} in the (P_{700}^+-P_{700}) FTIR DS were assigned to two 13^3 ester C=O groups of the Chl-*a* molecules of P_{700}. These assignments implied a dimeric structure for P_{700}. It was thought that the 13^1 keto C=O groups of both Chl-*a* molecules of P_{700} absorb at 1697 cm^{-1}. Alternatively, it was proposed that the difference band at 1656(+)/1637(-) cm^{-1} (Figure 1.16) could be due to the 13^1 keto C=O groups of one of the Chl-*a* molecules of P_{700}. However, the origin of such a large down-shift (~60 cm^{-1}) could not be explained.

In 1999, the ($^3P_{700}$-P_{700}) FTIR DS at 90 K was generated for the first time by Breton et al. using PS I particles from *S. 6803* that had the terminal iron sulfur clusters F_A and F_B removed. The direct comparison of the ($^3P_{700}$-P_{700}) to the (P_{700}^+-P_{700})FTIR DS provides a means to identify

the C=O vibrations of the chlorophylls of P_{700} in the neutral state [63]. In the ($^3P_{700}$-P_{700}) FTIR DS a negative band at 1637cm^{-1} was observed to down-shift to 1594 cm^{-1} but no band was observed at 1699 cm^{-1}. These results led to the assignment of the difference band at 1656(+)/1637(-) cm^{-1} (Figure 1.16) to the 13^1 keto C=O mode of one of the chlorophylls of P_{700}. The low frequency absorption of this C=O mode was explained by the hypothesis that one of the chlorophyll molecules of P_{700} is strongly hydrogen bonded [63]. The second chlorophyll molecule of P_{700} was assumed free of hydrogen bonding interaction with the protein. The ($^3P_{700}$-P_{700}) spectra shows a negative band at 1733 cm^{-1} around the same frequency of 1741(+)/1734(-) cm^{-1} in the (P_{700}^+-P_{700}) FTIR DS, which was assigned to the 13^3 ester C=O of one of the chlorophylls of P_{700} which could be hydrogen bonded to the protein environment [64].

The observation that the ($^3P_{700}$-P_{700}) FTIR DS shows the spectral signature of a single Chl-*a* led to the conclusion that the ^{3}P700 state is localized on a single Chl-*a* of P_{700}, P_A, that is involved in a hydrogen bonding interaction. From the (P_{700}^+-P_{700}) FTIR DS it was also shown that the positive charge on P_{700}^+ is shared among P_A and P_B. The peak-to-peak amplitude of the differential signals 1718(+)/1697(-) cm^{-1} and 1656(+)/1637(-) cm^{-1} were used to estimate the charge distribution on the 13^1 keto C=O group of the chlorophyll molecules, while the 1755(+)/1749(-) and 1741(+)/1734(-) cm^{-1} bands were used to estimate the charge distribution on the 13^3 ester C=O group [63, 65]. It was concluded from the (P_{700}^+-P_{700}) FTIR DS that there is strong delocalization of the positive charge over the two chlorophyll molecules of P_{700} at the excited state with a charge distribution ranging from 1:1 to 2:1 in favor of P_B [63, 65]. However, this conclusion was in complete disagreement with the ENDOR spectroscopic data that was available at that time, where the charge/spin distribution over the chlorophyll of P_{700}^+ was proposed to be in the range 1:6 to 1:9 thus suggesting a strong localization of the charge/spin on

to single chlorophyll of P_{700}^{+}. In addition, it was observed that the replacement of HisA676 and HisB656, the amino acid residues providing axial ligands to P_{700}, in *C. reinhardtii* with different amino acids through site-directed mutagenesis resulted in altered spectroscopic properties of P_{700} [66]. The effects of these mutations were pronounced when HisB656 was replaced compared to HisA676. Furthermore, the electron spin density distribution of P_{700}^{+}, obtained from ENDOR spectroscopic data showed significant changes only when there was a mutation for HisB656, which led to the conclusion that the ^{3}P700 state resides on P_B, the same chlorophyll that carries most of the electron density of P_{700}^{+} [66]. However, these conclusions were at odd with those proposed by Breton et al. [63], where the ^{3}P700 state was proposed to be concentrated on P_A, while the charge in $P700^{+}$ was shared between P_A and P_B. These discrepancy between the interpretations of the spectroscopic results led Hastings et al. [54] to re-evaluate the (P_{700}^{+}-P_{700}) FTIR DS of *C reinhardtii* and to propose a different set of assignments for the 13^1 keto C=O groups of P_{700}, which was considerably different from the earlier assignments proposed by Breton et al [63, 65].

A site-directed mutant from *C. reinhardtii* where the axial histidine ligand, HisA676, changed to serine was investigated by Hastings et al., and it was observed that the ~1700 cm^{-1} negative band was split into two components upon mutation [54]. This observation led to the conclusion that the negative band around 1700 cm^{-1} in the (P_{700}^{+}-P_{700}) FTIR DS is due to 13^1 keto C=O modes of both chlorophylls of P_{700}. It was also proposed that upon cation formation one of the C=O mode frequency up-shift to 1718 cm^{-1} while the other down-shifts to 1687 cm^{-1} thus being able to explain the presence of the big positive band around 1687 cm^{-1} [54] (Figure 1.16). The differential band at 1656(+)/1637(-) cm^{-1} in the assignment proposed by Hastings et

al. was assigned to one or both of the histidine residues that provide the axial ligands to P_A and P_B.

1.6.3 Isotope Labeling Studies of P_{700}

Isotope labeling is a method in which specific atoms in a molecule under consideration are replaced with a stable isotope. ^{15}N, ^{13}C, ^{18}O and ^{2}H are stable isotopes of ^{14}N, ^{12}C, ^{16}O and ^{1}H, respectively. Replacing atoms with their stable isotope results in a change in the reduced mass of the functional group including the atom, and causes a change in the vibrational frequency of the group (see Section 1.5.3). Isotope labeling, global and site specific, is a widely used strategy to distinguish the pigment vibrational modes from the protein backbone [29, 63, 67-69].

Wang et. al. obtained light induced (P_{700}^{+}-P_{700}) FTIR DS from PS I particles of *S. 6803* that are uniformly ^{2}H , ^{13}C and ^{15}N labeled [68]. Upon uniform ^{2}H labeling of PS I, it was shown that all difference bands associated with ester/keto carbonyl modes of the chlorophylls of P_{700} and P_{700}^{+} down-shift 4-5/1-3 cm^{-1}, respectively. Also, the observed ^{15}N and ^{2}H induced band shifts in the spectral region ~1700 cm^{-1} strongly support the idea that the 13^1 keto carbonyl modes of both chlorophylls of P_{700}contribute to this band [68]. It was also shown that the negative difference band at approximately 1637 cm^{-1} is somewhat modified in intensity, but unaltered in frequency, upon ^{2}H labeling. This observation is in line with the band assignments proposed by Hastings et. al. [54] and indicates that 1637 cm^{-1} band is not associated with a strongly hydrogen bonded keto carbonyl mode of one of the chlorophylls of P_{700}.

(P_{700}^{+}-P_{700}) FTIR DS from PS I particles with site specific isotope labeling, where the chlorophyll molecules comprising P_{700} were labeled *in situ* using ^{13}C, ^{18}O [69] and ^{2}H [70, 71] has also been obtained. Kim et. al. studied PS I particles in which the 13^4 methyl hydrogen atoms

of the Chl's of P_{700} have been deuterated (^2H labeled). Based on the observation that several derivative features spans the 1775-1675 cm^{-1} region in the (^1H-^2H) isotope edited (P_{700}^+-P_{700}) FTIR double difference spectra (DDS) from these particles, it was suggested that at least four distinct 13^3 ester C=O vibrations contribute to the spectra in this region[70].

(P_{700}^+-P_{700}) FTIR DS has been collected from PS I particles were specific carbons (C_2, $C_3{}^1$, C_7, $C_8{}^1$, C_{12}, $C_{13}{}^1$, $C_{17}{}^1$ and $C_{18,}$ see Figure 1.4) of the P_{700} chlorophylls were ^{13}C labeled [69]. Also, (P_{700}^+-P_{700}) FTIR DS for PS I particles were the oxygen atom of the 13^1 keto C=O group has been changed to ^{18}O has also been obtained [69]. Based on these studies it was proposed that P_A^+ give rise to two chlorophyll keto vibrational bands, with frequencies at 1656 and 1689 cm^{-1}. In contrast, it was proposed that P_A gives rise to one chlorophyll keto band at 1637 cm^{-1}. The assignment of two positive bands to P_A^+ keto frequencies was based on the assumption that the protein relaxation induces a distribution of hydrogen bond in the PS I particles upon cation formation.

1.6.4 Site-Directed Mutations Near P_{700}

Site-Directed Mutagenesis (SDM) is a method in which one or more amino acid residues at a specific location in a protein are exchanged by a different residue. Site-directed mutagenesis has been used to modify the amino acids that are in the vicinity of P_{700}. The assumption is that any change in the pigment-protein interaction will alter the spectroscopic properties of P_{700} in the ground and cation state and can be used to identify specific pigment-protein interactions.

Particularly, in *C. reinhardtii*, the histidine residues HisA676, HisB656 (*C. reinhardtii* sequence numbering, for *S. 6803* numbering see Table 1.1) which provides axial ligand to the chlorophyll molecules of P_{700} has been modified to, Glutamine (Gln), Serine (Ser), Cysteine (Cys), Glycine (Gly), and Asparagine (Asp). Only the substitutions with Ser, Gln and Asp

residues led to a significant accumulation of PSI in the thylakoid membranes. The ENDOR spectroscopy of these mutants showed that the electron spin density distribution of P_{700}^{+} was changed only upon mutation of HisB656 residue. These observed changes in the spectroscopic properties upon mutation led to the conclusion that the triplet state of P_{700} is mainly localized on P_B [66, 72]. Also, significant perturbation was observed for the bands associated with 13^1 keto C=O of P_{700} in the (P_{700}^{+}-P_{700}) FTIR DS of HisA676 mutant. This led Hastings et al. [54] to propose an assignment of bands for the 13^1 keto C=O groups of P_A that differs considerably from the previous assignments by Breton et al [63, 65].

The (P_{700}^{+}-P_{700}) FTIR DS of the mutants of *S. 6803*, where HisB651 (*S. 6803* sequence numbering), which provide the axial ligand to P_B, replaced by (Cysteine) Cys, (Glycine) Gly or (Leucine) Leu was obtained by Breton et al. in an attempt to investigate the extent of delocalization of the positive charge in the oxidized dimer of chlorophyll constituting P_{700} [73]. The conclusion that the charge of P_{700}^{+} is delocalized was supported by the new investigation, while the variations in the frequency and intensity of the C=O vibrational bands of the chlorophylls of P_{700} observed in the (P_{700}^{+}-P_{700}) FTIR DS of the histidine axial ligand mutants were attributed to the repositioning of the P_{700} dimer in the protein cavity [73].

The availability of the high resolution crystal structure of cyanobacterial PS I at 2.5Å resolutions made it possible to clearly identify the amino acid residues that might have an effect on the C=O mode vibrations of P_{700}. Following the high resolution structure, many studies have been performed with site-directed mutations for few selective *PsaA* and *PsaB* amino acids in close proximity of P_{700}. One of the first studies by FTIR difference spectroscopy of mutation induced effect to the C=O modes of P_A was with ThrA739 in *C. reinhardtii* replaced by Tyrosine (Tyr), Histidine (His) or Valine (Val) residues [74]. The (P_{700}^{+}-P_{700}) FTIR DS for the mutants

T(A739)V, T(A739)H, and T(A739)Y lacked the negative band at 1634 cm^{-1}, which was earlier assigned to the ground state absorption of P_A by Breton et al. [63, 65], and instead had new negative bands at 1672, 1669 and 1657 cm^{-1}, respectively. The band at 1634 cm^{-1} was hence assigned to the 13^1 keto C=O group of P_A, the up-shift of this band in mutants were attributed to the removal of the hydrogen bonding interaction to P_A upon mutation [74].

In an investigation following this, the residue ThrA739 was replaced by (Alanine) Ala in *C. reinhardtii*. The mutation of Thr residue to Ala considerably altered the (P_{700}^{+}-P_{700}) FTIR DS. The modification upon mutation of the (P_{700}^{+}-P_{700}) FTIR DS was explained using the band assignments proposed by Hastings et al. [54]. On comparison of the (P_{700}^{+}-P_{700}) FTIR difference spectra of the mutant to the wild type, Hastings et al. concluded that the hydrogen bond to the 13^1 keto C=O of P_A is still present in the T(A739)A mutant, and also proposed that this could be mediated through an introduced water molecule [75].

A series of mutations of the amino acid residues in the proximity of the C=O groups of P_A and P_B in *S. 6803* has been reported recently [76, 77]. On the *PsaA* protein a single mutation of ThrA739 to Phenylalanine (Phe) as well as a set of three mutations were ThrA739 changed to Tyrosine (Tyr), SerA603 to Glycine (Gly), and TyrA599 to Leucine (Leu) were performed. The aim of these mutations were to modify the hydrogen bonding interactions to the C=O groups of P_A by making the environment similar to the C=O groups of P_B, which exhibits no hydrogen bonding interaction with the protein backbone. A similar study where the amino acid residues in the vicinity of P_B were modified, in an attempt to introduce hydrogen bonding interaction to the C=O groups of P_B has also been reported [76]. On the *PsaB* protein, a single mutation of TyrB718 to Threonine (Thr), a double mutant were GlyB585 was changed to Serine (ser) and LeuB581 was changed to Tyrosine (Tyr) as well as a set of three mutations were TyrB718

changed to Threonine (Thr), GlyB585 to Serine (Ser), and LeuB581 to Tyrosine (Tyr) were performed.

(P_{700}^{+}-P_{700}) FTIR DS has been obtained from these different *PsaA* and *PsaB* mutants at 278K (5˚C). It was shown that when the residue ThrA739, which donates a hydrogen bond to the 13^1 keto C=O group of P_A, was changed to Phe, a differential signal at 1653(+)/1638(-) cm^{-1} in the (P_{700}^{+}-P_{700}) FTIR DS up-shifts by ~30-40 cm^{-1}. The same up-shift was also observed in the FTIR spectrum of a triple mutant in which the residues involved in the hydrogen bonding network to the 13^1 keto and bridging oxygen of the 13^3 ester C=O group of P_A have been changed to the amino acid side residues present around P_B. The down-shift of the difference band attributed to the 13^1 keto group of P_A upon mutation was taken as an indication of the rupture of the hydrogen bond or, at least, a strong decrease of its strength in the mutant(s). All of these observations were thought to support the assignment scheme proposed previously for the carbonyls of P_{700} and P_{700}^{+} [63]. But no explanation was provided why the band up-shifts only ~30-40 cm^{-1}, while the H-bond to the 13^1 keto C=O group of P_A is thought to be responsible for the ~60 cm^{-1} down-shift of the band compared to the 13^1 keto vibrational mode of P_B.

The FTIR study of the Y(B718)T mutant and the Y(B718)T/G(B585)S/L(B581)Y triple mutant where all the three amino acids near 13^1 keto and 13^3 ester C=O groups of P_B were replaced with the analogous residues on the P_A side shows significant modification for the 1718(+)/1698(-) cm^{-1} band attributed to the 13^1 keto group of P_B. A significant decrease in intensity of this band was observed in the mutants followed by the appearance of a new negative band at 1668(-) cm^{-1}. These observations were considered as an evidence that the 13^1 keto C=O group of P_B/P_B^{+} engages in a relatively strong hydrogen bonding interaction with the introduced amino acid residues in a significant fraction of the reaction centers. The crystal structure

provides no evidence for the possibility of a direct hydrogen bonding interaction between the 13^1 keto C=O group of P_B and the introduced amino acid residues in any of the mutants, and the assumption is that water molecule(s) introduced upon mutation could possibly mediate such an interaction.

Since the FTIR spectroscopy study of the different *PsaA* and *PsaB* protein left many questions unanswered regarding the protein-pigment interactions of P_{700} as well as the assignment of the difference bands in the (P_{700}^{+}-P_{700}) FTIR DS, these mutants were investigated using low temperature FTIR DS. A detailed discussion of the work is presented in Chapters 2 and 3.

1.7 The Directionality of Electron Transport in PS I

The electron transfer (ET) cofactors in PS I are arranged along two virtually identical branches extending across the thylakoid membrane from the primary electron donor, P_{700} (Figure 1.3). This highly symmetric arrangement of cofactors raises the question whether both branches of cofactors are equally active in PS I.

Pigments on the two branches are spectroscopically indistinguishable; hence the focus has been on creating site-directed mutants where point mutations are made for specific amino acids along the *PsaA* or *PsaB* branch. The ET directionality issue has been addressed using spectroscopic techniques like EPR, ENDOR and optical spectroscopy in these site-directed mutants [13, 20, 24, 26, 49, 78]. Most of the evidence for the directionality of ET has come from studies involving specific mutations around the phylloquinone secondary electron acceptor, A_1 [14, 17, 18, 23, 25].

Recently site-directed mutants where the methionine axial ligands to the A_0 primary electron acceptor, MetA684 and MetB664 in *C. reinhardtii* (MetA688 and MetB668 in *S. 6803*)

were changed have been constructed. For *S. 6803*, the methionine was changed to leucine or asparagine [13, 20] while for *C. reinhardtii*, the methionine was changed to histidine, leucine or serine [24, 26, 49]. The central magnesium atoms of each of the primary electron acceptor chlorophylls, A_0, are coordinated by sulfur atom of methionine (*PsaA*684 and *PsaB*664 for *C. reinhardtii*). This provides a weak ligand and the premise of the mutations of methionine at the binding site to histidine in *C. reinhardtii* (and asparagine in *S. 6803*) is that these polar amino acid groups have the potential to provide a stronger fifth ligand to the magnesium atom of the chlorophyll acceptor on the respective branches and thus alter the redox properties of A_0, which could result in different spectroscopic properties. These mutants have been studied by EPR and ultrafast optical spectroscopy. The optical and EPR studies on *C. reinhardtii* supported the hypothesis that both branches of ET are equally active while the analogous studies on *S. 6803* shows evidence for a uni-directional electron transfer.

The effect of the mutation of the axial ligands of A_0, on the (P_{700}^+-P_{700}) FTIR DS has been investigated in detail using *C. reinhardtii* PS I particles. The (P_{700}^+-P_{700}) FTIR DS obtained from these mutants clearly support the hypothesis that both branches of electron transfer are equally active. A detailed discussion of this study is presented in Chapter 4.

1.8 Vibrational Frequency Calculations of Chlorophyll-*a*

(P_{700}^+-P_{700}) FTIR DS has been obtained from PS I particles under many set of conditions: from PS I particles from different species, to particles with site-directed mutations near P_{700} and A_0, to globally and site specifically isotope labeled PS I particles [54, 71, 76, 77]. The frequency and intensity information available in these difference spectra provide a wealth of information on the axial ligands, hydrogen bonding status as well as the polarity of the environment of specific functional groups that are part of the chlorophyll molecules constituting P_{700}. However, given the

complexity of *in vivo* pigment-protein interactions, assignment of the FTIR bands to vibrational modes in specific types of environment is very difficult. There is a demonstrated need for a quantitative understanding of how vibrational mode frequencies and intensities change upon radical formation, and upon changes in environment introduced through site directed mutations.

Up until recently, quantum chemical computational methods have played only a minor role in FTIR spectral band interpretation and assignment, especially as it applies to large molecular systems like Chl-*a*. However, computational capabilities are increasing, and recently density functional theory (DFT) based vibrational mode frequency calculations for several Chl-*a* and Chl-a^+ model molecular systems has been undertaken [79, 80]. The calculated (Chl-a^+-Chl-*a*) IR DS in solvents shows remarkable similarity to the experimental (Chl-a^+-Chl-*a*) FTIR DS in THF. However, the compositions of the calculated vibrational modes are very different from that suggested from experiment. Based on the calculations new suggestions were proposed for the origin of the bands in experimental (Chl-a^+-Chl-*a*) FTIR DS. A detailed discussion of the calculation of the vibrational frequencies of Chl-*a* in solvents is presented in Chapter 5.

The effect of solvation on the calculated IR spectra of Chl-*a* has been mostly studied using the Polarizable Continuum Model (PCM) where the solvent is modeled as a dielectric continuum [79, 80]. But PCM method has limitations as they do not model possible axial ligands or hydrogen bonds to Chl-*a* molecule. Hence in order to include the effect of these possible interactions, on the vibrational modes of Chl-*a*, vibrational frequency calculations were performed in the presence of real solvent molecules using the QM/MM method. A detailed discussion of this study is presented Chapter 6.

The role and relevance of axial ligation to Chl's has been studied computationally before [81-83], and how axial ligation impacts the geometry, bond dissociation energies, reduction

potentials and visible absorption spectra has been studied [82-85]. Also, hydrogen bonding is the most significant non bonding interaction to Chl pigments in a protein environment, and the effect of peripheral hydrogen bonding on electron affinity and spin density of Chl has been investigated. It was shown that the spin density of Chl-a^+ could be regulated by peripheral H-bonding [84]. However, no investigation of how axial ligation and peripheral H-bonding impact the vibrational properties of Chl-*a*/Chl-*a*' have been undertaken. This is in spite of the fact that experimental FTIR DS is available for P_{700} with site specific mutations were the axial ligand [54] and the peripheral amino acid residues are modified [76, 77]. Hence, using DFT calculations, a detailed investigation of how axial ligation and H-bonding modify the vibrational properties of Chl-*a* was undertaken. A detailed description of this work is presented in Chapter 7.

The oxidation potential (E_{ox}) of P_{700} plays a significant role in determining the electron transfer kinetics in PS I. E_{ox} of P_{700} is ~440 mV [10], significantly lower than that of monomeric Chl-*a* (~800 mV) or P_{680} (~1200 mV), the homodimeric Chl-*a* species that functions as primary electron donor in PS II. One of the goals of computational research on photosynthetic reaction centers is to model these extreme redox properties of the dimeric donor cofactors. A detailed study of the calculated chemical properties of P_{700} using DFT methods is presented in Chapter 8.

CHAPTER 2

HYDROGEN BONDING TO CARBONYL GROUPS OF *PSAA* CHLOROPHYLL OF P_{700} INVESTIGATED USING FTIR DIFFERENCE SPECTROSCOPY AND SITE-DIRECTED MUTAGENESIS

2.1 Introduction

Photosystem I (PS I) is a pigment protein complex present in the thylakoid membrane of plants and bacteria that catalyses the light-induced transfer of electrons from plastocyanin across the membrane to ferredoxin. In PS I the electron transfer process is initiated by light induced oxidation of a hetero-dimeric chlorophyll-*a* / chlorophyll-*a*' (Chl-*a*/Chl-*a*') species called P_{700}. The electron from the light excited P_{700} is transferred across the membrane via a sequential series of electron transfer cofactors, A_0 (Chl-*a*), A_1 (phylloquinone), and F_X (an iron sulfur complex). In PS I, there are two symmetrical sets of electron transfer cofactors, bound to two membrane spanning proteins called *PsaA* and *PsaB*, and it is uncertain if electron transfer occurs down one or both of these symmetrical branches. Although the organization of the electron transfer cofactors along the two branches is symmetrical, the protein interaction to the primary electron donor P_{700} is highly asymmetric. This asymmetric interaction could determine the electronic and structural organization of P_{700}, which could likely influence the direction of electron transfer. Renewed interest in the electronic and physical organization of P_{700} stemmed from the possible role of P_{700} in modulating the directionality of electron transfer in PS I.

The two pigments of P_{700} bound by *PsaA* and *PsaB* proteins are called P_A (Chl-*a*') and P_B (Chl-*a*) respectively. These chlorophylls are asymmetrically bound, with P_A being involved in a hydrogen bond (H-bond) network with several surrounding amino acid residues and a water molecule (Figure 2.1). P_B is not involved in H bonding. Figure 2.1(a) shows the amino acids

residues that are in the vicinity of P_{700}. Figure 2.1(b) shows that the hydroxyl oxygen of ThrA739 (The amino acid numbering is according to the sequence of the cyanobacterium *Synechocystis* sp. PCC 6803) is 2.98 Å from the 13^1 keto carbonyl (C=O) oxygen of P_A and is suitably positioned to form a hydrogen bond. In addition, the ThrA739 hydroxyl oxygen is 2.7 Å from the oxygen atom of a water molecule (H_2O-19). The oxygen atom of H_2O-19 water molecule is 3.28 Å away from the methoxy oxygen of the 13^3 ester C=O of P_A, and is also within hydrogen bonding distance to TyrA599 and SerA603.The C=O groups of P_B on the other hand is free of any hydrogen bonding interactions.

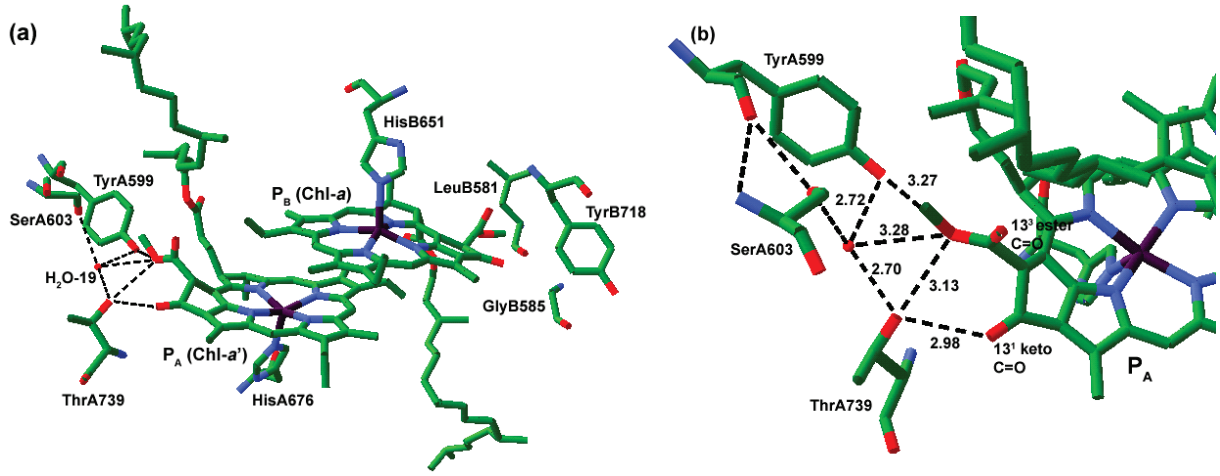

Figure 2.1: (a) Structure of P_{700} in wild type *Synechocystis* sp. PCC 6803 (b) Possible hydrogen bond interactions to the C=O group of P_A.

Removal of ThrA739, and the possible H-bond to the 13^1 keto C=O of P_A, could disrupt the H-bond network, which could alter the properties of P_{700}. To investigate these altered properties, a site-directed mutant from *Synechocystis* sp. 6803 (*S. 6803*) in which ThrA739 has been replaced by a non-polar amino acid, phenylalanine was studied. This mutant is termed the T(A739)F mutant. The modeled orientation of substituted phenylalanine using the crystal structure of PS I at 2.5 Å resolutions [6] is shown in Figure 2.2. The possible orientation/position of the introduced amino acids in the mutant was modeled using Swiss-Pdb viewer software. The structural model shown in Figure 2.2 shows the best rotomer of the mutated amino acid. The

best rotomer model is where the introduced amino acids has minimum clash with the backbone and side chain atoms of surrounding protein while having maximum possibility of forming H-bonds and S-S bonds.

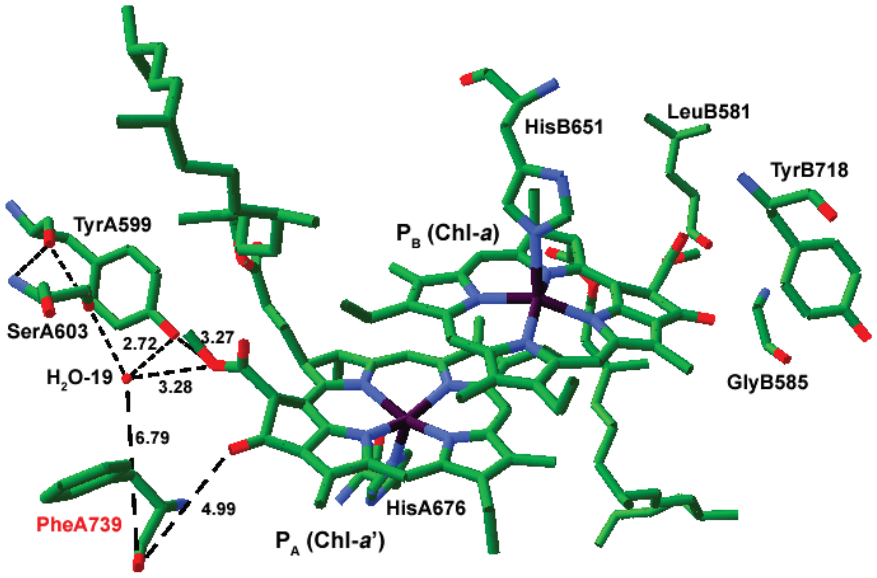

Figure 2.2: Modeled orientation of the substituted phenylalanine in T(A739)F mutant of *S. 6803* using crystal structure of PS I at 2.5 Å resolutions.

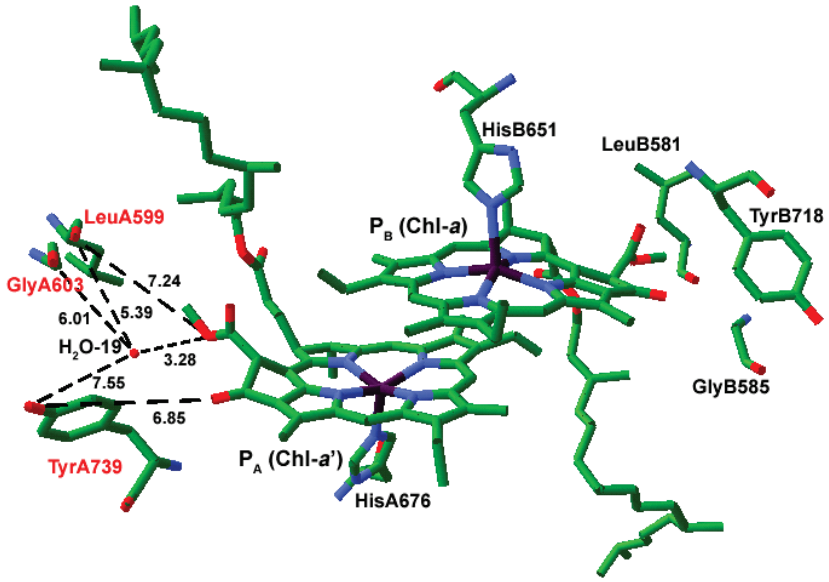

Figure 2.3: Modeled orientation of the substituted tyrosine, glycine and leucine in the *PsaA* triple mutant of *S. 6803* using crystal structure of PS I at 2.5 Å resolutions.

A triple mutant where ThrA739 is replaced by tyrosine, SerA603 is replaced by glycine and TyrA599 is replaced by leucine was also studied. This set of mutations were devised to alter the H-bonding pattern around the 13^1 keto C=O and 13^3 carbomethoxy groups of P_A by making the protein environment similar to P_B. P_B exhibits no H-bonding interaction with the protein. This triple mutant is termed the T(A739)Y/S(A603)G/Y(A599)L mutant and the modeled orientation of the substituted amino acids is shown in Figure 2.3.

Low temperature (P_{700}^{+}-P_{700}) FTIR difference spectroscopy (DS) was used to analyze mutation induced alterations in the molecular and electronic structure of P_{700} and P_{700}^{+} in these mutant species. FTIR spectroscopy is a sensitive molecular specific probe, and the (P_{700}^{+}-P_{700}) FTIR difference spectra provide specific structural information concerning P_{700}, the primary electron donor. In addition, these spectra will reflect the mutation induced changes in H-bond strengths and/or structural alterations of P_{700}. Room temperature (P_{700}^{+}-P_{700}) FTIR DS from these mutant species has been obtained before [77], but the study left many questions unanswered regarding the protein-pigment interactions of P_{700} as well as the assignment of the difference bands in the (P_{700}^{+}-P_{700}) FTIR DS. One of the problems in the RT studies is that multiple overlapping bands limits the interpretability of the spectra. The intention behind the low temperature measurements is to alter the difference bands so that underlying component bands and band-shifts can be detected.

To help interpret the FTIR DS associated with the mutants density functional theory (DFT) based methods were used to simulate the vibrational properties of Chl-*a* model systems, in the absence and presence of a H-bond to the 13^1 keto C=O group, to gain a more detailed understanding of not only how frequencies may shift upon removal of H bonding, but also how

band intensities are altered. Such information is vital for an understanding of mutation induced modifications in (P_{700}^{+}-P_{700}) FTIR DS.

2.2 Materials and Methods

2.2.1 Instrumentation

FTIR difference spectra were recorded using a Bruker IFS/66 FTIR spectrometer. Instrumental operation and spectral analysis were performed using the software package OPUS 4.0 supplied by Bruker Optics.

The experimental layout of equipment for steady state FTIR DS measurements at 77K is shown in Figure 2.4. The globar (silicon carbide) IR source is cooled by circulating water. The interferometer is equipped with a KBr beam-splitter which is transparent in 40,000-400 cm^{-1} region. KBr is hygroscopic and to prevent "fogging" of the beam splitter the entire FTIR spectrometer is continuously purged with dry air [86].

The FTIR spectrometer contains a helium neon (He-Ne) laser (not shown) which is collinear to the IR beam and tracks the position of the moving mirror. Interference fringes of the He-Ne laser beam are used to measure the optical path difference of the interferometer mirrors and the wavelength of 632.8 nm is used as an internal wavenumber standard in the spectrometer [86].

For all measurements described in this dissertation, a photoconductive mercury cadmium telluride (MCT) IR detector was used (Graseby D313). This detector has a 0.2-1 MHz bandwidth. The detector is sensitive in the 7000-600 cm^{-1} region and is liquid nitrogen cooled. The detector has a surface area of 1 mm^2, and is connected to a 200 kHz preamplifier with both AC and DC coupled outputs. For all rapid-scan steady state FTIR experiments, the preamplifier AC coupled output was used.

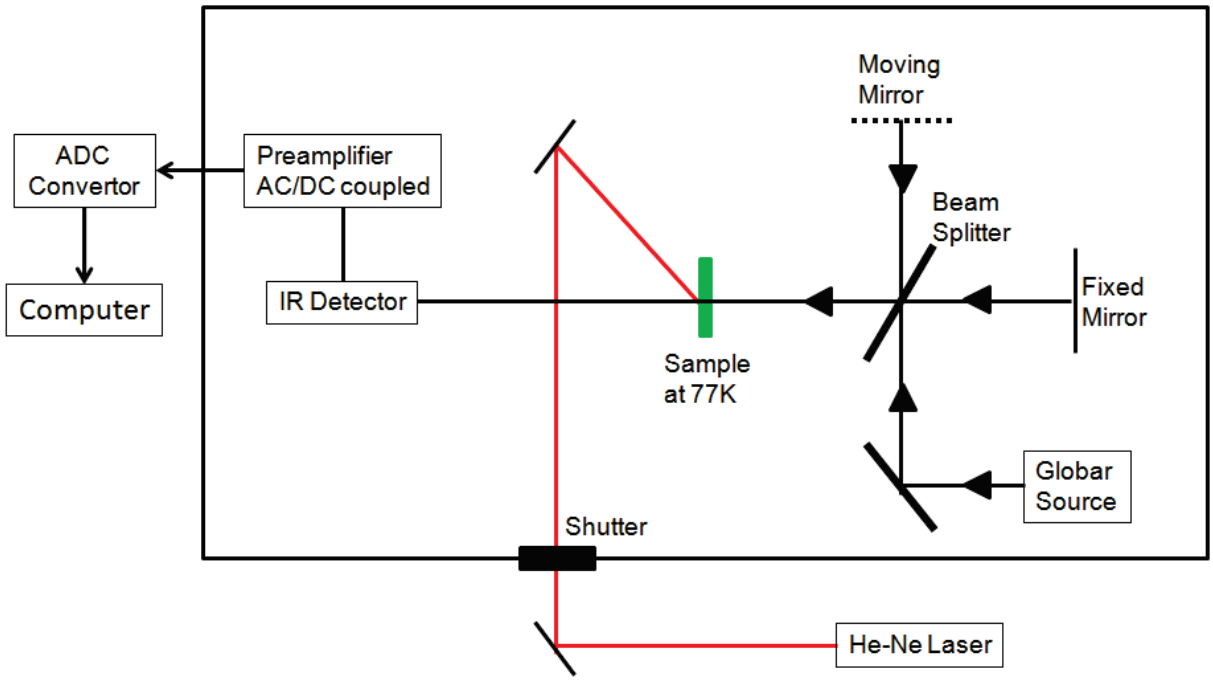

Figure 2.4: Schematic showing the layout of equipment for steady state (or static) photo-accumulation FTIR DS measurements at 77K.

A 17 mW He-Ne laser with output at 632.8 nm is used to photo-excite the samples. The laser beam is expanded to a diameter of ~10 mm at the sample to reduce any heating effects.

2.2.2 Steady State or Static FTIR Difference Spectroscopic Measurements

In FTIR DS measurements, a static or steady state population of $P_{700}^{+}F_{x}^{-}$ is generated by shining light on the PS I samples. The data was collected in the 7000-100 cm^{-1} region, at 4 or 2 cm^{-1} resolution. Sixty four interferrograms are collected and averaged before, during and after light excitation of PS I samples. These averaged interferrograms are fourier transformed and stored as single beam spectra.

A single beam spectrum of the sample is collected prior to light excitation (dark scan) and is used as the background spectrum for obtaining the absorption spectrum. Single beam spectrum collected in the presence of the light (light scan) is ratioed against the background spectrum to obtain the absorption spectrum of the excited sample. Repetitive dark scan measurements and/or 10-20 minutes of wait time is added in order to make sure the sample has

relaxed to the ground state before the next excitation. The difference between two such dark scans (dark minus dark spectrum) gives an overall measure of the noise level in the measurements. The whole procedure of repeating the dark-light-dark-dark …. scan cycle several hundred times is computer controlled using home-written macros within the environment of Opus 4.0 software from Bruker Optics.

2.2.3 Sample Preparation

For all FTIR experiments PS I particles were pelleted and placed between a pair of CaF_2 windows. The thickness of the sample was adjusted to give an absorption of about 0.8-1.0 OD unit at the maximum around 1656 cm^{-1}. No mediators were added in any of the measurements.

2.2.4 Computational Modeling of H-bonding Interaction to Chl-*a*

All geometry optimizations and harmonic normal mode vibrational frequency calculations were performed using density functional theory (DFT) as implemented in Gaussian 03 software, revision D.01 [87]. Unless stated, the B3LYP functional was used in combination with the 6-31G(d) basis set. At this level of theory, computed harmonic vibrational mode frequencies overestimate experimental anharmonic frequencies by approximately 5% [80, 88]. Radical induced frequency shifts are accurately calculated, however [80, 89]. No negative frequencies were calculated for any of the model molecular structures discussed here. To model solvent effects the integral equation formalism (IEF) of the polarizable continuum model (PCM) was used [90-95], as it is implemented in Gaussian 03, revision D.01.

The assignment of calculated vibrational frequencies to molecular groups is based upon visual identification, using software that animates the vibration (GaussView 4.0). The calculations produce normal mode vibrational frequency and intensity information. From this data infrared (IR) "stick" spectra can be constructed. By convolving these stick spectra with a

Gaussian function of 4 cm^{-1} half-width, more realistic looking spectra can be constructed. As previously described [89], these convolved stick spectra are referred to as absorption spectra.

2.3 Results

2.3.1 *PsaA*-T739F Mutant

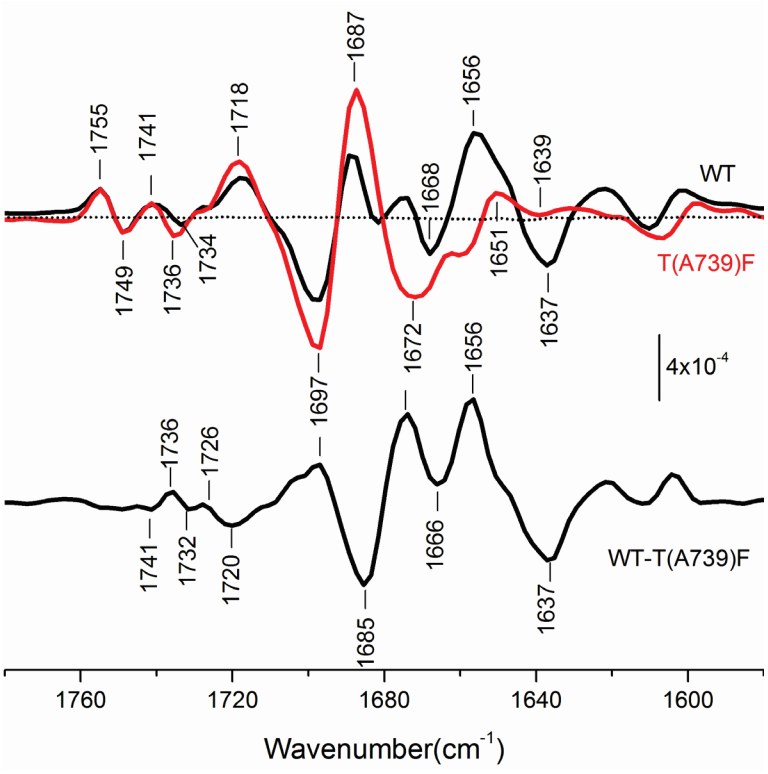

Figure 2.5: Light-induced (P_{700}^{+}-P_{700}) FTIR difference spectrum of T(A739)F mutant (*red*) PS I particles from *S. 6803* in the 1780-1580 cm^{-1} region at 77K at 4cm^{-1} resolution. The (P_{700}^{+}-P_{700}) FTIR DS of the WT species (*black*) at 77K is also shown for comparison. The double difference spectrum, wild type minus mutant, containing the changes induced by the mutation is also shown. An averaged dark minus dark noise spectrum (*dotted line*) is also shown.

Figure 2.5 shows a comparison of the light induced (P_{700}^{+}-P_{700}) FTIR DS obtained using wild type (WT) (*black*) and T(A739)F single mutant (*red*) PS I particles from *S. 6803* in the 1780-1580 cm^{-1} region at 77K. The two spectra were normalized by minimizing the residuals over the spectral range 1800-1200cm^{-1}. The WT-T(A739)F double difference spectrum (DDS) is also shown. An averaged dark-dark difference spectrum that is representative of the noise (*dotted line*) is also shown in Figure 2.5.

The most significant impact of the mutation on the (P_{700}^{+}-P_{700}) FTIR DS is that the 1656(+)/1637(-) cm^{-1} difference band in the WT spectrum is replaced by a difference band of significantly reduced amplitude and at 1651(+)/1639(-) cm^{-1} in the spectrum of the T(A739)F mutant (Figure 2.5). In addition a large negative band appears at 1672 cm^{-1} and a positive band at 1687 cm^{-1} that overlaps with the 1668(-) cm^{-1} and 1689(+) cm^{-1} band in the WT spectrum. These changes in the T(A739)F mutant spectrum relative to the WT give rise to the 1685(-)/ 1672(+)/1656(+)/1637(-) cm^{-1} quadruple feature in the WT minus T(A739)F mutant DDS. The differential signal at 1656(+)/1637(-) cm^{-1} in the WT FTIR DS is attributed to the 13^1 keto C=O group of P_A^{+}/P_A [65], and it is anticipated that this band should up-shift upon mutation. The significant decrease in intensity of the 1656(+)/1637(-) cm^{-1} along with the increase in intensity of the 1687(+)/1672(-) DS band in the T(A739)F mutant is consistent with the idea that the mutation leads to the removal/weakening of the H-bond interaction to the 13^1 keto C=O group of P_A.

The differential signal at 1718(+)/1697(-) cm^{-1} in the WT FTIR DS is attributed to the 13^1 keto C=O group of P_B^{+}/P_B [54, 65], the amplitude of the difference band is reduced by ~30% in the mutant.

Above the spectral region of 1720 cm^{-1} the impact of the mutation is mostly limited to the region assigned to absorption of the 13^3 ester C=O group of P_A^{+}/P_A. The differential signal at 1755(+)/1749(-) cm^{-1} previously assigned to the 13^3 ester C=O of P_B^{+}/P_B [54, 65] is not affected by the mutation while the 1741(+)/1734(-) cm^{-1} difference band assigned to the 13^3 ester C=O of P_A^{+}/P_A is impacted by the mutation. The 1734(-) cm^{-1} band up shifts ~ 2cm^{-1} in T(A739)F mutant.

The experimentally observed spectral changes for the difference bands previously assigned to the 13^1 keto and 13^3 ester C=O groups of P_A might be expected as the proposed structure in Figure 2.2 suggest significant modification in the H-bonding interaction to these groups upon mutation of ThrA739 to Tyr. Also the observed spectral changes in the FTIR DS at 77K is keeping with the room temperature (RT) data previously available [77].

2.3.2 *PsaA*-T739Y/S603G/Y599L Triple Mutant

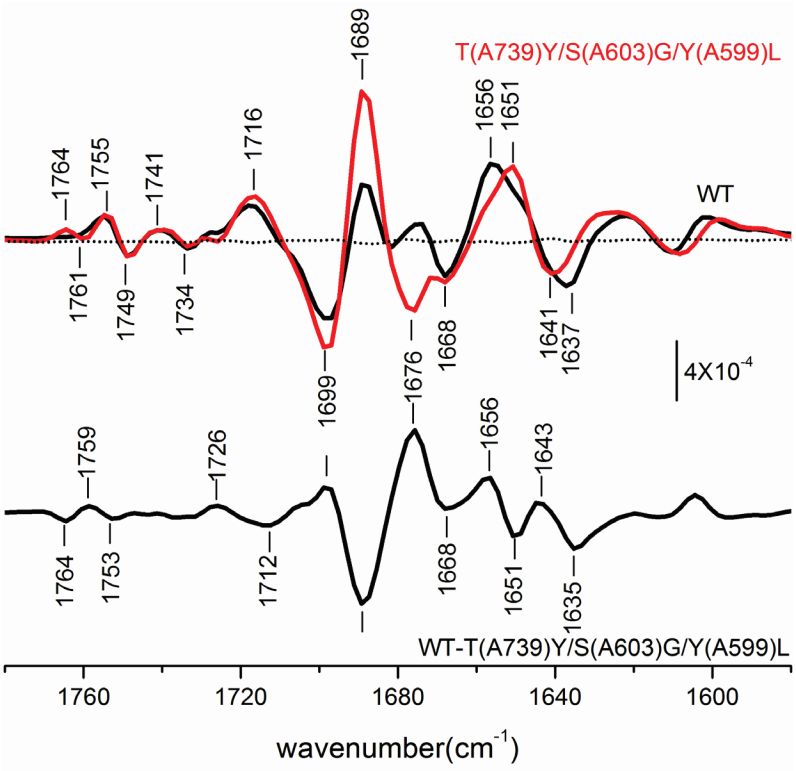

Figure 2.6: Light-induced (P_{700}^+-P_{700}) FTIR difference spectrum of T(A739)Y/S(A603)G/Y(A599)L mutant (*red*) PS I particles from *S. 6803* in the 1780-1580 cm^{-1} region at 77K at 4 cm^{-1} resolution. The (P_{700}^+-P_{700}) FTIR DS of the WT species (*black*) at 77K is also shown for comparison. The double difference spectrum, wild type minus mutant, containing the changes induced by the mutation is also shown. An averaged dark minus dark noise spectrum (*dotted line*) is also shown.

Figure 2.6 shows (P_{700}^+-P_{700}) FTIR DS for the T(A739)Y/S(A603)G/Y(A599)L triple mutant (*red*) and WT (*black*) PS I particles together with the corresponding double difference spectrum (DDS) and the noise level spectrum (*dotted line*) in the 1780-1580 cm^{-1} region at 77K.

The WT and the mutant spectra have been normalized by minimizing the residuals over the spectral range 1800-1200cm^{-1}.

The overall profile of the (P_{700}^{+}-P_{700}) FTIR DS of the T(A739)Y/S(A603)G/Y(A599)L triple mutant is quite different from that of T(A739)F single mutant. One significant change from the T(A739)F single mutant is that the 1656(+)/1637(-) cm^{-1} difference band in the WT is replaced by a difference band of almost similar intensity at 1651(+)/1641(-) cm^{-1} in the T(A739)Y/S(A603)G/Y(A599)L triple mutant. This difference band gives rise to the 1651(-)/1643(+) cm^{-1} feature observed in the DDS. These results are very different from corresponding FTIR DDS at room temperature, where the 1656(+)/1637(-) cm^{-1} difference band significantly decreased in intensity in the mutant spectra [77].

In the spectral region above 1720 cm^{-1}, characteristic of the ester C=O groups of chlorophylls, the triple mutation introduces a new positive band at 1764 cm^{-1} in the (P_{700}^{+}-P_{700}) FTIR DS. The differential signals at 1755(+)/1749(-) and 1741(+)/1734(-) cm^{-1} previously assigned to the 13^3 ester C=O of P_B^{+}/P_B and P_A^{+}/P_A respectively [54, 65], are not significantly impacted by the triple mutation.

(P_{700}^{+}-P_{700}) FTIR DS of the T(A739)F mutant and the triple mutant have been obtained before at or near room temperature (RT) [77]. These experimental spectra were interpreted based on the assignment scheme developed on the basis of the comparison of electrochemically generated (Chl-*a*$^{+}$-Chl-*a*), (pyroChl-*a*$^{+}$- pyroChl-*a*) FTIR DS in solution with the (P_{700}^{+}-P_{700}) spectra [64]. Vibrational frequency calculations of Chl-*a* model molecules in solution using DFT methods have shown that it is incorrect to consider the 13^1 keto and 13^3 ester (and in some cases the 17^3 ester) C=O modes as isolated groups [79]. These 13^1 keto and 13^3 ester C=O groups

couple, and it is best to consider anti-symmetric and symmetric coupled vibrations of both groups.

2.3.3 Calculated Vibrational Frequencies of Chl-*a*

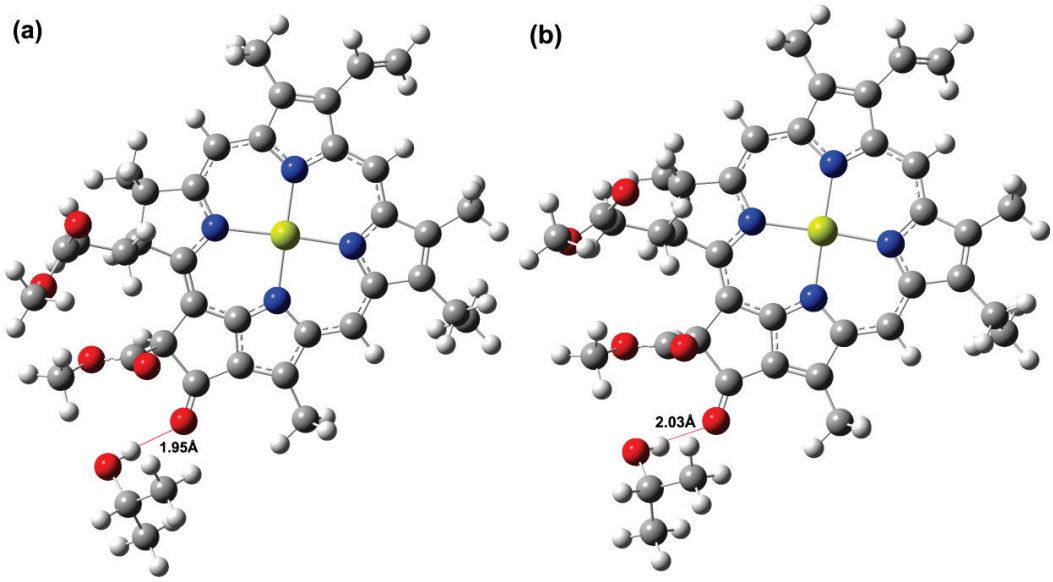

Figure 2.7: Geometry optimized molecular structures of (a) Chl-*a* and (b) Chl-a^+ in the presence of a threonine residue that provides an H-bond to the 13^1 keto C=O group. The distance between the H atom of Thr and 13^3 ester oxygen is 3.1/3.2Å for Chl-*a*/Chl-a^+, respectively. The distance between the H atom of Thr and the 13^3 ester carbonyl oxygen atom is 3.4/3.5 Å while the distance between the H atom of Thr and the 13^1 keto carbonyl oxygen atom is 1.95/2.03 Å for Chl-*a*/Chl-a^+, respectively.

To investigate the changes in vibrational features that may occur on the removal of a H-bond to the 13^1 keto C=O group of Chl-*a* we have used DFT to calculate the vibrational properties of H-bonded and isolated Chl-*a* molecules. The X-ray crystallographic coordinates of P_A chlorophyll of P_{700} along with the ThrA739 amino acid residue was used as the starting geometry for the calculations. The phytyl chain of the Chl molecule and the backbone of the Thr amino acid residue were truncated using methyl groups.

Figure 2.7 shows the geometry optimized model of Chl-*a* and Chl-a^+ in the presence of the ThrA739 residue. After geometry optimization the H atom of the hydroxyl group of Thr residue is at a distance of ~1.95Å and 2.03 Å from the 13^1 keto C=O oxygen for Chl-*a* in the neutral and cation state, respectively (Figure 2.7). Also the angle between the 13^1 keto C=O

oxygen and the hydroxyl group (O_{chl}-H_{thr}-O_{thr} angle) is ~168°/160°, for Chl-*a*/Chl-a^+, respectively. In these calculations, we have used the integral equation formalism of the polarizable continuum method (PCM) to simulate the dielectric environment. The dielectric constants near the pigments of P_{700} lies in the 2-7 range [96, 97], hence we have used CCl_4 and THF to simulate a dielectric constant of 2.228 and 7.58.

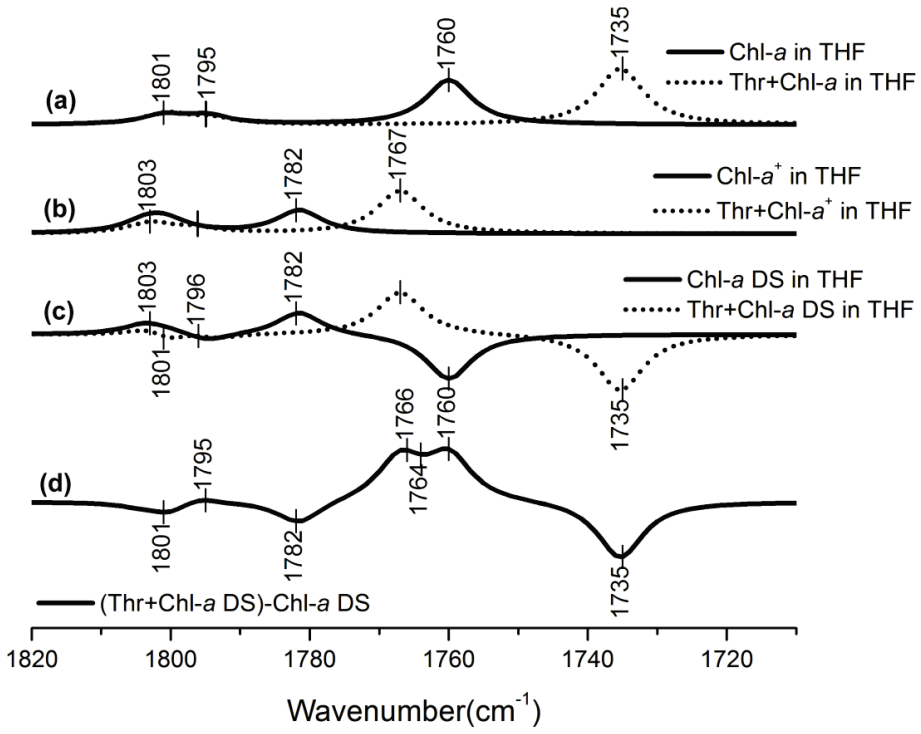

Figure 2.8: Calculated IR Spectra for (a) Thr+Chl-*a*/Chl-*a* and (b) Thr+Chl-a^+/Chl-a^+ in THF. The "cation minus neutral" IR DS are also shown (c). (d) H-bonded minus non H-bonded Chl-*a* DDS. The DDS clarifies the spectral changes that occur upon removal of the H-bond to the 13^1 keto C=O group.

Figures 2.8(a)/2.8(b) shows calculated IR spectra for Chl-*a*/Chl-a^+ in the presence (*dotted line*) and absence (*solid line*) of a Thr residue that is H-bonded to the 13^1 keto C=O group, in the presence of THF (dielectric constant of 7.58) simulated using the PCM, respectively. Figure 2.8(c) shows corresponding cation minus neutral IR DS. Similar spectra were calculated for Chl-*a* in CCl_4 (not shown). The harmonic vibrational mode frequencies and intensities associated with the C=O modes of Thr+Chl-*a*, Thr+Chl-a^+, Chl-*a* and Chl-a^+ in CCl_4 and THF are listed in Table 2.1.

Table 2.1: Calculated frequencies and intensities (in parenthesis [in km/mole]) for the different carbonyl modes of Thr+Chl-*a*, Chl-*a*, Thr+Chl-a^+ and Chl-a^+ in CCl_4 and THF.

Mode	Neutral	Shift Δν(ΔI)	Cation	Shift Δν(ΔI)
ν (13^3 C=O)				
Chl-a in CCl_4	1813(254)	0(-5%)	1813(311)	-5(13%)
Thr+Chl-*a* in CCl_4	1813(268)		1818(275)	
Chl-*a* in THF	1801(320)	0(-20%)	1801(414)	-2(13%)
Thr+Chl-*a* in THF	1801(398)		1803(368)	
ν (13^1 and 13^3 C=O) s				
Chl-*a* in CCl_4	1806(216)	0(18%)	1817(324)	10(145%)
Thr+Chl-a in CCl_4	1806(183)		1807(132)	
Chl-*a* in THF	1795(287)	1(41%)	1804(377)	8(123%)
Thr+Chl-*a* in THF	1794(203)		1796(169)	
ν (13^1 and 13^3 C=O) as				
Chl-*a* in CCl_4	1776(1047)	34(-32%)	1795(451)	13(-58%)
Thr+Chl-*a* in CCl_4	1742(1532)		1782(1061)	
Chl-*a* in THF	1760(1551)	25(-21%)	1782(802)	15(-46%)
Thr+Chl-*a* in THF	1735(1959)		1767(1496)	

The frequency shift induced by including the Thr H-bond to Chl-*a* for each calculation is shown along with the mode intensity change [in parenthesis (in%)].

The vibrational frequency calculations for Chl-*a* in the presence and absence of Thr H-bond to 13^1 keto C=O group of Chl-*a* shows that the 13^1 keto and 13^3 ester C=O vibrational modes show symmetric and anti-symmetric coupled vibrations in the neutral and cation states and unique vibrations of neither groups does not exists.

For neutral Chl-*a* in THF, the anti-symmetrically coupled 13^1 keto and 13^3 ester C=O vibration up-shifts 25 cm^{-1}, from 1735 to 1760 cm^{-1} and decreases in intensity by 21 % (Figure 2.8 and Table 2.1) upon removal of the H-bond interaction to the 13^1 keto C=O group. For neutral Chl-*a* in CCl_4, similar observations are made, where the anti-symmetrically coupled 13^1 keto and 13^3 ester C=O vibration up-shifts 34 cm^{-1} and decreases in intensity by 32 % upon removal of the H-bond interaction to the 13^1 keto C=O group.

For Chl-a^+ in CCl_4/THF, the frequency of the anti-symmetrically coupled mode increases by 13/15 cm^{-1} while the intensity decreases by 58/46 %, respectively (Table 2.1) upon removal of the H-bonding Thr amino acid.

For Chl-*a* that is H-bonded (in THF) the anti-symmetrically coupled 13^1 keto and 13^3 ester C=O vibration up-shifts 32 cm^{-1} upon cation formation and decreases in intensity by 24 %. In contrast for Chl-*a* that is not H-bonded (in THF) the up-shift is 22 cm^{-1}, and has a higher cation induced intensity decrease (48 %) (Table 2.1).

The intensity of the symmetrically coupled 13^1 keto and 13^3 ester C=O mode of Chl-*a* and Chl-a^+ is about an order of magnitude lower than that of the anti-symmetrically coupled mode. The effects of the removal of the H-bond to the 13^1 keto C=O group on the frequency of the symmetrically coupled mode of Chl-*a* and Chl-a^+ are also less pronounced than for the anti-symmetrically coupled mode. The intensity of the symmetrically coupled 13^1 keto and 13^3 ester C=O vibration of Chl-*a* increases by 18/41% in CCl_4/THF, respectively upon removal H-bond to the 13^1 keto C=O group. For Chl-a^+, the frequency of the symmetrically coupled mode of Chl-a^+ increases by 10/8 cm^{-1} while the intensity increases by 145/123 % in CCl_4/THF, respectively upon removal of the H-bond to the 13^1 keto C=O group.

The frequency of the 17^3 ester C=O group of Chl-*a* is independent of the presence/ absence of the H-bond to the 13^1 keto C=O group in both the solvents under consideration. The intensity of the 17^3 ester C=O group of Chl-*a* decreases by 5%/20% in CCl_4/THF, respectively upon removal of the H-bond to the 13^1 keto C=O group. For Chl-a^+ the frequency decreases by 5/2 cm^{-1} CCl_4/THF respectively followed by 13% increase in intensity in both solvents, upon removal of the H-bond to the 13^1 keto C=O group.

Figure 2.8(d) shows a double difference spectrum (DDS) obtained by subtracting the non H-bonded Chl-*a* DS from the H-bonded Chl-*a* DS and help visualize the calculated spectral perturbations that occur upon removal of the H-bond to the 13^1 keto C=O group. The calculated DDS in CCl_4 is similar. The DDS in Figure 2.8(d) displays several spectral features that span a

~70 cm^{-1} region. The FTIR DDS shown in Figure 2.8(d) could be representative of the WT minus mutant FTIR DDS shown in Figure 2.5. This is because the removal of the H-bonding ThrA739 amino acid should only affect the vibrational frequency modes of P_A. It should be pointed out that the calculated DDS in Figure 2.8(d) takes no account of mutation induced protein backbone alterations while such alterations are clearly present in the FTIR DDS in Figure 2.5.

2.4 Discussion

The present (P_{700}^{+}-P_{700}) FTIR spectroscopy investigation is the first report of the effect of mutation at the ThrA739 site and ThrA739/SerA603/TyrA599 sites in cynobacterium *S. 6803* at low temperature (77K). One previous study has reported FTIR DS of the mutants at 278 K [77]. Also, FTIR spectra from green algae *C.reinhardtii* with mutation at ThrA739 site, where the threonine residue has been replaced with tyrosine, histidine, valine (at 275K) [74] and Alanine (at RT) [75] has been reported. In all these (P_{700}^{+}-P_{700}) FTIR DS reported for ThrA739 site single mutation, a strong reduction of the intensity of the 1656(+)/1637(-) cm^{-1} differential signal in the wild type together with the appearance of a new differential signal centered at a higher frequency was observed. In the study of *C.reinhardtii* where ThrA739 residue was replaced by tyrosine, histidine and valine it was further observed that the frequency of the new differential signal appearing in the spectra of the mutants was dependent on the nature of the residue introduced at the mutated site [74].

The 13^1 keto and 13^3 ester C=O modes of the two chlorophylls of P_{700} has been assigned upon comparison of (P_{700}^{+}-P_{700}) and ($^3P_{700}$-P_{700}) FTIR DS combined with isotope labeled studies [63]. The availability of PS I crystal structure at 2.5Å resolutions [6] further helped confirming the assignment of the difference bands of (P_{700}^{+}-P_{700}) FTIR DS to the 13^1 keto and 13^3 ester C=O

modes of P_A, P_A^+, P_B and P_B^+. Still controversy persists on these assignments based on investigations of PS I particles with site-directed mutations, notably over the assignment of the 1656(+)/1637(-) cm^{-1} difference band, in the WT *S. 6803* PS I particles at 90K, to the up-shift upon photo oxidation of the 13^1 keto C=O of P_A which is involved in a H-bonding network with *PsaA* protein [54].

The motivation behind the modification of the T(A739) residue in the single mutant as well as the modification of three significant amino acid residues in the vicinity of P_A in the triple mutant is to modifying the H-bonding interactions to the C=O groups of P_A and thereby to be able to distinguish the mutation induced modification of the coupled vibrational modes of the C=O groups of P_A.

The nearly complete disappearance of the 1656(+)/1637(-) cm^{-1} difference band in the WT spectra upon mutation of ThrA739 to Phe fits the assignment of this difference band in WT to the 13^1 keto C=O group of P_A. The appearance of a new negative band at 1672(-) and the significant increase in intensity of the positive band at 1687(+) suggests that the functional group that absorbs at 1656(+)/1637(-) cm^{-1} in the WT is now absorbing at a higher energy. This ~30 cm^{-1} up-shift of the 1656(+)/1637(-) cm^{-1} differential signal suggests a perturbation of the H-bonding interaction to the 13^1 keto C=O group of P_A in the T(A739)F mutant. Also, the 25-30 cm^{-1} down-shift in frequency for the 13^1 keto C=O vibrational modes of P_A^+/P_A in the mutant compared to the P_B^+/P_B modes suggests that the protein environment of this functional group is still different in P_A compared to P_B.

The overall profile of the (P_{700}^+-P_{700}) FTIR difference spectra of the T(A739)Y/ S(A603)G/Y(A599)L triple mutant is quite different from the T(A739)F single mutant (Figure 2.6). Significant changes are observed in the region assigned to the 13^1 keto C=O vibrational

mode absorption of the P_A^+/P_A compared to the single mutant, where most of the intensity of the 1656(+)/1637(-) cm^{-1} difference band in the WT is still present in the triple mutant though observed at 1651(+)/1641(-) cm^{-1}. A new negative band is observed at 1676(-) cm^{-1} along with a sharp increase in intensity for the 1689(+) cm^{-1} band upon triple mutation. The appearance of this difference band at a higher frequency, which is also present in the T(A739)F single mutant, around ~1672 cm^{-1}, can be considered as an indication of the modification of the H-bonding interactions to 13^1 keto C=O group of P_A, which could lead to a higher energy absorption of these modes. Given this is the case, it is hard to explain the presence of an intense difference signal at 1651(+)/1641(-) cm^{-1} in the triple mutant which is absent in the single mutant. One explanation for this could be that the introduced tyrosine at the ThrA739 site along with the additional mutations at SerA603 and TyrA599 sites is able to introduce H-bonding interactions to the 13^1 keto C=O group of P_A in majority of the reaction centers in the triple mutant. Figure 2.3 shows the modeled orientation of the introduced amino acids in the triple mutant obtained from the crystal structure of PS I. It is clearly evident from Figure 2.3, that upon mutation the hydrogen bonding network in the vicinity of the 13^1keto and 13^3 ester C=O groups could be significantly modified. Given the likely orientation of the amino acid residues it is hard to imagine the possibility of a hydrogen bonding interaction to the 13^1 keto C=O group in the mutant. Hence the difference band at 1651(+)/1641(-) cm^{-1} could be due to a protein amide I mode rather than a 13^1 keto C=O mode. Also, it has been shown from RT FTIR measurements that upon ^{15}N labeling a difference band at 1651(+)/1642(-) cm^{-1} in the triple mutant downshifts 1-2 cm^{-1} [77] which is characteristic of a protein mode.

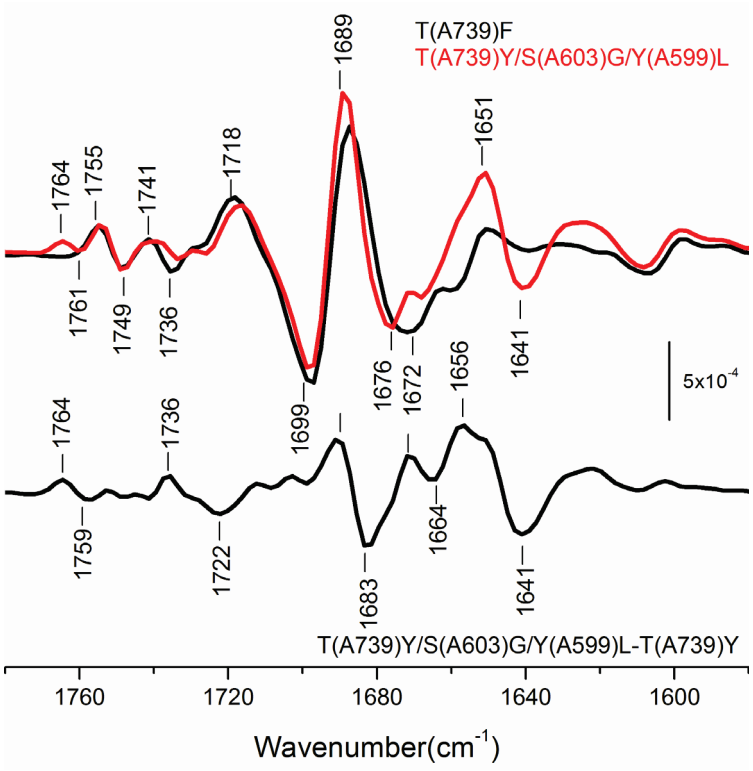

Figure 2.9: Light-induced (P_{700}^{+}-P_{700}) FTIR difference spectrum of T(A739)Y/S(A603)G/Y(A599)L triple mutant (*red*) and T(A739)F single mutant (*black*) PS I particles from *S. 6803* in the 1780-1580 cm^{-1} region at 77K at 4 cm^{-1} resolution. The double difference spectrum obtained by subtracting the single mutant spectrum from the triple mutant spectrum is also shown.

Figure 2.9 shows a comparison of the FTIR DS of T(A739)Y/S(A603)G/Y(A599)L triple mutant (*red*) and T(A739)F single mutant (black) PS I particles from *S. 6803* in the 1780-1580 cm^{-1} region. The double difference spectrum obtained by subtracting the single mutant spectrum from the triple mutant spectrum is also shown. Figure 2.9 help to clarify absorption changes associated with the protein modes as well as how the introduced amino acid side chains modify the spectra of the pigments. The triple mutant minus single mutant FTIR DDS is dominated by features at 1699(-)/1691(+)/1683(-) and 1664(-)/1656(+)/1641(-) cm^{-1}. Similar features (inverted) are found in the WT minus single and triple mutant FTIR DS in Figures 2.5 and 2.6. Since the second derivative features are present in both single and triple mutants it can be assumed that the features observed in the 1700-1635 cm^{-1} region have contributions from the protein amide modes.

The 1755(+)/1749(-) cm^{-1} difference band in the (P_{700}^{+}-P_{700}) FTIR difference spectrum of the WT is assigned to the up-shift of the 13^3 ester C=O mode of P_B upon cation formation [54, 63]. The observation that this difference band is intact, upon mutation of ThrA739 in the single mutant as well as upon the ThrA739/SerA603/TyrA599 mutation in the triple mutant is clearly in agreement with previous assignments.

The 1741(+)/1734(-) cm^{-1} difference band in the WT spectra is assigned to the light induced changes of 13^3 ester C=O modes of P_A [54, 63] and it is surprising that the T(A739)F single mutation and the T(A739)Y/S(A603)G/Y(A599) triple mutation has no significant implications on this difference band.

The (P_{700}^{+}-P_{700}) FTIR difference spectra of the T(A739)Y/S(A603)G/Y(A599)L triple mutant shows a new difference feature located at 1764(+)/1761(-) cm^{-1}. This band is clearly absent in the WT and T(A739)F mutant.

We have used DFT methods to calculate the vibrational frequencies of Chl-*a* model molecules under different set of condition, in solvent, in the presence H-bond interaction to the 13^1 and 13^3 ester C=O groups. These calculation show that it is incorrect to consider the 13^1 keto and 13^3 ester (and in some cases 17^3 ester) C=O modes as isolated groups. The 13^1 keto and 13^3 ester group vibrations are coupled and it is best to consider anti-symmetric and symmetric coupled vibrations of both groups. (P_{700}^{+}-P_{700}) FTIR DS obtained from the single and triple *PsaA* mutants show absorbance changes over a wide spectral region and hence support the proposed assignment of the difference band in the 1770-1630 cm^{-1} region to the coupled (symmetrically/anti-symmetrically) vibrations of the 13^1 and 13^3 ester C=O groups of P_A/P_B. Also, based on these assignments we were able to explain the mutation induced changes in the

(P_{700}^{+}-P_{700}) FTIR DS obtained from different site-directed mutants of *PsaB* protein (See chapter 3 for details).

2.5 Conclusions

The (P_{700}^{+}-P_{700}) FTIR DS obtained from the T(A739)F single mutant and T(A739)Y/S(A603)G/Y(A599)L triple mutant are consistent with the assignment of the 1656(+)/1637(-) difference band in the wild type to vibrational modes associated with the P_A chlorophyll of P_{700} as this difference band is significantly modified in both mutants. DFT based vibrational frequency calculations show that it is problematic to assign the difference band observed in the (P_{700}^{+}-P_{700}) FTIR DS to isolated keto and ester modes of the two chlorophylls of P_{700}. These calculations show that the 13^1 keto and 13^3 ester (and in some cases the 17^3 ester) C=O modes of chlorophyll molecules are coupled , and this coupling can explain the absorbance changes observed over a wide spectral range in the (P_{700}^{+}-P_{700}) FTIR DS of the different site-directed mutants of *PsaA* protein.

CHAPTER 3

INTRODUCING HYDROGEN BONDS TO THE B-SIDE CHLOROPHYLL OF P_{700}

3.1 Introduction

Photosystem I (PSI) is a large, multi-subunit, pigment-protein complex that uses light to catalyze the transfer of electrons from plastocyanin to ferredoxin, across the thylakoid membrane [33, 98]. In PSI the electron transfer (ET) process is initiated by light induced oxidation of a Chlorophyll-*a*/Chlorophyll-*a*'(Chl-*a*/Chl-*a*') heterodimeric species called P_{700}. From P_{700}, an electron is transferred across the membrane via a sequential series of electron transfer (ET) cofactors called A_0 (chlorophyl-*a*), A_1 (phylloquinone), F_X, F_A and F_B (iron sulfur clusters) [10].

In PS I, there are two pseudo-symmetrical sets of ET cofactors, bound to two interlinked membrane spanning proteins called *PsaA* and *PsaB*, and it is uncertain if ET occurs down one or both of these symmetrical branches [99]. Although the organization of the ET cofactors along the two branches is quite symmetrical, pigment-protein interactions associated with the two P_{700} pigments are highly asymmetric. The two pigments of P_{700} are bound to the *PsaA* and *PsaB* membrane-spanning proteins, and are called P_A and P_B, respectively. The two chlorophyll (Chl) molecules are asymmetrically bound, with P_A being involved in a hydrogen bond (H-bond) network with three surrounding amino acid residues and a water molecule (Figure 3.1). P_B is not involved in H bonding [6, 100].

Figure 3.1 shows an image depicting the structure of the P_{700} Chl's and several of the surrounding amino acids, derived from the high resolution crystal structure of PSI at 2.5 Å resolutions (PDB file 1JB0) [6]. Figure 3.1 shows that the hydroxyl oxygen of ThrA739 is 2.98 Å from the 13^1 keto carbonyl (C=O) oxygen of P_A and is suitably positioned/oriented to form an H-bond. For P_B the amino acid that corresponds to ThrA739 is TyrB718. The crystal structure

(Figure 3.1) indicates that the hydroxyl group of TyrB718 is not oriented in a manner that is appropriate for H bonding to the 13^1 keto C=O of P_B. In attempt to decrease the asymmetry in the protein environment between P_A and P_B one approach is to change TyrB718 to Thr. Figure 3.2 shows the modeling of such an amino acid into the PSI crystal structure. The mutant in which TyrB718 is replaced by Thr is termed the Y(B718)T mutant in this chapter.

The modeled orientation of ThrB718 in Figure 3.2 indicates that the hydroxyl group of Thr should be well positioned and oriented to provide a strong H-bond to the 13^3 ester C=O of P_B, and possibly also to the bridging ester oxygen. The hydroxyl oxygen atom of ThrB718 is modeled to be 3.89 Å from the 13^1 keto carbonyl oxygen atom of P_B. This would suggest that if an H-bond could be formed then it is likely to be quite weak.

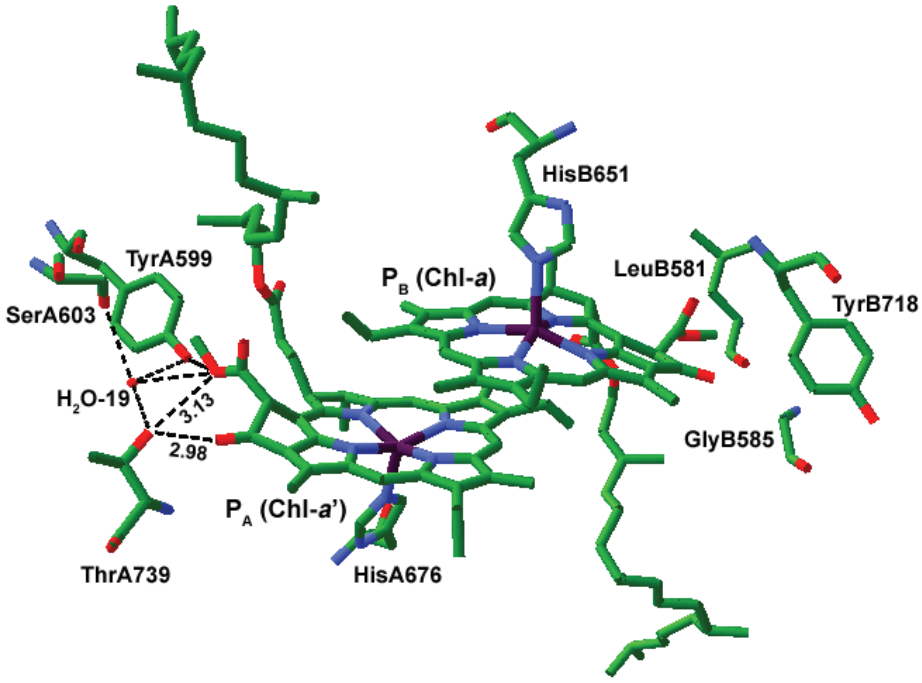

Figure 3.1: Structure of P_{700} in trimeric PSI particles from *Thermosynecoccocus* (*T*) *elongatus*. Possible hydrogen (H) bond interactions to the C=O groups of P_A are shown as dotted lines. *Synechocystis* sp. PCC 6803 (*S. 6803*) amino acid numbering is used. The amino acids LeuB581, GlyB585 and TyrB718 near P_B correspond to TyrA599, SerA603 and ThrA739, respectively.

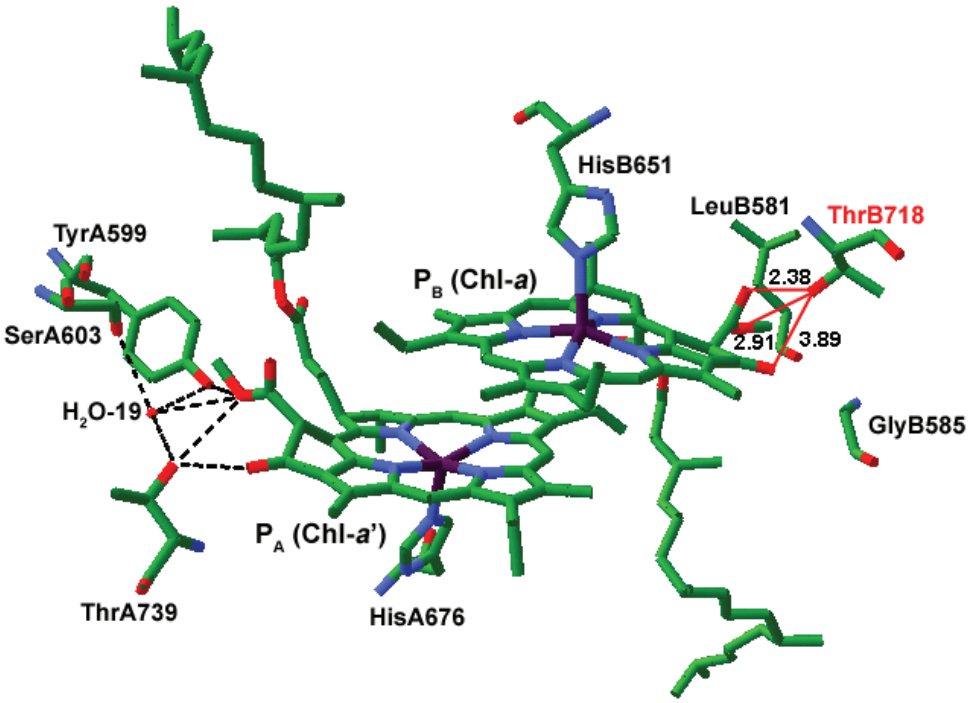

Figure 3.2: Modeled orientation of the substituted Thr in the Y(B718)T single mutant of *S. 6803*. Other orientations of the Thr hydroxyl group that point away from the ester C=O are equally valid.

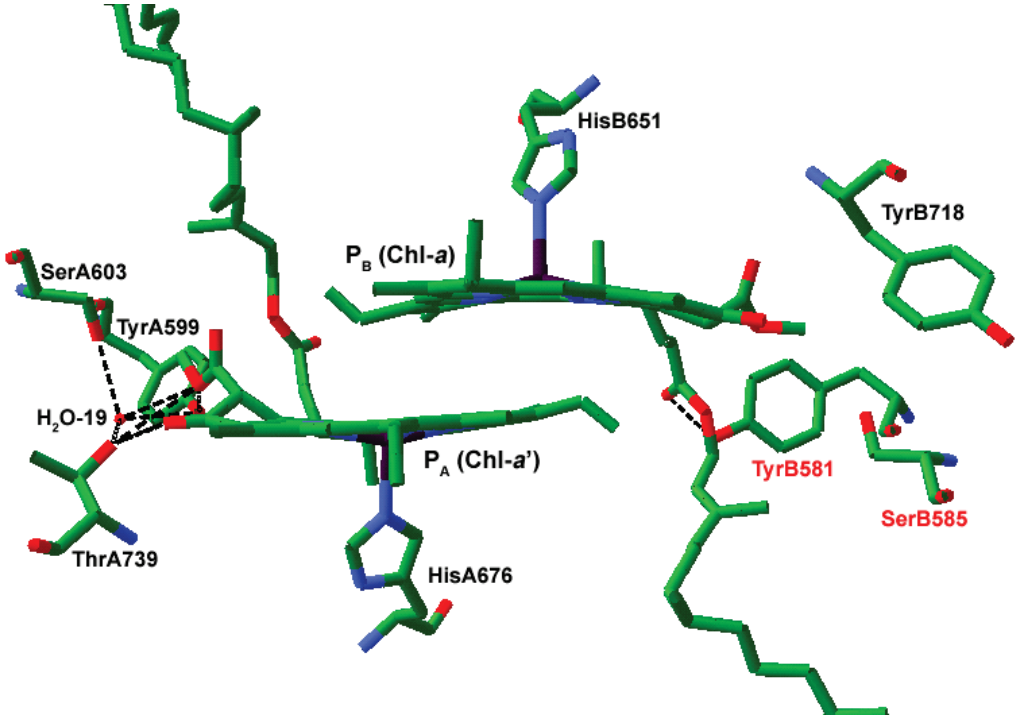

Figure 3.3: Modeled orientation of the substituted tyrosine and serine in the *PsaB* double mutant of *S. 6803*.

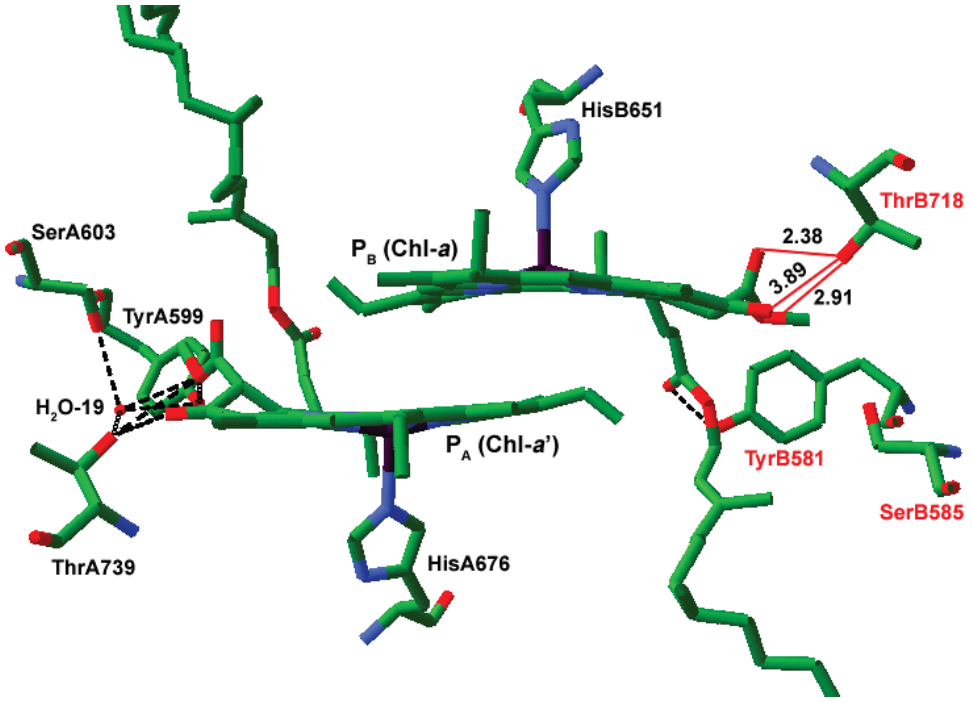

Figure 3.4: Modeled orientation of the substituted threonine, tyrosine and serine in the *PsaB* triple mutant of *S. 6803*.

A double mutant in which GlyB585 is changed to Ser and LeuB581 is changed to Tyr has also been constructed. Figure 3.3 shows the modeling of these two amino acids into the PSI crystal structure. The double mutant is termed the G(B585)S/L(B581)Y mutant. The two introduced amino acid side chains are far from the 13^1 keto and 13^3 ester C=O groups of P_B, although the hydroxyl oxygen of the introduced Tyr is 2.27 Å from the 17^3 ester carbonyl oxygen. One might expect the two introduced amino acids to have little impact on P_B, although protein backbone alterations may occur to accommodate the different side chains.

It could be expected that changing TyrB718 to Thr will have a large impact on the P_B pigment of P_{700}. It may also be expected that there will be protein backbone alterations introduced in the double mutant. In order to investigate if mutation induced effects are cumulative or additive a triple mutant in which TyrB718 is changed to Thr, GlyB585 is changed to Ser and LeuB581 is changed to Tyr has also been studied. Figure 3.4 shows the modeling of these three amino acids into the PSI crystal structure. The triple mutant is termed the

Y(B718)T/G(B585)S/L(B581)Y mutant in this chapter. Notice that the introduced Thr at B718 has a virtually identical modeled orientation in the single and triple mutant. Notice also that the introduced Tyr at B585 has a virtually identical modeled orientation in the double and triple mutant. This implies that the introduced serine at B585 in the triple or double mutant makes virtually no difference to the orientation of the side chains of the introduced Thr and/or Tyr amino acids in the double or triple mutants.

FTIR difference spectroscopy (DS) has been used to provide detailed structural information concerning primary electron donor cofactors [55, 65]. The technique is sensitive to small changes in H-bonding and other structural alterations that are below crystallographic resolution limits. In addition, FTIR DS can provide structural information on the cation radical excited state. Such information is difficult to obtain using X-ray crystallography. FTIR DS has been used to study P_{700}, and several groups have published (P_{700}^{+}-P_{700}) FTIR DS, for PSI particles from several species, and PSI mutants in which the environment of P_{700} has been altered [101].

Virtually all of the previous studies of P_{700} mutants were undertaken at or near room temperature (RT). Indeed, RT (P_{700}^{+}-P_{700}) FTIR DS for the three mutant strains investigated here have been obtained [76, 77]. However, this latter study left many ambiguities, and unanswered questions regarding the pigment-protein interactions of P_{700} in the mutants. Here FTIR DS at 77 K was used to analyze mutation induced alterations in the molecular and electronic structure of P_{700} and P_{700}^{+} in the above three B-side mutant strains. One of the problems in the RT studies is that multiple overlapping bands limited the interpretability of the spectra. The intention behind the low temperature measurements is to alter the difference bands so that underlying component bands and band-shifts can be detected.

In previous RT FTIR studies of the B-side single double and triple mutants, a very unappealing model was proposed in which the mutants introduced alterations in only a fraction of the PSI particles. This was primarily because the nature of the normal modes associated with the C=O groups of P_A and P_B were misunderstood.

To help interpret the FTIR DS associated with the mutants, density functional theory (DFT) based methods were used to simulate the vibrational properties of Chl-*a* model systems in the absence and presence of H-bonding to gain a more detailed understanding of not only how frequencies may shift upon H bonding, but also how band intensities are altered. Such information is vital for an understanding of mutation induced modifications in (P_{700}^{+}-P_{700}) FTIR DS.

3.2 Materials and Methods

3.2.1 Experimental Setup

FTIR DS were recorded using a Bruker IFS/66 FTIR spectrometer. Instrumental operation and spectral analysis were performed using the software package OPUS 4.0 supplied by Bruker Optics. The interferometer is equipped with a KBr beam-splitter that is transparent in 40,000-400 cm^{-1} region. The entire FTIR spectrometer is continuously purged with dry air. For all measurements described here a liquid nitrogen cooled, photoconductive mercury cadmium telluride (MCT) IR detector was used (Graseby D313). This detector is sensitive in the 7000-600 cm^{-1} region. The detector has a surface area of 1 mm^2, and is connected to a 200 kHz preamplifier with both AC and DC coupled outputs. For all FTIR experiments, the preamplifier AC coupled output was used (See section 2.2.1 for details on instrumentation).

A 17 mW helium-neon laser with output at 632.8 nm is used to photo-excite the PS I samples. The laser beam is expanded to a diameter of ~10 mm at the sample to reduce/eliminate sample heating effects.

In FTIR DS measurements, a static or steady state population of $P_{700}^{+}F_{A,\,B}^{-}$ is generated by shining light on the PS I samples. Data was collected in the 7000-100 cm^{-1} region, at 4 cm^{-1} resolution. Sixty four interferrograms are collected and averaged before, during and after light excitation of PS I samples. These averaged interferrograms are fourier transformed and stored as single beam spectra. A single beam spectrum of the sample is collected prior to light excitation (dark scan) and is used as the background spectrum. A single beam spectrum collected in the presence of the light (light scan) is ratioed against the background spectrum to obtain an absorption difference spectrum. Repetitive dark scan measurements, and/or 10-20 minutes of wait time, is added in order to make sure the sample has relaxed to the ground state before the next light excitation. The difference between two such dark scans (dark minus dark spectrum) gives an (over) estimate of the noise level in the measurements. The whole procedure of repeating the dark-light-dark-dark …. scan cycle several hundred times is computer controlled using home-written code operated within Opus 4.0 software.

For all FTIR experiments PS I particles were pelleted and placed between a pair of CaF_2 windows. The thickness of the sample was adjusted to give an absorption of about 0.8-1.0 OD unit at the maximum absorption peak around 1656 cm^{-1}. No mediators were added. A sample temperature of 77 K was maintained using a helium gas flow cryostat.

The possible orientation/position of the introduced amino acids in the three different mutants were modeled using Swiss-Pdb viewer software. The structural models shown in Figures 3.2-3.4 show the best rotomers of the mutated amino acid(s). The best rotomer model is where

the introduced amino acids has minimum clash with the backbone and side chain atoms of surrounding protein while having maximum possibility of forming H-bonds and S-S bonds.

3.2.2 Computational Modeling of H-bonding Interaction to Chl-*a*

All geometry optimizations and harmonic normal mode vibrational frequency calculations were performed using density functional theory (DFT) as implemented in Gaussian 03 software, revision D.01 [87]. Unless stated, the B3LYP functional was used in combination with the 6-31G(d) basis set. At this level of theory, computed harmonic vibrational mode frequencies overestimate experimental anharmonic frequencies by approximately 5% [80, 88]. Radical induced frequency shifts are accurately calculated, however [80, 89]. No negative frequencies were calculated for any of the model molecular structures discussed here. To model solvent effects the integral equation formalism (IEF) of the polarizable continuum model (PCM) was used [90-95], as it is implemented in Gaussian 03, version D.01.

The assignment of calculated vibrational frequencies to molecular groups is based upon visual identification, using software that animates the vibration (Gaussview 4.0). The calculations produce normal mode vibrational frequency and intensity information. From this data infrared (IR) "stick" spectra can be constructed. By convolving these stick spectra with a Gaussian function of 4 cm^{-1} half-width, more realistic looking spectra can be constructed. As previously described [89], these convolved stick spectra are referred to as absorption spectra.

3.3 Results

3.3.1 The G(B585)S/L(B581)Y Double Mutant

Figure 3.5 shows the light induced (P_{700}^{+}-P_{700}) FTIR DS obtained using WT (*black*) and G(B585)S/L(B581)Y mutant (*red*) PS I particles from *S. 6803*, in the 1780-1580 cm^{-1} spectral region at 77 K. The two spectra were normalized by minimizing the residuals over the 1800-

1200 cm^{-1} spectral range. The "WT minus mutant" FTIR double difference spectrum (DDS) is also shown along with the dark-dark spectrum that is indicative of the noise level in the experiment (*dotted line*).

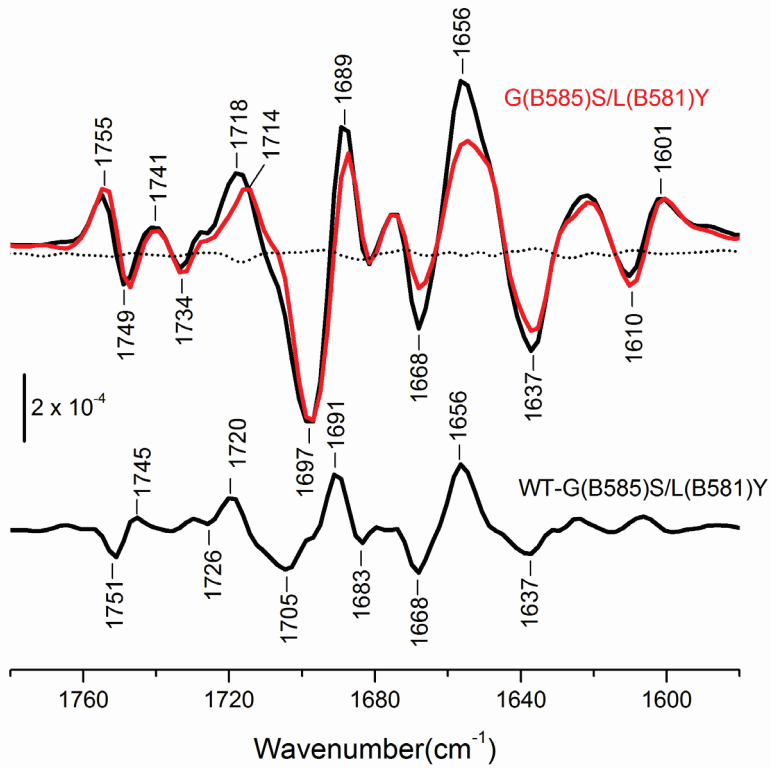

Figure 3.5: (P_{700}^{+}-P_{700}) FTIR DS for WT (*black*) and G(B585)S/L(B581)Y double mutant (*red*) PS I particles from *S. 6803*, in the 1780-1580 cm^{-1} region at 77 K. The "WT minus mutant" FTIR DDS and an averaged dark minus dark spectrum (*dotted*) that is indicative of the noise level in the experiment are also shown.

The WT and double mutant FTIR DS are quite similar, with no obvious large shift in frequency of any of the difference bands. The FTIR DDS in Figure 3.5 makes the detailing of small shifts simpler. There are several noteworthy similarities and differences in the FTIR DS in Figure 3.5.

First the 1741(+)/1734(-) cm^{-1} difference band is basically unaltered. This may be expected as this band is thought to be associated with C=O vibrational modes of P_A [101].

Second, the 1755(+)/1749(-) cm^{-1} difference band in the WT FTIR DS is modified upon mutation, resulting in a derivative feature at 1751(-)/1745(+) cm^{-1} in the FTIR DDS. The

1755(+)/1749(-) cm^{-1} difference band in the WT FTIR DS is thought to be associated with the 13^3 ester C=O of P_B [101], but a single derivative feature in the FTIR DDS is difficult to rationalize. Such a feature could suggest that the 1755(+)/1749(-) cm^{-1} bands (for both the excited/ground state) increase in intensity upon mutation. In corresponding FTIR DDS at RT, such a feature is also observed in the FTIR DDS, albeit with decreased intensity [76].

The 1755(+)/1749(-) cm^{-1} difference band is thought to be associated with the 13^3 ester C=O of P_B [101]. The double mutation induced alteration of the 1755(+)/1749(-) cm^{-1} difference band in the WT FTIR DS is surprising, since neither of the mutations are expected to have an impact on the 13^3 ester C=O group of P_B (Figure 3.3). The Tyr residue introduced at B581 position could form an H-bond with the 17^3 ester C=O group of P_B, so one hypothesis is that the feature in the FTIR DDS is due to the 17^3 ester C=O group of P_B. However, the 17^3 ester C=O groups of P_{700} are thought to contribute negligibly to (P_{700}^+-P_{700}) FTIR DS.

Third, there are several alterations in the 1680-1630 cm^{-1} region, leading to the triple feature at 1668(-)/1656(+)/1637(-) cm^{-1} in the FTIR DDS. Bands associated with P_B are not expected in this region, so it is likely that the 1668(-)/1656(+)/1637(-) cm^{-1} feature in the FTIR DDS is associated with mutation induced changes in amide I modes of the protein backbone. In support of this we also observe bands in the FTIR DDS in the 1560-1540 cm^{-1} region (not shown), which are likely due to mutation induced alterations in amide II modes of the protein backbone. These results are very different from corresponding FTIR DDS at RT, where no clear mutation induced alteration of amide I bands were detected in the 1680-1630 cm^{-1} region [76].

Fourth, there are several alterations in the 1725-1685 cm^{-1} region, leading to a quadruple feature at 1720(+)/1705(-)/1691(+)/1683(-) cm^{-1} in the FTIR DDS. This quadruple feature is somewhat similar to that found in corresponding FTIR data at RT. Bands associated with the 13^1

keto C=O group of P_B are expected in this spectral region [101]. However, it is not at all obvious that this double mutation will have any impact the 13^1 keto C=O group of P_B (Figure 3.3). In addition, why only a portion of the band at 1720 cm^{-1} (or 1687 cm^{-1}) in the WT FTIR DS is impacted by the double mutation is difficult to rationalize.

3.3.2 The Y(B718)T Single Mutant

Figure 3.6 shows (P_{700}^{+}-P_{700}) FTIR DS of WT (*black*) and Y(B718)T (*red*) mutant PS I particles from *S. 6803*. The WT minus mutant FTIR DDS is also shown. The WT and mutant spectra were normalized by minimizing the residuals over the 1800-1200 cm^{-1} spectral range. Above ~1680 cm^{-1} there are several large mutation induced alterations in the FTIR DS.

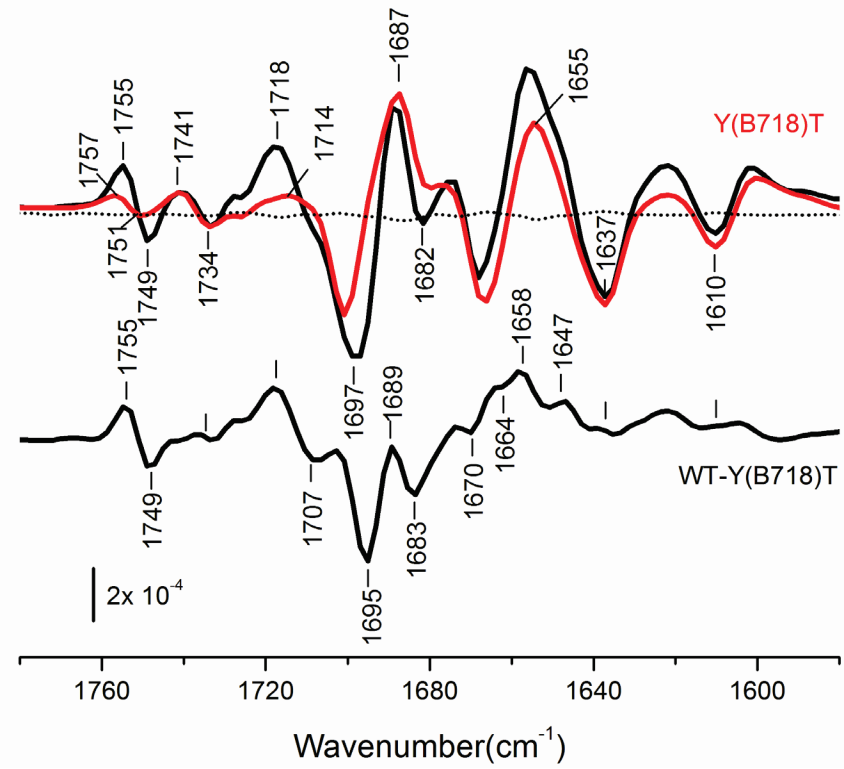

Figure 3.6: Light-induced (P_{700}^{+}-P_{700}) FTIR DS of WT (*black*) and Y(B718)T mutant (*red*) PS I particles from *S. 6803*, in the 1780-1580 cm^{-1} region at 77 K. The WT minus mutant FTIR DDS is also shown (*bottom*). The averaged dark minus dark spectrum (*dotted*) is also shown.

First, the 1755(+)/1749(-) cm^{-1} difference band in the WT FTIR DS is greatly reduced in intensity. It is not obvious to where this difference band could shift upon mutation. It seems that

the derivative feature just disappears. The 1755(+)/1749(-) cm^{-1} difference band is thought to be due to the 13^3 ester C=O mode of P_B^+/P_B [54, 65]. It is not clear whether the mutation induced changes in the 1755(+)/1749(-) cm^{-1} difference band support this idea.

Second, the 1718(+)/1697(-) cm^{-1} difference band is heavily impacted by the Y(B718)T mutation. The differential signal at 1718(+)/1697(-) cm^{-1} in the WT FTIR DS is attributed to the 13^1 keto C=O group of P_B^+/P_B [54, 65], and it is anticipated that this band should downshift upon mutation. However, a band is still found at 1701/1714 cm^{-1} in the FTIR DS of the single mutant. One interpretation of the FTIR DDS in Figure 3.6 is that most/part of the 1718/1697 cm^{-1} band downshifts 35/33 cm^{-1} to 1683/1664 cm^{-1} upon mutation. This interpretation is consistent with the idea that the mutation introduces a strong H bond to the 13^1 keto C=O group of P_B in a portion of the PSI particles. We note again, however, that the introduction of such a strong H-bond is not in keeping with our modeling based on the crystal structure (Figure 3.3).

3.3.3 The Y718T/G585S/L581Y Triple Mutant

Figure 3.7 shows the light induced (P_{700}^+-P_{700}) FTIR DS of WT (*black*) and Y(B718)T/ G(B585)S/L(B581)Y (*red*) mutant PS I particles along with the FTIR DDS. The WT and triple mutant spectra were normalized by minimizing the residuals over the spectral range 1800-1200cm^{-1}.

The mutation induced changes in the triple mutant are somewhat similar to the changes induced by the Y(B718)T single mutation. That is, a large mutation induced decrease in the intensity of the 1755(+)/1749(-) cm^{-1} band with an up-shift of 1-3 cm^{-1}. A similar change was observed in RT FTIR DS but no hypothesis for this behavior was presented [76].

In addition, part of the 1697 cm^{-1} band in the WT spectrum downshifts 29 cm^{-1} to 1668 cm^{-1} while nearly all of the positive band at 1718 cm^{-1} downshifts 35 cm^{-1} to 1683 cm^{-1}. Such

shifts are expected for a 13^1 keto C=O mode of P_B that becomes strongly H bonded. However, why all of the positive 1718 cm^{-1} band shifts and only part of the 1697 cm^{-1} band shifts has not been considered or explained.

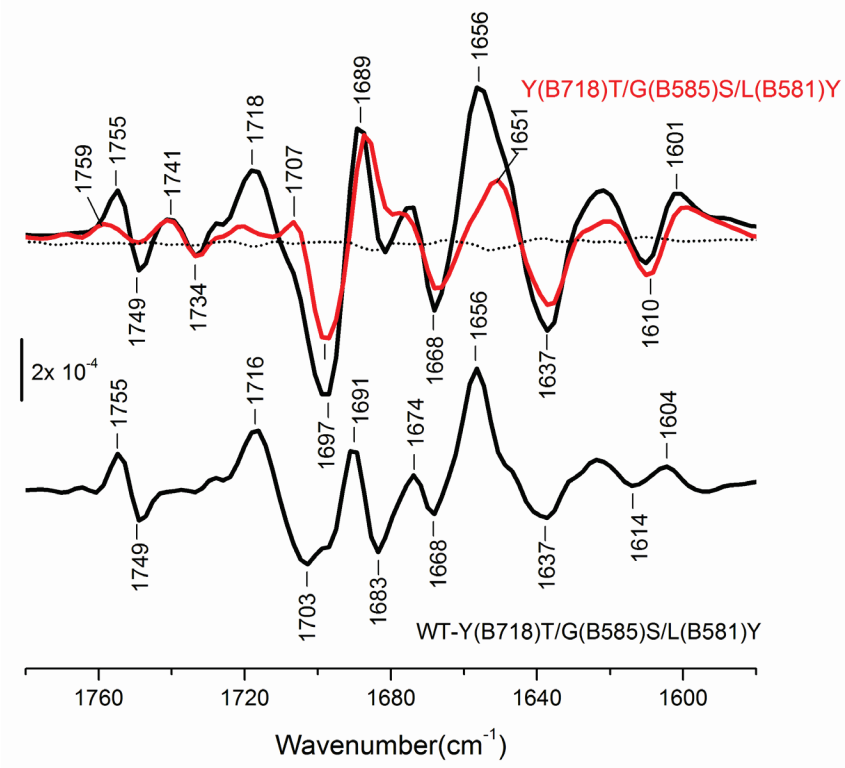

Figure 3.7: (P_{700}^+-P_{700}) FTIR DS for WT (*black*) and Y(B718)T/G(B585)S/L(B581)Y triple mutant (*red*) PS I particles from *S. 6803* at 77K. The FTIR DDS and the dark minus dark noise spectrum (*dotted*) are also shown.

The mutation induced changes at 1656(+) and 1637(-) cm^{-1} are probably related to changes in the protein backbone (amide I modes) caused by steric effects due to the different side chains of the three introduced amino acids.

In an attempt to clarify absorption changes associated with protein modes, or how distant amino acid side chains modify the spectra of the pigments, Figure 3.8 compares single and triple mutant FTIR DS. The triple mutant minus single mutant FTIR DDS is dominated by features at 1714(-)/1703(+)/1693(-) and 1666(+)/1655(-)/1637(+) cm^{-1}. Similar features (inverted) are found in the WT minus double mutant FTIR DDS in Figure 3.5. This suggests that the single and double mutation induced spectral alterations are roughly additive, and therefore independent.

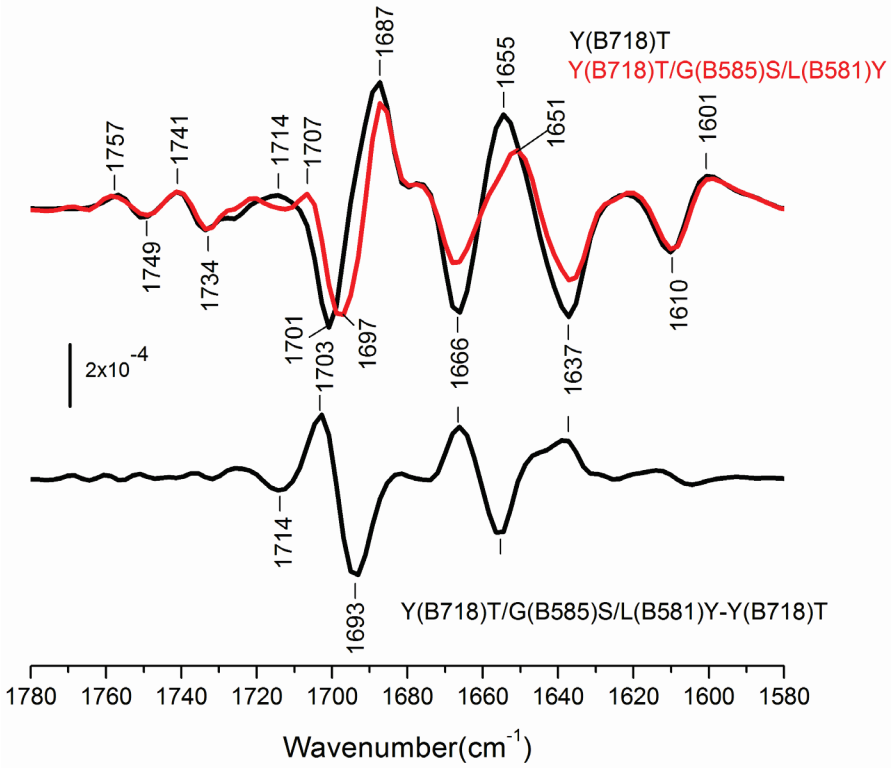

Figure 3.8: (P_{700}^{+}-P_{700}) FTIR DS for single (*black*) and triple (*red*) mutant PS I particles from *S. 6803* at 77 K. The FTIR DDS is also shown.

In the last several years (P_{700}^{+}-P_{700}) FTIR DS have been obtained for PS I particles with site directed mutations near P_{700} [73, 76] and for isotope labeled PS I particles with specific labeling of the chlorophyll molecules [69, 71]. In all cases the spectra could only be interpreted in terms of heterogeneity, where only a fraction of the reaction centers were modified by the isotope labeling or mutagenesis procedure. This rationalization arose because only fractions of difference bands were affected. Such explanations were different populations of reaction centers are invoked are unsatisfying, and recently, DFT methods were used to calculate the vibrational properties of Chl-*a* model molecules in solution, and it has been shown that it is incorrect to consider the 13^1 keto and 13^3 ester (and in some cases the 17^3 ester) C=O modes as isolated groups. These 13^1 keto and 13^3 ester C=O groups couple, and it is best to consider anti-symmetric and symmetric coupled vibrations of both groups. An important realization was that it is very difficult to near impossible to predict *a priori* how the intensity and frequency of the

coupled modes may change upon perturbation, and it is now clear that any interpretation of FTIR DS associated with Chl molecules should be undertaken in combination with vibrational mode frequency calculations.

3.3.4 Calculated Vibrational Frequencies of Chl-*a*

To investigate the types of changes in vibrational features that may occur upon H bonding in Chl-*a* DFT was used to calculate the vibrational properties of isolated and H-bonded Chl-*a* molecules. The X-ray crystallographic coordinates of the P_B Chl of P_{700} was used as the starting geometry for the Chl-*a* model. An H-bond was introduced to the 13^1 keto C=O group of the model Chl-*a* by introducing a Thr residue at a distance <3Å.The backbone of the Thr residue was truncated using methyl groups.

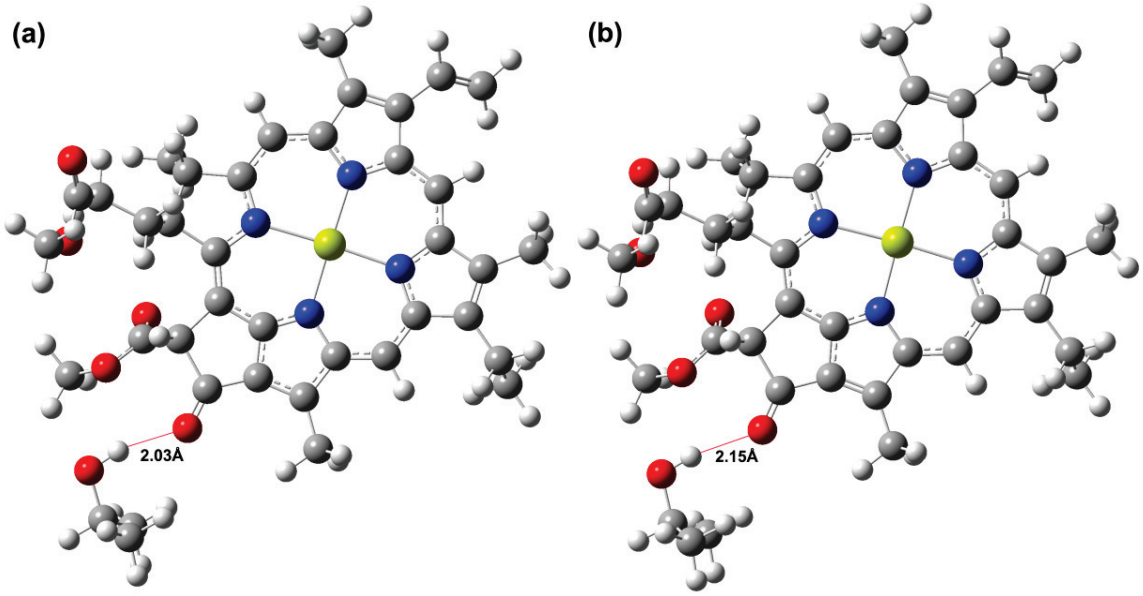

Figure 3.9: Geometry optimized molecular structures of (a) Chl-*a* and (b) Chl-a^+ in the presence of a Thr residue that provides an H-bond to the 13^1 keto C=O group. The distance between the H atom of Thr and 13^3ester oxygen is 2.5Å in both cases. The distance between the H atom of Thr and the 13^3 ester carbonyl oxygen atom is 4.4-4.5 Å. The distance between the H atom of Thr and the 13^1 keto carbonyl oxygen atom is 2.03-2.15 Å.

Figure 3.9 shows the geometry optimized model of Chl-*a* and Chl-a^+ in the presence of a Thr residue where the hydroxyl proton is 2.03 and 2.15 Å from the 13^1 keto carbonyl oxygen, respectively. Also the angle between the 13^1 keto carbonyl oxygen and the hydroxyl group (O_{Chl}-

H_{Thr}-O_{Thr} angle) is ~165/169° in the neutral/cation state, respectively. At such a distance and orientation a strong H-bond is expected. The models shown in Figure 3.9 contain all of the atoms found in Chl-*a* except the phytyl chain, which is terminated with a methyl group at the 17^4 position. To simulate the dielectric environment the integral equation formalism (IEF) of the polarizable continuum method (PCM) was used. CCl_4 and THF solvents were used to simulate a dielectric constant of 2.228 and 7.58. It is thought that the dielectric constant near the pigments of P_{700} lies in the 2-7 range [96, 97].

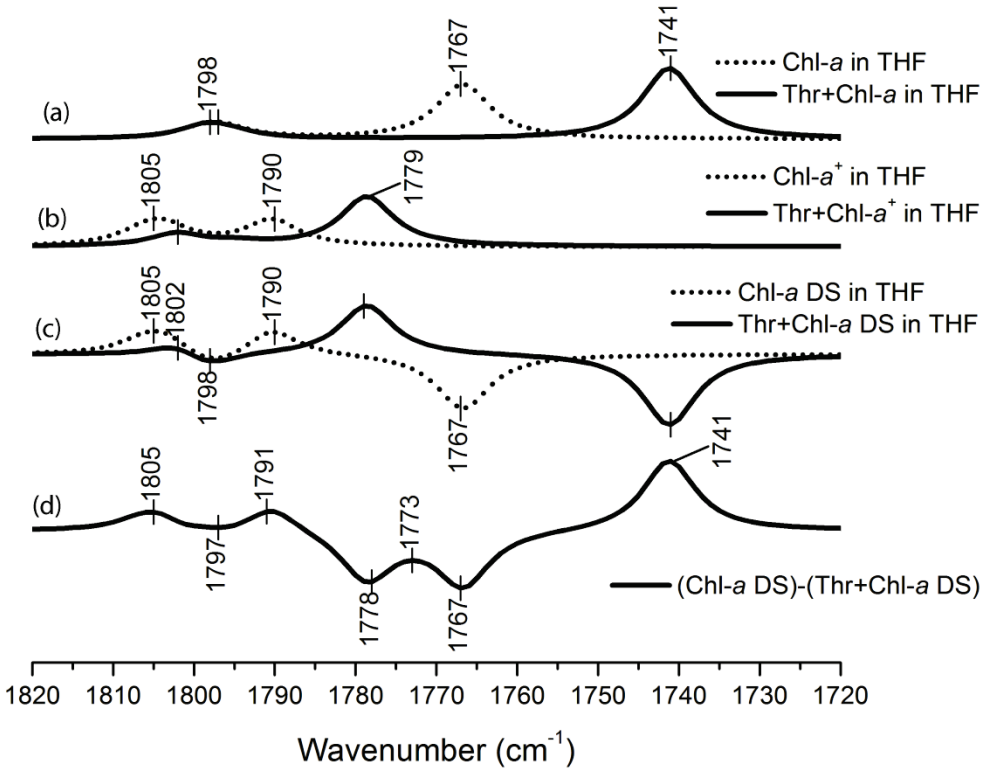

Figure 3.10: Calculated IR Spectra for Thr+Chl-a/Chl-a (a) and Thr+Chl-a+/Chl-a+ (b) in THF. The "cation minus neutral" IR DS are also shown (c). (d) Non H-bonded minus H-bonded Chl-a DDS. The DDS clarifies the spectral changes that occur upon H-bonding to the 131 keto C=O group.

Figures 3.10a/b shows calculated IR spectra for Chl-*a*/Chl-a^+ in the presence of a Thr residue that is H-bonded to the 13^1 keto C=O group, in the presence of THF (ε=7.58) simulated using the PCM, respectively. The "cation minus neutral" IR DS is also shown in Figure 3.10 (c). The calculated IR spectra for Chl-*a* in THF, in the absence of H-bonding, are also shown for

comparison (*dotted*). Similar spectra were calculated for Thr+Chl-*a* in CCl_4 (not shown). The harmonic vibrational mode frequencies and intensities associated with the C=O modes of Thr+Chl-*a*, Thr+Chl-a^+, Chl-*a* and Chl-a^+ in CCl_4 and THF are listed in Table 3.1. The calculations overestimate the vibrational frequencies by 4-5%. However, the primary focus of the calculations are the cation or mutation induced frequency shifts. These shifts are accurately calculated, presumably because the same errors are present in both calculations and disappear when the difference is taken.

Table 3.1: Calculated frequencies and intensities (in parenthesis [in km/mole]) for the different carbonyl modes of Thr+Chl-*a*, Chl-*a*, Thr+Chl-a^+ and Chl-a^+ model systems in CCl_4 and THF.

Mode	Neutral	Shift $\Delta\nu(\Delta I)$	Cation	Shift $\Delta\nu(\Delta I)$
ν (17^3 C=O)				
Thr+Chl-*a* in CCl_4	1813 (304)	0 (6%)	1820 (293)	1 (35%)
Chl-*a* in CCl_4	1813 (287)		1819 (217)	
Thr+Chl-*a* in THF	1799 (360)	0 (30%)	1802 (363)	-2 (-30%)
Chl-*a* in THF	1799 (276)		1804 (520)	
ν (13^1 and 13^3 C=O) s				
Thr+Chl-*a* in CCl_4	1802 (137)	-2 (9%)	1803 (74)	-14 (-87%)
Chl-*a* in CCl_4	1804 (126)		1817 (568)	
Thr+Chl-*a* in THF	1796 (177)	0 (-31%)	1795 (105)	-11 (-69%)
Chl-*a* in THF	1796 (255)		1806 (336)	
ν (13^1 and 13^3 C=O) as				
Thr+Chl-*a* in CCl_4	1757 (1665)	-28 (46%)	1794 (1129)	-4 (193%)
Chl-*a* in CCl_4	1785 (1142)		1798 (385)	
Thr+Chl-*a* in THF	1741 (2104)	-26 (29 %)	1779 (1474)	-11 (91%)
Chl-*a* in THF	1767 (1637)		1790 (771)	

The frequency shift induced by including the Thr H-bond to Chl-*a* for each calculation is shown along with the mode intensity change [in parenthesis (in %)].

The vibrational frequency calculations for Chl-*a* shows that the 13^1 keto and 13^3 ester C=O modes show symmetric and anti-symmetric coupled vibrations in the neutral and cation states.

For neutral Chl-*a* in THF, the anti-symmetrically coupled 13^1 keto and 13^3 ester C=O vibration downshifts 26 cm^{-1}, from 1767 to 1741 cm^{-1} and increases in intensity by 29 % (Figure 3.10 and Table 3.1) upon H-bonding to the 13^1 keto C=O group. For neutral Chl-*a* in CCl_4,

similar observations are made, where the anti-symmetrically coupled 13^1 keto and 13^3 ester C=O vibration downshifts 28 cm^{-1} and increases in intensity by 46 % upon H bonding to the 13^1 keto C=O group.

For Chl-a^+ in CCl_4/THF, the frequency of the anti-symmetrically coupled mode decreases by 4/11 cm^{-1} while the intensity increases by 193/91 %, respectively, (Table 3.1) upon H-bonding to the 13^1 keto C=O group.

For Chl-*a* in THF the anti-symmetrically coupled 13^1 keto and 13^3 ester C=O vibration up-shifts 23 cm^{-1} upon cation formation and decreases in intensity by 53 %. In contrast for Chl-*a* that is H bonded (in THF) the up-shift is 38 cm^{-1}, and the cation induced intensity decrease is smaller (30 %) (Table 3.1).

The intensity of the symmetrically coupled 13^1 keto and 13^3 ester C=O mode of Chl-*a* and Chl-a^+ is about an order of magnitude lower than that of the anti-symmetrically coupled mode. The effects of H-bonding to the 13^1 keto C=O group on the frequency of the symmetrically coupled mode of Chl-*a* and Chl-a^+ are also less pronounced than for the anti-symmetrically coupled mode. The intensity of the symmetrically coupled 13^1 keto and 13^3 ester C=O vibration of Chl-*a* increases by 9% in CCl_4, but decreases by 31% in THF upon H-bonding to the 13^1 keto C=O group. For Chl-a^+, the frequency of the symmetrically coupled mode of Chl-a^+ decreases by 14/11 cm^{-1} while the intensity decreases by 87/69 % in CCl_4/THF, respectively.

To more clearly visualize the calculated spectral perturbations that occur upon H-bonding to the 13^1 keto C=O group the calculated DDS obtained for non H-bonded minus H-bonded Chl-*a* is shown in Figure 3.10(d). The calculated DDS in CCl_4 is similar. The DDS in Figure 3.10(d) displays several spectral features that span a ~60 cm^{-1} region. The FTIR DDS shown in Figure 3.10(d) could be representative of the WT minus mutant FTIR DDS shown in Figure 3.6. This is

because the introduced H-bond should only affect P_B. However, the introduced mutations could alter the orientation of P_B slightly, which in turn could modify the electronic configuration of P_A, leading to mutation induced modifications of the C=O modes of P_A. In addition, the calculated DDS in Figure 3.10(d) takes no account of mutation induced protein backbone alterations. Such alterations are clearly present in the FTIR DDS in Figures 3.5-3.8.

3.4 Discussion

In the last several years (P_{700}^{+}-P_{700}) FTIR DS have been obtained for PSI particles with site directed mutations near P_{700} [73, 76] and for isotope labeled PS I particles with specific labeling of the Chl molecules [69, 71]. In all cases the spectra could only be interpreted in terms of heterogeneity, where only a fraction of the reaction centers were modified by the isotope labeling or mutagenesis procedure. This rationalization arose because only fractions of the difference bands in the spectra were affected. In addition, many of the explanations required the presence of water molecules to provide H-bonds to the C=O modes, because the distance between the H bonding partners, as visualized in the PSI crystal structure, were too large.

Such explanations were different populations of reaction centers are invoked, that may or may not include the presence of additional water molecules, are suspect. Recently, DFT methods were used to calculate the vibrational properties of Chl-*a* model molecules in solution, and it has been shown that it is incorrect to consider the 13^1 keto and 13^3 ester (and in some cases the 17^3 ester) C=O modes as isolated groups [79]. These 13^1 keto and 13^3 ester C=O groups couple, and it is best to consider anti-symmetric and symmetric coupled vibrations of both groups. With such an interpretation it is possible to explain why absorption changes in (P_{700}^{+}-P_{700}) FTIR DS are observed over a wide spectral region (1740-1670 cm^{-1}) when the methyl hydrogen atoms of only the 13^3 ester group of Chl-*a* are specifically deuterated [79]. Prior to this interpretation the

explanation for these changes was that there were at least four spectrally distinct 13^3 ester C=O vibrations that contributed to the (P_{700}^+-P_{700}) FTIR DS, covering the 1740-1670 cm^{-1} region [71].

Many of the puzzling mutation induced features in the (P_{700}^+-P_{700}) FTIR DS observed here can be simply explained when the 13^1 keto and 13^3 ester C=O groups are considered as coupled modes, and there is no need to consider heterogeneous populations of reaction centers in which specific interactions are found in only fractional populations [71, 76].

For example, the 1755(+)/1749(-) cm^{-1} band in the WT FTIR DS up-shifts and decreases in intensity in both the single and triple mutant FTIR DS (Figures 3.6 and 3.7). This 1755(+)/1749(-) cm^{-1} band was previously thought to be due to the 13^3 ester C=O mode of P_B. If an H-bond is introduced to one of the C=O modes of P_B then this observation is difficult to rationalize. However, Figure 3.10 indicates how such a feature can be explained. In Figure 3.10(b) the positive band near 1805 cm^{-1} appears to decrease considerably in intensity and down-shift in frequency by 2 cm^{-1}. For the calculations in CCl_4 a corresponding positive band near 1818 cm^{-1} also appears to decrease considerably in intensity and up-shift in frequency (Table 3.1). The calculated spectra indicate that the shift (whether up or down) is dependent on the dielectric constant of the environment, with an up-shift calculated for a low dielectric constant environment. Since an up-shift is experimentally observed for the 1755(+) cm^{-1} band upon mutation of TyrB718 to Thr, this could be an indication that the dielectric constant in the vicinity of the C=O modes of P_B is closer to 2.2 than to 7.58.

An explanation for the experimental observations is available from the calculated data, since the normal mode compositions of all the bands are known (Table 3.1). The 1817(+)/1806(+) cm^{-1} band for Chl-a^+ in CCl_4/THF, respectively, is due to the symmetric coupled 13^1 keto and 13^3 ester C=O mode (Table 3.1). This mode decreases in intensity by

87/69% when the 13^1 keto C=O group is H-bonded. In addition, the 17^3 ester C=O mode of Chl-a^+ in CCl_4/THF is at 1819/1804 cm^{-1}, and is similar in intensity to the symmetric coupled 13^1 keto and 13^3 ester C=O mode. This 17^3 ester C=O mode of Chl-a^+ can down-shift or up-shift in intensity and frequency, depending on the solvent. The net result therefore appears to be due to a contribution from two modes, whose intensity and frequency behavior upon H-bonding is far from obvious. The calculated spectra provide a satisfying explanation for experimental data that is very difficult to explain based on vibrational modes of isolated C=O groups.

The double and triple mutant FTIR DDS (Figures 3.5 and 3.7) display a second derivative feature at 1668(-)/1656(+)/1637(-) cm^{-1}. Such a feature is lacking in the FTIR DDS of the single mutant (Figure 3.6). In addition a second derivative feature at 1667(+)/1655(-)/1637(+) cm^{-1} is observed in the triple minus single mutant FTIR DDS (Figure 3.8). All of these indications taken together suggest that this triple feature is associated with the G(B585)S and L(B581)Y mutations. The most likely conclusion is that the triple feature is due to a modification of the protein backbone caused by the introduced Ser and Tyr amino acids. How each amino acid individually contributes to backbone alterations was not assessed.

The double and triple mutant FTIR DDS (Figures 3.5 and 3.7) also display a derivative feature at 1691(+)/1683(-) cm^{-1}. The 1683(-) cm^{-1} feature is more intense in the triple mutant FTIR DDS. A negative band is also observed at 1683 cm^{-1} in the single mutant FTIR DDS (Figure 3.6). These observations indicate that the double mutation results in a positive band shifting from 1691 cm^{-1} in the WT spectrum to 1683 cm^{-1} in the double mutant spectrum. This could be due to amide backbone modes or a mutation induced alteration in the coupling of the 13^1 keto and 13^3 ester C=O modes. How the G(B585)S and L(B581)Y mutations could lead to an alteration in the coupling of the 13^1 keto and 13^3 ester C=O modes can be hypothesized from the

structure in Figure 3.4, which suggests that the hydroxyl group of the introduced Tyr residue could be H-bonded to the 17^3 ester C=O group of P_B. If all of the C=O modes of P_B are coupled then a mutation that alters the 17^3 ester C=O group of P_B could conceivably lead to spectral changes at 1691(+)-1683(-) cm^{-1}.

3.5 Conclusions

The Y(B718)T single mutation and the Y(B718)T/G(B594)S/L(B590)Y triple mutation in *S. 6803* PS I particles leads to a significant changes in IR spectral regions attributed to both the 13^1 keto and 13^3 ester C=O modes of P_B. It has been shown from DFT based calculations of Chl-*a* model structures in the presence and absence H-bond interactions to the 13^1 keto C=O group, that the changes observed over the wide spectral region of 1740-1670 cm^{-1} in the experimental FTIR DS of the mutants can be explained by considering the 13^1 keto and 13^3 ester C=O groups as coupled modes. Importantly, there is no need to invoke the existence of heterogeneous populations of mutant reaction centers, which has been the dominant hypothesis used to explain the complex mutation induced FTIR spectral alterations in the past.

CHAPTER 4

THE MUTATION OF THE METHIONINE AXIAL LIGAND TO PRIMARY ELECTRON ACCEPTOR A_0 AND ITS EFFECT ON (P_{700}^{+}-P_{700}) FTIR DIFFERENCE SPECTRA IN *C. REINHARDTII*

4.1 Introduction

The electron transfer cofactors in Photosystem I (PS I) protein complexes are arranged along two branches with respect to the axis perpendicular to the membrane plane (Figure 4.1). Cofactors bound to *PsaA*/*PsaB* proteins are designated with a subscript A/B. The highly symmetric arrangement of pigments seen in Figure 4.1 raises the question of whether the electron transfer (ET) process is bidirectional, with both branches are equally active, or unidirectional, where ET occurs along one branch.

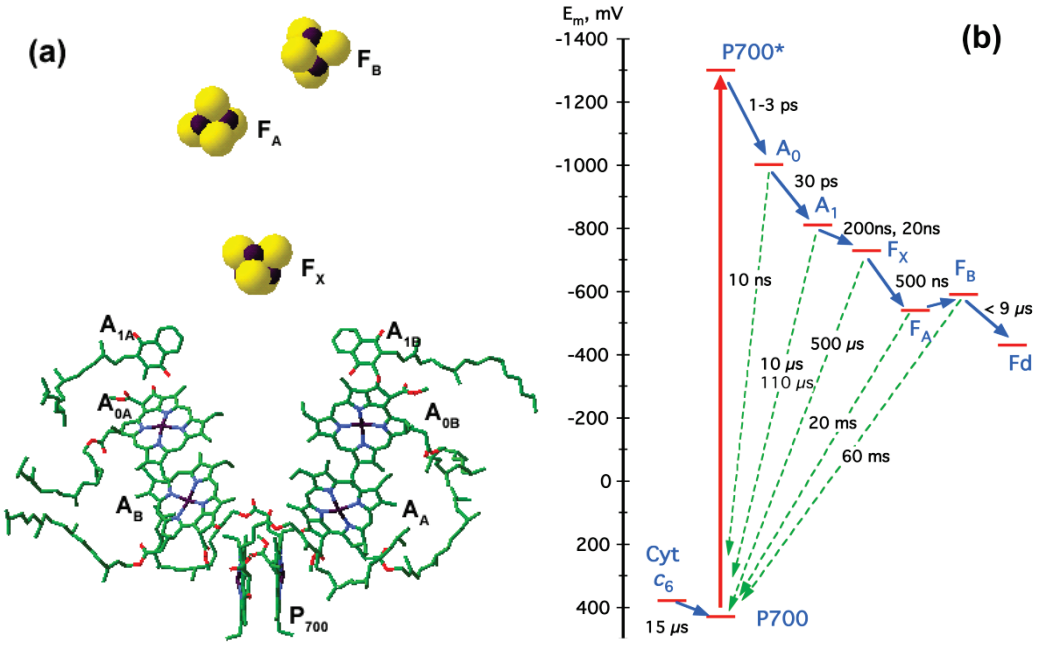

Figure 4.1: (a) Electron transfer chain in PS I (b) RT Electron transfer rates in cyanobacterial PS I [27].

Bi-directionality of ET has been demonstrated using PS I particles from the green algae, *Chlamydomonas reinhardtii* (*C. reinhardtii*) [24, 25, 102] while studies of PS I particles from the

cyanobacterium, *Synechocystis* sp. PCC 6803 (*S. 6803*) [13, 20], indicate unidirectional ET along the *PsaA* branch dominates. These conflicting studies suggest that the directionality of ET is species specific.

Pigments on the two branches are spectroscopically indistinguishable, hence the focus has been on creating site-directed mutants where point mutations are made for specific amino acids along the *PsaA* or *PsaB* branch. The ET directionality issue has been addressed using spectroscopic techniques like EPR, ENDOR and optical spectroscopy in these site-directed mutants [13, 20, 24, 26, 49, 78]. Most of the evidence for the directionality of ET has come from studies involving specific mutations around the phylloquinone secondary electron acceptor called A_1 [14, 17, 18, 23, 25]. Recently site-directed mutants where the methionine axial ligands to the A_0 primary electron acceptor, MetA684 and MetB664 in *C. reinhardtii* (MetA688 and MetB668 in *S. 6803*) were changed have been constructed. For *S. 6803*, the methionine was changed to leucine or asparagine [13, 20] while for *C. reinhardtii*, the methionine was changed to histidine, leucine or serine [24, 26, 49].

The central magnesium atoms of each of the primary electron acceptor chlorophylls, A_0, are coordinated by sulfur atom of methionine (*PsaA*684 and *PsaB*664 for *C. reinhardtii*). This provides a weak ligand and the premise of the mutations of methionine at the binding site to histidine in *C. reinhardtii* (and asparagine in *S. 6803*) is that these polar amino acid groups have the potential to provide a stronger fifth ligand to the magnesium atom of the chlorophyll acceptor on the respective branches and thus alter the redox properties of A_0, which could result in different spectroscopic properties.

4.1.1 Steady State Visible Spectroscopy Studies

The (P_{700}^{+}-P_{700}) visible absorbance difference spectra has been obtained for PS I particles from WT, M(A688)L, M(A688)N, M(B668)L, and M(B668)N mutants of *S. 6803* [20]. The major photo bleaching band centered at ~700nm attributed to the bleaching of the P_{700} absorption is intact in the spectra obtained from all the four mutants [20]. This was taken as an indication that the changes (mutation) around A_0 have little or no effect on the properties of the primary electron donor [20]. Similar results are obtained for WT, M(A684)H, and M(B664)H mutant PS I particles from *C. reinhardtii* [50].

Significant deviation from the WT spectrum is observed for the narrow absorption band centered around ~680 nm in M(A688)L and M(A688)N mutants of *S. 6803* , although relatively minor changes are observed in corresponding B side mutants [20]. Similar changes were observed for the M(A684)H mutant from *C. reinhardtii* while the corresponding B side mutant M(B664)H lacks any modification for the 680 nm band [50]. The ~680 nm band has been tentatively assigned to the absorption from a neutral monomeric chlorophyll, that emerges when P_{700} becomes oxidized, and several possible explanations for the modification of this band upon mutation have been provided, including a more symmetric distribution of the charge over the two chlorophylls in P_{700}^{+}, a change in electrochromic band shift of chlorophylls near P_{700}, or a change in the excitonic coupling between P_{700} and the neighboring chlorophylls [20].

4.1.2 Ultrafast Pump Probe Spectroscopy Studies at RT

Ramesh et. al. [24, 26] performed RT ultrafast transient absorbance measurements on wild type (WT) and M(A684)H, M(A684)L, M(A684)S, M(B664)H, M(B664)L, and M(B664)S mutant PS I particles from *C. reinhardtii*. The (A_0^{-}-A_0) visible absorbance DS of these mutants were obtained as an additional non-decaying component superimposed on the (P_{700}^{+}-P_{700})

spectrum. From these measurements it was shown that similar amount of A_0^- was accumulated in all six mutants, although the amplitude of the bleaching signal attributed to A_0^- is approximately half that from wild type [26]. This was taken as an indication that electron transfer occurs along either branch to approximately the same extent. In order to determine whether the ET from A_0^- is blocked or slowed down in these mutants they also performed transient absorption experiments on a longer time scale of 4ns. The data from these measurements showed that the accumulation of A_0^- is transient and that the ET from A_0^- to A_1 is considerably slowed from ~20-30 ps in WT to 1760±150 ps in M(A684)H, 1780±150 ps in M(B664)H, 1770±150 ps in M(A684)L, 1700±150 ps in M(B664)L, 1100±150 ps in M(A684)S, and 1150±150 ps in M(B664)S [26].

Ultra fast pump probe spectroscopy at 690nm and 390 nm was used to study the dynamics of primary charge separation and secondary electron transfer in WT, M(A688)L, M(A688)N, M(B668)L, and M(B668)N mutants of *S. 6803* [20]. The time-resolved profiles at 690 nm and 390 nm for M(B668)L and M(B668)N mutants were almost identical to that of the WT *S. 6803* samples suggesting the primary charge separation and the rate of secondary electron transfer is unaffected by mutations on *PsaB* branch of the reaction center. On the other hand, the time resolved profiles at 690nm and 390 nm for M(A688)L and M(A688)N mutants where significantly modified compared to the WT. The electron transfer from A_0 to A_1 was considerably slowed in these mutants, for the M(A688)L mutant the intrinsic time of the electron transfer was 100±10 ps while for the M(A688)N mutant the time was 112±10ps which is almost an order of magnitude slower than secondary electron transfer in WT. These results were taken as an indication that the ET in *S. 6803* is asymmetric and occur primary along the *PsaA* branch of cofactors.

4.1.3 Transient EPR Spectroscopy Studies at 80K

Directionality of ET in WT and mutant PS I particles from *C. reinhardtii* was also studied using transient EPR spectroscopy at 80K [50].

The idea behind the EPR investigation is, assuming the mutation effectively blocks ET along the respective branches the signals measured for the mutants should be indicative of the electron transfer capabilities and directionality of electron transfer. Also, if the electron transfer is bi-directional then the transient EPR signals ($P_{700}^{+}A_1^{-}$ radical pair formation) that are measured for the M(A684)H and M(B664)H mutants should be identical. But the transient EPR spectra collected from the PS I particles of the mutants at 80 K are clearly different (intensity of the $P_{700}^{+}A_1^{-}$ radical pair for the M(A684)H mutant was very small compared to the M(B664)H mutant and WT) and hence does not support the bi-directional electron transfer mechanism [50].These results are completely in disagreement with the RT ultrafast transient absorbance measurements on the same PS I particles which showed that similar amount of A_0^{-} was accumulated in all six mutants. It could be argued that the disagreement in these two spectroscopic methods point to the possibility that the ET mechanism is different at RT and cryogenic temperatures.

Also it is worth mentioning that the 80K transient EPR data collected from WT, M(A684)H and M(B664)H PS I particles from *C. reinhardtii* is almost identical to the data collected for PS I particles from WT, M(A688)N and M(B668)N mutants in *S. 6803* [50].

4.1.4 Rationale for Current FTIR Spectroscopy Studies

The light induced P_{700}^{+}/P_{700} visible difference spectra clearly show that both *PsaA* branch and *PsaB* branch mutation impact the spectra. The assumption is that A_0^{-} also contributes to the P_{700}^{+}/P_{700} difference spectra in the visible region and hence the changes observed in the mutant

spectra are due to the mutation induced changes to the position/orientation/redox properties of the chlorophyll pigments that constitute A_0. If that is the case then the (P_{700}^+-P_{700}) FTIR DS of the mutants also should show significant difference from the wild type spectra. By comparing the wild type FTIR DS with the *PsaA* branch and *PsaB* branch mutants the spectral signatures of the A_0 chlorophyll may be identified.

Also, the ultrafast measurements of Ramesh et. al. [26] indicate that the amount of charge separation making use of the A-branch or B-branch of electron cofactors is not affected upon mutation of the ligand to the A_0 chlorophylls on these branches as the same amount of A_0^- is accumulated in these mutants and supports the bi-directional electron transfer mechanism in *C. reinhardtii*. Transient EPR measurements on the other hand, support asymmetric electron transfer mechanism favoring the A-branch of electron transfer cofactors. The observation that the mutation on the A-branch nearly eliminates the $P_{700}^+A_1^-$ radical pair signal while the identical mutation on the B-branch has no effect on the $P_{700}^+A_1^-$ signal was the basis of this conclusion.

The EPR measurements were performed at low temperature and hence these measurements are only sensitive to those reaction centers undergoing reversible charge separation. The RT ultrafast measurements on the other hand can observe the entire PS I population. Hence it is very important to distinguish between the electron transfer mechanisms in these two different populations of reaction centers.

Static FTIR measurements at RT are made by repetitive excitation of the radical species ($P_{700}^+F_{A/B}^-$) that recombine to form the neutral state as soon as the excitation source is turned off. RT static FTIR measurements observe the entire PS I population while low temperature measurements can observe only the population of reaction centers undergoing reversible charge separation. A single flash excitation method (see Materials and Methods for details) was used to

measure the (P_{700}^{+}-P_{700}) FTIR Difference spectra of the irreversibly reduced population. Thus by monitoring both reversible and irreversible population of reaction centers, it can be demonstrated that the (P_{700}^{+}-P_{700}) FTIR Difference spectra of these two population are essentially the same.

4.2 Materials and Methods

The CC125 strain of *C. reinhardtii* was the recipient strain for the mutations. The M(A684)H and M(B664)H mutants along with their wild type strain were investigated in the work presented here. For detailed information on site directed mutagenesis and isolation and purification of the PS I complexes from *C. reinhardtii* see Ramesh et. al. 2004 [24].

4.2.1 Static FTIR Difference Spectroscopy

(P_{700}^{+}-P_{700}) FTIR DS was obtained for WT PS I particles from *C. reinhardtii* at 77,100, 130, 160, 190, 220, 250 and 270K. For M(A684)H and M(B664)H mutant PS I particles, (P_{700}^{+}-P_{700}) FTIR DS were obtained at several temperatures between RT and 77K.

FTIR spectra were recorded using a Bruker IFS/66 FTIR spectrometer (for details on instrumentation and measurements see section 2.2.1). PS I samples were concentrated and suspended in Tris buffer, pH 8.0 and was placed between a pair of CaF_2/BaF_2 windows. Spectra were collected at 4 or 2 cm^{-1} resolution. The IR absorbance of the sample in the CaF_2/BaF_2 sample holder was 0.8-1.2 at the peak of the amide I absorption band (about 1656 cm^{-1}). Sixty-four interferrograms were collected before, during, and after light excitation from a helium-neon laser. The spectra collected before illumination were ratioed directly against the spectra collected during and after illumination. Thus, the absorption spectra collected represent true DS. The DS collected after light excitation were subtracted from the DS collected during excitation to cancel any residual effects of water vapor. In most cases in a well purged instrument this was not strictly necessary.

4.2.2 Single Flash Excitation FTIR Difference Spectroscopy

(P_{700}^{+}-P_{700}) FTIR DS was collected for WT, M(A684)H, and M(B664)H mutant PS I particles of *C. reinhardtii* using a single flash excitation method (See Figure 4.2 for the schematic representation of the experimental procedure). For these measurements the sample was cooled to 100K in complete darkness. Sixty-four interferograms were collected before, during, and after light excitation from a helium-neon laser. After collecting 10 'dark' spectra the sample temperature was raised to 230 K. A wait time of 20 minutes was added to make sure that all reaction centers relax back to neutral ground state. The sample was then cooled back to 100 K and the measurement repeated. A pair of 2000-1000 cm^{-1} cut-off filters were used for all measurements, one before the sample and one mounted on the detector.

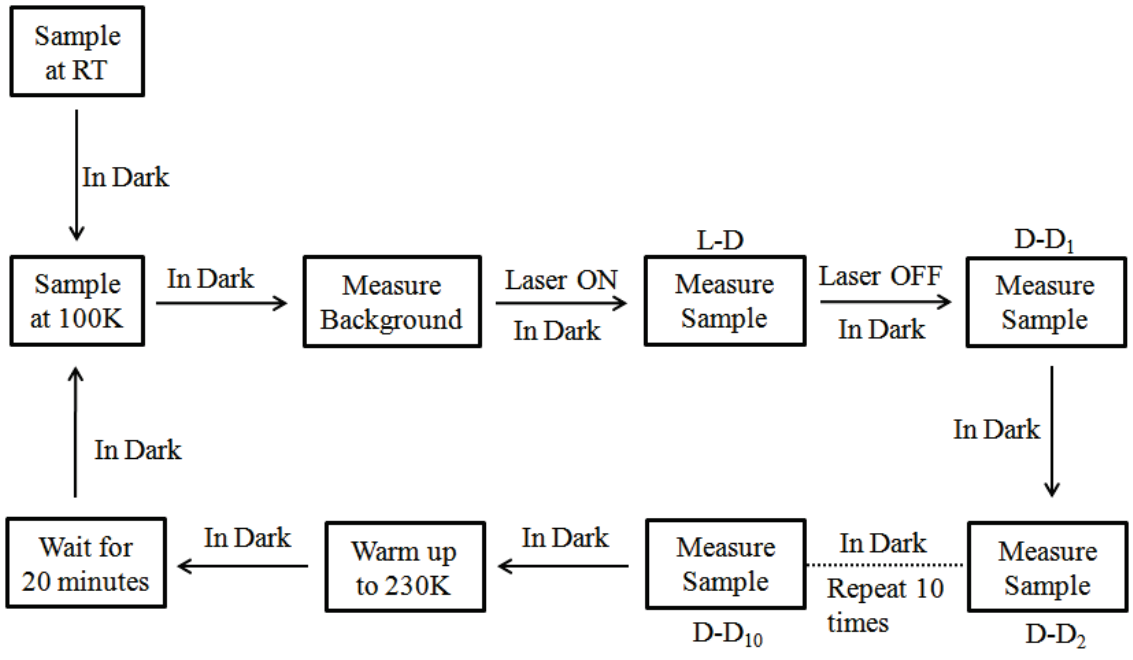

Figure 4.2: Schematic representation of the Single Flash excitation FTIR experimental setup.

4.3 Results and Discussion

4.3.1 Steady State FTIR Difference Spectroscopy Measurements at RT

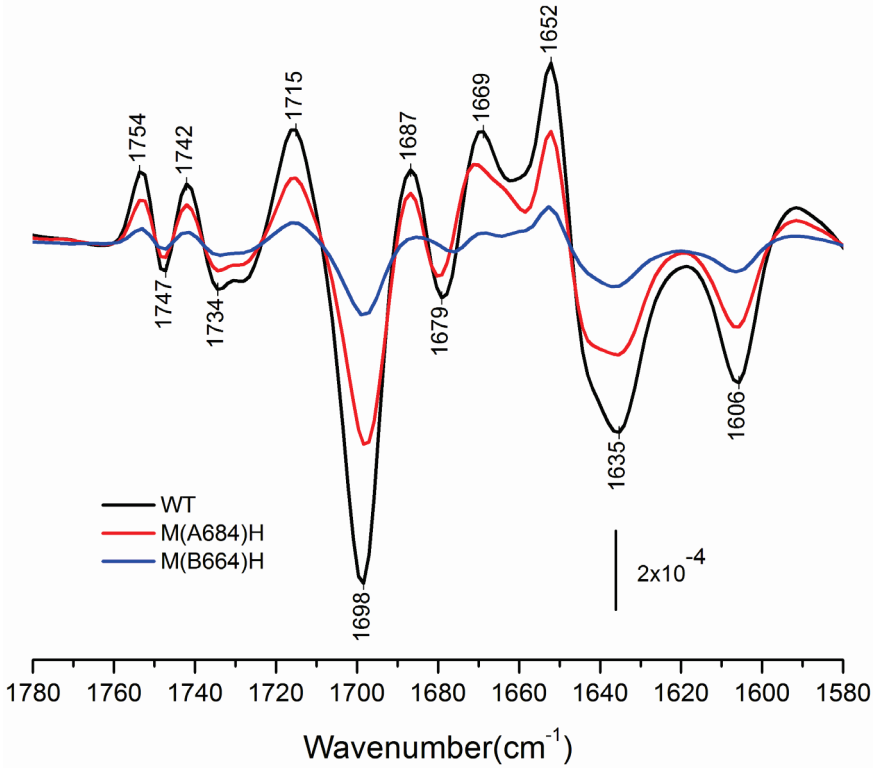

Figure 4.3: Light-induced (P_{700}^{+}-P_{700}) FTIR DS of WT (*black*), M(A684)H (*red*) and M(B664)H (*blue*) mutant PS I particles of *C. reinhardtii* in the frequency region 1780-1580 cm^{-1} obtained at RT.

Figure 4.3 shows (P_{700}^{+}-P_{700}) FTIR DS in the 1780-1580 cm^{-1} region obtained from PS I particles of WT, M(A684)H, and M(B664)H mutants at 4cm^{-1} resolution collected at RT. The (P_{700}^{+}-P_{700}) FTIR DS is the average of spectra from over 100 Light minus Dark (L-D) cycles. Multiple dark spectra are measured after each light excitation to make sure that all reaction centers relax back to neutral state before the next light excitation. The multiple difference bands present in the (P_{700}^{+}-P_{700}) FTIR DS in the 1780-1580 cm^{-1} region have been assigned to the C=O groups of the two chlorophyll molecules constituting P_{700}. In particular, the 1715(+)/1698(-) cm^{-1} difference band has been assigned to the 13^{1} keto C=O of P_B^{+}/P_B and the difference band at 1652(+)/1635(-) cm^{-1} has been assigned to the 13^{1} keto C=O group of P_A^{+}/P_A [101]. The peak-to

peak amplitude of these two difference signals can be used as an estimate of the population of the reaction centers in a given measurement.

The (P_{700}^{+}-P_{700}) FTIR DS obtained for the A and B side mutants of *C. reinhardtii* are significantly reduced in amplitude compared to the WT PS I particles. The 1715(+)/1698(-) cm^{-1} band of M(A684)H mutant is ~40% smaller than the corresponding band in the WT, while in M(B664)H mutant the band is ~80% smaller. A straight forward interpretation of this observation is that, in the mutants if ET is slowed as shown from ultrafast measurements of Ramesh et. al. [26], the recombination and fluorescence competes effectively with the forward ET. Hence fewer electrons reach the $F_{A/B}$, leading to a decrease in the $P_{700}^{+}F_{A/B}^{-}$ signal amplitude. Figure 4.5 shows a schematic representation of the proposed electron transfer mechanism in the M(A684)H and M(B664)H mutants in *C.reinhardtii*.

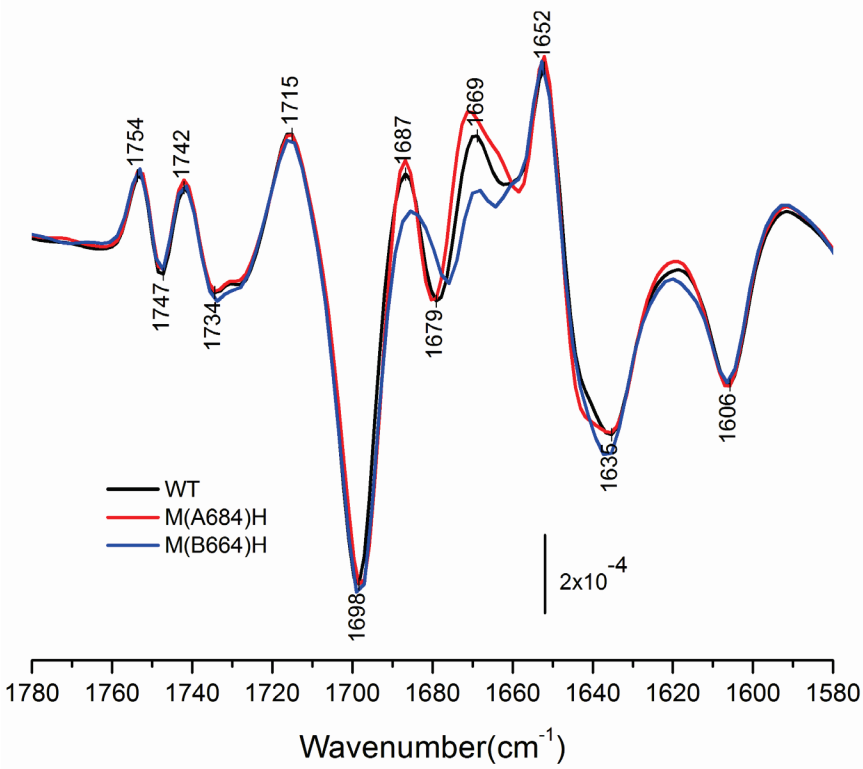

Figure 4.4: Light-induced (P_{700}^{+}-P_{700}) FTIR DS of PS I particles from the WT (*black*), M(A684)H (*red*) and M(B664)H (*blue*) mutants in the frequency region 1780-1580 cm^{-1} obtained at RT. The three spectra are normalized to the 1715(+)/1698(-) cm^{-1} band in WT.

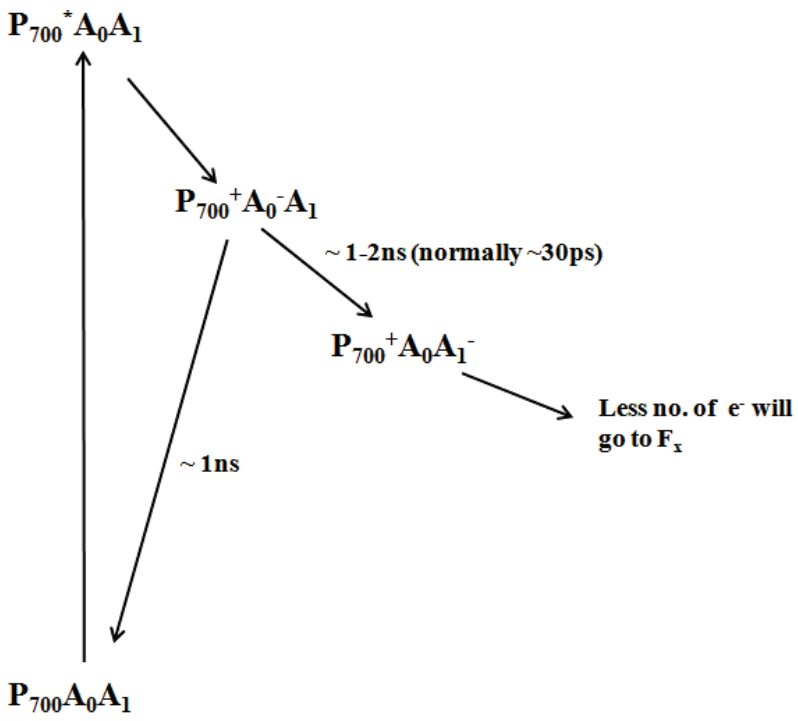

Figure 4.5: Schematic representation of the proposed electron transfer mechanism in the M(A684)H and M(B664)H mutants.

The (P_{700}^{+}-P_{700}) FTIR DS of M(A684)H and M(B664)H mutants in Figure 4.3 were scaled to the size of wild type spectra to investigate whether there is any shift in frequency of the bands in the spectra. The scaled spectra are presented in Figure 4.4.

It is clearly evident from Figure 4.4 that the difference bands in the 1780-1580 cm^{-1} region attributed to the C=O groups of P_{700} are little impacted by the mutation on the A and B branches as all the band in the WT and mutant spectra overlap perfectly. A slight modification is observed in the region 1987-1660 cm^{-1}, especially for the B branch mutant. A specific assignment for the band in this region is not available as it is thought that protein modes, perturbed by the positive charge on P_{700}^{+}, absorb in this frequency region. The observed changes in this frequency region upon mutation of the methionine residue, which acts as the ligand to the central Mg^{2+} of A_0, indicate that the mutation has caused changes in orientation and/or chemical properties of the protein backbone. The observation that the mutation induced changes are more

pronounced in the B branch mutant could be taken as an indication that positive charge on P_{700}^{+} is localized to some extend on the P_B chlorophyll. Such a proximity to the positive charge on P_{700}^{+} can explain the observed modification in the B branch mutant. Also, the FTIR difference spectroscopy data clearly indicates that protein environment of P_{700} is intact upon mutation as the frequency of the C=O modes are not impacted.

4.3.2 Steady State FTIR Difference Spectroscopy Measurements at 77K

(P_{700}^{+}-P_{700}) FTIR DS was also collected at 77K for WT, M(A684)H, and M(B664)H mutant PS I particles. At 77K it had been shown, for cyanobacterial PS I particles, that the radical pair $P_{700}^{+}F_x^{-}$ recombines in only ~20% of the PS I particles (Figure 4.8) [31]. This population can be observed using FTIR DS.

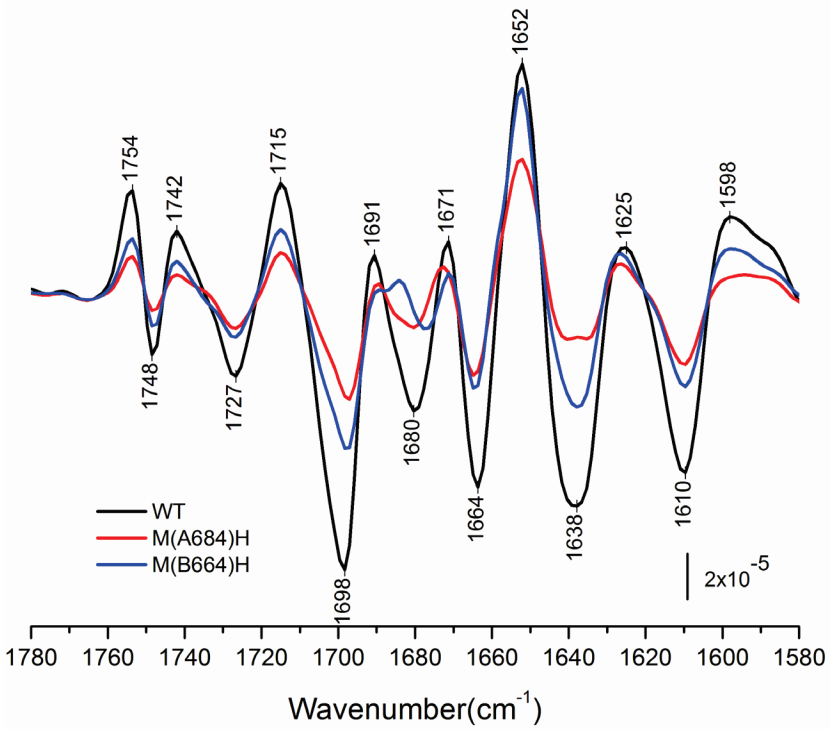

Figure 4.6: Light-induced (P_{700}^{+}-P_{700}) FTIR DS of PS I particles from the WT (*black*), M(A684)H (*red*) and M(B664)H (*blue*) mutants in the frequency region 1780-1580 cm^{-1} obtained at 77K.

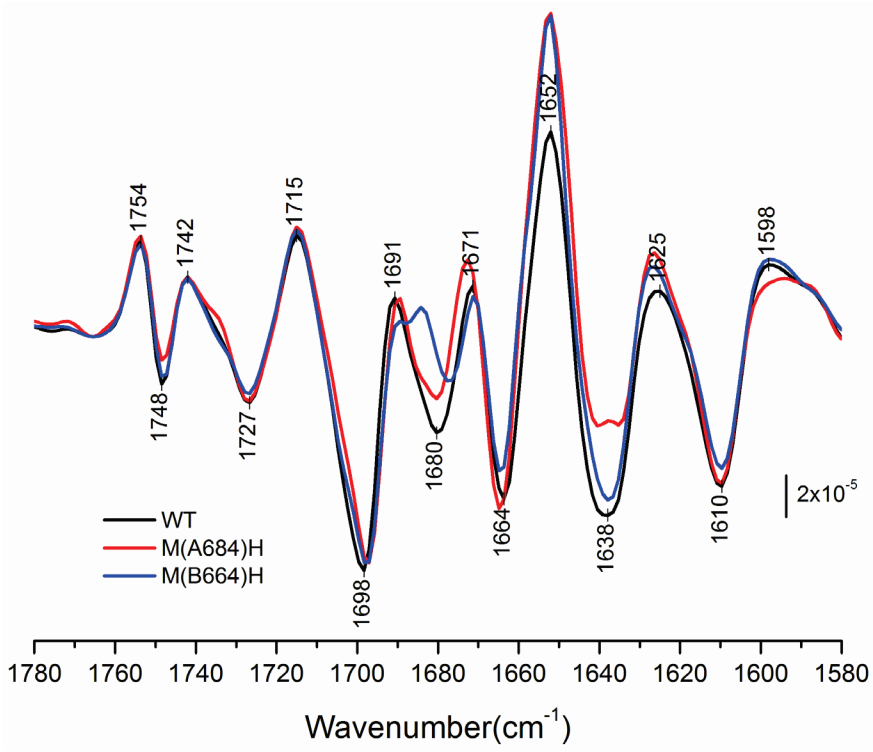

Figure 4.7: Light-induced (P_{700}^{+}-P_{700}) FTIR DS of PS I particles from the WT (*black*), M(A684)H (*red*) and M(B664)H (*blue*) mutants in the frequency region 1780-1580 cm^{-1} obtained at 77K. The three spectra are normalized to the 1715(+)/1698(-) cm^{-1} band in WT.

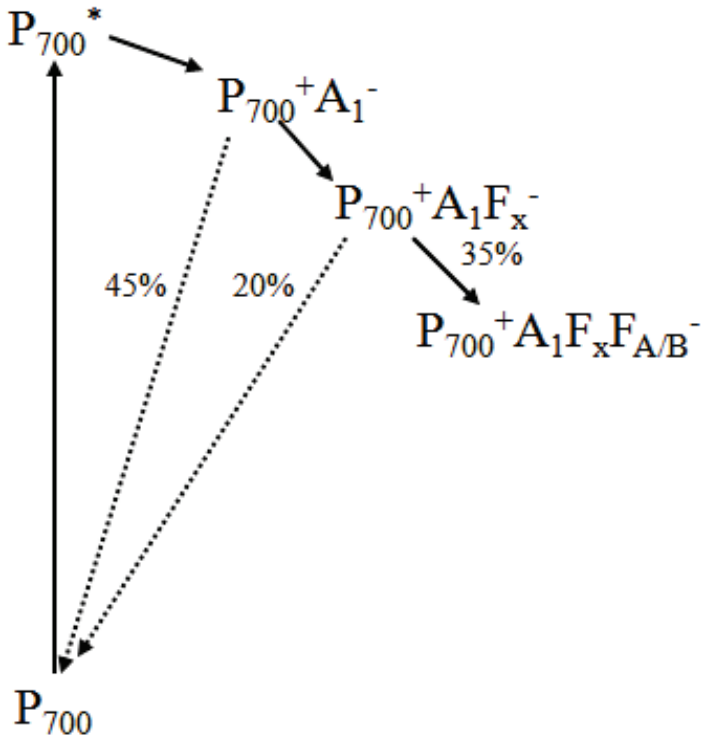

Figure 4.8: Schematic representation of the proposed electron transfer mechanism at low temperature for *S. 6803*.

It is clearly evident from Figure 4.6 that the reaction center population that is active at 77K is significantly modified upon mutation leading to a less intense (P_{700}^{+}-P_{700}) FTIR DS from these mutants. The 1715(+)/1698(-) cm^{-1} band of M(A684)H mutant is 60% smaller than the corresponding band in the WT, while in M(B664)H mutant the band is 40% smaller. Hence upon mutation the amplitude of the (P_{700}^{+}-P_{700}) FTIR DS is significantly impacted in the RT as well as in the 77K measurements. This observation is in line with the suggestion that the mutation, irrespective of A branch or B branch, leads to fewer electrons reaching F_x, thus causing a decrease in amplitude of the (P_{700}^{+}-P_{700}) FTIR difference signal.

Normalized (P_{700}^{+}-P_{700}) FTIR DS of the mutants at 77K is presented in Figure 4.7 and it can be seen that there is little impact on the frequency of vibration ascribed to the C=O modes of P_{700}^{+}/P_{700}. The only change observed is for the M(B664)H mutant where ~3cm^{-1} down-shift in frequency is observed for a negative band at 1680(-) cm^{-1} in the WT and M(A684)H mutant. Also, a new positive band appears at 1684(+) cm^{-1} which is absent in WT and M(A684)H mutant. A slight modification for this frequency region is also observed in the RT measurements of M(B664)H mutant. This cannot be an indication of mutation induced changes of P_{700}, as any such change will result in significant modification of the C=O vibrational frequencies and amplitudes. The bands in region are thought to be due to protein modes, as significant modification in frequency is observed, in the case of cyanobacterial PS I, in this region upon ^{15}N labeling. So the only conclusion that can be derived is that the protein is more perturbed by the mutation on the B side.

(P_{700}^{+}-P_{700}) FTIR DS obtained from the *PsaA* and *PsaB* branch mutants at RT and 77K indicates that the mutation causes fewer electrons to reach the terminal electron acceptor in PS I. The mutation along both branches has similar effect on the (P_{700}^{+}-P_{700}) FTIR DS, which clearly

indicates that both branches of electron transfer are active and support the bi-directionality of electron transfer proposed in the case of *C. reinhardtii*.

4.3.3 Single Flash Excitation FTIR DS Measurements

Figure 4.9 shows (P_{700}^{+}-P_{700}) FTIR DS in the 1800-1100 cm^{-1} region obtained using wild type PS I particles collected at 77, 100, 130, 160, 190, 220, 250, 270, and 298 K. The spectra are the average of 306, 420, 530, 350, 290, 204, 260, 239, and 138 L- D measurements, respectively. These measurements monitor only the subset of particles in which P_{700}^{+} is reversibly re-reduced between measurements. The signals at 298 K are ~six times larger than the signals at 77 or 100 K, notably, the signals at 77K or 100 K are almost a factor of two smaller than the signals at 130 K. If it is assumed that P_{700}^{+} in all PS I particles is re-reduced between measurements at 298 K. Then it would appear that that P_{700}^{+} is re-reduced in only ~17% of the PS I particles at 77 or 100 K. In cyanobacterial PS I particles it is known that P_{700}^{+} is re-reduced in ~20% of the PS I particles (Figure4.8) at 77K [31]. Hence it looks like the reversible population of PS I reaction centers is comparable in both species.

In static EPR spectroscopy of P_{700}^{+} it is the PS I particles that have P_{700}^{+} irreversibly oxidized that are monitored. Figure 4.9 suggests that, in this case ~83% of the PS I particles have P_{700}^{+} irreversibly oxidized at 77 or 100 K. Therefore, EPR signals will also be most intense at 77 or 100 K. Since static EPR and FTIR spectroscopy monitor different subpopulations of PS I particles, one question of interest then is: are the (P_{700}^{+}-P_{700}) FTIR DS the same for the reversibly and irreversibly reduced components in the different subsets of PS I particles. This is worth answering to make sure EPR and FTIR measurements are done on same species.

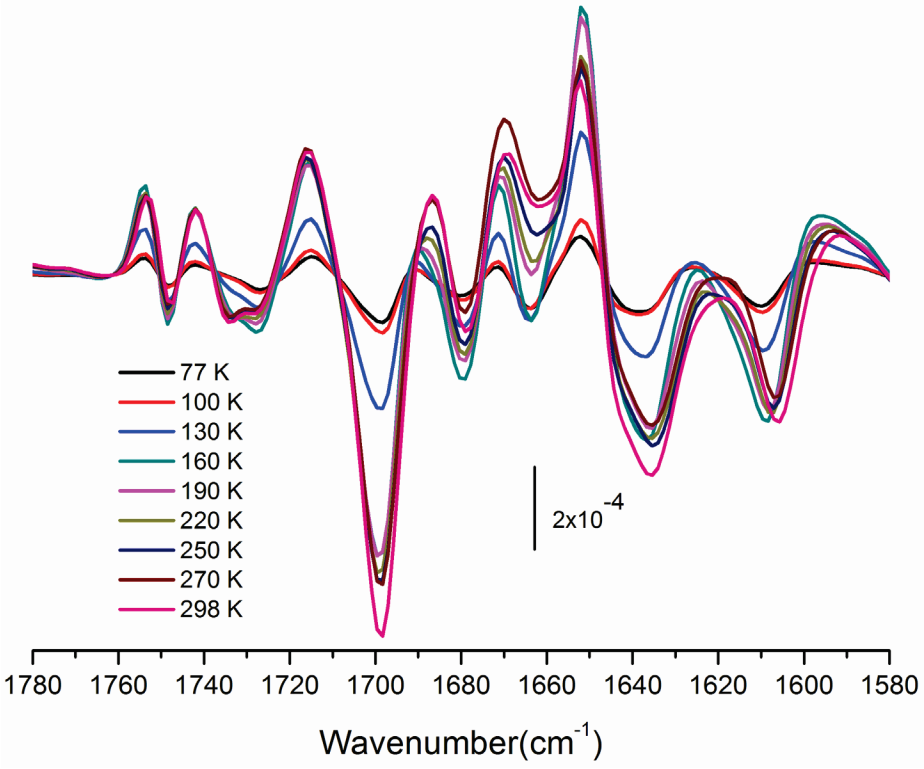

Figure 4.9: Light-induced (P_{700}^{+}-P_{700}) FTIR DS of wild type PSI particles from *C. reinhardtii* obtained at 77, 100, 130, 160, 190, 220, 250, 270 and 298 K.

One way to address this question is to do single flash excitation FTIR DS experiment, where the measurements are made on PS I samples cooled down to 100 K in complete darkness. The assumption is that by keeping the sample in complete darkness, all the P_{700} reaction center population will be in the ground state prior to light excitation. When the sample is excited with light, presumably all the reaction center population will get excited, hence the (P_{700}^{+}-P_{700}) DS obtained for the first excitation contain the signature from all the P_{700} population in the sample, both reversible and non-reversible. By exciting the sample again, (P_{700}^{+}-P_{700}) spectra shows only the portion of the reaction centers that are reversible, in which $P_{700}^{+}F_x^{-}$ recombines, and have come back to the ground state by recombination. Subtraction of the spectrum obtained from the average of the consecutive flashes (reversible fraction of P_{700}) from the first flash spectrum (complete population of P_{700} in the ground state) provides the information and spectral signatures of the portion of the reaction center that is irreversibly reduced.

The (P_{700}^{+}-P_{700}) FTIR DS from the first flash for WT, M(A684)H, and M(B664)H mutants are presented in Figure 4.10. It is assumed that the first flash spectrum has contribution from all of the P_{700} reaction centers. The amplitude of the 13^1 keto C=O group of P_B^{+}/P_B in the (P_{700}^{+}-P_{700}) FTIR DS of the mutants are ~60% reduced compared to the corresponding difference band in the WT spectrum. This is again an indication that fewer electrons are reaching the terminal electron acceptor F_x in these mutants. It is also interesting to note that both mutation has similar effect on the amplitude of the (P_{700}^{+}-P_{700}) FTIR DS, and could be taken as an indication that the electron transfer is bi-directional.

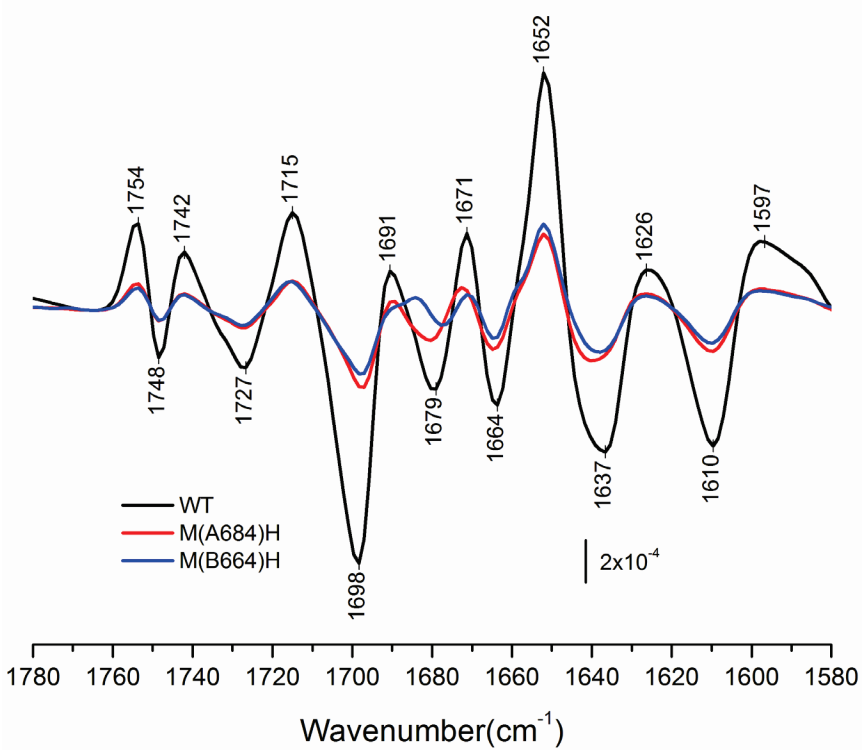

Figure 4.10: Light-induced (P_{700}^{+}-P_{700}) FTIR DS of wild type, M(A684)H and M(B664)H mutant PSI particles from *C. reinhardtii* obtained at 100K using single flash excitation experiment.

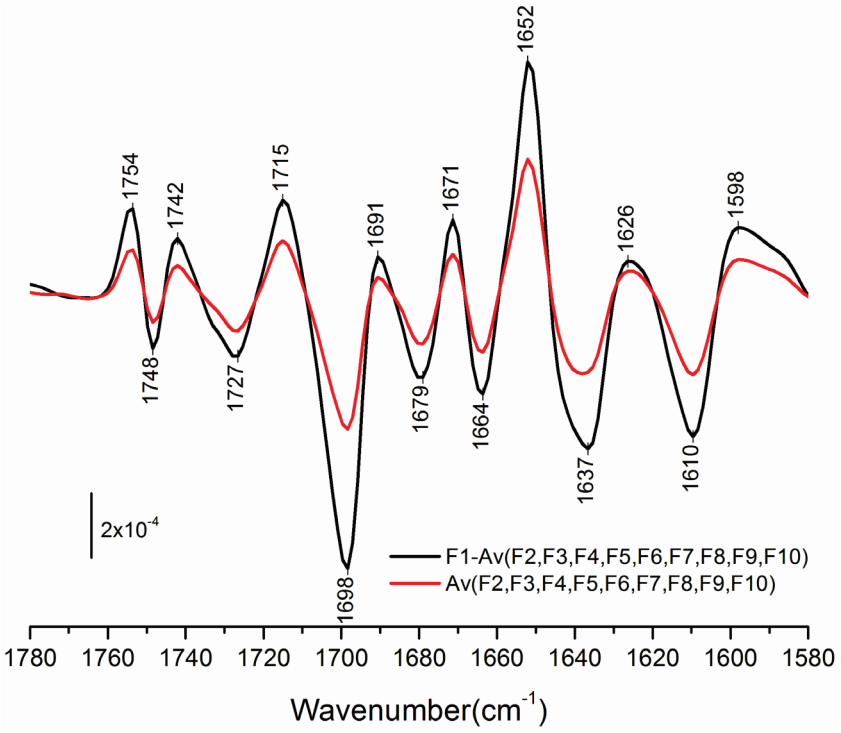

Figure 4.11: (P_{700}^{+}-P_{700}) spectra of the PS I population that is irreversible (*black color*) and the (P_{700}^{+}-P_{700}) spectra of the PS I population that is reversible (*red color*) in wild type *C. reinhardtii* species.

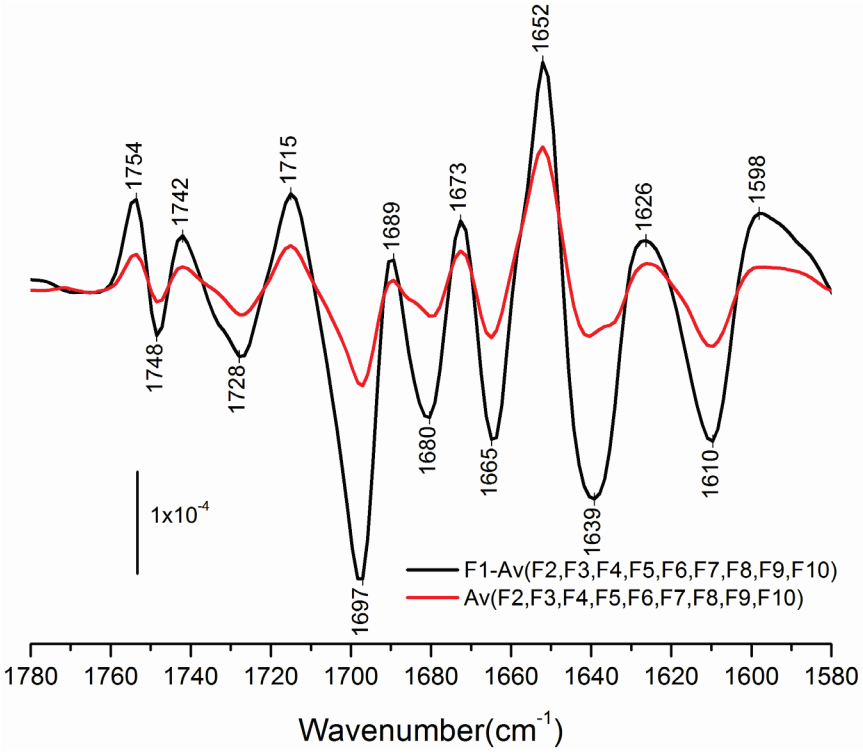

Figure 4.12: (P_{700}^{+}-P_{700}) spectra of the PS I population that is irreversible (*black color*) and the (P_{700}^{+}-P_{700}) spectra of the PS I population that is reversible (*red color*) in M(A684)H mutant *C. reinhardtii* species.

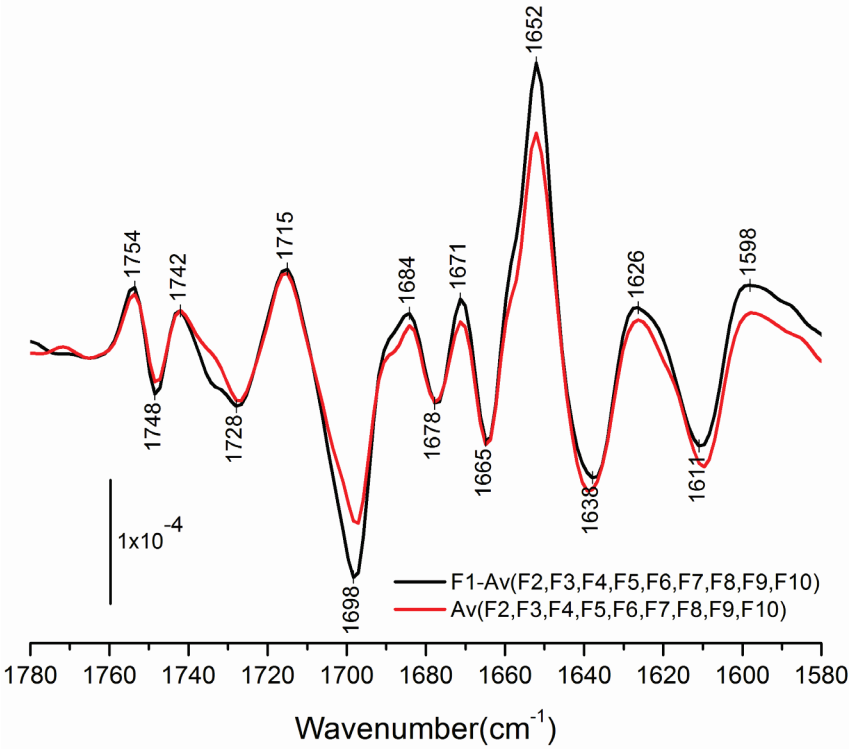

Figure 4.13: (P_{700}^{+}-P_{700}) spectra of the PS I population that is irreversible (*black color*) and the (P_{700}^{+}-P_{700}) spectra of the PS I population that is reversible (*red color*) in M(B664)H mutant *C. reinhardtii* species.

The (P_{700}^{+}-P_{700}) FTIR DS of the reversible and irreversibly reduced components of P_{700} obtained from wild type, M(A684)H, and M(B664)H mutants are presented in Figures 4.11, 4.12 and 4.13 respectively. The ratio of the 1715(+)/1698(-) cm^{-1} band of the irreversibly reduced component of P_{700} to the reversible component from Figures 4.11, 4.12 and 4.13 are ~2/1, 3/1, 1.2/1 respectively. These results show that mutation of the A_0 ligand on the A branch leads to an increase in the irreversibly reduced component of P_{700} while the mutation on the B branch lead to a decrease in the irreversibly reduced component. This is a valuable result as the low temperature transient EPR and low temperature static FTIR measures the population of reaction centers that is reversible. Hence the observation that the mutation of A_0 ligand along the two branches induces a change in the fraction of the reversible/irreversible population of reaction center is extremely important. The fact that the mutation along the A branch causes a significant decrease in intensity of the $P_{700}^{+}A_1^{-}$ radical pair signal in transient EPR measurements for the M(A684)H

mutant can now be easily explained as the single flash excitation FTIR measurements upon mutation along A branch shows that there is a significant decrease in the reversible component of reaction centers. Also, single flash excitation measurements show that mutation along B branch lead to a decrease in the irreversibly reduced component which means the fraction of reversible component is more and will give intense $P_{700}^{+}A_1^{-}$ radical pair signal from transient EPR measurements.

4.4 Conclusions

(P_{700}^{+}-P_{700}) FTIR DS of PS I particles from WT, M(A684)H, and M(B664)H mutant species of *C. reinhardtii* were collected at RT and 77K/100K under different set of conditions. The intensity of the (P_{700}^{+}-P_{700}) FTIR DS for the *PsaA* and *PsaB* branch mutants are significantly reduced in comparison with the wild type spectra. The change in intensity of the spectra from the mutants was comparable and this indicates that both branches are impacted to a similar extent upon mutation. Also no shift in frequency was observed for the C=O modes of P_{700}^{+}/P_{700} which indicates that the mutation of the histidine ligands of A_0 has no effect on the structure/protein interactions of the primary electron donor. The transient EPR measurements at low temperature are only sensitive to those reaction centers undergoing reversible charge separation while the RT ultrafast measurements observe the entire PS I population. Using single flash excitation FTIR DS measurements it is possible to observe these two different populations of reaction centers. Single flash excitation FTIR DS measurements indicates that mutation of the A_0 ligand on the A branch leads to an increase in the irreversibly reduced component of P_{700} while the mutation on the B branch lead to a decrease in the irreversibly reduced component. Hence it is clearly evident that the conflicting conclusions made from transient EPR and RT ultrafast measurements were due to the different populations of reaction centers under observation. Also the FTIR DS results indicate

that both branches of electron transfer are active to the same extent at least in the case of *C. reinhardtii* PS I reaction centers.

CHAPTER 5

CALCULATION OF THE VIBRATIONAL PROPERTIES OF CHLOROPHYLL-*A* IN SOLUTION

5.1 Introduction

Photosynthesis is the process in which solar energy is captured and converted into products essential for the maintenance of life on earth (food, fuel, oxygen) [103]. In photosynthetic oxygen evolving organisms the molecular species at the heart of all solar capture and conversion processes is Chlorophyll-*a* (Chl-*a*), either in monomeric or dimeric forms [33, 104] Given the importance of Chl-*a* in oxygenic photosynthesis, one research goal is the development of a quantitative understanding of Chl-*a*, its isomers and multimeric forms, as found in photosynthetic protein complexes. Of particular interest is an understanding of how various molecular parameters modulate the electronic properties of Chl-*a*. It is the electronic properties of Chl-*a*, and the resulting thermodynamic properties, that ensures ultra efficient solar energy capture and conversion.

Unfortunately a fully quantum mechanical (QM) calculation of the chemical properties of dimeric Chl-*a* in the gas phase or a protein matrix, are still far off due to limitations in computational capabilities. However, it is computationally feasible to calculate (at the QM level) properties of isolated Chl-*a* molecules in both the neutral and radical forms [80]. Such calculations are a prerequisite, not only for future calculations on naturally occurring dimeric Chl-*a* systems, but also for the theoretical study of isolated or multimeric Chl molecules that can be bound to surfaces to make artificial solar converting constructs.

The primary electron donor in photosystem I (PS I) is a dimeric Chl-*a* species called P_{700}. (P_{700}^{+}-P_{700}) FTIR difference spectra (DS) have been obtained [101]. Interpretation of the bands in

this spectrum are based upon comparison to corresponding electrochemically generated (Chl-a^+-Chl-*a*) and (pyroChl-a^+-pyroChl-*a*) FTIR DS [64, 101]. PyroChl-*a* is similar to Chl-*a* but lacks a 13^3 ester group (Figure 5.1(a) shows the structure and numbering scheme for Chl-*a*). The conclusions drawn from the electrochemistry experiments seemed clear cut, and so they have never been tested or questioned in any way. In the last decade, however, (P_{700}^+-P_{700}) FTIR DS have been obtained under many sets of conditions: from PS I particles from different strains [54], to particles with site directed mutations near the P_{700} and A_0 Chl's [54, 74, 76], to specifically isotope labeled PS I particles [71]. From these studies controversy persists concerning the interpretation of bands in (P_{700}^+-P_{700}) FTIR DS. The aim is to show that much of this controversy could arise because of incorrect interpretation and assignment of bands in electrochemically generated (Chl-a^+-Chl-*a*) FTIR DS.

The frequency and intensity information available in (P_{700}^+-P_{700}) FTIR DS provides a wealth of information on the hydrogen bonding status as well as on the polarity of the environment of specific functional groups that are part of P_{700}. However, if the origin of the bands in the spectra is misinterpreted, then conclusions derived will be incorrect. Clearly, there is a demonstrated need for a precise understanding of vibrational properties of Chl-*a* and Chl-a^+.

Up until recently, quantum chemical computational methods have played only a minor role in FTIR spectral band interpretation and assignment, especially as it applies to large molecular systems like Chl-*a*. However, computational capabilities are increasing, and recently density functional theory (DFT) based vibrational mode frequency calculations (at the B3LYP/6-31G(d) level) for several Chl-*a* and Chl-a^+ model molecular systems have been undertaken [80]. It has been shown that using only simple gas-phase calculations the experimental (pyroChl-a^+-pyroChl-*a*) FTIR DS can be accurately simulated. However, for Chl-*a* model molecular systems

that contain both the 13^1-keto and 13^3 ester carbonyl (C=O) groups, there is a strong coupling between the two carbonyl modes of the neutral Chl-*a* [80]. For Chl-a^+ it is also found that the calculated 13^1-keto C=O mode frequency is higher than that of the 13^3 ester carbonyl mode (although the two modes are no longer coupled) [80]. These calculated results disagree with assignments based on experimental data [64]. Previous normal mode vibrational frequency calculations were for a Chl-*a* model in the gas phase, with no consideration given to solvent effects [80]. It is possible that this lack of consideration of solvent effects could be at the heart of the above described discrepancies between the calculated and experimental data. Therefore, several new sets of calculations on Chl-*a* in the presence of solvents is presented here, in order to investigate if or how solvents impact the C=O mode vibrations.

In type I photosynthetic reaction centers it has been suggested the primary electron donor species is invariably a heterodimeric Chl/Chl' species [105-107]. Chl-*a*' is a 13^2 epimer of Chl-*a*. In view of this, the vibrational properties of both Chl-*a* and Chl-*a*' model systems were obtained in different solvents.

The calculated (Chl-a^+-Chl-*a*) IR DS, for both Chl-*a* and Chl-*a*' in different solvents, bear a remarkable similarity to the corresponding experimental spectra. The mode compositions, however, for the bands in the calculated spectra are very different from those assigned experimentally. Based on these calculation it was proposed that the bands in the experimental spectra may have been miss-assigned and further sets of calculations on isotope labeled Chl-*a* and Chl-*a*' was undertaken to further demonstrate the validity of the hypothesis.

5.2 Materials and Methods

All geometry optimizations and harmonic normal mode vibrational frequency calculations were performed using DFT as implemented in Gaussian 03 software, revision D.01.

[87]. Unless stated, the B3LYP functional was used in combination with the 6-31G(d) basis set. At this level of theory, computed harmonic vibrational mode frequencies overestimate experimental anharmonic frequencies by approximately 5% [80, 88]. Radical induced frequency shifts are accurately calculated, however [80, 89]. No negative frequencies were calculated for any of the model molecular structures discussed here. To model solvent effects the integral equation formalism (IEF) of the polarizable continuum model (PCM) was used [90-95], as it is implemented in Gaussian 03, version D.01.

The assignment of calculated vibrational frequencies to molecular groups is based upon visual identification, using software that animates the vibration (Gaussview 4.0). The calculations produce normal mode vibrational frequency and intensity information. From this data infrared (IR) "stick" spectra can be constructed. By convolving these stick spectra with a Gaussian function of 4 cm^{-1} half-width, more realistic looking spectra can be constructed. As previously described [89], these convolved stick spectra is referred to as absorption spectra.

5.3 Results and Discussion

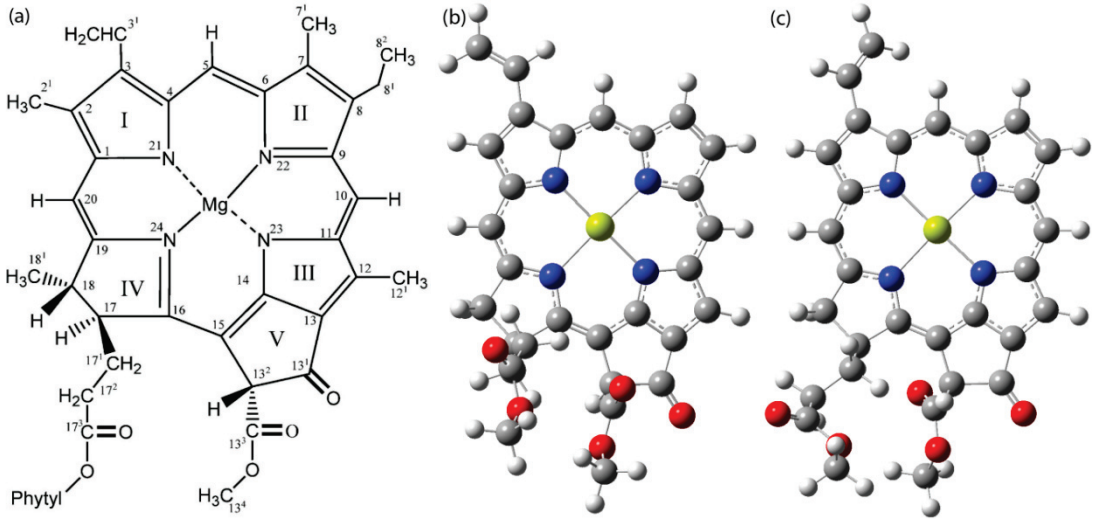

Figure 5.1: (a) Structure and IUPAC numbering scheme for Chl-*a*. (b) Chl-a_4 and (c) Chl-a_5 geometry optimized (energy minimized) molecular structural models of Chl-*a*.

Figure 5.1(a) shows the structure and IUPAC numbering scheme for Chl-*a*. Figure 5.1(b) shows the optimized geometry of the most sophisticated Chl-*a* model that was studied previously [80]. This model is called Chl-a_4. Chl-a_4 is representative of a Chl-*a*' species. Chl-*a*' is a 13^2 epimer of Chl-*a*. In view of the fact that the primary donor species in many type I reaction centers is a Chl/Chl' dimer [105-107] it is worthwhile calculating the vibrational properties of both Chl-*a* and Chl-*a*'. Figure 5.1(c) shows the model that is representative of Chl-*a*. This species is referred to as Chl-a_5 in this chapter. For Chl-a_4/Chl-a_5 the 13^2 hydrogen atom points down/up out of/into the plane of the macrocycle while the 13^3 ester C=O points up/down into the plane of the macrocycle, respectively. For Chl-a_4 and Chl-a_5 the portion of the phytyl chain following the 17^3 ester oxygen is replaced with a methyl group. In addition the molecular groups at positions 2, 8, 12 and 18 are replaced with hydrogen atoms. Chl-a_4 and Chl-a_5 also differ in the orientation of the vinyl group at the 3 position. The vinyl group orientation for Chl-a_5 is in line with that found in for example the cofactor Chl-*a* molecules in the PS I crystal structure.

Chl-a_4 and Chl-a_5 have 64 atoms, and displays 186 normal modes of vibration. Most of these modes have very low intensity and are undetectable in calculated IR absorption spectra. Such spectra are thus useful for direct consideration of the most intense modes of vibration. Figure 5.2 shows calculated IR absorption spectra for Chl-a_4, Chl-a_4^+, Chl-a_5 and Chl-a_5^+ in the 1870-1770 cm^{-1} region. The calculated (Chl-a_4^+-Chl-a_4) and (Chl-a_5^+-Chl-a_5) [cation minus neutral] IR DS are also shown.

The harmonic vibrational mode frequencies and intensities associated with the C=O modes of Chl-a_4, Chl-a_4^+, Chl-a_5 and Chl-a_5^+ are listed in Table 5.1. The calculations in Figure 5.2 are for molecules in the gas phase, and vibrational frequencies have not been scaled. As

indicated above, frequency scaling is unimportant, since the interest is in frequency differences, which are accurately calculated [80].

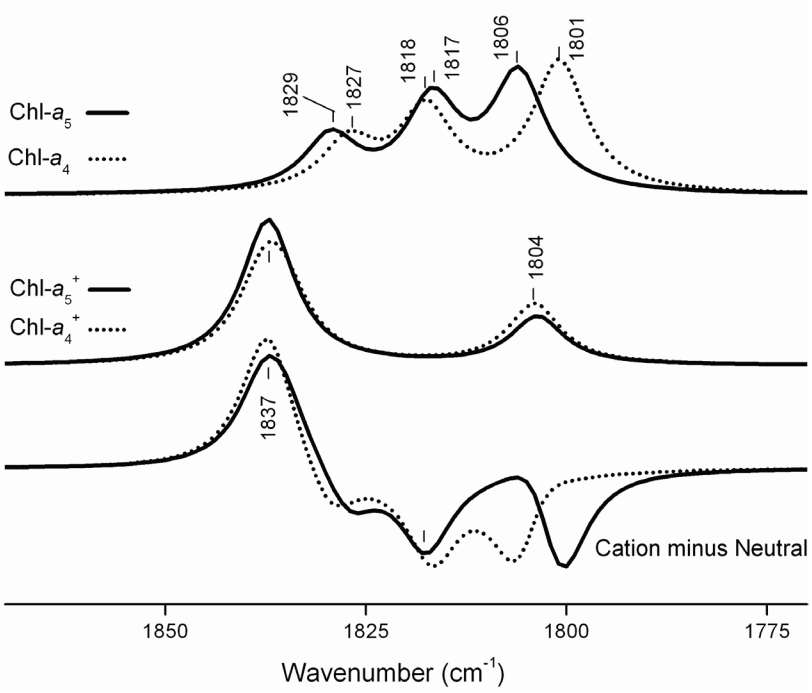

Figure 5.2: Calculated IR spectra for Chl-a_4/Chl-a_5 (top) and Chl-a_4^+/Chl-a_5^+ (middle) in the gas phase. The "cation minus neutral" IR DS are also shown (bottom). The Chl-a_4 spectra have been presented previously [80].

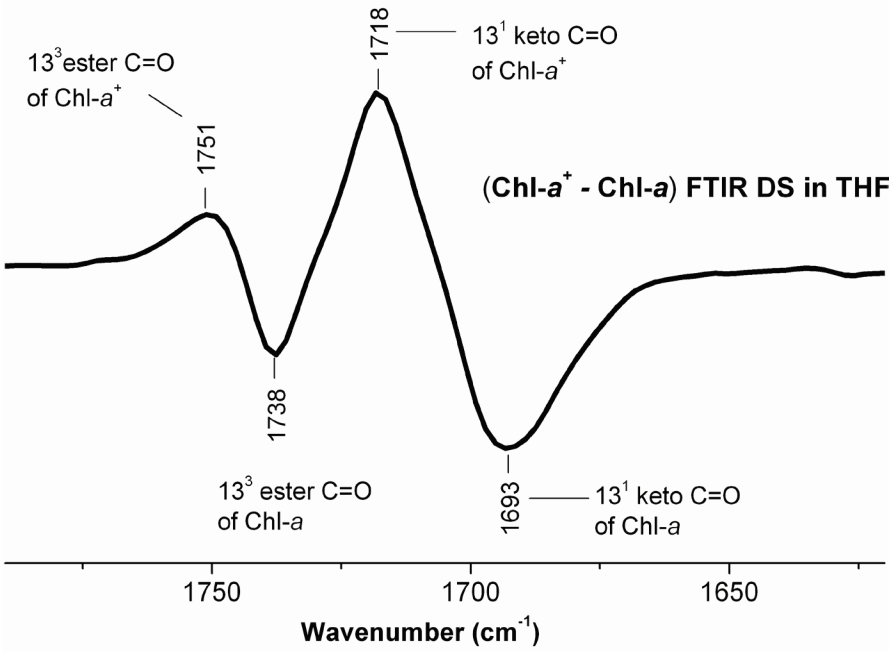

Figure 5.3: Electrochemically generated (Chl-a^+-Chl-a) FTIR DS, for Chl-a in THF [Reprinted with permission from Biochem. 1990, 29, 3242-3247. Copyright 2000 American Chemical Society]. Proposed band assignments are also indicated in the figure.

Table 5.1: Calculated frequencies and intensities (in parenthesis [in km/mole]) for the different carbonyl modes of Chl-a_4, Chl-a_5, Chl-a_4^+ and Chl-a_5^+.

Mode	Chl-a_4 ν(I)	Chl-a_4^+ ν(I)	Shift Δν(ΔI)	Chl-a_5 ν(I)	Chl-a_5^+ ν(I)	Shift Δν(ΔI)
ν(17^3 C=O)						
Gas phase	1827(211)	1835(230)	8(9%)	1829(233)	1837(498)[1]	
CCl_4	1812(268)	1818(257)	6(-4%)	1816(282)	1820(377)	4(29%)
THF	1799(325)	1803(265)	4(-20%)	1800(302)	1804(471)	4(44%)
H_2O	1789(371)	1793(224)	4(-49%)	1790(310)	1792(499)	2(47%)
ν(13^1 C=O) Gas phase		1838(337)			1838(123)[2]	
ν(13^1 and 13^3 C=O) s						
Gas phase	1818(347)			1817(379)		
CCl_4	1805(234)	1823(533)	18(78%)	1806(253)	1824(501)	18(66%)
THF	1794(243)	1806(693)	12(96%)	1796(271)	1809(621)	13(78%)
H_2O	1785(286)	1794(769)	9(92%)	1788(339)	1797(480)	9(34%)
ν(13^1 and 13^3 C=O) as						
Gas phase	1801(556)			1806(496)		
CCl_4	1786(1128)	1797(442)	11(-87%)	1792(1072)	1798(323)	6(-107%)
THF	1767(1724)	1785(861)	18(-67%)	1771(1681)	1791(686)	20(-84%)
H_2O	1753(2118)	1773(1336)	20(-45%)	1756(2136)	1779(1331)	23(-46%)
ν(13^3 C=O) Gas phase		1804(258)			1804(204)	

The cation induced frequency shift of the modes for each calculation is shown along with the mode intensity change [in parenthesis (in%)].

[1] Antisymmetric vibration of the 17^3 ester and 13^1 keto C=O groups.

[2] Symmetric vibration of the 17^3 ester and 13^1 keto C=O groups.

For comparison, the electrochemically generated (Chl-a^+-Chl-a) FTIR DS for Chl-a in tetrahydrofuran (THF) is shown in Figure 5.3. Electrochemically generated (Chl-a^+-Chl-a) FTIR difference spectra in the 1800-1600 cm^{-1} region have been obtained only for Chl-a in THF. Spectra in other solvents have not been reported, mainly because most other solvents absorb infrared radiation strongly in the 1800-1600 cm^{-1} region. Examination of the calculated and experimental difference spectra in Figures 5.2 and 5.3 indicate that the calculated frequencies are about 6% higher than the experimental frequencies. The calculated and experimental difference spectra also have very different overall spectral profiles.

In Figure 5.3 the 1693 cm^{-1} band was assigned to the 13^1 keto C=O mode of neutral Chl-a, which up-shifts 27 cm^{-1} upon cation formation. The 1738 cm^{-1} band was assigned to the 13^3

ester C=O mode of neutral Chl-*a*, which up-shifts 12 cm^{-1} upon cation formation. These assignments were based solely on comparison with electrochemically generated cation minus neutral FTIR DS for pyroChl-*a*, which lacks the 13^3 ester C=O group [64]. In the (pyroChl-a^+-pyroChl-*a*) FTIR DS only a single negative band is found at 1686 cm^{-1}, that up-shifts to 1712 cm^{-1} upon cation formation. The suggestion is that the 1738(-)/1751(+) cm^{-1} difference band that is present in the (Chl-a^+-Chl-*a*) FTIR DS but not in the (pyroChl-a^+-pyroChl-*a*) FTIR DS has to be due to the 13^3 ester C=O group. However, if there is a complicated coupling between the 13^3 ester and 13^1 keto C=O modes then the comparison of spectra for pyroChl-*a* and Chl-*a* is not meaningful (see below).

In the calculated spectrum for neutral Chl-a_4/Chl-a_5 in the gas phase the band at 1827/1829 cm^{-1} is due to only the 17^3 ester C=O group, respectively. This mode up-shifts ~8 cm^{-1} upon cation formation and changes little in intensity (Table 5.1). For Chl-a_4^+ in the gas phase the 17^3 ester C=O mode is found at 1835 cm^{-1} while the 13^1 keto C=O is found at 1838 cm^{-1}. Given the proximity of these modes in frequency one could expect them to be somewhat coupled. This is in fact what is found for Chl-a_5^+, where the symmetric/anti-symmetric coupled vibrations of the 13^1 keto and 17^3 ester C=O modes are calculated at 1838/1837 cm^{-1}, respectively (Table 5.1).

For neutral Chl-a_4 and Chl-a_5 in the gas phase the 13^1 keto and 13^3 ester C=O groups are strongly coupled, and unique vibrations of either of the C=O groups do not exist. The anti-symmetric vibration of the ester and keto C=O groups is found to occur at a lower frequency than the symmetric vibration. For Chl-a_4^+ and Chl-a_5^+ the 13^1 keto C=O vibration is separated from the 13^3 ester C=O vibration. However, the 13^1 keto C=O group vibrates at a higher frequency compared to the 13^3 ester C=O group (Table 5.1). This result is surprising.

5.3.1 Calculated Solvent Effects

The difference spectra in Figures 5.2 and 5.3 have very different profiles. The calculated mode compositions are also very different to that suggested from experiment [64]. One hypothesis for these discrepancies is that solvent effects were not considered in the calculations. Given this the vibrational properties of Chl-a_4 and Chl-a_5 in CCl_4, THF and H_2O, were calculated using the IEF PCM [90-95], as implemented within Gaussian 03, version D.01. The three solvents chosen cover a broad range of dielectric constants. For CCl_4, THF and H_2O the dielectric constants are 2.23, 7.58, and 78.39, respectively.

In the following only the vibrational modes associated with the C=O groups are considered. Table 5.1 lists the frequencies (and intensities) that were calculated for C=O modes in the gas phase, and in the three solvents. Table 5.1 indicates that inclusion of a solvent generally causes a decrease in frequency of the C=O modes. In this sense the calculations including solvent are an improvement over the gas phase calculations. However, inclusion of a solvent does not lead to a change in the calculated mode compositions, so that they become similar to that suggested from experiment [64] (see below).

5.3.2 The 17^3 Ester C=O Mode

For Chl-a_4 in the gas phase the 17^3 ester C=O mode up-shifts ~8 cm^{-1} and increases only slightly in intensity upon cation formation. The mode is a pure C=O vibration in both the neutral and cation states. For Chl-a_4 in CCl_4 and THF similar results are obtained; however, the mode intensity decreases upon cation formation. For Chl-a_4 in CCl_4 the mode is a pure C=O stretching vibration in both the neutral and cation states. In THF and water, however, the 17^3 and 13^3 ester C=O's are somewhat asymmetrically coupled, in both the neutral and cation states. In addition some mixing with the 13^1 keto C=O mode is observed. As pointed out above, for Chl-a_5^+ in the

gas phase the 17^3 ester and 13^1 keto C=O modes are similar in frequency, and strongly couple. For Chl-a_5^+ in CCl_4 and THF, however, this coupling decreases, resulting in an almost pure 17^3 ester C=O mode (Table 5.1).

5.3.3 The 13^1 Keto and 13^3 Ester C=O Modes

For Chl-a_4^+ and Chl-a_5^+ in the gas phase the 13^3 ester and 13^1 keto C=O modes are quite pure, although the keto vibration is at a higher frequency than the ester vibration (Table 5.1). As pointed out above, this result is difficult to rationalize [52]. For Chl-a_4^+ and Chl-a_5^+ in all of the solvents, the 13^3 ester and 13^1 keto C=O modes are coupled, as they are for neutral Chl-a_4 and Chl-a_5. So, the solvent increases the extent of coupling of the 13^1 keto and 13^3 ester C=O groups of Chl-a_4^+ and Chl-a_5^+.

For Chl-a_4 in CCl_4/THF/H_2O the symmetrically coupled 13^1 and 13^3 C=O mode up-shifts ~18/12/9 cm^{-1} and increases in intensity by 78/96/92 % upon cation formation, respectively. In contrast, in CCl_4/THF/H_2O the anti-symmetrically coupled 13^1 and 13^3 C=O mode up-shifts ~11/18/20 cm^{-1} and decreases in intensity by 87/67/45 % upon cation formation, respectively. Similar results are obtained for Chl-a_5 (Table 5.1). So, for both Chl-a_4 and Chl-a_5 the anti-symmetric and symmetric 13^1 and 13^3 C=O modes both up-shift upon cation formation, but the symmetric/anti-symmetric mode increases/decreases in intensity, respectively.

These calculated results are far from intuitive. To visualize these results Figure 5.4 shows calculated IR DS for Chl-a_4, Chl-a_5, Chl-a_4^+ and Chl-a_5^+ in THF. The calculated (Chl-a_4^+-Chl-a_4) and (Chl-a_5^+-Chl-a_5) IR DS are also shown. Clearly, calculated cation minus neutral IR DS for Chl-a in the gas phase or in solvent are very different. However, comparing the calculated cation minus neutral IR DS with the electrochemically generated (Chl-a^+-Chl-a) FTIR DS it is clear there is considerable similarity in the overall shape of the spectra. To highlight this

similarity, Figure 5.4 shows the calculated and experimental DS together, where the experimental spectrum has been shifted in frequency and scaled so that the bands are similar in intensity.

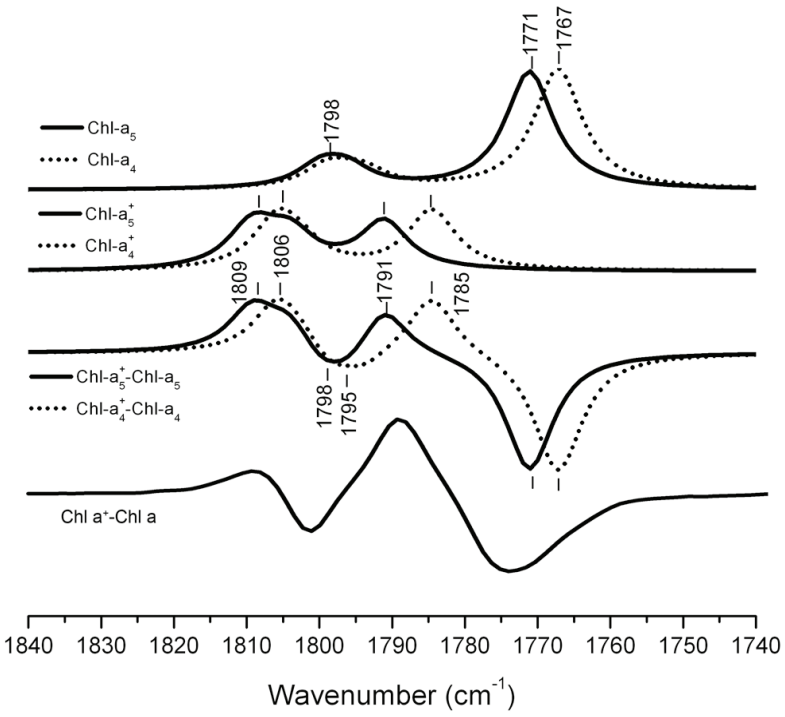

Figure 5.4: Calculated IR DS for Chl-a_4, Chl-a_4^+, Chl-a_5 and Chl-a_5^+ in THF. The calculated (Chl-a_4^+-Chl-a_4) and (Chl-a_5^+-Chl-a_5) IR DS are also shown. (Bottom): Experimental (Chl-a^+-Chl-a) FTIR DS obtained for Chl-a in THF (from Figure 5.3). Spectrum has been scaled and shifted for the sake of comparison.

Figure 5.4 shows the calculated and experimental spectra for Chl-a in THF. This is because THF is the only solvent in which experimental (Chl-a^+-Chl-a) FTIR DS have been obtained. It is very unlikely that (Chl-a^+-Chl-a) FTIR DS for Chl-a in H_2O or CCl_4 will ever be obtained. However, for completeness, the vibrational mode frequencies calculated for Chl-a in the three solvents are included in Table 5.1. From Table 5.1 it appears that the polarizable continuum method predicts that the vibrational mode frequencies will decrease as the solvent dielectric constant increases.

The calculated IR DS in Figure 5.4 accurately models the overall shape of the (Chl-a^+-Chl-a) electrochemically generated FTIR DS. It has been showed previously that the calculated

(pyroChl-a^+-pyroChl-a) IR DS is in keeping with experiment [80]. However, the mode compositions associated with the bands in the calculated and experimental DS are very different. As pointed out above, the complicated mode composition of the C=O bands in the (Chl-a^+-Chl-a) electrochemically generated FTIR DS would not be apparent from a simple comparison with the (pyroChl-a^+-pyroChl-a) FTIR DS.

On the basis of the calculations, a new set of assignments for the bands in the experimental (Chl-a^+-Chl-a) FTIR DS in Figure 5.3 is proposed.

From Figure 5.4 the suggestion is that the calculated difference band at 1767/1785 or 1771/1791 cm^{-1} for Chl-a_4 or Chl-a_5, respectively, corresponds to the experimental difference band at 1693/1718 cm^{-1}. The calculated negative band at 1767 or 1771 cm^{-1} for Chl-a_4 or Chl-a_5 is due to the anti-symmetric vibration of the 13^1 keto and 13^3 ester C=O groups. This band up-shifts 18 or 20 cm^{-1} and decreases in intensity by 67 or 84 % upon cation formation, respectively. Therefore, the 1693 cm^{-1} band in the experimental spectrum (Figure 5.3)is assigned to the anti-symmetric vibration of the 13^1 keto and 13^3 ester C=O groups, which up-shifts 25 cm^{-1} upon cation formation and decreases considerably in intensity.

The calculated difference band at 1795/1806 or 1798/1809 cm^{-1} for Chl-a_4 or Chl-a_5, respectively, corresponds to the experimental difference band at 1738/1751 cm^{-1} (Figure 5.4). For Chl-a_4/Chl-a_5 the negative band at 1795/1798 cm^{-1} is due to the symmetrically coupled vibration of the 13^1 keto and 13^3 ester C=O groups, respectively. This band up-shifts 11/11 cm^{-1} upon cation formation. Therefore, the 1738 cm^{-1} band in the experimental spectrum in Figure 5.3 is assigned to the symmetric vibration of the 13^1 keto and 13^3 ester C=O groups, which up-shifts 13 cm^{-1} upon cation formation. The experimental data suggests an intensity decrease but the calculations indicate that the symmetrically coupled vibration of the 13^1 keto and 13^3 ester C=O

groups increases in intensity. The calculated and experimental spectra look similar, however, because of overlapping bands associated with the 17^3 ester C=O modes.

The overall similarity in spectral profile (distribution of positive and negative bands) between the calculated and experimental spectra for Chl-*a* in solvent could be viewed as somewhat fortuitous. It should be pointed out, that the calculated (Chl-a^+-Chl-*a*) FTIR DS in all of the solvents look similar (not shown) and do not resemble at all the calculated gas phase (Chl-a^+-Chl-*a*) FTIR DS. In addition, the calculated difference spectrum for BChl-*a* in THF and methanol using the IEF PCM method also resemble experimental difference spectra (not shown), with the calculated gas phase difference spectra again being very different. Difference spectra calculated for the triplet state of Chl-*a* in THF also resemble experimental difference spectra, while calculated gas phase spectra do not (not shown). Difference spectra calculated, with solvent effects included, clearly lead to a more accurate description or simulation of experimental FTIR DS than do calculations that do not include solvent effects.

Polarizable continuum methods are limited in the sense that they do not model possible axial ligands or hydrogen bonds to the Chl-*a* molecule. The vibrational properties of Chl-*a* has been obtained in explicit solvents, using QM/MM methods (see Chapter 6). These calculations show that even for solvents that can form ligands and/or hydrogen bonds to the carbonyl groups, the 13^1 keto and 13^3 ester carbonyl groups in the neutral and cation states are still coupled. Calculations for Chl-*a* models in which the central magnesium atom is ligated, and/or the carbonyl groups are hydrogen bonded, are presented in Chapter 7.

Now the question to be answered is: Are there any experimental data available that can be used to test or validate the proposed assignments? FTIR DS for specifically isotope labeled Chl-*a* samples has never been obtained. However, P_{700} in photosystem I (PS I) is a dimeric Chl-*a*

species [6], and (P_{700}^{+}-P_{700}) FTIR DS have been obtained using PS I particles in which only the 13^4 methyl hydrogen atoms of Chl-*a* have been deuterated [71]. Using labeled and unlabeled PS I particles, a (^{1}H-^{2}H) isotope edited (P_{700}^{+}-P_{700}) FTIR double difference spectrum (DDS) was constructed. This spectrum showed several derivative features spanning the 1775-1675 cm^{-1} region. Later it was suggested that this DDS indicated the presence of at least four distinct 13^3 ester C=O vibrations [70].

This interpretation is problematic. If P_{700} is a dimeric Chl-*a* species then the suggestion is that both Chl-*a* molecules of P_{700} contribute two 13^3 ester C=O modes. Apart from the fact that ester C=O modes of any molecule are unknown in the ~1680 cm^{-1} region, the interpretation of at least four distinct 13^3 ester C=O vibrations implies modification of the Chl-*a* molecules of P_{700} by the protein, in about one half of the PS I particles (that is, some level of heterogeneity in the P_{700} binding site is required, for only the ester C=O modes). Given the new interpretation of bands in (Chl-a^{+}-Chl-*a*) FTIR DS, the presence of multiple derivative features in the isotope edited FTIR DDS, spanning a broad frequency region, is readily understood.

To help visualize this (Chl-a^{+}-Chl-*a*) IR DS for Chl-a_4 and Chl-a_5 in THF was calculated, in which the three 13^4 methyl hydrogen atoms are either unlabeled or deuterated (Figure 5.5). From the unlabeled and deuterated DS (^{1}H-^{2}H) IR DDS was obtained (Figure 5.5). Multiple (four) derivative features across a broad spectral region are observed in the calculated (^{1}H-^{2}H) IR DDS. These features all show up because the anti-symmetric and symmetric modes are differently shifted by deuteration. In addition, the deuteration induced shifts are larger for both modes in the cation state compared to the neutral state. The calculated IR DDS is certainly reminiscent of the observations made in the (^{1}H-^{2}H) (P_{700}^{+}-P_{700}) FTIR DDS presented previously [71]. Off course P_{700} is dimeric, so one could expect even more than four derivative features to

be observed in the experimental DDS, and this is clearly found to be the case in the previously presented isotope edited DDS [71]. Thus the new band assignment hypothesis can also reasonably explain some hitherto incomprehensible experimental results.

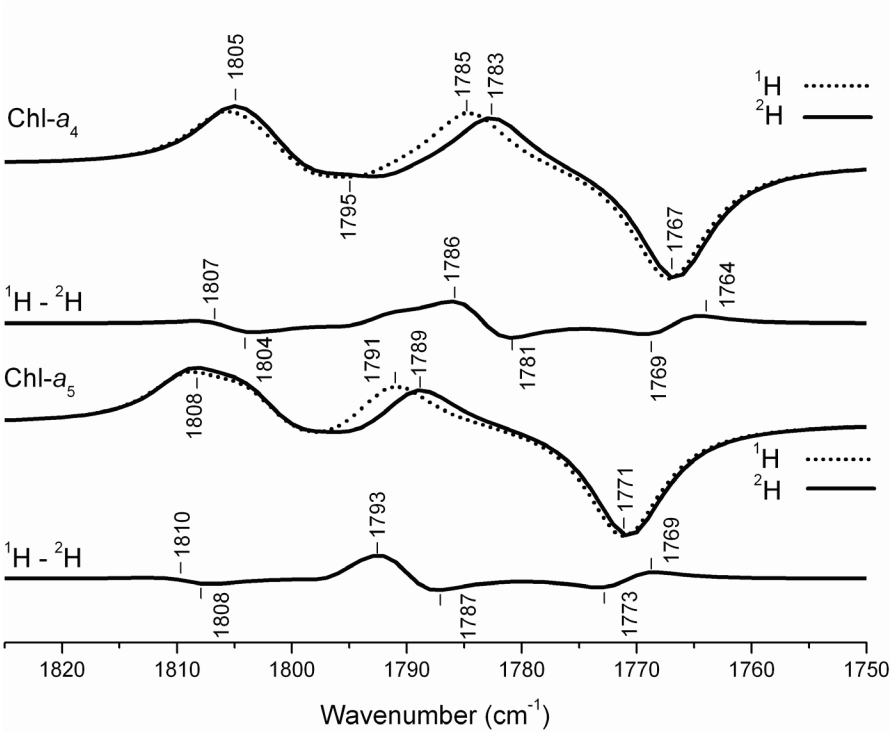

Figure 5.5: Calculated (Chl-a_4^+-Chl-a_4) (*Top*) and (Chl-a_5^+-Chl-a_5) IR DS (*bottom*) for unlabeled (^{1}H, dotted) and deuterated (^{2}H, *solid line*) Chl-*a* in THF. For the ^{2}H labeled molecule it is only the 13^4 methyl hydrogen atoms that have been deuterated. Results obtained by subtracting the unlabeled from the labeled spectrum (referred to as a (^{1}H-^{2}H) IR DDS) are also shown.

All of the experimental data for Chl-*a* in solvent, for pyroChl-*a* in solvent, and for (P_{700}^+-P_{700}) FTIR DS, for P_{700} with specifically labeled Chl-*a*, can be explained using the proposed set of band assignments. Any other model necessarily has to infer some sort of sample heterogeneity to explain all of the data. The fact that the proposed band assignments can explain several disparate experimental results is strong support for its validity. The implications of the proposed model on the interpretation of "cation minus neutral" FTIR DS obtained for many different types of photosynthetic complexes will be investigated in the future.

The new assignments presented here have implications beyond the realms of FTIR studies of photosynthetic systems. With knowledge that the vibrational frequency calculations on Chl-*a* do in fact correctly describe experimental data, the applicability of these computational methods for the evaluation of other chemical properties of Chl-*a*, such as electron affinities and ionization potentials, and hence cofactor redox potentials can be validated.

5.4 Conclusions

New assignments for some of the bands in electrochemically generated (Chl-a^+-Chl-*a*) FTIR DS has been proposed. A difference band that was previously assigned to a cation induced up-shift of a pure 13^1 keto C=O mode is shown to be due to a mode that is the anti-symmetrically coupled vibration of both the 13^1 and 13^3 ester C=O modes. This coupled anti-symmetric dual C=O vibration still up-shifts upon cation formation, and still decreases in intensity.

A difference band that was previously assigned to a cation induced up-shift of a pure 13^3 ester C=O mode is shown to be due to a mode that is the symmetrically coupled vibration of both the 13^1 and 13^3 ester C=O modes. This coupled symmetric C=O vibration still up-shifts upon cation formation, but actually increases slightly in intensity.

These new assignments allow a new rationalization of some previously very puzzling experimental (P_{700}^+-P_{700}) FTIR DS.

CHAPTER 6

CALCULATION OF THE VIBRATIONAL PROPERTIES OF CHLOROPHYLL-*A* IN SOLUTION: COMPARISON OF POLARIZABLE CONTINUUM METHODS WITH QM/MM METHODS USING EXPLICIT SOLVENT MOLECULES.

6.1 Introduction

Chlorophylls (Chl) play a vital role in electron transfer process in photosynthesis [33]. In photosynthetic reaction centers of plants and bacteria, electron transfer leads to one electron oxidation of a special pair of chlorophyll/bacteriochlorophyll pigments (known as the primary electron donor). To understand the mechanism of charge separation in these primary donor species, spectroscopic techniques such as fourier transform infrared (FTIR) difference spectroscopy (DS) has been used [101]. FTIR spectroscopy can be used to probe both neutral and radical forms and changes in the frequencies of the vibrational bands upon radical pair formation provides valuable information on the electronic state as well as the structure including the protein-pigment interactions upon oxidation or reduction (see Chapter 1 for details). The primary electron donor in photosystem I (PS I) is a dimeric Chlorophyll-*a*/Chlorophyll-*a*' (Chl-*a*/Chl-*a*') species called P_{700} [6]. (P_{700}^{+}-P_{700}) FTIR difference spectra (DS) have been obtained under various conditions, for PS I particles from different strains, to particles with site directed mutations near the P_{700} and A_0 Chl's, to specifically isotope labeled PS I particles [54, 74, 76] (see Chapters 2 ,3and 4). From these studies controversy persists concerning the interpretation of bands in (P_{700}^{+}-P_{700}) FTIR DS. One of the aims of our computational research in photosynthesis is to simulate the vibrational properties of P_{700} in the cation and neutral state in order to assist in the assignments of FTIR difference bands observed in experimental spectra.

An in depth understanding of the *in vitro* vibrational properties of Chl-*a* in both the neutral and cation state is the first step in our quest to understand (P_{700}^{+}-P_{700}) FTIR DS quantitatively.

With this goal in mind density functional theory (DFT) based vibrational mode frequency calculations for several Chl-*a* model structures in the gas phase as well as in different solvents were undertaken [79] (See Chapter 5). Solvents were modeled using the Polarizable Continuum Model (PCM). In PCM calculations the solvent is modeled as a dielectric continuum. The calculated (Chl-a^{+}-Chl-*a*) IR DS of Chl-*a* in solvents, obtained using the PCM model, bear remarkable similarity to the corresponding experimental spectra [79] (See Chapter 5). The mode compositions of the carbonyl groups of Chl-*a* in the calculated spectra, however, are very different from the experimentally assigned mode compositions. Based on these solvent calculations new band assignments were proposed for some of the bands in electrochemically generated (Chl-a^{+}-Chl-*a*) FTIR DS [79]. Here our vibrational frequency studies of Chl-*a* are extended to explicitly include solvent molecules using Quantum Mechanical/Molecular Mechanics methods (QM/MM) and a comparison of the two solvation models is presented.

6.2 Materials and Methods

All vibrational frequency calculations were performed using Gaussian03 software, Revision D.01 [87]. The starting coordinates for the chlorophyll structures were obtained from the crystal structure of PS I [6]. Specifically, the CL11021 pigment which constitutes one of the chlorophylls of the P_{700} dimer was used. All atoms were included, except the phytyl chain was truncated at 17^{4} position with a methyl group. This model contains 82 atoms. The structure starting from the crystal structure was fully geometry optimized at B3LYP/6-31G(d) level in the

gas phase. The fully geometry optimized gas phase structure was used as the starting geometry for QM/MM calculations, including solvents.

The (Chl-a^+-Chl-*a*) experimental FTIR DS has been obtained in THF [64] and the intent is to be able to simulate the spectra using DFT based vibrational frequency calculations.

6.2.1 QM/MM Method

The QM/MM method models the solvent effect by including the actual solvent molecules around the pigment of interest. Here two solvents were considered, with dielectric constants in the range of the overall dielectric of the photosynthetic protein complexes, CCl_4 (ε =2.228) and THF (ε = 7.58). For the QM/MM calculations,70 THF molecules and 96 CCl_4 solvent molecules were added around the Chl-*a* molecule, using the solvent cluster utility in the VegaZZ program [108]. The model, including the pigment and solvent molecules, was fully geometry optimized using a two-level ONIOM (our Own N-layer Integrated molecular Orbital molecular Mechanics) method as implemented in Gaussian03 [109-116].

The ONIOM method treats the pigment(s) of interest at the quantum mechanical (QM) level and includes the influence of the surroundings (e.g. solvent molecules) at the molecular mechanical (MM) level and is one of the many QM/MM methods available. In a two layer ONIOM calculation, the total energy of the system is obtained from three independent calculations:

$$E^{ONIOM\,(QM:MM)} = E^{QM}_{model} + E^{MM}_{real} - E^{MM}_{model} = E^{high}_{model} + E^{low}_{real} - E^{low}_{model}$$

the real system contains all the atoms, Chl-*a* and the solvent molecules in this case, and is calculated only at the MM level. The model system contains only the Chl-*a* pigment that is treated at the QM level. To evaluate the ONIOM energy, both QM and MM calculations need to be carried out for the Chl-*a* pigment [116].Thus by treating only the pigment of interest at the

QM level the computational expense of the calculation is reduced to a large extent. Because of the favorable computational cost of the QM/MM methods they are increasingly used to model large molecules in the presence of solvents or proteins [117].

The ONIOM scheme can be divided into two groups, mechanical embedding (ME) and electrostatic embedding (EE) depending on the treatment of the electrostatic interaction between the pigment of interest (QM level) and the solvent molecules (MM level) [118]. The electrostatic embedding scheme in ONIOM method was used in the calculations presented here. In this method, the partial charges from the MM region (solvent) are included in the QM Hamiltonian. Thus a more accurate description of the electrostatic interaction between the layers is obtained [117, 119, 120].

The Chl-*a* pigment at the higher level calculation was treated using DFT (B3LYP/6-31G(d)) while the solvent was treated using AMBER. The AMBER force field parameters for the solvents were derived using the Antechamber program [121, 122]. For chlorophyll, the *ab initio* force field developed for chlorophyll cofactors were used [123, 124], which is parameterized to reproduce density functional theory vibrational modes.

6.2.2 Polarizable Continuum Model

The Polarizable Continuum Model (PCM) is one of the most frequently used methods to model the effect of solvent. In this method the solvent is treated as a continuum of dielectric constant ε and the pigment of interest is placed in a cavity within the solvent [92]. Here the Integral Equation Formalism (IEF) method of the PCM was used [87]. Geometry optimization and vibrational frequency calculation of Chl-*a* were performed in two different solvents of dielectric constants 2.228 (CCl_4) and 7.58 (THF). The calculated vibrational mode frequencies were compared to the corresponding calculations using QM/MM methods.

6.3 Results and Discussion

Figure 6.1(a) shows the structure and IUPAC numbering scheme for Chl-*a*. Figure 6.1(b) shows the geometry optimized structure model for Chl-*a* used in the calculations. The coordinates for the Chl-*a* molecule was obtained from the crystal structure of PS I [6]. The phytyl chain in the model was replaced by a methyl group at the 17^4 position. Figure 6.2 shows the geometry optimized structure of neutral Chl-*a* using QM/MM methods.

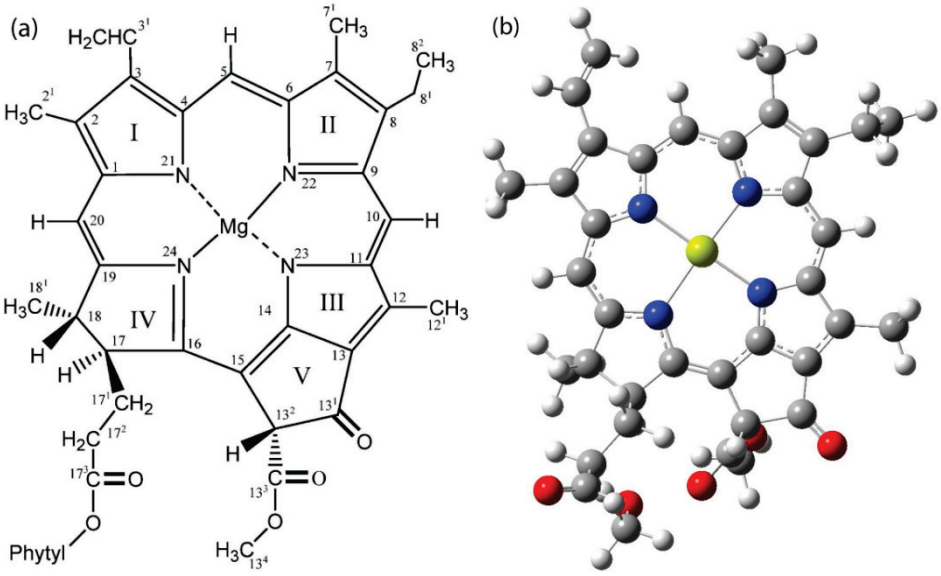

Figure 6.1: (a) Structure and IUPAC numbering scheme for Chl-*a*. (b) The geometry optimized (gas phase) model molecular structure of Chl-*a* used in this study. The phytyl chain following the 17^3 ester oxygen was replaced with a methyl group in the model. No other atoms were deleted.

6.3.1 Geometry Optimization

The fully geometry optimized structure of neutral Chl-*a* using QM/MM methods is shown in Figure 6.2. The principle bond distances for Chl-*a* in the neutral and cation states (in parenthesis) obtained after geometry optimization in the gas phase and in different solvents is presented in Table 6.1. Small changes in bond length are observed upon geometry optimization in the presence of solvents. Also small but significant changes are observed for bonds in the cation state compared to the neutral state. Of particular significance is the decrease in the $C_{13}{}^1$=O bond length upon cation formation in all the calculations. This group is an important marker used

in FTIR difference spectroscopy studies of P_{700} where the frequency of the intense C=O stretching mode has been used to monitor oxidation and reduction of the primary electron donor [101].

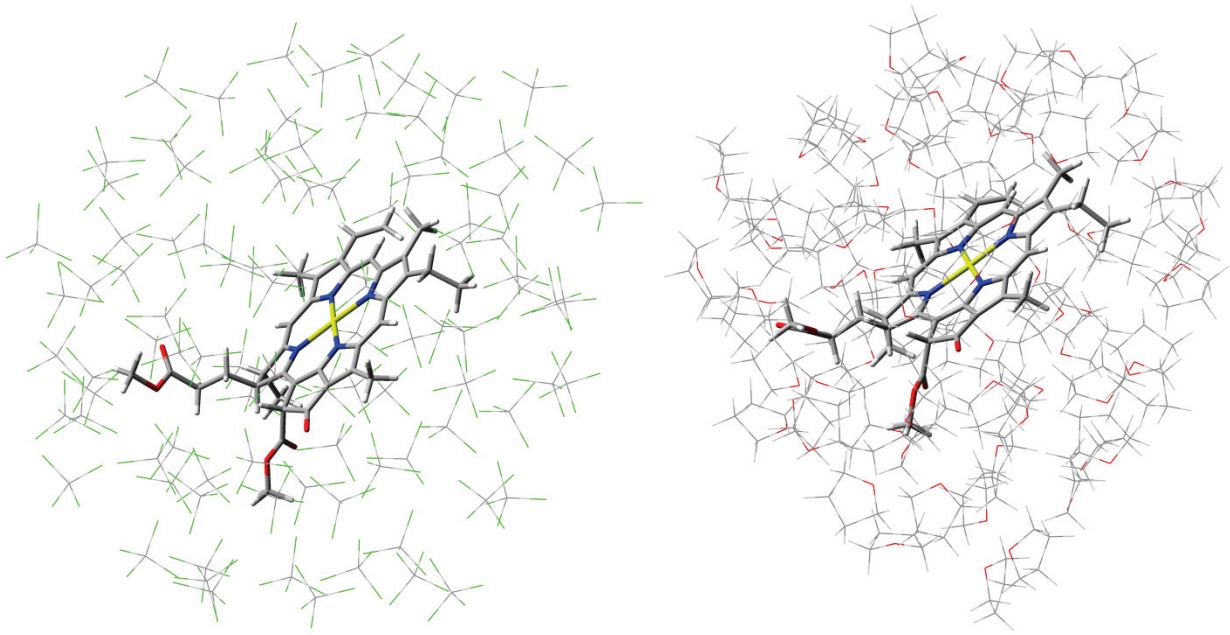

Figure 6.2: Geometry optimized structure of Chl-*a* using the QM/MM method (a) Chl-*a* in CCl_4 and (b) Chl-*a* in THF. The phytyl chain following the 17^3 ester oxygen was replaced with a methyl group in both models. In a/b 74/96 CCl_4/THF molecules were used.

Table 6.1: Selected optimized bond lengths (in Å) for Chl-*a* models in the neutral and cation (in parenthesis) states.

	Chl-*a* (GasPhase)	Chl-*a* in CCl_4 (PCM)	Chl-*a* in CCl_4 (QM/MM)	Chl-*a* in THF (PCM)	Chl-*a* in THF (QM/MM)
$Mg\text{-}N_{21}$	2.031 (2.024)	2.035 (2.027)	2.035 (2.025)	2.038 (2.032)	2.029 (2.025)
$Mg\text{-}N_{22}$	2.073 (2.067)	2.077 (2.072)	2.069 (2.066)	2.082 (2.076)	2.066 (2.067)
$Mg\text{-}N_{23}$	2.018 (2.013)	2.022 (2.017)	2.015 (2.011)	2.027 (2.022)	2.017 (2.014)
$Mg\text{-}N_{24}$	2.150 (2.138)	2.154 (2.141)	2.139 (2.129)	2.157 (2.144)	2.143 (2.132)
$C_1\text{-}C_2$	1.450 (1.463)	1.452 (1.464)	1.450 (1.462)	1.454 (1.466)	1.450 (1.462)
$C_2\text{-}C_3$	1.380 (1.372)	1.380 (1.373)	1.381 (1.373)	1.380 (1.372)	1.382 (1.372)
$C_3\text{-}C_4$	1.463 (1.476)	1.464 (1.477)	1.461 (1.476)	1.466 (1.478)	1.460 (1.472)
$C_1\text{-}N_{21}$	1.363 (1.371)	1.362 (1.371)	1.363 (1.371)	1.362 (1.370)	1.363 (1.373)
$N_{21}\text{-}C_4$	1.381 (1.370)	1.381 (1.366)	1.380 (1.369)	1.379 (1.364)	1.382 (1.365)
$C_4\text{-}C_5$	1.391 (1.401)	1.392 (1.404)	1.390 (1.401)	1.392 (1.406)	1.389 (1.403)
$C_5\text{-}C_6$	1.412 (1.402)	1.414 (1.401)	1.410 (1.401)	1.415 (1.400)	1.412 (1.398)
$C_6\text{-}N_{22}$	1.365 (1.370)	1.364 (1.370)	1.363 (1.368)	1.363 (1.369)	1.365 (1.372)
$N_{22}\text{-}C_9$	1.379 (1.370)	1.379 (1.368)	1.378 (1.370)	1.380 (1.366)	1.380 (1.369)
$C_9\text{-}C_{10}$	1.404 (1.410)	1.404 (1.412)	1.403 (1.410)	1.403 (1.414)	1.403 (1.413)
$C_{10}\text{-}C_{11}$	1.399 (1.394)	1.401 (1.393)	1.399 (1.394)	1.403 (1.393)	1.399 (1.390)
$C_{11}\text{-}N_{23}$	1.394 (1.383)	1.394 (1.382)	1.393 (1.382)	1.394 (1.382)	1.397 (1.387)
$N_{23}\text{-}C_{14}$	1.336 (1.341)	1.335 (1.339)	1.334 (1.339)	1.333 (1.336)	1.336 (1.337)
$C_{14}\text{-}C_{15}$	1.413 (1.403)	1.415 (1.405)	1.415 (1.402)	1.416 (1.407)	1.413 (1.406)

C_{15}-C_{16}	1.381 (1.393)	1.381 (1.392)	1.381 (1.391)	1.381 (1.391)	1.380 (1.384)
C_{16}-N_{24}	1.377 (1.378)	1.376 (1.377)	1.378 (1.376)	1.376 (1.377)	1.377 (1.383)
N_{24}-C_{19}	1.358 (1.357)	1.357 (1.354)	1.358 (1.357)	1.355 (1.352)	1.358 (1.349)
C_{19}-C_{20}	1.390 (1.402)	1.392 (1.405)	1.390 (1.402)	1.394 (1.407)	1.389 (1.407)
C_{20}-C_1	1.410 (1.398)	1.411 (1.397)	1.410 (1.398)	1.411 (1.397)	1.410 (1.391)
C_{13}^1-O	1.215 (1.208)	1.218 (1.211)	1.214 (1.208)	1.221 (1.213)	1.217 (1.209)
C_{13}^3-O	1.214 (1.214)	1.215 (1.215)	1.214 (1.214)	1.216 (1.216)	1.215 (1.215)
C_{17}^3-O	1.212 (1.210)	1.214 (1.213)	1.212 (1.212)	1.217 (1.215)	1.211 (1.213)

6.3.2 Calculated Vibrational Frequencies

The changes in the harmonic frequencies and intensity of all the three C=O groups of Chl-*a* in different solvents are listed in Table 6.2. The Chl-*a* model used here has 82 atoms and displays 240 normal modes of vibration. Most of these modes are very low intensity and are undetectable in calculated IR absorption spectra. On the contrary, the C=O groups of Chl-*a* gives intense modes of vibration and can be used to monitor the electronic structure in the neutral and cation states.

Table 6.2: Calculated frequencies and intensities for the different carbonyl modes of Chl-*a* and Chl-a^+ in the gas phase and in solvents.

Mode	Chl-*a* ν(I)	Chl-a^+ ν(I)	Shift Δν(ΔI)
ν(17^3 C=O)			
gas phase	1829(235)	1836(213)	7(-10%)
CCl_4(PCM)	1813(287)	1819(217)	6(-27%)
CCl_4 (QM/MM)	1828(170)	1826(187)	-2(10%)
THF (PCM)	1799(276)	1804(520)	5(61%)
THF(QM/MM)	1836(302)	1821(219)	-15(-32%)
ν(13^1 and 13^3 C=O) s			
gas phase	1812(129)	1830(397)	18(102%)
CCl_4(PCM)	1804(126)	1817(568)	13(127%)
CCl_4 (QM/MM)	1816(160)	1836(354)	20(75%)
THF (PCM)	1796(255)	1806(336)	10(27%)
THF(QM/MM)	1815(63)	1834(485)	18(154%)
ν(13^1 and 13^3 C=O) as			
gas phase	1801(719)	1805(215)	4(-108%)
CCl_4(PCM)	1785(1142)	1798(385)	13(-99%)
CCl_4 (QM/MM	1807(687)	1814(205)	7(-108%)
THF (PCM)	1767(1637)	1790(771)	23(-72%)
THF(QM/MM)	1798(985)	1796(123)	-2(-156%)

The cation induced frequency shift of the modes for each calculation is also shown along with the mode intensity change (in %) in parenthesis.

6.3.2.1 Gas Phase Calculations

Figure 6.3(a) shows calculated IR difference spectrum (cation minus neutral) for Chl-*a* in the gas phase. Figure 6.3(b) shows the electrochemically generated (Chl-a^+-Chl-*a*) FTIR DS for Chl-*a* in tetrahydrofuran (THF) for comparison [64].Electrochemically generated (Chl-a^+-Chl-*a*) FTIR DS has been obtained only for Chl-*a* in THF. FTIR DS for Chl-*a* in no other solvent has been reported, mainly because most other solvents absorb infrared radiation strongly in the 1800-1600 cm^{-1} region.

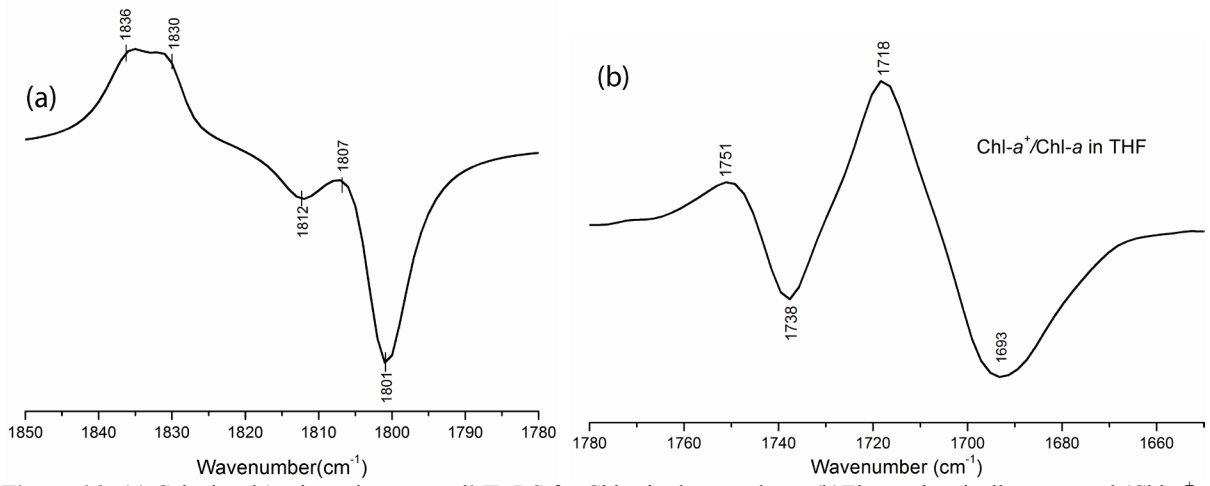

Figure 6.3: (a) Calculated 'cation minus neutral' IR DS for Chl-*a* in the gas phase. (b)Electrochemically generated (Chl-a^+-Chl-*a*) FTIR DS for Chl-*a* in THF.

The calculated Chl-*a* spectrum in the gas phase has a different overall profile compared to the experimental spectrum. Also the mode compositions are different to that suggested from the experiment [64]. In Figure 6.3(b), the 1693 cm^{-1} band was assigned to the 13^1 keto C=O mode of neutral Chl-*a*, which up-shifts 27 cm^{-1} upon cation formation. The 1738 cm^{-1} band was assigned to the 13^3 ester C=O mode of neutral Chl-*a*, which up-shifts 12 cm^{-1} upon cation formation (See Chapter 5). These assignments were based on comparison with electrochemically generated cation minus neutral FTIR DS for Chl-*a* and pyroChl-*a*, which lacks the 13^3 ester C=O group [64]. In the (pyroChl-a^+-pyroChl-*a*) FTIR DS only a single negative band is found at 1686 cm^{-1}, which up-shifts to 1712cm^{-1} upon cation formation. The suggestion is that the 1738(-

)/1751(+) cm^{-1} difference band that is present in the (Chl-a^+-Chl-*a*) FTIR DS but not in the (pyroChl-a^+-pyroChl-*a*) FTIR DS has to be due to the 13^3 ester C=O group. The calculated vibrational modes of Chl-*a* in the gas phase show strong coupling between the 13^1 keto and 13^3 ester C=O groups in both neutral and cation states. Since pyroChl-*a* lacks the 13^3ester C=O group, if there is a complicated coupling between the 13^1 and 13^3 ester C=O groups as suggested by the gas phase calculations, the comparison of spectra of pyroChl-*a* and Chl-*a* for the assignment of the bands in the latter DS spectra is problematic.

6.3.2.2 Solvent Calculations Using Polarizable Continuum Model

The calculated IR difference spectra of Chl-*a* in the gas phase has a very different overall profile compared to the experimental (Chl-a^+-Chl-*a*) FTIR DS in THF. Also the observed vibrational mode compositions of the difference band are very different from the proposed band assignments for the experimental (Chl-a^+-Chl-*a*) FTIR DS. The assumption was that the lack of consideration of solvent effects could be the reason for the disagreement between the calculated and experimental spectra. Therefore, vibrational frequency calculations for Chl-*a* model in the presence of various solvents, including CCl_4, THF and H_2O were undertaken using the PCM model to further investigate the discrepancies between the calculated and experimental Chl-*a* IR DS [79]. THF is the only solvent in which experimental (Chl-a^+-Chl-*a*) FTIR DS have been obtained. However, for completeness, the vibrational frequencies calculated for Chl-*a* in CCl_4 is also included in the discussion. The calculated IR DS spectra of Chl-*a* in the presence of CCl_4 and THF using the PCM model is presented in Figure 6.4.

Figure 6.4 clearly shows that the calculated cation minus neutral IR DS for Chl-*a* in the solvents is very different from the corresponding IR DS in the gas phase. However, comparing the calculated cation minus neutral IR DS in solvents with the electrochemically generated (Chl-

a^+-Chl-*a*) FTIR DS, it is clear there is considerable similarity in the overall shape of the spectra as found previously (see Chapter 5). However, the mode compositions associated with the bands in the calculated spectra in solvents are similar to the gas phase calculations, where a strong coupling is observed between the 13^1 keto and 13^3 ester C=O modes both in the neutral and cation states. On the basis of these calculations a new set of assignments for the bands in the experimental (Chl-a^+-Chl-*a*) FTIR DS in Figure 6.3(b) was proposed [79].

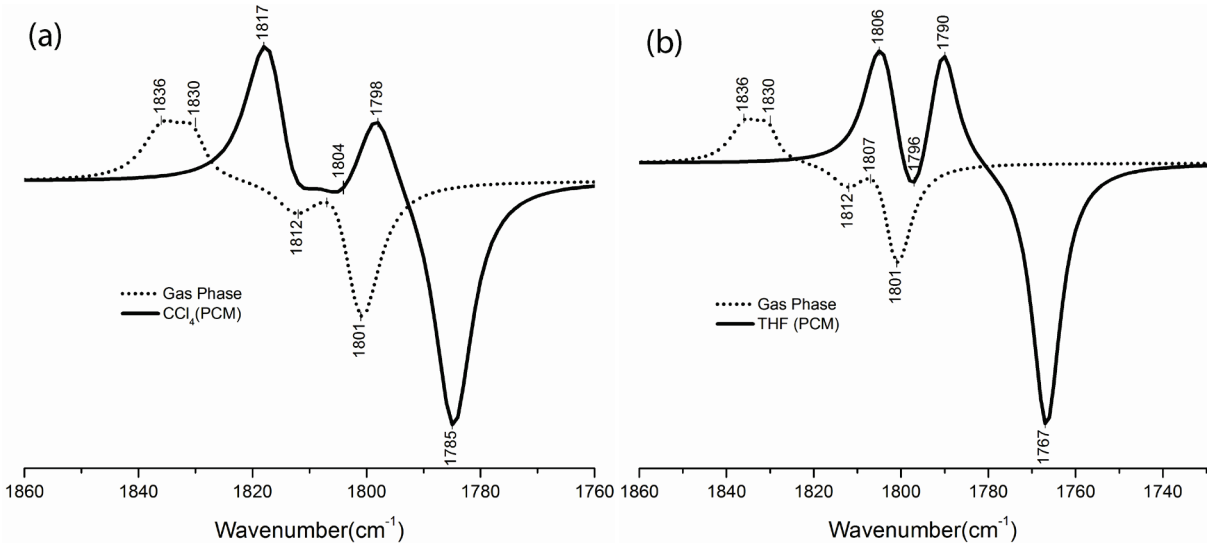

Figure 6.4: (a) Calculated 'cation minus neutral' IR DS for Chl-*a* in CCl_4 obtained using PCM method. (b). Corresponding IR DS for Chl-*a* in THF. The calculated gas phase IR DS (*dotted line*) is also shown for comparison.

Upon comparison of calculated IR DS in Figure 6.4 to the experimental (Chl-a^+-Chl-*a*) FTIR DS in Figure 6.3(b), the suggestion is that the calculated difference band at 1798(+)/1785(-) or 1790(+)/1767(-) cm^{-1} for Chl-*a* in CCl_4 or THF respectively, corresponds to the experimental difference band at 1718(+)/1693(-) cm^{-1}. The calculated negative band at 1785 or 1767 cm^{-1} is due to the anti-symmetrically coupled vibration of the 13^1 keto and 13^3ester C=O groups of Chl-*a*. This band up-shifts 13 or 23 cm^{-1} and decreases in intensity by 99 or 72% upon cation formation, respectively (see Table 6.2). Therefore the 1693 cm^{-1} band in the experimental spectrum (Figure 6.3(b)) was assigned to the anti-symmetric vibration of the 13^1 keto and 13^3

ester C=O groups, which up shifts 25 cm^{-1} upon cation formation and decreases considerably in intensity as described previously in Chapter 5.

The calculated difference band at 1817(+)/1804(-) or 1806(+)/1796(-) cm^{-1} for Chl-*a* in CCl_4 or THF respectively, corresponds to the experimental difference band at 1751(+)/1738(-) cm^{-1} (Figures 6.4 and 6.3(b)). For Chl-*a* in CCl_4/THF the negative band at 1804/1796 cm^{-1} is due to the symmetrically coupled vibration of the 13^1 keto and 13^3ester C=O groups of Chl-*a* , respectively. This band up-shifts 13/10 cm^{-1} upon cation formation (see Table 6.2). Therefore, the 1738 cm^{-1} band in the experimental spectrum in Figure 6.3(b) is assigned to the symmetric vibration of the 13^1 keto and 13^3 ester C=O groups, which up-shifts 13 cm^{-1} upon cation formation. The calculations indicate that the symmetrically coupled vibration of 13^1 keto and 13^3 ester C=O group increases in intensity by 127%/27% in CCl_4/THF respectively. The experimental data, on the other hand, suggests a decrease in intensity of the mode upon cation formation. The overall profile of the calculated spectra is similar to the experimental spectra however, because of the overlapping bands associated with the 17^3 ester C=O modes. Thus the difference spectra calculated with solvent effects included, clearly leads to a more accurate simulation of experimental FTIR DS compared to calculations in the gas phase.

The overall similarity in spectral profile between the calculated and experimental spectra for Chl-*a* in solvent could be viewed as somewhat fortuitous. Also, the use of polarizable continuum methods to model the solvent effects has limitations in the sense that they do not model possible axial ligands or hydrogen bonds to Chl-*a* molecule. Hence in order to include the effect of these possible interactions, on the vibrational modes of Chl-*a*, vibrational frequency calculations were performed in the presence of real solvent molecules.

6.3.2.3 Solvent Calculations Using QM/MM Method

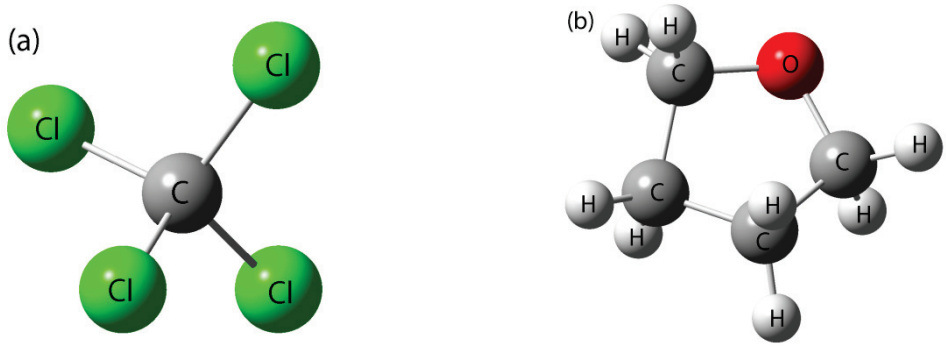

Figure 6.5: Structure of solvent molecules used in QM/MM method. (a) CCl_4 and (b) THF

Figure 6.2 shows the optimized geometry of the Chl-*a* molecule in the presence of CCl_4 and THF solvents using QM/MM methods. For the calculation of Chl-*a* in CCl_4, 96 molecules of the solvent were introduced around the pigment while for the calculation in THF, 70 molecules of the solvent were introduced. Figure 6.5 shows the structure of the solvent molecules, CCl_4 and THF, used in the calculations. The details of the computational method are presented in section 6.2.1.

Figures 6.6 and 6.7 show calculated IR absorption spectra for Chl-*a* and Chl-a^+ in CCl_4 and THF, respectively, obtained using QM/MM methods. The calculated cation minus neutral IR DS are also shown in the figures. Also shown in Figures 6.6 and 6.7, are the calculated IR absorption spectra of Chl-*a* and Chl-a^+ in the gas phase along with the cation minus neutral IR difference spectra (dotted lines).

The harmonic vibrational mode frequencies and intensities associated with the C=O modes of Chl-*a* and Chl-a^+ in CCl_4 and THF are listed in Table 6.2. The vibrational frequencies have not been scaled as we are interested in only the frequency differences induced by cation formation.

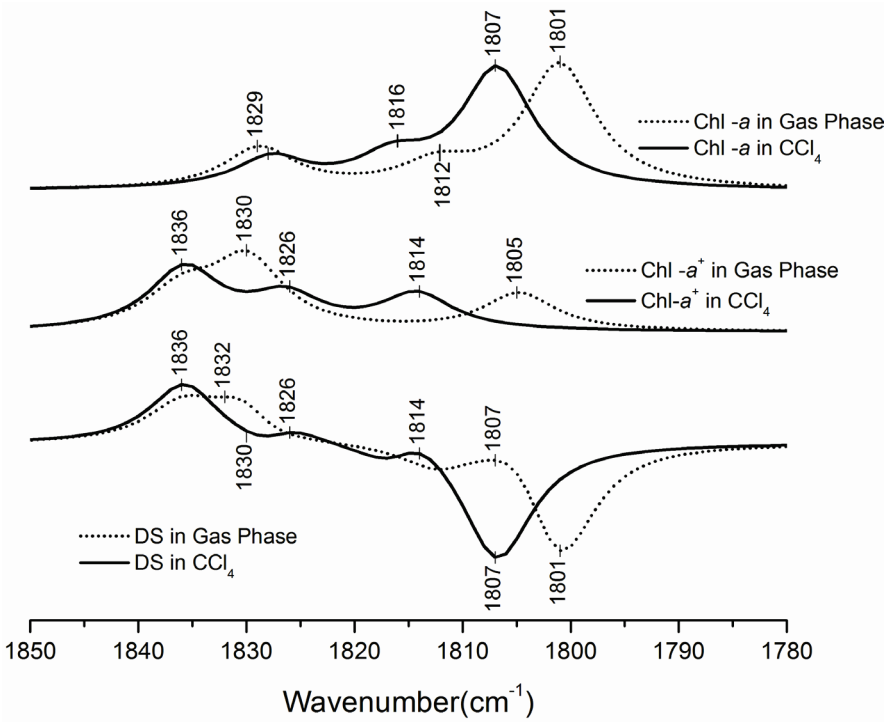

Figure 6.6: Calculated IR absorption spectra for Chl-*a* (top) and Chl-a^+ (middle) in CCl_4 obtained using QM/MM method. The cation minus neutral IR DS is also shown (bottom). The gas phase IR absorption spectra for Chl-*a* and Chl-a^+ along with the DS (dotted line) is also shown for comparison.

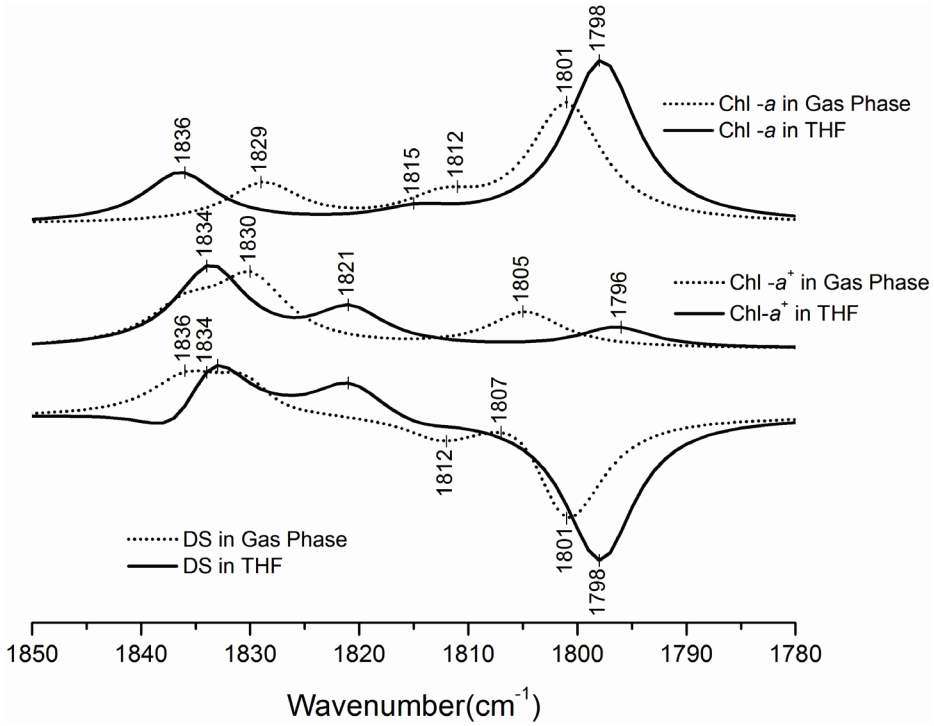

Figure 6.7: Calculated IR absorption spectra for Chl-*a* (top) and Chl-a^+ (middle) in THF obtained using QM/MM method. The cation minus neutral IR DS is also shown (bottom). The gas phase IR absorption spectra for Chl-*a* and Chl-a^+ along with the DS (dotted line) is also shown for comparison.

6.3.2.4 17^3 Ester C=O Mode

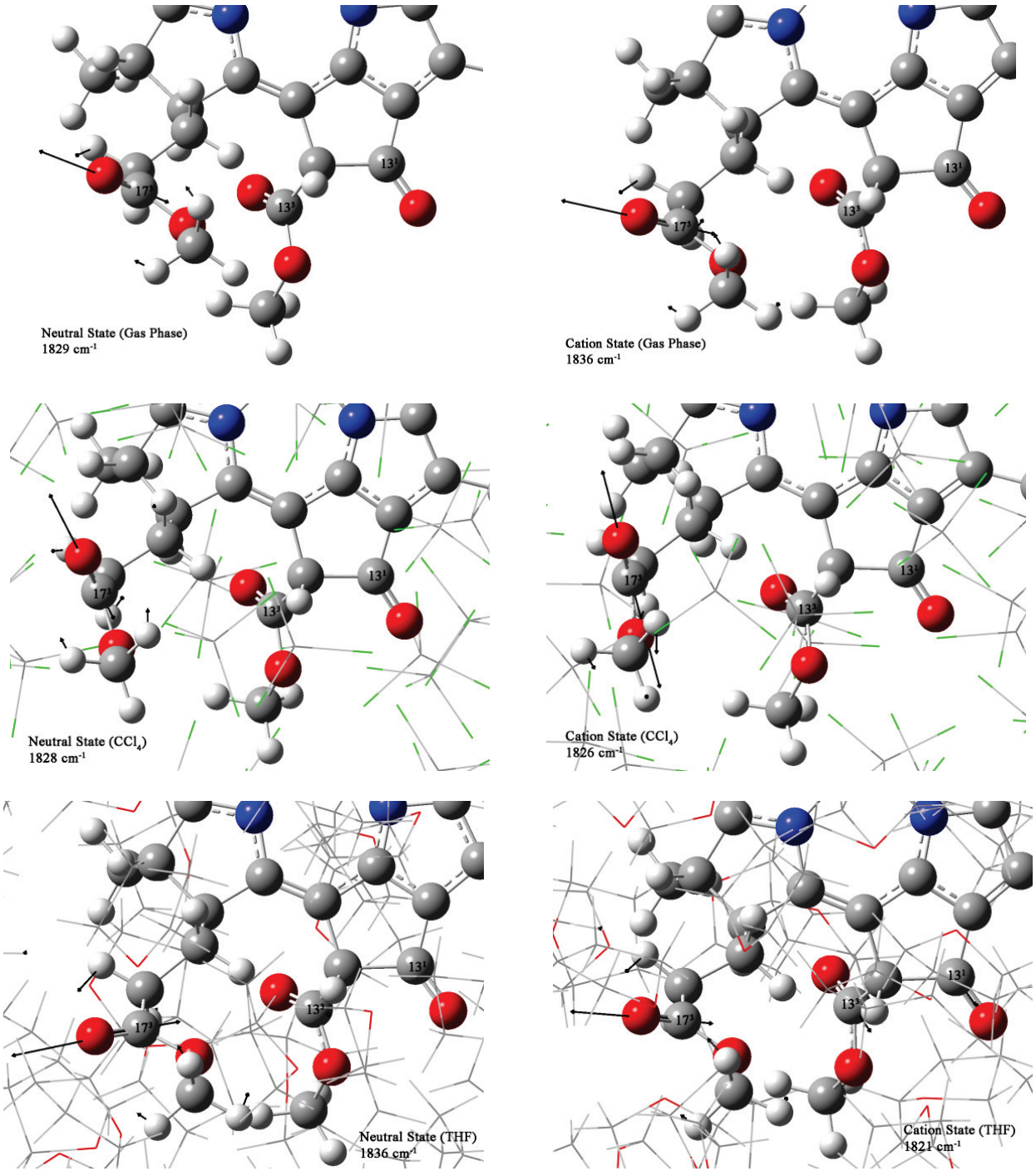

Figure 6.8: Atomic displacements of the 17^3 ester C=O group vibrational modes in the gas phase, CCl_4 and THF for the neutral and cation states. The length of the arrow is representative of the magnitude of the movement of the atom upon vibration.

For Chl-*a* in the gas phase the 17^3 ester C=O mode up-shifts ~7 cm^{-1} and decreases slightly in intensity upon cation formation. This mode is pure C=O vibration in both the neutral

and cation states (Figure 6.8). For Chl-*a* in CCl_4/THF in the explicit solvent model, the frequency of the mode down-shifts upon cation formation by ~2/15 cm^{-1}, respectively. The intensity of the mode slightly increases in CCl_4, while it decreases in THF. In CCl_4 the 17^3 ester C=O vibration has some mixing with the 13^1 keto and 13^3 C=O modes in the cation state. For Chl-*a* in THF the 17^3 ester C=O mode is coupled to the 13^1 keto and 13^3 ester C=O modes both in the neutral and cation states (Figure 6.8).

6.3.2.5 13^1 Keto and 13^3 Ester C=O Modes

For Chl-*a* in the gas phase, the 13^1 keto and 13^3 ester C=O group vibrations are symmetrically/anti-symmetrically coupled for both neutral and cation state. In the neutral state the symmetrically coupled 13^1 keto and 13^3ester C=O mode absorbs at 1812 cm^{-1}. Upon cation formation, this mode up-shift ~18 cm^{-1} and increases in intensity by 102%. In the cation state the mode is mostly due to 13^1 keto C=O group vibration and is slightly coupled to 13^3 ester C=O group (symmetrically) and 17^3 ester C=O group (anti-symmetrically) vibrations (Figure 6.9).

For Chl-*a* in explicit CCl_4, in the neutral state, the symmetrically coupled vibration of 13^1 keto and 13^3 ester C=O groups absorb at 1816 cm^{-1}. Upon cation formation the band up-shift by ~ 20cm^{-1} and absorbs at 1836 cm^{-1} .In the cation state this mode is mostly due to the 13^1 keto C=O group vibration and is slightly coupled (symmetrically) with the 13^3 ester C=O vibration (Figure 6.9). The intensity of the band increases by 75% upon cation formation.

For Chl-*a* in THF, the 13^1 keto and 13^3 vibrations are coupled to the 17^3 ester C=O group vibration both in the neutral and cation states. In the neutral state, the symmetrically coupled 13^1 keto and 13^3 ester vibrational mode absorbs at 1815 cm^{-1}. This vibrational mode is also symmetrically coupled to the 17^3 ester C=O mode (Figure 6.9).

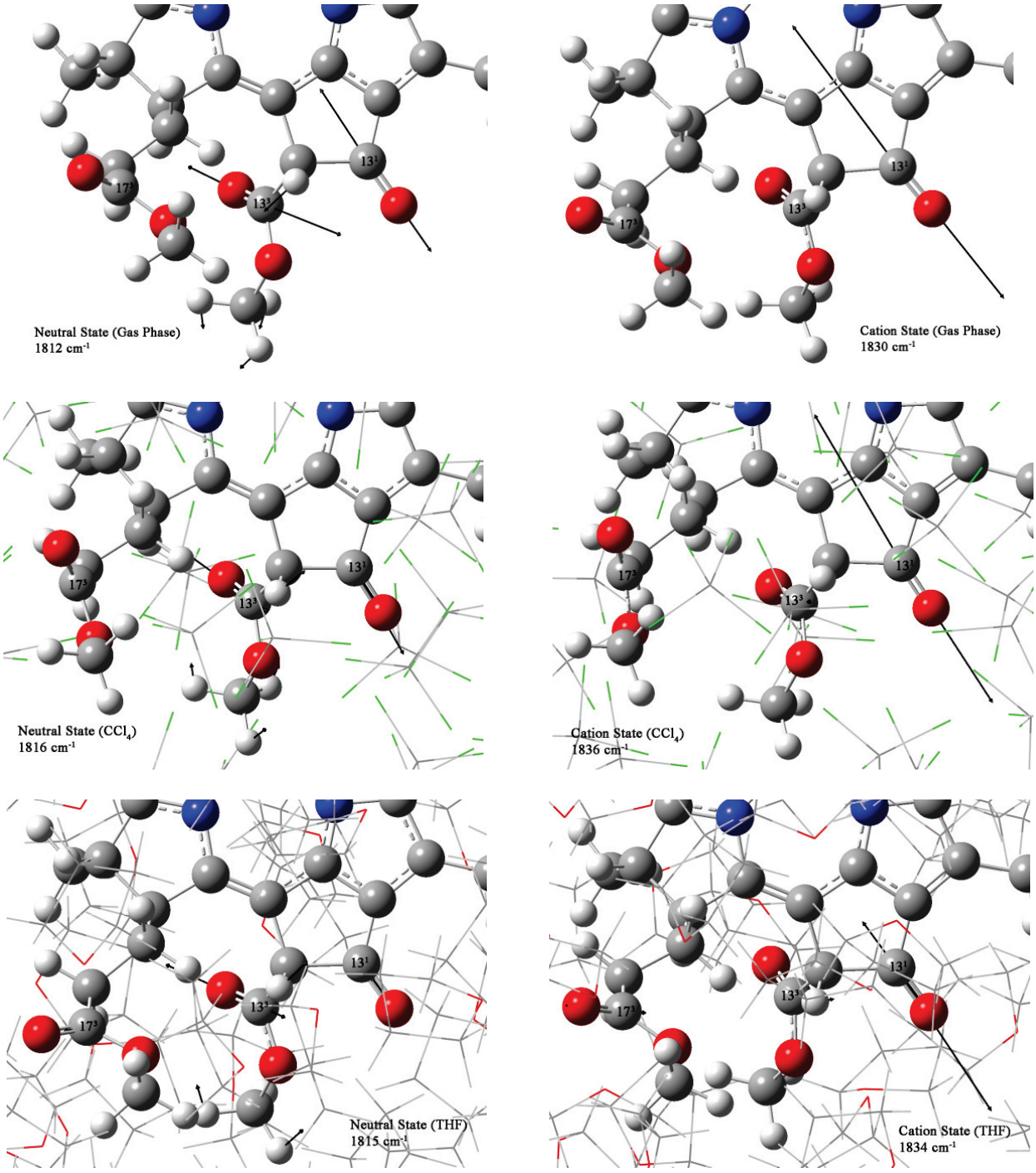

Figure 6.9: Atomic displacements of the symmetrically coupled 13^1 keto and 13^3 ester C=O group vibrational modes in the gas phase, CCl_4 and THF for the neutral and cation states. The length of the arrow is representative of the magnitude of the movement of the atom upon vibration.

Upon cation formation, the symmetrically coupled 13^1 keto and 13^3ester mode vibration up-shift ~18 cm^{-1} and absorbs at 1834 cm^{-1}. The intensity of the mode increases by 154% upon cation formation. In the cation state the vibrational mode is mostly due to 13^1 keto C=O group

and is slightly coupled to 13^3 ester C=O group (symmetrically) and 17^3 ester C=O group (anti-symmetrically) vibration (Figure 6.9).

For Chl-*a* in gas phase, in the neutral state, the anti-symmetrically coupled 13^1 keto and 13^3 ester C=O mode vibration absorbs at 1801 cm^{-1}. Upon cation formation this band up-shifts ~4 cm^{-1} and absorbs at 1805 cm^{-1}. The intensity of the mode decreases by 108% upon cation formation. In the cation state the mode is mostly due to 13^3 ester C=O group vibration and is slightly coupled (symmetrically) to the 13^1 keto C=O group (Figure 6.10).

For Chl-*a* in CCl_4, in the neutral state, the anti-symmetrically coupled 13^1 keto 13^3 ester C=O mode vibration absorbs at 1807 cm^{-1}. Upon cation formation the band up-shifts ~7 cm^{-1} and absorbs at 1814 cm^{-1}. The intensity of the mode decreases by 108% upon cation formation. In the cation state the vibrational mode is mostly due to 13^3 ester C=O group vibration which is slightly coupled (anti-symmetrically) to the 13^1 keto and 17^3 ester C=O groups (Figure 6.10).

For Chl-*a* in THF, in the neutral state, the anti-symmetrically coupled 13^1 keto and 13^3 ester C=O mode absorbs at 1798 cm^{-1}. This mode is also slightly coupled to the 17^3 ester C=O group vibration. Upon cation formation the anti-symmetrically coupled 13^1 keto and 13^3 ester C=O mode down-shifts ~2cm^{-1} and absorbs at 1796 cm^{-1}. The intensity of the mode decreases by 156% upon cation formation. In the cation state the mode is mostly due to the 13^3 ester C=O group vibration and is slightly coupled to the 13^1 keto C=O group (anti-symmetrically) and 17^3 ester C=O group (symmetrically) vibration.

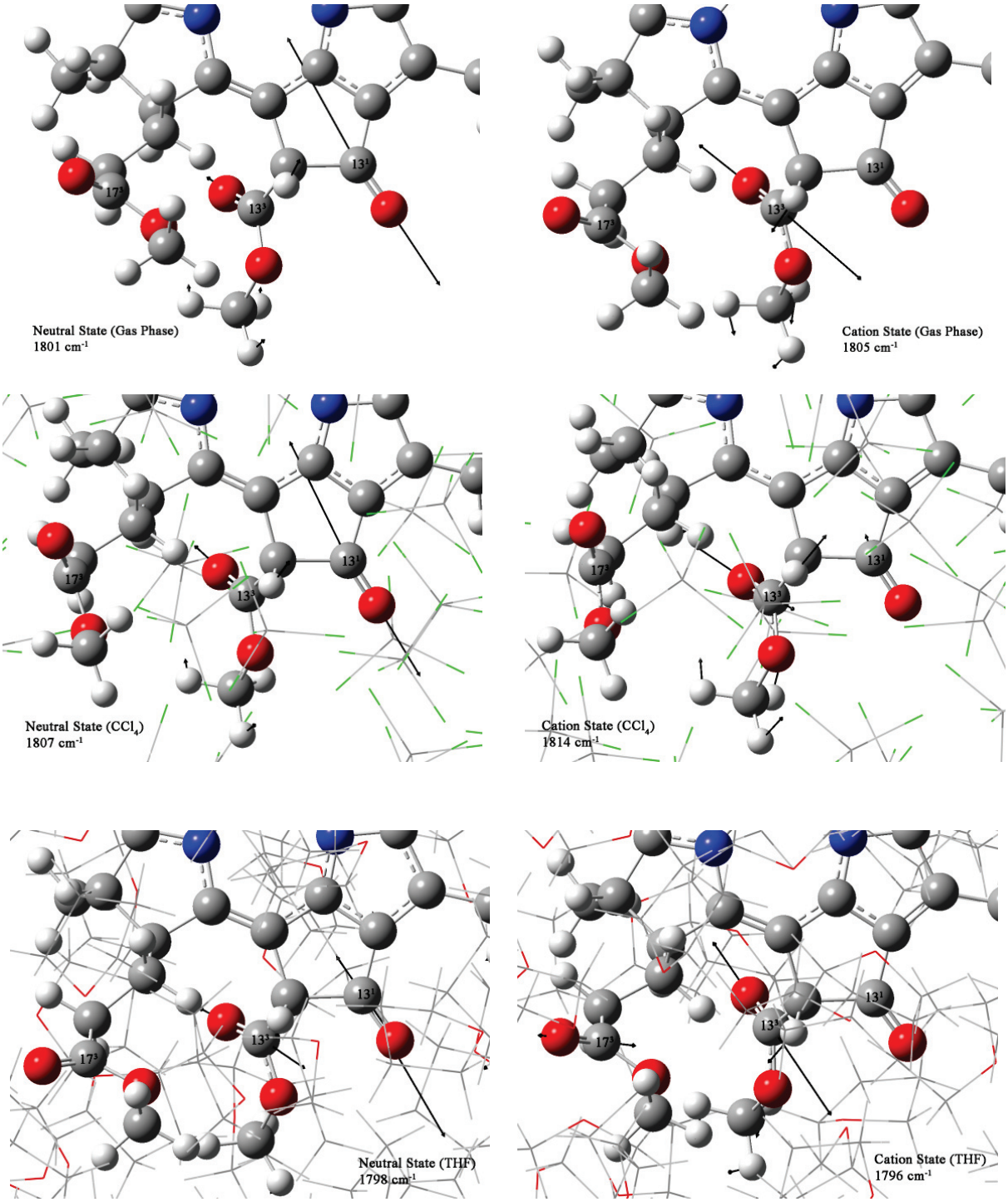

Figure 6.10: Atomic displacements of the anti-symmetrically coupled 13^1 keto and 13^3 ester C=O group vibrational modes in CCl_4 and THF for the neutral and cation states. The length of the arrow is representative of the magnitude of the movement of the atom upon vibration.

The down-shift of the anti-symmetrically coupled 13^1 keto and 13^3 ester C=O mode upon cation formation is a strange phenomenon. Table 6.1 shows that the bond length of the 13^1 keto

C=O group decreases upon cation formation while the 13^3 ester C=O group bond length is unchanged. Bond order increases/decreases with decrease/increase in bond length, making the bond stronger/weaker. A stronger bond absorbs at higher energy, which means the band will up-shift upon cation formation. While on the other hand if a bond becomes weaker upon cation formation it down-shifts in frequency. Vibrational frequency calculations of Chl-*a* in THF using PCM model predicts a 23 cm^{-1}up-shift in frequency upon cation formation (Table 6.2), which is more in line with the experimentally observed up-shift of ~25 cm^{-1}.

The vibrational frequency calculations of Chl-*a*, in the gas phase as well as in solvents, shows that the 13^1 keto and 13^3 ester C=O group vibrations are coupled and unique vibrations of either C=O groups do not exist in the neutral or cation states. Also, for both gas phase and QM/MM calculations, upon cation formation, the anti-symmetrically coupled C=O mode is dominated by 13^3 ester C=O vibration (Figure 6.10) while the symmetric C=O mode is dominated by the 13^1 keto C=O vibration (Figure 6.9). These results are quite different from the PCM calculations were the 13^1 keto and 13^3ester C=O group vibrations are strongly coupled both in the neutral and cation state.

Figure 6.11 shows a comparison of the calculated cation minus neutral IR difference spectra of Chl-*a* obtained using the PCM method and QM/MM method. The calculated IR difference spectra of Chl-*a* in the gas phase (dotted line) is also shown for comparison. It is clearly evident from Figure 6.11 that the overall profile of the calculated IR spectra obtained using the QM/MM method is very similar to the gas phase spectra. The calculated vibrational mode compositions of the C=O groups in the QM/MM model are also very similar to the gas phase calculation. The fact that the calculated IR DS of Chl-*a* in the presence of explicit solvent molecules is almost identical to the gas phase calculations question the ability of two-level

ONIOM method to incorporate the solvent interactions to the pigment in calculations. Hence, at least for vibration frequency calculation purposes, the two-level ONIOM method is not the best way to study solvation effects.

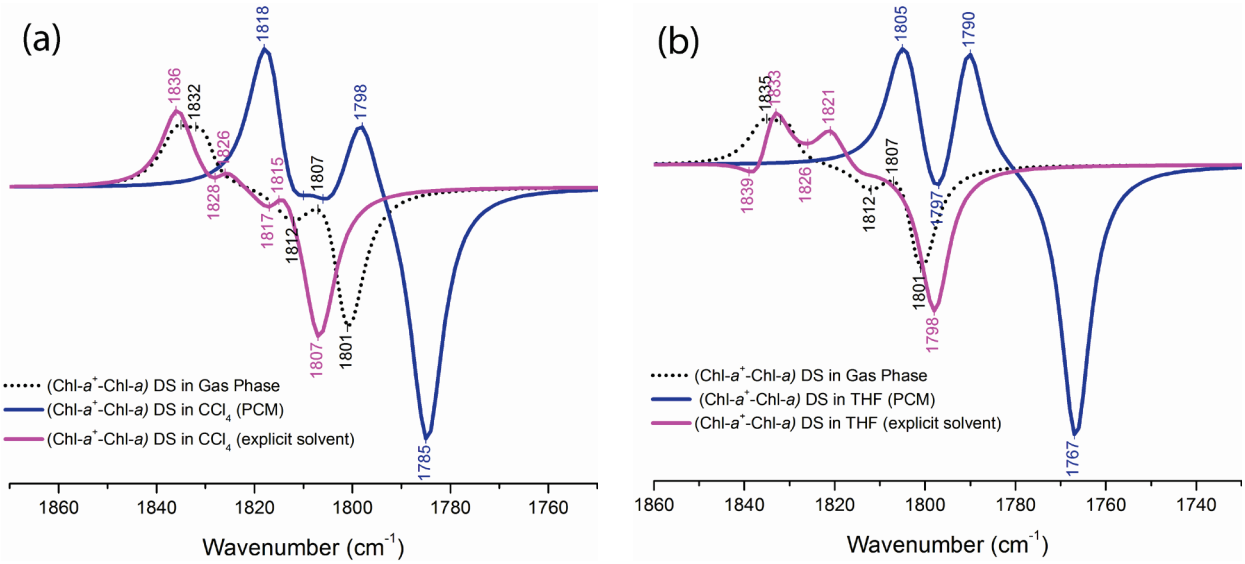

Figure 6.11: Comparison of the calculated 'cation minus neutral' IR difference spectra of Chl-*a* obtained using the PCM method and QM/MM method (a) CCl_4 and (b) THF. The calculated IR difference spectra of Chl-*a* in the gas phase (dotted line) is also shown for comparison.

The IR difference spectra obtained using the PCM on the other hand is very different from the spectra obtained using QM/MM model. Also, comparing the calculated (PCM) cation minus neutral IR DS with the electrochemically generated (Chl-a^+-Chl-*a*) FTIR DS in Figure 6.3(b), it is clear there is considerable similarity in the overall shape of the spectra.

6.3.3 Calculated Redox Properties

The oxidation potential (E_{ox}) of the primary electron donor, P_{700}, in PS I is extremely low (~ 440 mV) compared to the E_{ox} values of isolated Chl-*a* in organic solvents (~740-930 mV) [10, 125-130]. It is also known that the local dielectric constant in the photosynthetic protein is usually in the 2-7 range [96, 97, 131-134]

The effect of the dielectric environment on the E_{ox} of Chl-*a* was investigated by calculating the relative energy of Chl-*a* in different solvents, in the neutral and cation states,

using QM/MM as well as PCM methods. The ionization potential (IP) of Chl-*a* in each solvent (dielectric medium) was estimated as the difference in electronic energy (E_{elec}) between Chl-*a* and Chl-a^+. The oxidation potential was estimated from the IP of Chl-*a* by the equation,

$$E_{OX} = IP - 4.43$$

where the factor 4.43eV is an estimate of the potential of the standard hydrogen electrode [135]. The calculated electronic energies, IP's and redox potential values for Chl-*a* using QM/MM and PCM methods are presented in Table 6.3.

The calculated IP of Chl-*a* in the gas phase is ~ 6.0 eV. The electronic energies used here are obtained from the geometry optimization calculations at the B3LYP/6-31G(d) or B3LYP/6-31G(d)/AMBER level for Chl-*a* in PCM model or QM/MM model, respectively. It has been shown that the 6-31G(d) basis-set provides smaller E_{ox} values (by ~ 0.28V) [136, 137]. Considering this, the calculated IP of ~6.0V is in good agreement with the IP of 6.23V estimated for Chl-*a* in gas phase by Hasegawa et. al. [137].

Redox potential calculations of Chl-*a* in solvent using PCM model shows that the E_{ox} value decreases as the dielectric constant of the media increases (Table 6.3). The calculated E_{ox} for Chl-*a* in various solvents using PCM methods [137] and well as the experimental values of the oxidation potential of Chl-*a* measured in various solvents [10, 125-130] support this observation.

The calculated redox potential of Chl-*a*, using the QM/MM model, in CCl_4 is ~1845mV, while in THF the corresponding value is ~852mV (Table 6.3). Thus, the calculated E_{ox} of Chl-*a* is higher in CCl_4 while it is significantly lower in THF (~50% lower). There is no direct explanation for this behavior as it is observed from experiments as well as different

computational studies that the redox potential of Chl-*a* decreases with increase in dielectric constant of the medium.

Table 6.3: Calculated electronic energy of Chl-*a* and Chl-a^+ in various solvents along with the IP's and E_{ox} values.

	E_{elec}(eV)		IP(eV)	E_{ox}^{cal}(V)=IP-4.43
	Chl *a*	Chl a^+		
Gas Phase	-59563.26	-59557.28	5.982	1.552
CCl_4(PCM)	-59563.61	-59558.26	5.353	0.9228
CCl_4(QM/MM)	-59596.52	-59590.24	6.275	1.845
THF (PCM)	-59563.98	-59559.02	4.958	0.5282
THF(QM/MM)	-59558.99	-59553.71	5.282	0.8522
H_2O (PCM)	-59564.33	-59559.58	4.754	0.3235

The comparison of the calculated IR cation minus neutral DS and the redox properties of Chl-*a*, in different solvents, obtained using the QM/MM model and the PCM model shows that the latter method gives results that are closer to experiment. Also, the calculated IR DS using PCM model more closely resemble the experimentally observed DS, while the QM/MM calculated spectra are similar to the gas phase calculations.

Vibrational frequency calculations of Chl-*a* in the gas phase and in solvent using various methods shows that unique vibrations of the 13^1 keto and 13^3 ester C=O group do not exist in the neutral or cation state. The 13^1 keto and 13^3 ester C=O group vibrations are symmetrically/anti-symmetrically coupled and support the new assignments proposed for some of the bands in the electrochemically generated (Chl-a^+-Chl-*a*) FTIR DS [79] (see Chapter 5).

6.4 Conclusions

The vibrational frequencies of Chl-*a* were calculated in the gas phase and in solvents using the PCM (at B3LYP/6-31G(d) level) as well as QM/MM (at B3LYP/6-31G(d)/AMBER level) methods. The calculated cation minus neutral IR difference spectra of Chl-*a* using PCM model clearly resembles the electrochemically generated (Chl-a^+-Chl-*a*) FTIR DS. The calculated cation minus neutral IR difference spectra obtained using QM/MM methods, on the

other hand, are very similar to the gas phase calculations. Hence, at least for the purpose of vibrational frequencies studies, at this level of theory, PCM model is superior to QM/MM methods. The comparison of the calculated redox properties of Chl-*a* using the two models shows that the results of the PCM model calculations are closer to the observed (experimental) values.

The calculated vibrational frequency mode compositions for the C=O groups of Chl-*a* in the gas phase as well as the two solvation methods are very different from the experimentally assigned mode compositions but support the new band assignments proposed earlier [79] (Chapter 5) for some of the bands in electrochemically generated (Chl-a^{+}-Chl-*a*) Fourier Transform IR (FTIR) DS.

CHAPTER 7

HOW AXIAL LIGATION AND HYDROGEN BONDING IMPACT THE CALCULATED VIBRATIONAL MODES OF CHLOROPHYLL-*A*.

7.1 Introduction

Photosynthesis is the process in which solar energy is harvested by plants, algae and bacteria to produce biomass which is used for food and fuel [103]. Chlorophyll molecules dominate photosynthetic energy conversion as these pigments function as the primary electron donors and acceptors in the photosynthetic reaction centers.

The primary reactions of photosynthesis takes place in two pigment-protein complexes, called photosystem I and II (PS I and PS II). The primary electron donor in the reaction center of PS I is called P_{700}, which is a Chlorophyll-a/Chlorophyll-a' hetero-dimer (Chl-*a*/Chl-*a*'). Chl-*a*' is a 13^2 stereoisomer of Chl-*a*. The electron transfer cofactors in PS I are bound to two membrane spanning proteins called *PsaA* and *PsaB*. The pigments and the protein subunits display a partial or pseudo C_2 symmetry. The Chl-*a*/Chl-*a*' pigments of P_{700} are bound to *PsaB*/*PsaA*, and are termed P_B/P_A, respectively.

The 2.5 Å crystal structure of PS I [6] shows that P_A and P_B are ligated by histidine residues. Also, the 13^1 keto C=O group and the bridging oxygen atom of the 13^3 ester C=O group of P_A are involved in an H-bonding network with several amino acids of *PsaA*. The P_B molecule of P_{700} is free from any such interactions. The axial ligation and peripheral H-bond interactions to the two Chl's of P_{700} are of importance as they play a role in establishing the unique redox properties of P_{700}.

FTIR difference spectroscopy is a sensitive, molecular specific probe and (P_{700}^+-P_{700}) FTIR DS have been obtained under many sets of conditions. Unfortunately, these difference

spectra are poorly understood [79].The goal is to develop methods to gain a more quantitative understanding of these difference spectra. From this, a quantitative understanding of how specific molecular parameters impact the chemical properties of P_{700} can be obtained.

Calculation of the vibrational properties of dimeric Chl species at a reasonable quantum mechanical level is still computationally prohibitive. This is not the case for single Chl-*a* molecules, however, and density functional theory (DFT) based vibrational mode frequency calculations for several Chl-*a*/Chl-*a*' model structures in the gas phase as well as in different solvents have been undertaken [79, 80]. The calculated (Chl-a^+-Chl-*a*) FTIR Difference Spectra (DS) in solvents for both Chl-*a* and Chl-*a*' bear a remarkable similarity to the corresponding experimental spectra [79]. The mode compositions of the carbonyl groups of the Chl's that give rise to the bands in the calculated spectra, however, are very different from that assigned experimentally [79]. Based on the calculations for Chl-*a*, Chl-a^+, Chl-*a*' and Chl-a'^+ in various solvents, new assignments for the bands in experimental (Chl-a^+-Chl-*a*) FTIR DS were proposed [79] (See Chapter 5 for details).

A comprehensive understanding of the vibrational properties of the C=O modes of Chl-*a* and Chl-*a*' in solvent has been gained. The goal is to extend these studies to Chl-*a* and Chl-*a*' in a protein environment.

Here the vibrational frequency studies on Chl-*a*/Chl-*a*' models has been extended to include the effect of axial ligation and H-bond interactions to the Chl-*a*/Chl-*a*' pigments. In addition to this it is well known that the overall dielectric constant of the environment for pigments in photosynthetic proteins is usually in the 2-7 range [96, 97, 131-134]. For this reason the vibrational properties of axially ligated and H-bonded Chl-*a*/Chl-*a*' models were studied, in solvents with dielectric constant between 2.2-7.5.

The role and relevance of axial ligation to chlorophylls has been studied computationally before [81-83], and how axial ligation impacts the geometry, bond dissociation energies, reduction potentials and visible absorption spectra has been studied [82-85]. H-bonding is the most significant non bonding interaction to chlorophyll pigments in a protein environment, and the effect of peripheral H-bonding on electron affinity and spin density of Chl has been investigated. It was shown that the spin density of Chl-a^+ could be regulated by peripheral H-bonding [84]. However, no investigation of how axial ligation and peripheral H-bonding impact the vibrational properties of Chl-*a*/Chl-*a*' have been undertaken. This is in spite of the fact that experimental FTIR DS is available for P_{700} with site specific mutations were the axial ligand [54] and the peripheral amino acid residues are modified [76, 77].

One aim of this study is to investigate how axial ligation and H-bonding modify the vibrational properties of Chl *a*/Chl-*a*'. Therefore, the vibrational mode frequencies of Chl-*a*/Chl-*a*' with a methyl imidazole ligand, to stimulate the histidine ligand to P_{700} chlorophylls in PS I, was calculated. The starting coordinates for these models were obtained from the PS I crystal structure. For Chl-*a*/Chl-*a*' the P_B/P_A [CL11021/CL11011] coordinates along with their ligating histidine's, HisB660/HisA680 (amino acid numbering for *Thermo-synechococcus elongatus*) were used [6]. The histidine group was modified to methyl imidazole and the phytyl chain of the chlorophyll molecule was replaced with a methyl group at 17^4 position in these models (Figure 7.1).

Also, it is evident from the PS I crystal structure that the 13^1 keto C=O group of P_A (Chl-*a*') is involved in a H-bond with ThrA743 residue (See Chapter 2). This H-bonding interaction is modeled by considering Chl-*a'* directly H-bonded to a Thr residue. In PS I the 13^1 keto C=O of P_B appears to be free of H-bond interactions. The corresponding residue to ThrA743 on *PsaB* is

TyrB727. To simulate the effect of H bonding interactions to P_B, the Tyr residue was changed to a Thr residue and the vibrational mode frequencies and intensities for this Chl-*a* model was calculated. It should be pointed out that this mutation has been made experimentally and studied using FTIR DS [76] (See Chapter 3 for details). The effect of H-bonding to the 13^1 keto C=O group of the Chl-*a* and Chl-*a*' was further investigated by modeling the pigments with a H_2O molecule in the vicinity of 13^1 keto C=O group. Finally the effect of axial ligation and H-bonding is investigated by modeling Chl-*a*/Chl-*a*' in the presence of both axial ligand and H-bond interactions.

7.2 Materials and Methods

All geometry optimizations and harmonic normal mode vibrational frequency calculations were performed using DFT as implemented in Gaussian 03 software, revision D.01. [87]. Unless stated, the B3LYP functional was used in combination with the 6-31G(d) basis set. This has been shown to be the minimum level of theory that is required for the calculation. It has been shown that the radical induced frequency shifts are accurately calculated at this level of theory [80, 89]. To model solvent effects, the integral equation formalism (IEF) of the polarizable continuum model (PCM) [93] was used, as it is implemented in Gaussian 03.

7.3 Results

Figure 7.1(a) shows the structure and IUPAC numbering scheme of Chl-*a*. Figures 7.1(b) and (c) shows the geometry optimized structural models that were used to represent Chl-*a* and Chl-*a'*. Chl-*a*' is a 13^2 stereoisomer of Chl-*a*. The starting coordinates for the two Chl's of P_{700} were obtained from the crystal structure of PS I [6]. In the structural models the phytyl chain is replaced with a methyl group at the 17^4 position. Both Chl-*a* and Chl-*a'* models have 82 atoms. Previously, Chl-*a* and Chl-*a*' models in which the molecular groups at positions 2, 8, 12 and 18

were replaced with hydrogen have been studied [79]. This model structure was called Chl-a_5. Chl-a_5 has 64 atoms and will be referred to here as Chl-a_{64}/Chl-a'_{64}.

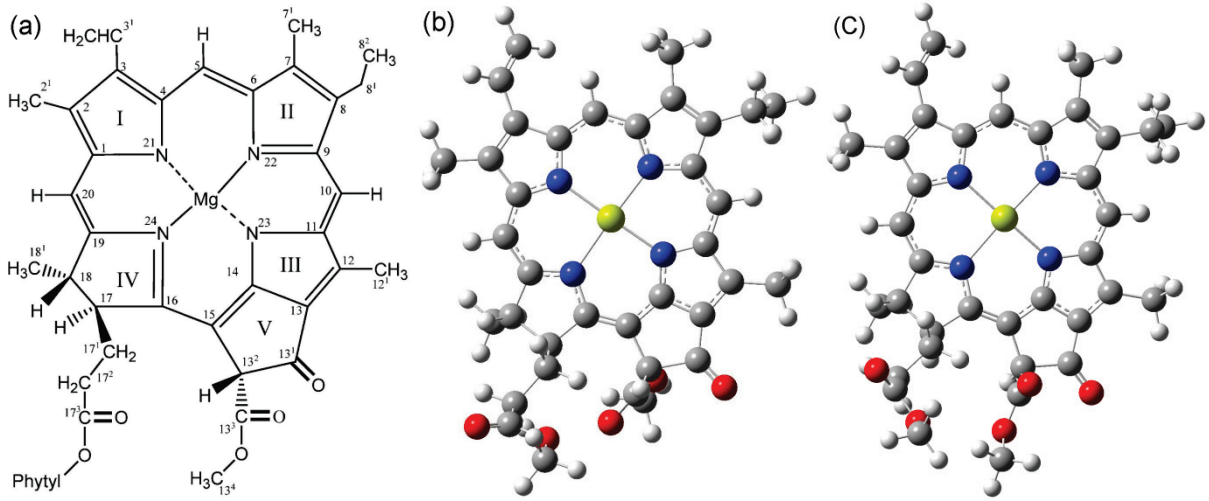

Figure 7.1: (a) Structure and IUPAC numbering scheme for Chl-*a*. (b) Chl-*a* and (c) Chl-*a'* geometry optimized (energy minimized) model molecular structures used here. The model structures are identical to Chl-*a*/*a*', except that the phytyl chain following the 17^3 ester oxygen is replaced with a methyl group.

7.3.1 Effects the Peripheral Methyl Groups Have on the Vibrational Properties of Chl-*a*/*a*'

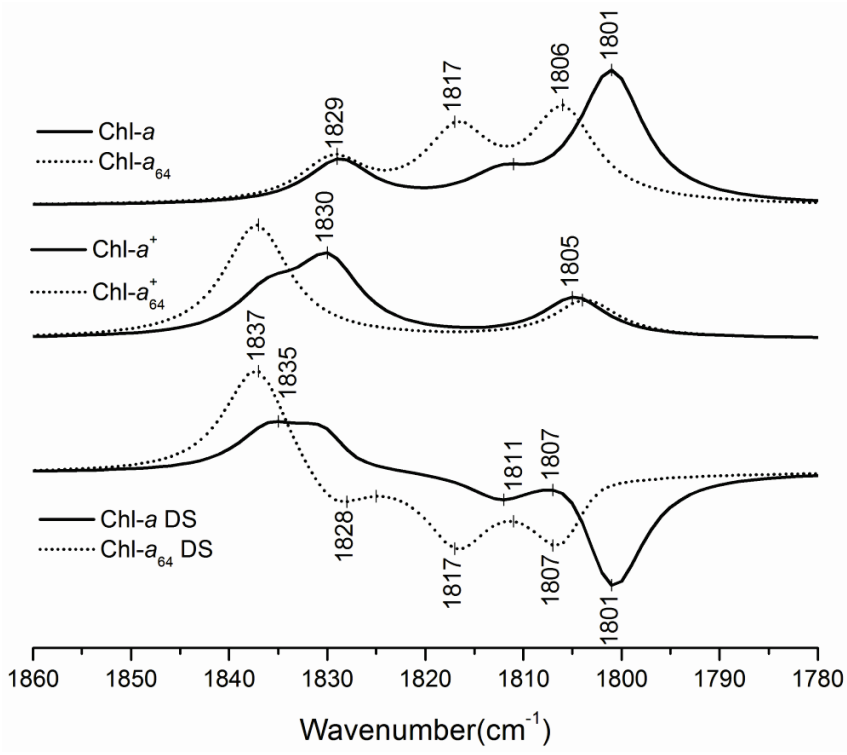

Figure 7.2: Calculated IR spectra for Chl-*a*/Chl-a_{64} (top) and Chl-a^+/Chl-a^+_{64} (middle) in the gas phase. The cation minus neutral IR DS are also shown (bottom).

Calculated gas phase IR absorption spectra for Chl-*a*/Chl-*a*' are shown in Figures 7.2/7.3, respectively. Spectra for the neutral and cation state, along with the "cation minus neutral" difference spectra (DS) are shown. Also shown for comparison (dotted) are the corresponding gas phase spectra for Chl-a_{64}/Chl-a'_{64}.

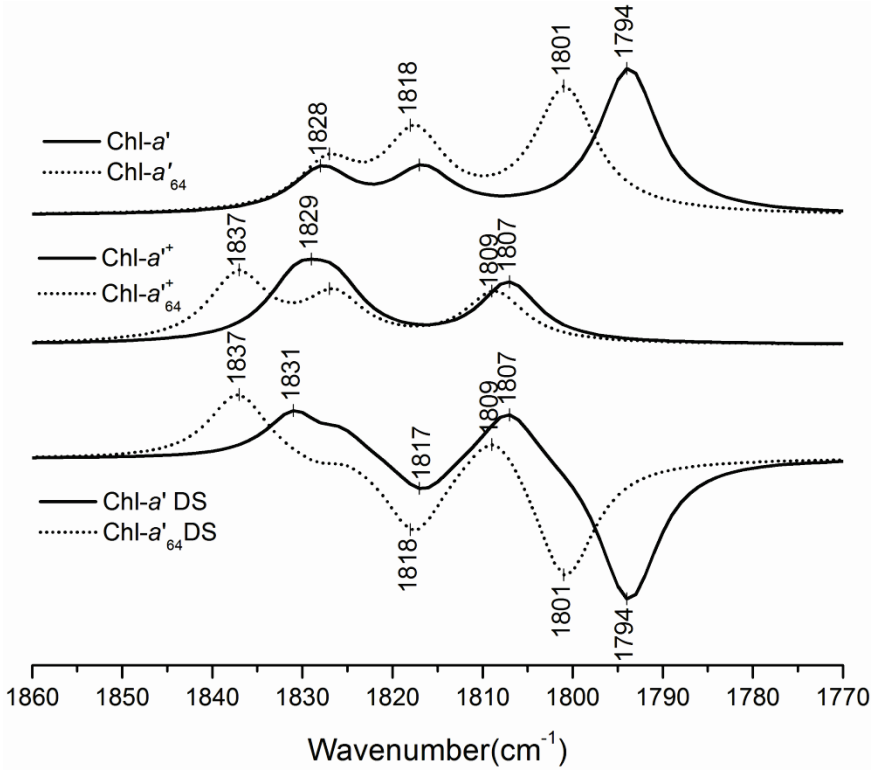

Figure 7.3: Calculated IR spectra for Chl-*a*'/Chl-a'_{64}(top) and Chl-a'^{+}/Chl-a'^{+}_{64} (middle) in the gas phase. The cation minus neutral IR DS are also shown (bottom).

Figure 7.4(a) shows a comparison of the calculated DS of Chl-*a* and Chl-*a*'. Figure 7.4(b) shows the electrochemically generated (Chl-a^{+}-Chl-*a*) FTIR DS in THF. The harmonic, vibrational mode frequencies and intensities associated with the C=O modes of Chl-*a*/Chl-*a*', Chl-a^{+}/Chl-a'^{+}, Chl-a_{64}/Chl-a'_{64} and Chl-a^{+}_{64}/Chl-a'^{+}_{64} are listed in Table 7.1.

Figure 7.2/7.3 and the data from Table 7.1 shows that for both Chl-*a* and Chl-*a*' the inclusion of methyl groups at position 2, 8, 12 and 18 causes a 1-7 cm^{-1} change in frequency of the C=O modes along with significant change in intensities. In addition, the overall shape of the

calculated cation minus neutral IR DS for Chl-*a*/Chl-*a*' is very different from that of Chl-a_{64}/Chl-a'_{64} spectra.

Table 7.1: Calculated frequencies and intensities (in parenthesis [in km/mole]) for the different carbonyl modes of Chl-*a*/*a*', Chl-a_{64}/a'_{64}, Chl-a^+/a'^+ and Chl-a^+_{64}/a'^+_{64}.

Mode	Neutral	Shift Δν(ΔI)	Cation	Shift Δν(ΔI)
ν (17^3 C=O)				
Chl-*a*	1829 (235)	1(1%)	1836 (213)	-2(73%)
Chl-a_{64}	1830 (233)		1838 (123)	
Chl-*a*'	1828 (194)	-1(2%)	1826 (226)	0(11%)
Chl-a'_{64}	1829 (191)		1826 (204)	
ν (13^1 and 13^3 C=O) s				
Chl-*a*	1812 (129)	-5(-66%)	1830 (397)	-7(-20%)
Chl-a_{64}	1817 (379)		1837 (498)	
Chl-*a*'	1817 (186)	-3(-38%)	1831 (250)	-6(-18%)
Chl-a'_{64}	1820 (299)		1837 (305)	
ν (13^1 and 13^3 C=O) as				
Chl-*a*	1801 (719)	-5(45%)	1805 (215)	1(5%)
Chl-a_{64}	1806 (496)		1804 (204)	
Chl-*a*'	1794 (652)	-6(15%)	1807 (267)	-2(18%)
Chl-a'_{64}	1800 (566)		1809 (227)	

The frequency shift induced by including the methyl groups of Chl-*a*/Chl-*a*' for each calculation is shown along with the mode intensity change [in parenthesis (in%)].

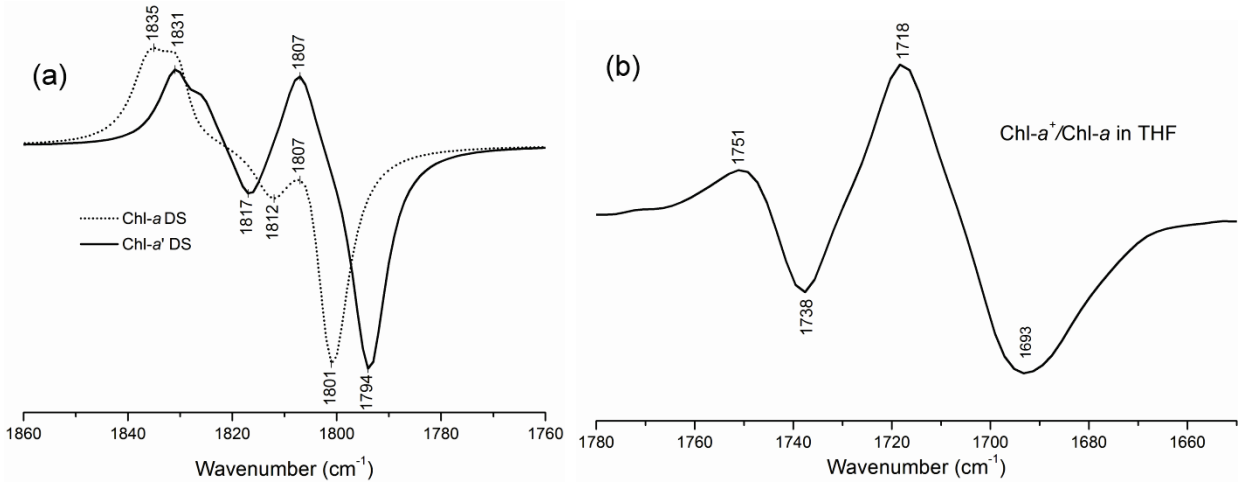

Figure 7.4: (a) Comparison of calculated IR DS of Chl-*a* and Chl-*a*' in the gas phase (b) Experimental (Chl-a^+-Chl-*a*) FTIR DS in THF[64].

Previously it has been shown that it is more appropriate to consider the 13^1 keto and 13^3 ester C=O modes as a coupled pair, that display symmetric and anti-symmetric vibrations [79] (Chapter 5). Figure 7.2/7.3 and Table 7.1 indicate that, for the neutral state of Chl-*a*/ Chl-*a*', the

inclusion of methyl groups increases the intensity of the anti-symmetrically coupled mode by 45% /15%, while decreasing its frequency by 5/6 cm^{-1}. The frequency of the anti-symmetrically coupled mode of Chl-a^+ or Chl-a'$^+$ are not significantly affected by inclusion of the methyl groups. The intensity of the anti-symmetrically coupled mode of both Chl-a^+ and Chl-a'$^+$ increases by 5% and 18%, respectively, upon including the methyl groups (Table 7.1).

Different results are calculated for the symmetrically coupled 13^1 keto and 13^3 ester C=O mode. For the neutral state of Chl-*a*/ Chl-*a*', inclusion of methyl groups *decreases* the intensity of the symmetrically coupled mode by 66%/38%, along with a 3-5 cm^{-1} decrease in frequency. The inclusion of methyl groups also alter the intensity and frequency of the symmetrically coupled mode of Chl-a^+/ Chl-a'$^+$, where the frequency and intensity decreases by 7/6 cm^{-1} and 20%/18% respectively (Table 7.1).

The inclusion of methyl groups does not affect the intensity and frequency of the vibrational modes of the 17^3 ester C=O group of Chl-*a* and Chl-*a*'. For Chl-a^+ the intensity of mode increases 73% while the frequency of the mode decreases by 2 cm^{-1}. For Chl-a'$^+$ the intensity of mode increases 11% while the frequency of the mode remains unchanged (Table 7.1).

It has been pointed out previously that the calculated cation minus neutral IR DS for Chl-a_{64}/ Chl-a'$_{64}$ displays no resemblance to electrochemically generated (Chl-a^+-Chl-*a*) FTIR DS [64]. However, the calculated cation minus neutral IR DS for Chl-*a*/Chl-*a*' does appear more similar in shape to electrochemically generated (Chl-a^+-Chl-*a*) FTIR DS (Figure 7.4) [64]. This is in spite of the fact that the calculated spectra in Figure 7.4(a) are in the gas phase. The mode compositions associated with the bands in the calculated Chl-*a*/Chl-*a*' IR spectra are in agreement with the previous work, however [79]. The spectra in Figure 7.4(a) and 7.4(b)

indicate that, at least for simulation of FTIR DS, it is necessary to include the substituent methyl groups in the model Chl's. Similarly Heimdal et. al., demonstrated that the inclusion of the peripheral groups in Chl models leads to a simulated visible absorption spectra that more closely matches experimental spectra [83]. In most previous computational studies of the properties of Chl-*a* the methyl groups are ignored, especially in studies aimed at modeling the magnetic spectroscopic properties of Chl-*a*.

7.3.2 Effect of Fifth Ligand on Vibrational Modes of Chl-*a*/Chl-*a*'

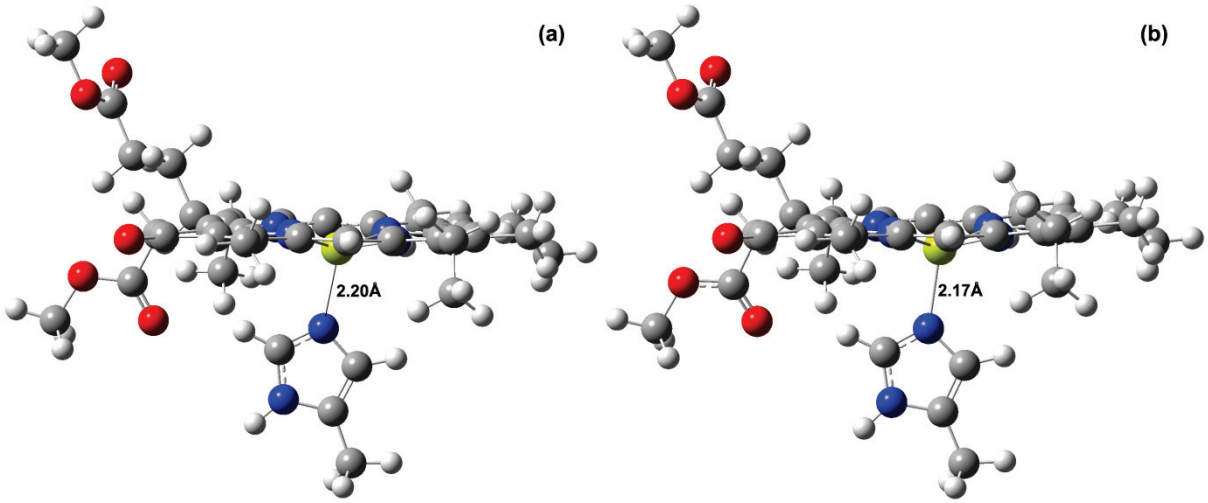

Figure 7.5: Geometry optimized molecular structures of Chl-*a* and Chl-a^+ in the presence of methyl imidazole that provides an axial ligand (a) neutral and (b) cation states.

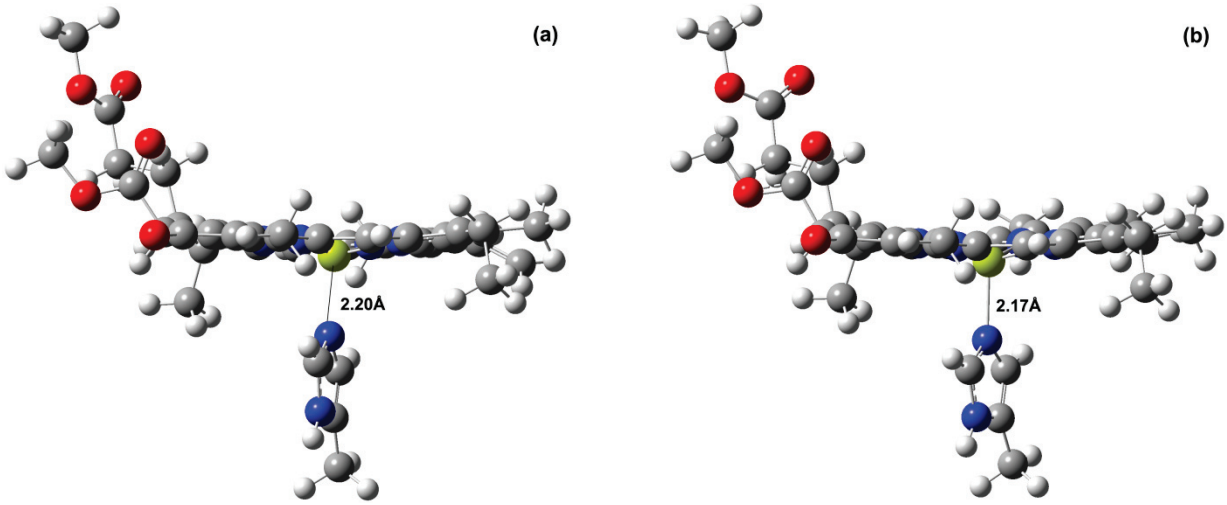

Figure 7.6: Geometry optimized molecular structures of Chl-*a*' and Chl-a'^+ in the presence of methyl imidazole that provides an axial ligand (a) neutral and (b) cation states.

Normal mode vibrational frequencies and intensities were calculated for Chl-*a*/Chl-*a*' in the presence of methyl imidazole that provides a ligand to the central magnesium atom of the chlorophyll. Again, the starting geometries for the Chl-*a*/Chl-*a*' plus imidazole [termed ligand+Chl-*a*/ligand+Chl-*a*'] were obtained from the PS I crystal structure using P_A and HisA680 or P_B and HisB660 [6]. The histidine residue from the crystal structure was modified to a methyl imidazole. The geometry optimized structures of Chl-*a*/Chl-*a*' including the ligating imidazole, in the neutral and cation states, are shown in Figures 7.5 and 7.6. After optimization, the ligating imidazole nitrogen is ~2.20 and 2.17 Å from the central magnesium atom of Chl-*a*/Chl-*a*' in the neutral and cation states, respectively. This ligand bond length is in agreement with bond lengths reported in literature [83]. In the crystal structure of PS I the ligand bond length is ~2.26 Å for P_A and ~2.36 Å for P_B.

The orientation of the imidazole ring with respect to the chlorin plane is significantly different in the geometry optimized structure of Chl-*a* compared to the starting geometry from the crystal structure. In the geometry optimized structure the imidazole ring is rotated ~ 45 degrees (Figure 7.5), while the orientation of the imidazole ring in Chl-*a*' structure remains virtually the same as the crystal structure (Figure 7.6). The fact that geometry optimization of the structure of Chl-*a* with the imidazole ligand leads to a ligand orientation different from the crystal structure is an interesting observation that may indicate the steric hindrance on the imidazole (histidine) ligating P_B in PS I is significant in holding the pigment in place.

The calculated IR spectra for the cation and neutral states of the models in Figures 7.5 and 7.6, along with the corresponding cation minus neutral IR DS, are shown in Figures 7.7 and 7.8. The solid lines in Figure 7.7/7.8 show the calculated spectra in the presence of the imidazole ligand. The calculated IR spectra for Chl-*a*/Chl-*a*' are also shown (*dotted*) for comparison.

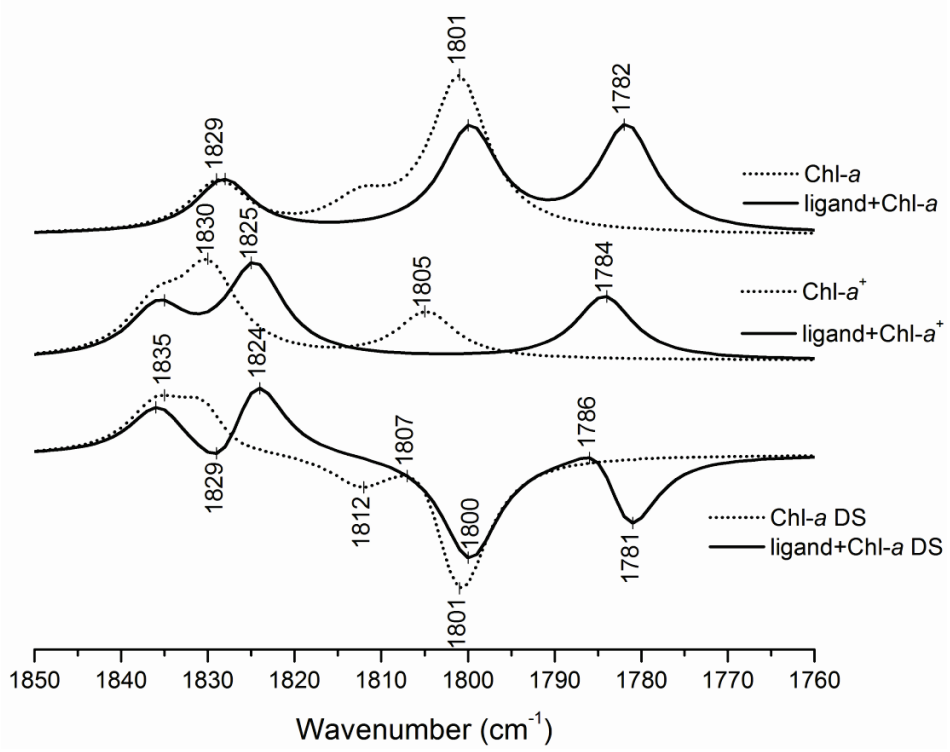

Figure 7.7: Calculated IR spectra for ligand+Chl-*a*/Chl-*a* (*top*) and ligand+Chl-a^+/Chl-a^+ (*middle*). The "cation minus neutral" IR DS are also shown (*bottom*).

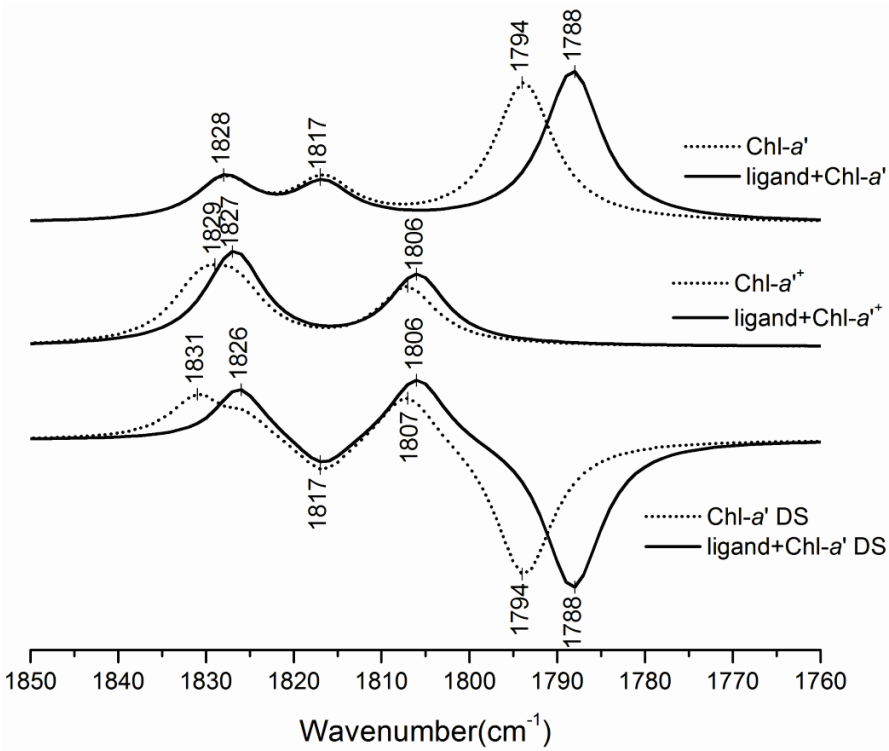

Figure 7.8: Calculated IR spectra for ligand+Chl-*a*'/Chl-*a*' (top) and ligand+Chl-a'^+/Chl-a'^+ (middle). The "cation minus neutral" IR DS are also shown (bottom).

The harmonic vibrational mode frequencies and intensities associated with the C=O modes of ligand+Chl-*a*/ligand+Chl-*a*', ligand+Chl-a^+/ligand+Chl-a'^+, Chl-*a*/*a*' and Chl-a^+/Chl-a'^+ are listed in Table 7.2.

Figure 7.7 and Table 7.2 indicate that, for the neutral state of Chl-*a*, the ligand decreases the intensity and frequency of the anti-symmetrically coupled 13^1 keto and 13^3 ester C=O mode by 32% and 19 cm^{-1} respectively. For neutral Chl-*a*' the results are quite different (Figure 7.8). The inclusion of the ligand causes a small increase in intensity (8%) of the anti-symmetrically coupled mode, and a 6 cm^{-1} decrease in frequency. For the cation state, Chl-a^+, the ligand increases the intensity of the anti-symmetrically coupled mode by 35%, while the frequency decreases by 21 cm^{-1}. In the case of Chl-a'^+, the differences induced by the inclusion of the ligand are much less pronounced, where the frequency decreases by 1 cm^{-1} and the intensity increases 21% (Table 7.2).

Table 7.2: Calculated frequencies and intensities (in parenthesis [in km/mole]) for the different carbonyl modes of ligand+Chl-*a*/*a*', Chl-*a*/*a*', ligand+Chl-a^+/$a'^+$and Chl-a^+/a'^+.

Mode	Neutral	Shift Δν(ΔI)	Cation	Shift Δν(ΔI)
ν (17^3 C=O)				
ligand+Chl-*a*	1828(245)	-1(4%)	1836(230)	0(8%)
Chl-*a*	1829(235)		1836(213)	
ligand+Chl-*a*'	1828(201)	0(4%)	1828(62)	2(-73%)
Chl-*a*'	1828(194)		1826(226)	
ν (13^1 and 13^3 C=O) s				
ligand+Chl-*a*	1800(480)	-12(272%)	1825(424)	-5(7%)
Chl-*a*	1812(129)		1830(397)	
ligand+Chl-*a*'	1817(167)	0(-10%)	1827(379)	-4(52%)
Chl-*a*'	1817(186)		1831(250)	
ν (13^1 and 13^3 C=O) as				
ligand+Chl-*a*	1782(486)	-19(-32%)	1784(291)	-21(35%)
Chl-*a*	1801(719)		1805(215)	
ligand+Chl-*a*'	1788(706)	-6(8%)	1806(324)	-1(21%)
Chl-*a*'	1794(652)		1807(267)	

The frequency shift induced by including the ligand of Chl-*a*/Chl-*a*' for each calculation is shown along with the mode intensity change [in parenthesis (in%)].

The frequency of the symmetrically coupled 13^1 keto and 13^3 ester C=O mode of Chl-*a* decreases by 12 cm^{-1} while the intensity of the mode increases by 272% in the presence of the ligand. In the case of Chl-a^+ the frequency of the symmetrically coupled C=O mode decreases by 5 cm^{-1}, while the intensity of the mode increases by 7%. For Chl-*a*' the symmetrically coupled C=O mode frequency is unaffected in the presence of the ligand while the intensity decreases by 10%. In the cation state, Chl-a'^+, the frequency of the couple mode decreases by 4 cm^{-1} while the intensity of the mode increases by 52% (Table 7.2).

The 17^3 ester C=O mode vibration of Chl-*a* and Chl-*a*' is not significantly affected by the presence of the ligand. The frequency of the 17^3 ester C=O mode is essentially unaffected for Chl-*a*' while decreases by 1cm^{-1} for Chl-*a*. The intensity of the mode in both cases increases by 4%. For Chl-a^+ the frequency of the 17^3 ester C=O mode is unchanged and the intensity increase by 8% while for Chl-a'^+ the ligand causes a slight increase in frequency (2 cm^{-1}) while the intensity is significantly reduced (73%) (Table 7.2). This significant reduction in intensity of the 17^3 ester C=O mode of Chl-a'^+ is due to the coupling between the 13^3 ester, 13^1 keto and 17^3 ester C=O modes upon cation formation.

The gas phase calculations of Chl-*a*/Chl-*a*' in the presence of the axial ligand to the central Mg atom shows that the 13^1 keto and 13^3 ester C=O modes show symmetric and anti-symmetric coupled vibrations. The 17^3 ester group vibration of Chl-*a* is not coupled to the 13^1 keto and 13^3 ester C=O group vibrations in the neutral or cation state. For Chl-*a*' the 17^3 ester group vibration is independent of the 13^1 keto and 13^3 ester C=O group vibrations in the neutral state but is strongly coupled in the cation state. Also the calculations show that effect of the axial ligand on the frequency and intensity of the symmetrically and anti-symmetrically coupled 13^1 keto and 13^3 ester C=O group vibrations and the 17^3 ester group vibration is subtle.

7.3.3 Effect of Fifth Ligand and Dielectric Media on the Vibrational Modes of Chl-a/Chl-a'

The overall dielectric constant of the environment for pigments in photosynthetic proteins is usually in the 2-7 range [96, 97, 131-134]. For this reason the vibrational properties of axially ligated Chl-*a*/Chl-*a*' models were also studied in solvents with dielectric constants of 2.228 (CCl_4) and 7.58 (THF). The Chl-*a*/Chl-*a*' models were fully geometry optimized in the dielectric media, and after optimization, the ligating imidazole nitrogen is ~2.19 Å from the central magnesium atom in the neutral state in CCl_4 and THF. For the cation state the corresponding distance is ~2.16 Å in both CCl_4 and THF.

The calculated IR spectra for the cation and neutral states for Chl-*a*/Chl-*a*', along with the corresponding cation minus neutral IR DS in CCl_4 and THF, are shown in Figures 7.9/7.10 and 7.11/7.12, respectively. The solid lines in Figures 7.9/7.10 and 7.11/7.12 show the calculated spectra of ligand+Chl-*a*/ligand+Chl-*a*' in CCl_4 and THF, respectively. The calculated IR spectra for Chl-*a*/Chl-*a*' in CCl_4 and THF are also shown (*dotted*) for comparison. The harmonic vibrational mode frequencies and intensities associated with the C=O modes of ligand+Chl-*a*/ligand+Chl-*a*', ligand+Chl-a^+/ligand+Chl-a'^+, in the dielectric media are listed in Tables 7.3 and 7.4.

The calculated IR spectra in the presence of ligand shows that the frequency of the anti-symmetrically coupled 13^1 keto and 13^3 ester C=O vibration of Chl-*a* decrease by 10 cm^{-1} in CCl_4 and 6 cm^{-1} in THF while the intensity increases by 1% and 7%, respectively. The frequency of the anti-symmetrically coupled C=O vibrations of Chl-*a*' decreases by 5 cm^{-1} in CCl_4 and 9cm^{-1} in THF while the intensity increases by 7% in both cases. For Chl-a^+ in CCl_4 the anti-symmetrically coupled C=O vibrations decreases in frequency by 13 cm^{-1} while the intensity of the vibration increase by 9%. For Chl-a^+ in THF the anti-symmetrically coupled C=O vibrations

decreases in frequency by 8 cm^{-1} while the intensity of the vibration slightly decreases. For Chl-*a*'$^{+}$ the anti-symmetrically coupled C=O vibrations decreases in frequency by 2 cm^{-1} in CCl_4 and by 4 cm^{-1} in THF while the intensity of the vibration increase by 26% and 12%, respectively (Tables 7.3 and 7.4).

Table 7.3: Calculated frequencies and intensities (in parenthesis [in km/mole]) for the different carbonyl modes of ligand+Chl-*a*/*a*', Chl-*a*/*a*', ligand+Chl-a^{+}/$a'^{+}$and Chl-a^{+}/a'^{+} in CCl_4.

Mode	Neutral	Shift Δν(ΔI)	Cation	Shift Δν(ΔI)
ν (17^3 C=O)				
ligand+Chl-*a* in CCl_4	1814(300)	1(5%)	1819(268)	0(24%)
Chl-*a* in CCl_4	1813(287)		1819(217)	
ligand+Chl-*a*' in CCl_4	1814(260)	1(2%)	1815(134)	2(-60%)
Chl-*a*' in CCl_4	1813(254)		1813(311)	
ν (13^1 and 13^3 C=O) s				
ligand+Chl-*a* in CCl_4	1791(249)	-13(98%)	1813(600)	-4(6%)
Chl-*a* in CCl_4	1804(126)		1817(568)	
ligand+Chl-*a*' in CCl_4	1806(211)	0(-2%)	1814(422)	-3(30%)
Chl-*a*' in CCl_4	1806(216)		1817(324)	
ν (13^1 and 13^3 C=O) as				
ligand+Chl-*a* in CCl_4	1775(1148)	-10(1%)	1785(421)	-13(9%)
Chl-*a* in CCl_4	1785(1142)		1798(385)	
ligand+Chl-*a*' in CCl_4	1771(1116)	-5(7%)	1793(569)	-2(26%)
Chl-*a*' in CCl_4	1776(1047)		1795(451)	

The frequency shift induced by including the ligand of Chl-a/Chl-a' for each calculation is shown along with the mode intensity change [in parenthesis (in%)].

Table 7.4: Calculated frequencies and intensities (in parenthesis [in km/mole]) for the different carbonyl modes of ligand+Chl-*a*/*a*', Chl-*a*/*a*', ligand+Chl-a^{+}/a'^{+} and Chl-a^{+}/a'^{+} in THF.

Mode	Neutral	Shift Δν(ΔI)	Cation	Shift Δν(ΔI)
ν (17^3 C=O)				
ligand+Chl-*a* in THF	1800(355)	1(29%)	1803(216)	-1(-58%)
Chl-*a* in THF	1799(276)		1804(520)	
ligand+Chl-*a*' in THF	1799(334)	-2(4%)	1802(281)	1(-32%)
Chl-*a*' in THF	1801(320)		1801(414)	
ν (13^1 and 13^3 C=O) s				
ligand+Chl-*a* in THF	1788(193)	-8(-24%)	1801(779)	-5(132%)
Chl-*a* in THF	1796(255)		1806(336)	
ligand+Chl-*a*' in THF	1794(276)	-1(-4%)	1800(463)	-4(23%)
Chl-*a*' in THF	1795(287)		1804(377)	
ν (13^1 and 13^3 C=O) as				
ligand+Chl-*a* in THF	1761(1755)	-6(7%)	1782(764)	-8(-1%)
Chl-a_{82} in THF	1767(1637)		1790(771)	
ligand+Chl-*a*' in THF	1751(1663)	-9(7%)	1778(899)	-4(12%)
Chl-*a*' in THF	1760(1551)		1782(802)	

The frequency shift induced by including the ligand of Chl-*a*/Chl-*a*' for each calculation is shown along with the mode intensity change [in parenthesis (in%)].

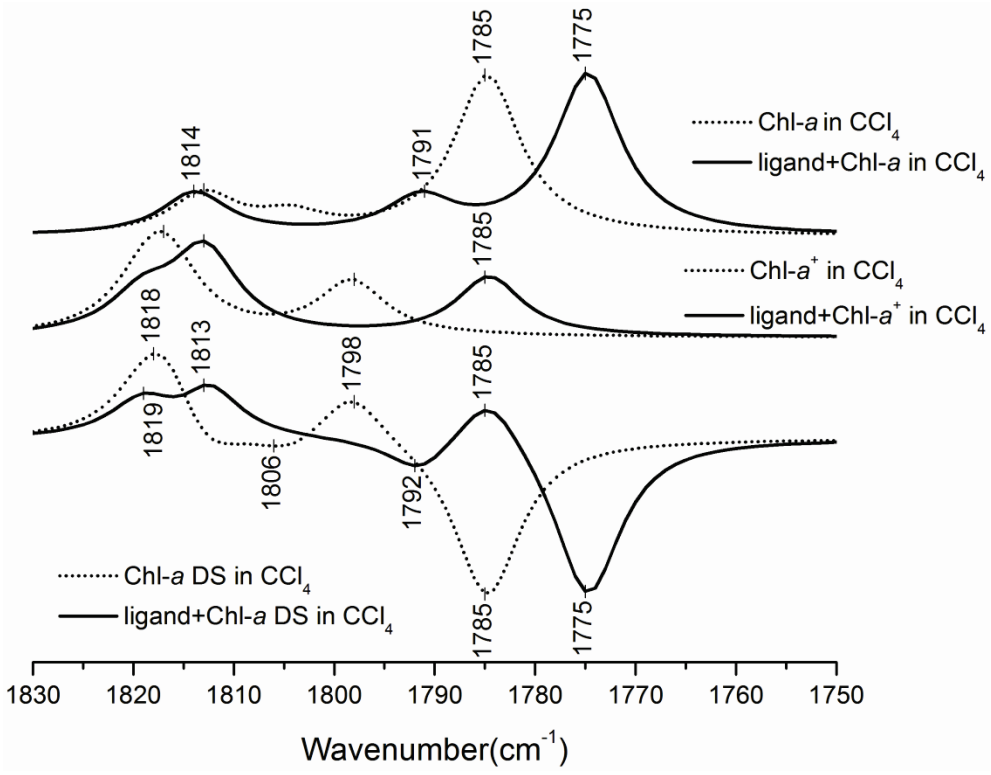

Figure 7.9: Calculated IR spectra for ligand+Chl-*a*/Chl-*a* (*top*) and ligand+Chl-a^+/Chl-a^+ (*middle*) in CCl_4. The "cation minus neutral" IR DS are also shown (*bottom)*.

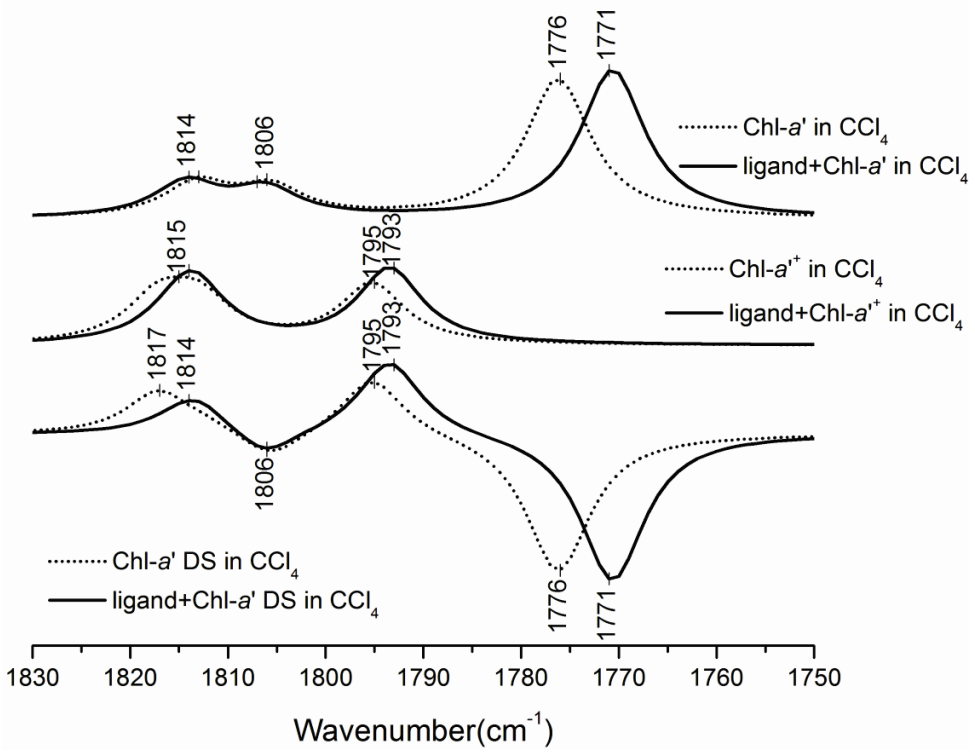

Figure 7.10: Calculated IR spectra for ligand+Chl-*a'*/Chl-*a'* (*top*) and ligand+Chl-a'^+/Chl-a'^+ (*middle*) in CCl_4. The "cation minus neutral" IR DS are also shown (*bottom)*.

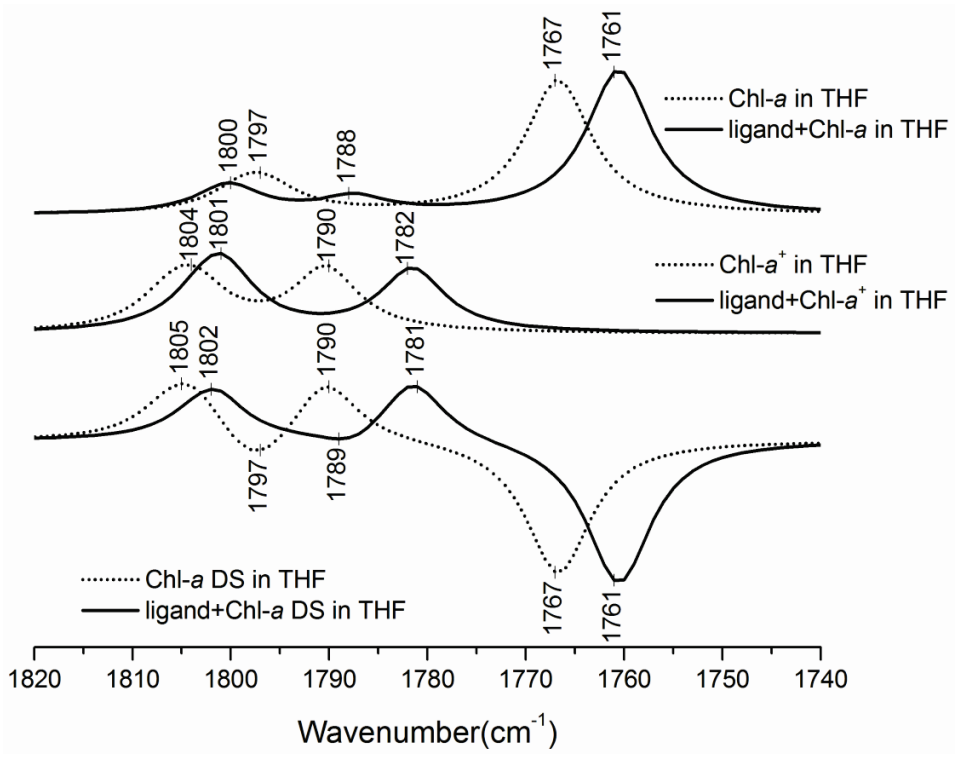

Figure 7.11: Calculated IR spectra for ligand+Chl-*a*/Chl-*a* (*top*) and ligand+Chl-a^+/Chl-a^+ (*middle*) in THF. The "cation minus neutral" IR DS are also shown (*bottom)*.

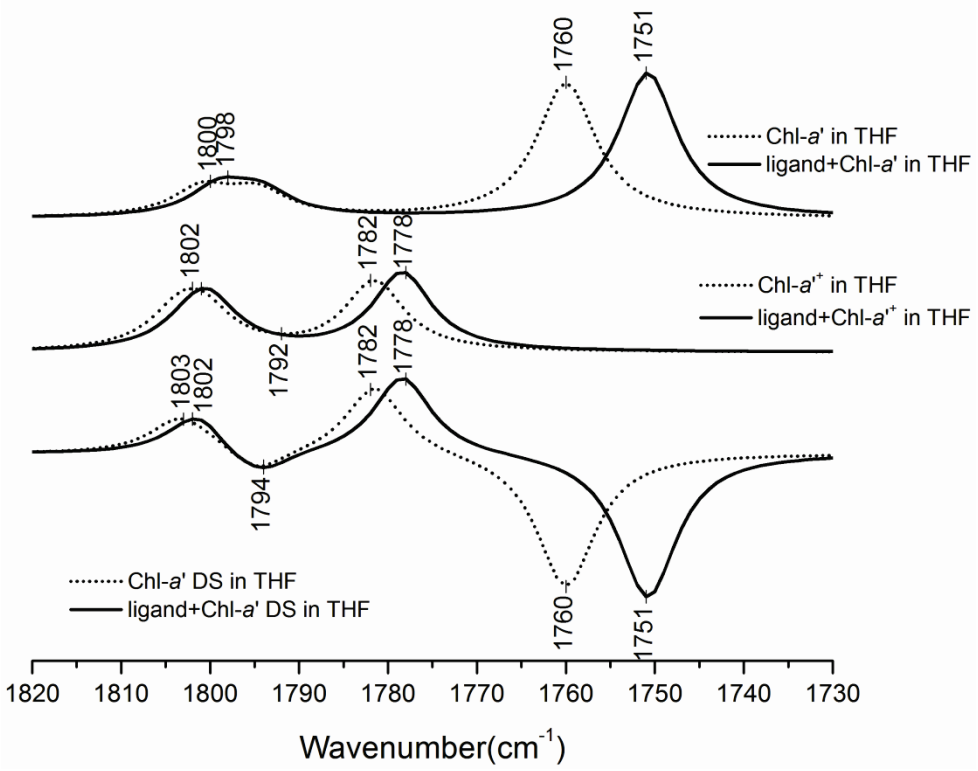

Figure 7.12: Calculated IR spectra for ligand+Chl-*a'*/Chl-*a'* (*top*) and ligand+Chl-a'^+/Chl-a'^+ (*middle*) in THF. The "cation minus neutral" IR DS are also shown (*bottom)*.

The frequency of the symmetrically coupled 13^1 keto and 13^3 ester C=O vibrational mode of Chl-*a* decreases by 13 cm^{-1} and 8 cm^{-1} respectively in CCl_4 and THF, while the intensity increases by 98% in CCl_4 and decreases by 24% in THF. For Chl-a^+, the frequency the symmetrically coupled 13^1 keto and 13^3 ester C=O vibrational mode decreases by 4/5 cm^{-1} in CCl_4/THF. The intensity of the mode increases 132% in THF while in CCl_4 only a slight increase is observed. The significant increase in intensity for the symmetrically coupled 13^1 keto and 13^3 ester C=O vibrational mode of Chl-a^+ in THF can be attributed to strong coupling to the 17^3 ester C=O mode upon cation formation. For Chl-*a*', inclusion of the ligand has no significant effect on the frequency or intensity of the symmetrically coupled 13^1 keto and 13^3 ester C=O vibrational mode. For Chl-a'^+, the effect of the ligand is similar in both solvents were the frequency down-shift 3-4 cm^{-1} while the intensity increase by 23-30% (Tables 7.3 and 7.4).

The frequency of the 17^3 ester C=O mode is mostly unaffected by the ligand while a slight increase in intensity is observed for Chl-*a*/Chl-*a*' in both solvents. The most significant change is observed for Chl-*a* in THF where the intensity of the mode increases by 29%. In the cation state of Chl-a^+/Chl-a'^+, again the effect of the ligand on the frequency of the 17^3 ester C=O group is negligible, though significant changes in intensity is observed. For Chl-a^+, the intensity increase by 24 % in CCl_4 while decreases by 58% in THF. In the case of Chl-a'^+ the intensity decreases by 60% in CCl_4 and by 32% in THF (Tables 7.3 and 7.4).

The calculations of Chl-*a*/Chl-*a*' in solvents in the presence of the axial ligand to the central Mg atom shows that the 13^1 keto and 13^3 ester C=O modes show symmetric and anti-symmetric coupled vibrations. The 17^3 ester group vibration of Chl-*a*/ Chl-*a*' is not coupled to the 13^1 keto and 13^3 ester C=O group vibrations in the neutral state in both CCl_4 and THF. In the cation state the 17^3 ester, 13^1 keto and 13^3 ester C=O groups show strong coupling for Chl-*a*/Chl-

a' in both solvents. Also the calculations in solvents show that effect of the axial ligand on the frequency and intensity of the symmetrically and anti-symmetrically coupled 13^1 keto and 13^3 ester C=O group vibrations and the 17^3 ester group vibration is small as in the case of gas phase calculations.

7.3.4 Calculated Redox Potential of ligand+Chl-*a*/Chl-*a*'

The ionization potential (IP) of Chl-*a*/Chl-*a*' was calculated as described by Hasegawa et. al. [137] (See section 6.3.3 for details). As expected, the calculated total energy and the IP's for Chl-*a* and Chl-*a*' are essentially the same.

The calculated redox potential of Chl-*a*/Chl-*a*' is significantly affected in the presence of ligand leading to ~ 380-400 mV decrease in the gas phase (Tables 7.14 and 7.15). The calculated redox potential of Chl-*a*/Chl-*a*' is 636/621 (in CCl_4) and 345/333 mV (in THF), respectively. The calculated redox potential of Chl-*a* is significantly lower than the experimental observed value of 800mV[138]. This decrease in redox potential can be attributed to the strong axial ligand. A suggestion could be that the unpaired electron of the histidine ligand stabilizes the charge on Chl-a^+/Chl-a'^+ thereby lowering the redox potential. The effect of the ligands on the redox potential of chlorophylls and bacteriochlorophylls has been extensively investigated by Heimdal et al.[83] and it was shown that the axial ligands decrease the redox potential. The calculated redox potential values for Chl-*a* are in agreement with the results of Heimdal et al.

7.3.5 Effect of Thr H-bond Interactions on Vibrational Modes of Chl-*a*/Chl-*a*'

To investigate the effect of H-bonding interactions to the 13^1 keto C=O group of Chl-*a*/*a*', the vibrational mode frequencies and intensities were calculated in the presence of a threonine residue where the hydroxyl proton is < 3Å from the 13^1 keto C=O oxygen of Chl-*a*/Chl-*a*'. The PS I crystal structure at 2.5Å resolutions [6] reveals that the 13^1 keto C=O group

of P_A (Chl-*a*') is involved in H-bonding with ThrA743. This H-bonding interaction is modeled by considering Chl-*a'* directly H-bonded to ThrA743 residue, as in the X-ray crystal structure geometry (Figure 7.14) [6]. To simulate the effect of H bonding interactions to P_B (Chl-*a*), the Tyr727 residue was changed to a Thr residue and the vibrational mode frequencies and intensities for the Chl-*a* model system was calculated (Figure 7.13). It is worth mentioning that this mutation has been implemented in cyanobacterial PS I particles from *Synechocystis* sp. PCC 6803 and the experimental (P_{700}^{+}-P_{700}) FTIR DS is available for this mutants (See Chapter 3 for details).

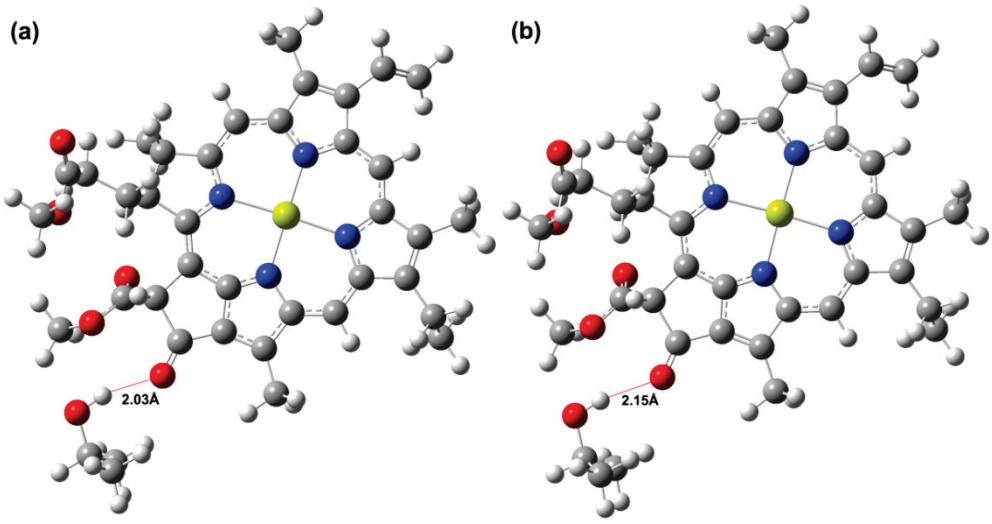

Figure 7.13: Geometry optimized molecular structures of Chl-*a* and Chl-a^+ in the presence of a threonine residue that provides H-bond to the 13^1 keto C=O group (a) neutral and (b) cation states.

Figures 7.13 and 7.14 show the geometry optimized structures of Thr+Chl-*a*/Thr+Chl-*a*'. The carboxyl and amino end of the Thr residue was truncated using a methyl group. After geometry optimization the H atom of the hydroxyl group of Thr residue is at a distance of ~2.03Å and 2.15 Å from the 13^1 keto C=O oxygen for Chl-*a* in the neutral and cation state, respectively (Figure 7.13). For Chl-*a*' the corresponding distances are 1.95Å and 2.03Å for the neutral and cation states, respectively (Figure 7.14). Also the angle between the 13^1 keto C=O oxygen and the hydroxyl group (O_{chl}-H_{thr}-O_{thr} angle) is ~ 165/168° for Chl-*a*/Chl-*a*' in the

neutral state, respectively. In the cation state the corresponding angles for Chl-a^+/Chl-a'$^+$ are ~169/160°, respectively.

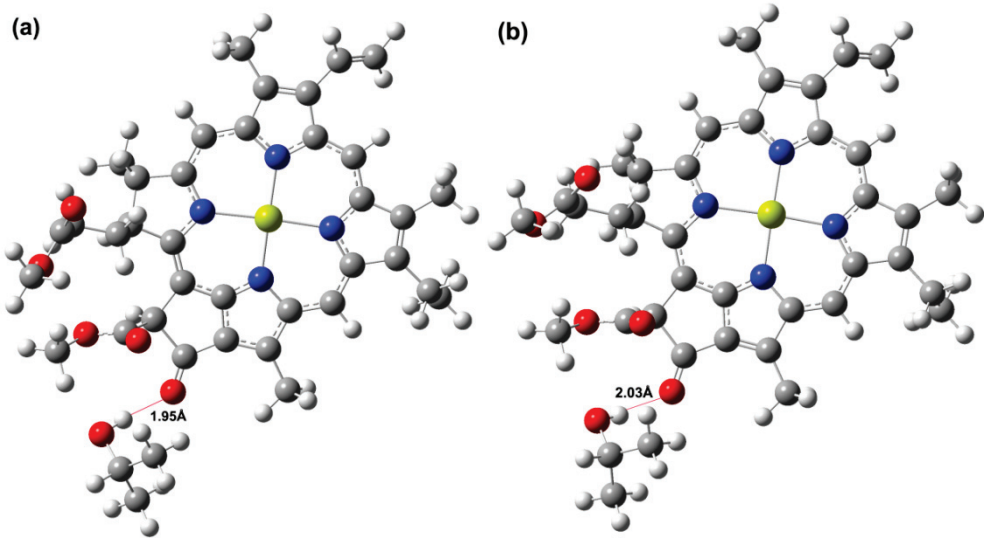

Figure 7.14: Geometry optimized molecular structures of Chl-*a*' and Chl-*a*'$^+$ in the presence of a threonine residue that provides H-bond to the 13^1 keto C=O group (a) neutral and (b) cation states.

The calculated IR spectra for the cation and neutral states of the models in Figures 7.13 and 7.14, along with the corresponding cation minus neutral IR DS are shown in Figure 7.15/7.16. The solid lines in Figure 7.15/7.16 show the calculated spectra in the presence of the H-bond provided by the threonine residue. The calculated IR spectra for Chl-*a*/*a*' model without the H-bond (dotted line) are also shown for comparison.

The harmonic vibrational mode frequencies and intensities associated with the C=O modes of Thr+Chl-*a*/Thr+Chl-*a*', Thr+Chl-a^+/Thr+Chl-a'$^+$, Chl-*a*/*a*' and Chl-*a*/*a*'$^+$ are listed in Table 7.5.

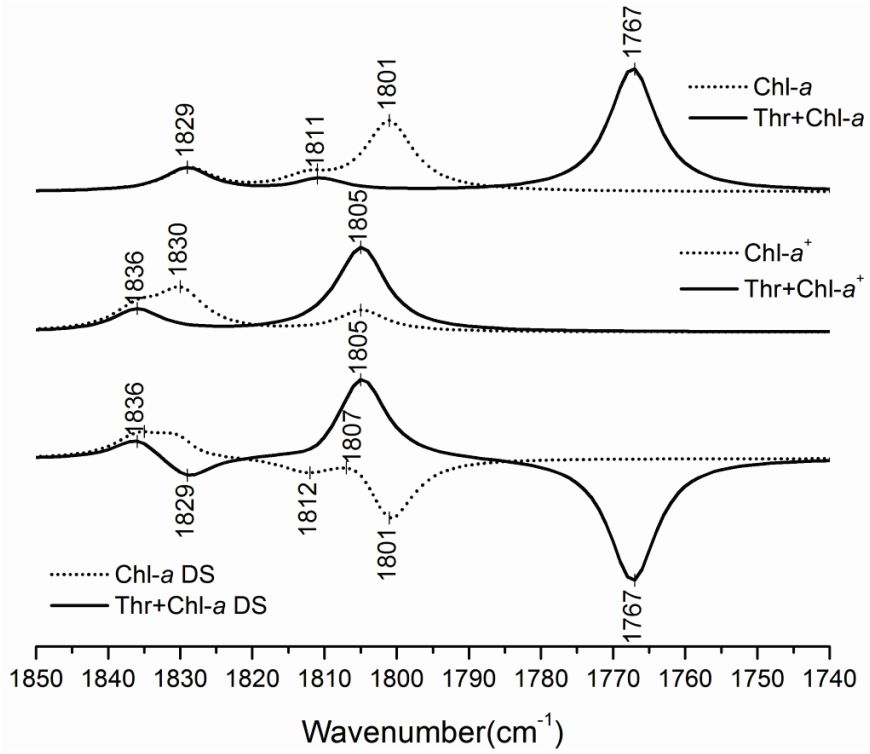

Figure 7.15: Calculated IR spectra for Thr+Chl-*a*/Chl-*a* (*top*) and Thr+Chl-a^+/Chl-a^+ (*middle*) in the gas phase. The "cation minus neutral" IR DS are also shown (*bottom*).

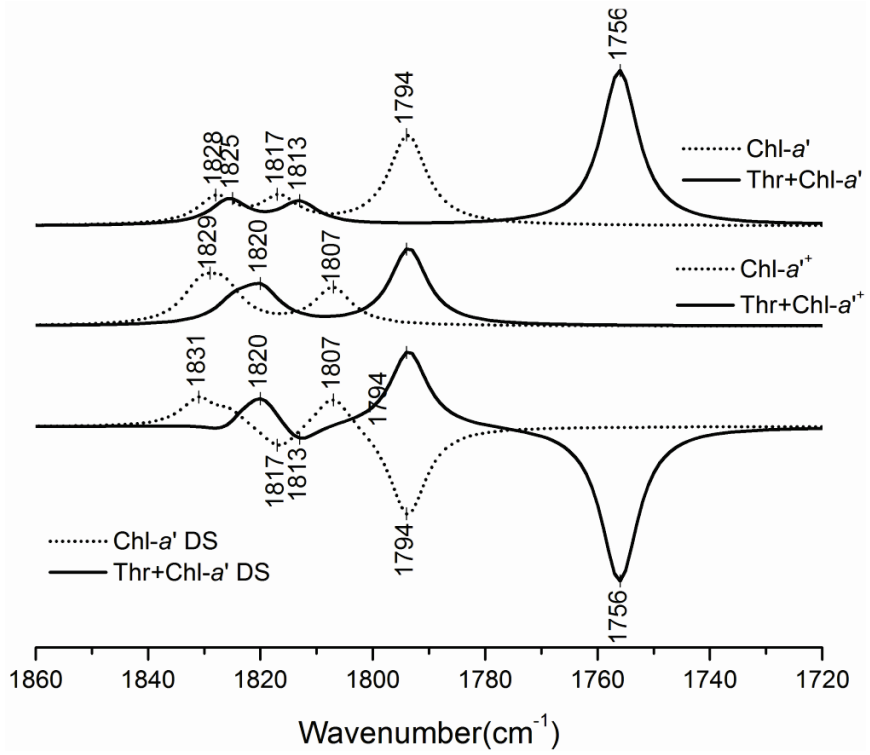

Figure 7.16: Calculated IR spectra for Thr+Chl-*a*'/Chl-*a*' (*top*) and Thr+Chl-a'^+/Chl-a'^+ (*middle*) in the gas phase. The "cation minus neutral" IR DS are also shown (*bottom*).

Table 7.5: Calculated frequencies and intensities (in parenthesis [in km/mole]) for the different carbonyl modes of of Thr+Chl-*a*/Thr+Chl-*a*', Chl-*a*/*a*', Thr+Chl-a^+/Thr+Chl-$a'^+$and Chl-a^+/a'^+.

Mode	Neutral	Shift Δν(ΔI)	Cation	Shift Δν(ΔI)
ν (17^3 C=O)				
Thr+Chl-*a*	1829(242)	0(3%)	1836(230)	0(8%)
Chl-*a*	1829(235)		1836(213)	
Thr+Chl-*a*'	1826(180)	-2(-7%)	1824(151)	-2(33%)
Chl-*a*'	1828(194)		1826(226)	
ν (13^1 and 13^3 C=O) s				
Thr+Chl-*a*	1811(124)	-1(-4%)	1808(67)	-22(-83%)
Chl-*a*	1812(129)		1830(397)	
Thr+Chl-*a*'	1813(160)	-4(-14%)	1820(229)	-11(-8%)
Chl-*a*'	1817(186)		1831(250)	
ν (13^1 and 13^3 C=O) as				
Thr+Chl-*a*	1767(1272)	-34(77%)	1805(829)	0(286%)
Chl-*a*	1801(719)		1805(215)	
Thr+Chl-*a*'	1756(1119)	-38(72%)	1794(554)	-13(107%)
Chl-*a*'	1794(652)		1807(267)	

The frequency shift induced by including the Thr H-bond to Chl-*a*/Chl-*a*' for each calculation is shown along with the mode intensity change [in parenthesis (in%)].

The calculated IR spectra in the presence of Thr H-bond shows that the frequency of the anti-symmetrically coupled 13^1 keto and 13^3 ester C=O vibration of Chl-*a*/Chl-*a*' decrease by 34/38 cm^{-1} while the intensity increases by 77%/72%. For Chl-a^+ the frequency of the anti-symmetrically coupled C=O vibrations is unaffected while the intensity increases by 286%. For Chl-a'^+ on the other hand the frequency of the anti-symmetrically coupled C=O group decreases by 13 cm^{-1} while the intensity of the vibration increase by 107% (Table 7.5).

The effect of the Thr H-bond on the symmetrically coupled 13^1 keto and 13^3 ester C=O vibration of Chl-*a*/Chl-*a*' is moderate compared to the effect on asymmetrically coupled modes. The frequency of Chl-*a*/Chl-*a*' decreases by 1/4 cm^{-1} in the presence of the Thr H-bond while the intensity decreases by 4%/14%. For the cation state of Chl-a^+/Chl-a'^+ the frequency decreases by 22/11 cm^{-1} while the intensity decreases by 83%/8%. The decrease in intensity of the symmetrically coupled 13^1 keto and 13^3 ester C=O vibrational modes is opposite to what is observed for the anti-symmetrically coupled modes where the intensities increased significantly in the presence of the Thr H-bond (Table 7.5).

The frequency and intensity of the 17^3 ester C=O group is mostly unaffected by the H-bond interaction to the 13^1 keto C=O group of Chl-*a*/Chl-*a*' an exception being the Chl-*a*'$^+$ state where the intensity of the vibration increases by 33% compared to the model where the Thr H-bond is absent (Table 7.5).

The gas phase calculations of Chl-*a*/Chl-*a*' in the presence of Thr directly H-bonded to 13^1 keto C=O group shows that the 13^1 keto and 13^3 ester C=O modes still show symmetric and anti-symmetric coupled vibrations. The 17^3 ester group vibration of Chl-*a*/Chl-*a*' is not coupled to the 13^1 keto and 13^3 ester C=O group vibrations in the neutral or cation state. The calculations show that the H-bond to 13^1 keto C=O group of Chl-*a*/Chl-*a*' cause the frequency of symmetrically and anti-symmetrically coupled 13^1 keto and 13^3 ester C=O modes to down-shift. Also, the effect on the symmetrically coupled mode is smaller compared to the effect on the anti-symmetrically coupled mode.

7.3.6 Effect of Thr H-bond and Dielectric Media on Vibrational Modes of Chl-*a*/Chl-*a*'

The vibrational frequencies of Chl-*a*/Chl-*a*' in the presence of Thr H-bond was also calculated in CCl_4 and THF to simulate the dielectric properties of PS I protein. The calculated IR spectra for the cation and neutral states of Chl-*a*/Chl-*a*' in CCl_4 and THF along with the corresponding cation minus neutral IR DS are shown in Figures 7.17/7.18 and 7.19/7.20, respectively. The solid lines in Figures 7.17/7.18 and 7.19/7.20 show the calculated spectra in the presence of the H-bond provided by the threonine residue in CCl_4 and THF. The calculated IR spectra for Chl-*a*/*a*' in solvents in the absence of the Thr H-bond (dotted line) are also shown for comparison. The harmonic vibrational mode frequencies and intensities associated with the C=O modes of Thr+Chl-*a*/Thr+Chl-*a*'$_{82}$, Thr+Chl-*a*$^+$/Thr+Chl-*a*'$^+$, Chl-*a*/*a*' and Chl-*a*$^+$/*a*'$^+$ in CCl_4 and THF are listed in Tables 7.6 and 7.7.

Table 7.6: Calculated frequencies and intensities (in parenthesis [in km/mole]) for the different carbonyl modes of Thr+Chl-*a*/*a*', Chl-*a*/*a*', Thr+Chl-a^+/a'^+ and Chl-a^+/a'^+ in CCl_4.

Mode	Neutral	Shift Δν(ΔI)	Cation	Shift Δν(ΔI)
ν (17^3 C=O)				
Thr+Chl-*a* in CCl_4	1813(304)	0(6%)	1820(293)	1(35%)
Chl-*a* in CCl_4	1813(287)		1819(217)	
Thr+Chl-*a*' in CCl_4	1813(268)	0(6%)	1818(275)	5(-12%)
Chl-*a*' in CCl_4	1813(254)		1813(311)	
ν (13^1 and 13^3 C=O) s				
Thr+Chl-*a* in CCl_4	1802(137)	-2(9%)	1803(74)	-14(-87%)
Chl-*a* in CCl_4	1804(126)		1817(568)	
Thr+Chl-*a*' in CCl_4	1806(183)	0(-15%)	1807(132)	-10(-59%)
Chl-*a*' in CCl_4	1806(216)		1817(324)	
ν (13^1 and 13^3 C=O) as				
Thr+Chl-*a* in CCl_4	1757(1665)	-28(46%)	1794(1129)	-4(193%)
Chl-*a* in CCl_4	1785(1142)		1798(385)	
Thr+Chl-*a*' in CCl_4	1742(1532)	-34(46%)	1782(1061)	-13(135%)
Chl-*a*' in CCl_4	1776(1047)		1795(451)	

The frequency shift induced by including the Thr H-bond to Chl-*a*/Chl-*a*' for each calculation is shown along with the mode intensity change [in parenthesis (in%)].

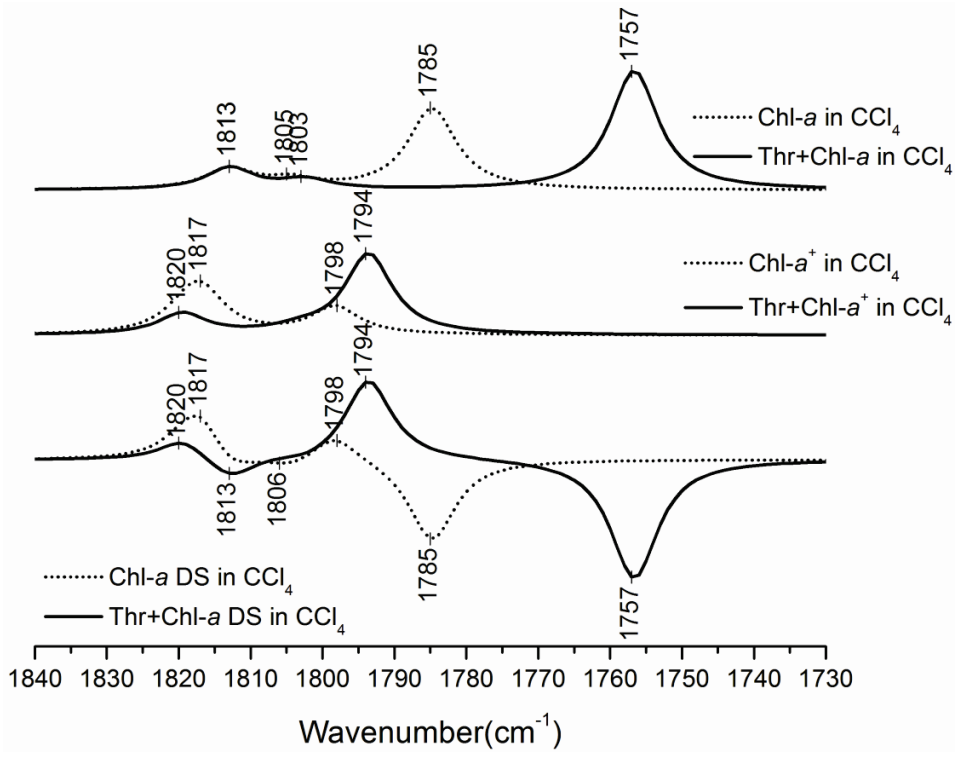

Figure 7.17: Calculated IR Spectra for Thr+Chl-*a*/Chl-*a* (top) and Thr+Chl-a^+/Chl-a^+ (*middle*) in CCl_4. The "cation minus neutral" IR DS are also shown (*bottom*).

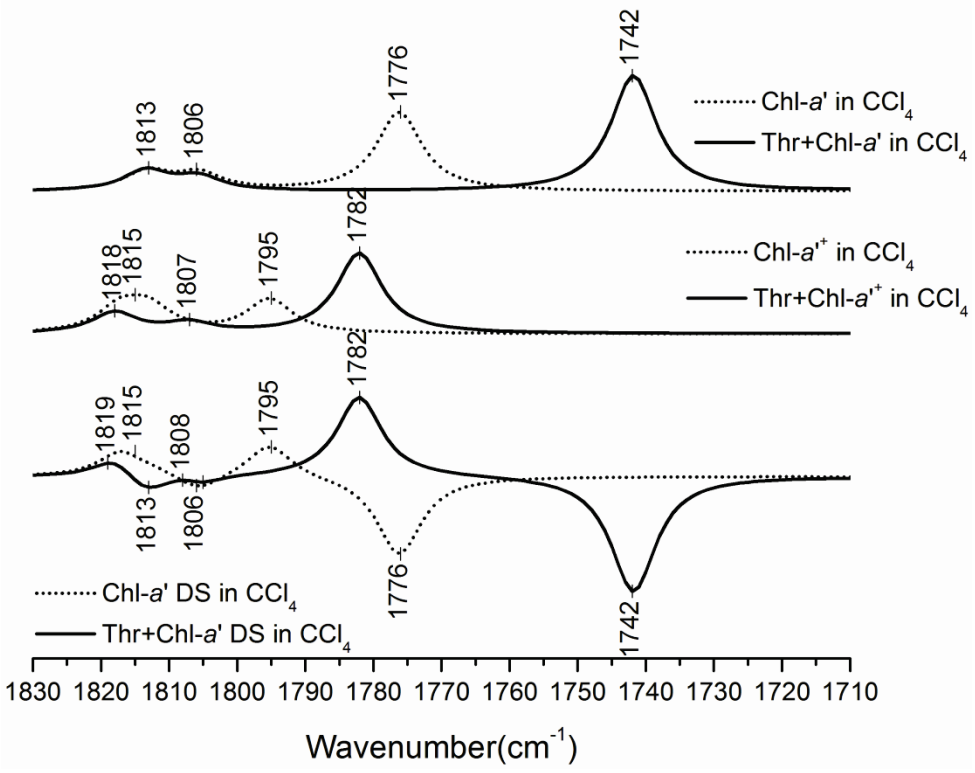

Figure 7.18: Calculated IR Spectra for Thr+Chl-*a*'/Chl-*a*' (top) and Thr+Chl-*a*'$^{+}$/Chl-*a*'$^{+}$ (*middle*) in CCl_4. The "cation minus neutral" IR DS are also shown (*bottom*).

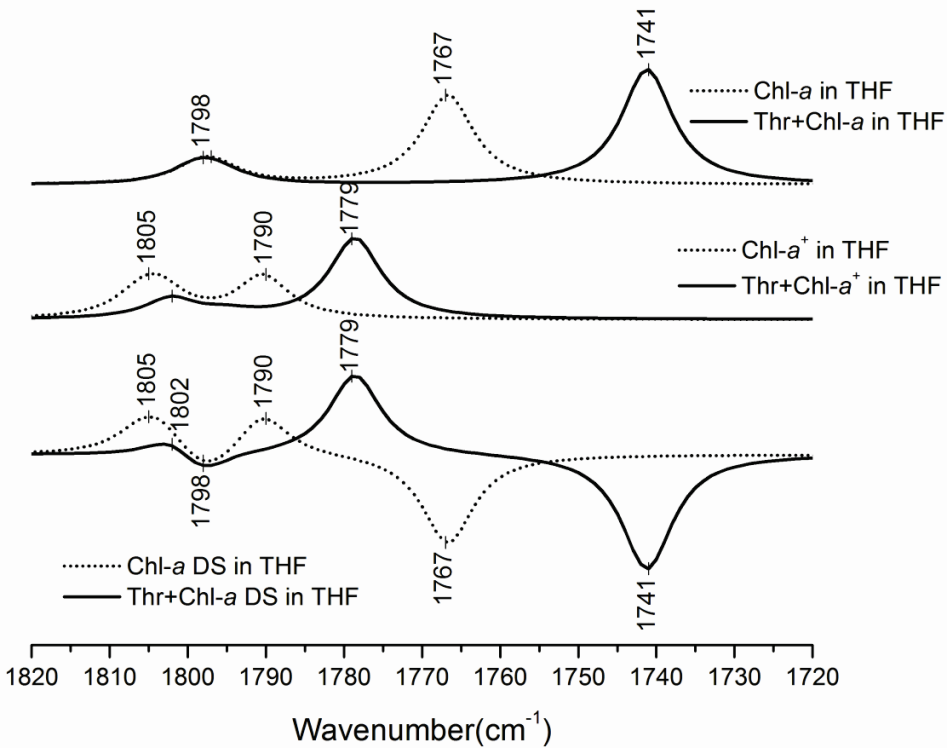

Figure 7.19: Calculated IR Spectra for Thr+Chl-*a*/Chl-*a* (top) and Thr+Chl-*a*$^{+}$/Chl-*a*$^{+}$ (*middle*) in THF. The "cation minus neutral" IR DS are also shown (*bottom*).

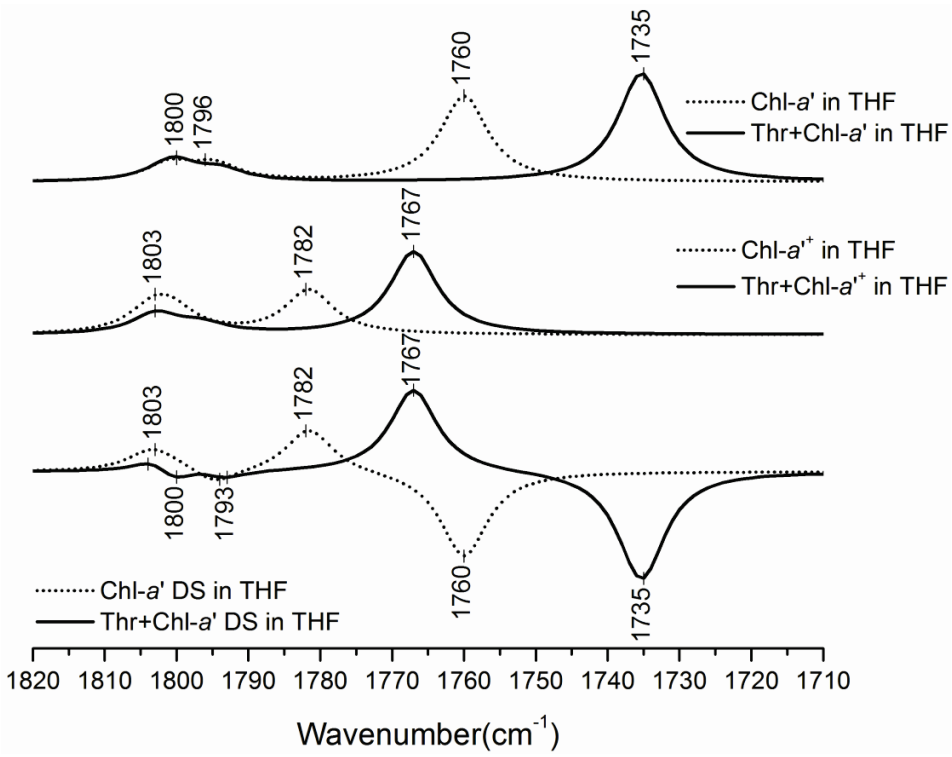

Figure 7.20: Calculated IR Spectra for Thr+Chl-*a*'/Chl-*a*' (top) and Thr+Chl-*a*'$^{+}$/Chl-*a*'$^{+}$ (*middle*) in THF. The "cation minus neutral" IR DS are also shown (*bottom*).

Table 7.7: Calculated frequencies and intensities (in parenthesis [in km/mole]) for the different carbonyl modes of Thr+Chl-*a*/*a*', Chl-*a*/*a*', Thr+Chl-*a*$^{+}$/*a*'$^{+}$ and Chl-*a*$^{+}$/*a*'$^{+}$ in THF.

Mode	Neutral	Shift Δν(ΔI)	Cation	Shift Δν(ΔI)
ν (17^3 C=O)				
Thr+Chl-*a* in THF	1799(360)	0(30%)	1802(363)	-2(-30%)
Chl-*a* in THF	1799(276)		1804(520)	
Thr+Chl-*a*' in THF	1801(398)	0(24%)	1803(368)	2(-11%)
Chl-*a*' in THF	1801(320)		1801(414)	
ν (13^1 and 13^3 C=O) s				
Thr+Chl-*a* in THF	1796(177)	0(-31%)	1795(105)	-11(-69%)
Chl-*a* in THF	1796(255)		1806(336)	
Thr+Chl-*a*' in THF	1794(203)	-1(-29%)	1796(169)	-8(-55%)
Chl-*a*' in THF	1795(287)		1804(377)	
ν (13^1 and 13^3 C=O) as				
Thr+Chl-*a* in THF	1741(2104)	-26(29%)	1779(1474)	-11(91%)
Chl-*a* in THF	1767(1637)		1790(771)	
Thr+Chl-*a*' in THF	1735(1959)	-25(26%)	1767(1496)	-15(87%)
Chl-*a*' in THF	1760(1551)		1782(802)	

The frequency shift induced by including the Thr H-bond to Chl-*a*/Chl-*a*' for each calculation is shown along with the mode intensity change [in parenthesis (in%)].

The calculated IR spectra of Chl-*a*/Chl-*a*' in solvents in the presence of Thr H-bond shows that the frequency and intensity of the anti-symmetrically coupled 13^1 keto and 13^3 ester

C=O vibration is significantly impacted by the H-bond interaction. The frequency of the anti-symmetrically coupled mode decreases by 28/34 cm^{-1} for Chl-*a*/Chl-*a*' in CCl_4 while in THF the corresponding decrease in frequency is 26/25 cm^{-1}. The intensity of the anti-symmetrically coupled 13^1 keto and 13^3 ester C=O vibration increases on the other hand, by 46% for both Chl-*a* and Chl-*a*' in CCl_4, while in THF the corresponding increase is 29% for Chl-*a* and 26 % for Chl-*a*' (Tables 7.6 and 7.7). For cation states of Chl-*a*/Chl-*a*' in solvents the effect of H-bond interaction to Thr is similar to the neutral state where the frequency of the vibrations decreases while the intensity increases. The frequency of the anti-symmetrically coupled mode decreases by 4/13 cm^{-1} for Chl-a^+/Chl-a'^+ in CCl_4 while the intensity increases by 193%/135%. The frequency of the anti-symmetrically coupled modes of Chl-a^+/Chl-a'^+ decreases by 11/15 cm^{-1} in THF along with an increase in intensity of 91%/87% (Tables 7.6 and 7.7).

The effect of H-bonding interaction on the frequency of the symmetrically coupled 13^1 keto and 13^3 ester C=O groups of Chl-*a*/Chl-*a*' is subtle compared to the effect on the anti-symmetrically coupled modes. Also, unlike the anti-symmetrically coupled modes the frequency and intensity of the symmetrically coupled mode decreases upon the introduction of H-bond to the 13^1 keto C=O group. The intensity of the symmetrically coupled 13^1 keto and 13^3 ester C=O vibration of Chl-*a* increases by 9% in the presence of the H-bond, while for Chl-*a*', the intensity of the mode decreases by 15% in CCl_4. In THF, Chl-*a* and Chl-*a*' experience a decrease in intensity by 31% and 29%, respectively. In the cation state, the frequency of the symmetrically coupled modes of Chl-a^+/Chl-a'^+ decreases by 14/10 cm^{-1} while the intensity decreases by 87%/59% in CCl_4. In THF the corresponding decrease in frequency and intensity are 11/8 cm^{-1} and 69%/55% respectively (Tables 7.6 and 7.7).

The frequency of the 17^3 ester C=O group in CCl_4 and THF is mostly unaffected by the H-bond introduced to 13^1 keto C=O group of Chl-*a*/Chl-*a*' while the intensity of the vibrational mode is slightly affected. The intensity of the 17^3 ester C=O group vibration increases by 6% for both Chl-*a* and Chl-*a*' in CCl_4 while the corresponding increase in THF is 30% and 24% respectively. For the cation state of Chl-a^+, the intensity increases by 35% while for Chl-a'^+ the intensity decreases by 12% in CCl_4. In THF the intensity of 17^3 ester C=O group of Chl-a^+/Chl-a'^+ decreases by 30%/11% (Tables 7.6 and 7.7).

The vibrational frequency calculations of Chl-*a*/Chl-*a*' in solvents in the presence of Thr directly H-bonded to 13^1 keto C=O group shows that the 13^1 keto and 13^3 ester C=O modes still show symmetric and anti-symmetric coupled vibrations. The 17^3 ester group vibration of Chl-*a*/Chl-*a*' is not coupled to the 13^1 keto and 13^3 ester C=O group vibrations in the neutral or cation state. The calculations show that the H-bond to 13^1 keto C=O group of Chl-*a*/Chl-*a*' cause the frequency of symmetrically and anti-symmetrically coupled 13^1 keto and 13^3 ester C=O modes to down-shift. The effect of H-bond to the 13^1 keto C=O group on the symmetrically coupled mode is smaller compared to the effect on the anti-symmetrically coupled mode.

7.3.7 Calculated Redox Potential of Chl-*a*/Chl-*a*' in the Presence of Thr H-bond

The ionization potential (IP) of Chl-*a*/Chl-*a*' in the presence of Thr H-bond was calculated as discussed before. The calculated total energy and the IP's for Chl-*a* and Chl-*a*' are given in Tables 7.14 and 7.15.

The calculated redox potential of Chl-*a*/Chl-*a*' in the presence of Thr H-bond in the gas phase as well as solvents shows that the redox potential is essentially independent of the H-bond interaction to the 13^1 keto group. This was further investigated by modeling the H-bond interaction to 13^1 keto group using a H_2O molecule (see section 7.3.10).

7.3.8 Effect of H_2O H-bond Interactions on Vibrational Modes of Chl-*a*/Chl-*a*'

The effect of H–bonding to the 13^1 keto C=O group of the Chl-*a*/*a*' was further investigated by modeling the pigments with a H_2O molecule H-bonded directly to the 13^1 keto C=O group (Figures 7.21 and 7.22). Figures 7.21 and 7.22 show the geometry optimized structures of H_2O+Chl-*a*/H_2O+Chl-*a*'. The nearest hydrogen atom of water molecule for the geometry optimized structure is at a distance of ~1.90/1.91Å from the oxygen atom of 13^1 keto C=O group of Chl-*a*/Chl-*a*'in the neutral state (Figures 7.21 and 7.22). For the cation state the corresponding distance is 1.96/1.97Å (Figures 7.21 and 7.22).

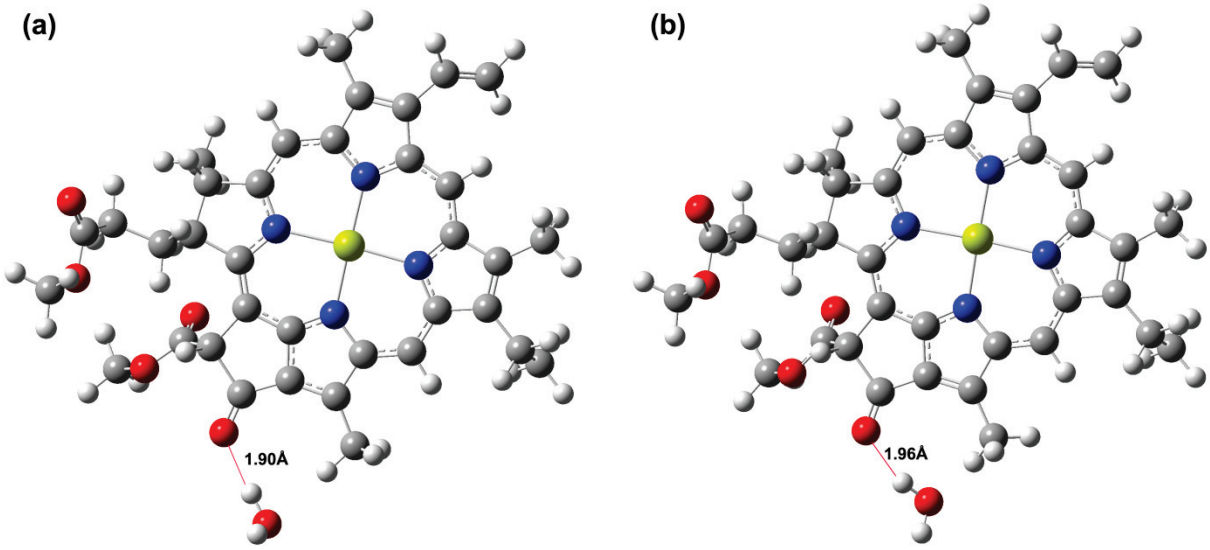

Figure 7.21: Geometry Optimized molecular structures of Chl-*a* and Chl-a^+ in the presence of a water molecule that provides H-bond to the 13^1 keto C=O group (a) neutral and (b) cation states.

The calculated IR spectra for the cation and neutral states of the models in Figures 7.21 and 7.22, along with the corresponding cation minus neutral IR DS are shown in Figure 7.23/7.24. The solid lines in Figure 7.23/7.24 show the calculated spectra in the presence of H_2O molecule H-bonded to the 13^1 keto C=O of Chl-*a*/Chl-*a*'. The calculated IR spectra for Chl-*a*/Chl-*a*' model without the H-bond (dotted line) are also shown for comparison. The harmonic

vibrational mode frequencies and intensities associated with the C=O modes of H_2O+Chl-*a*/H_2O+Chl-*a*', H_2O+Chl-*a*$^+$/H_2O+Chl-*a*'$^+$, Chl-*a*/*a*' and Chl-*a*$^+$/*a*'$^+$ are listed in Table 7.8.

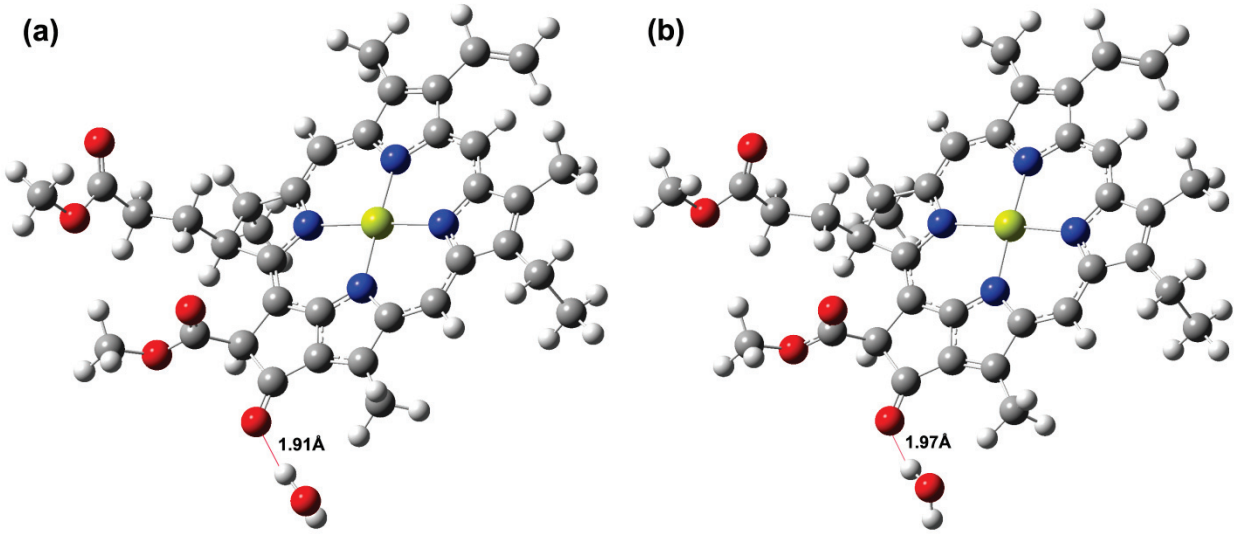

Figure 7.22: Geometry optimized molecular structures of Chl-*a*' and Chl-*a*'$^+$ in the presence of a water molecule that provides H-bond to the 13^1 keto C=O group (a) neutral and (b) cation states.

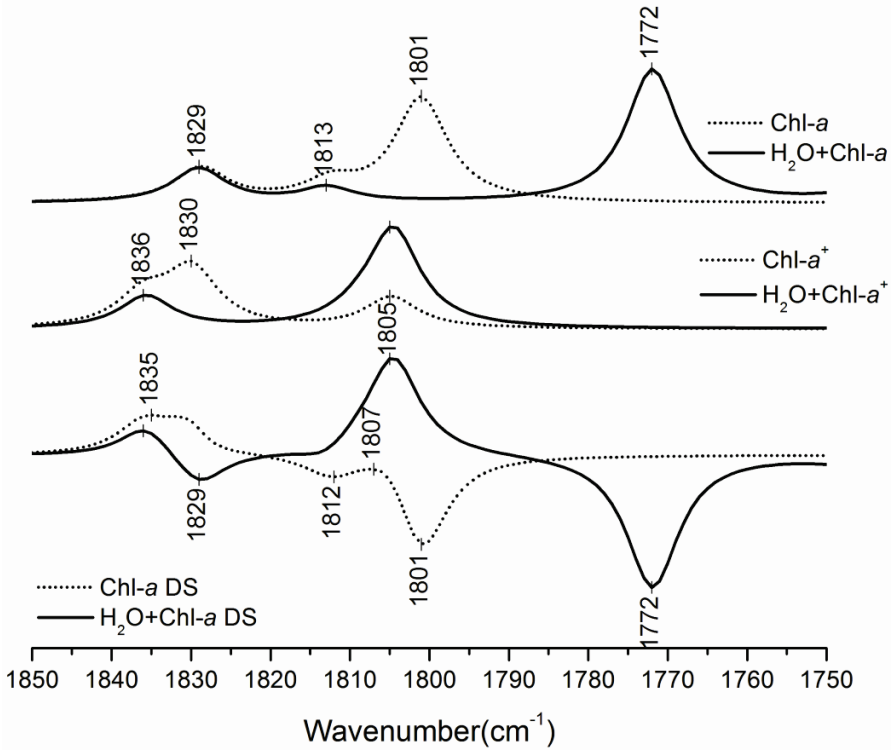

Figure 7.23: Calculated IR Spectra for H_2O+Chl-*a*/Chl-*a* (top) and H_2O+Chl-*a*$^+$/Chl-*a*$^+$ (*middle*) in the gas phase. The "cation minus neutral" IR DS are also shown (*bottom*).

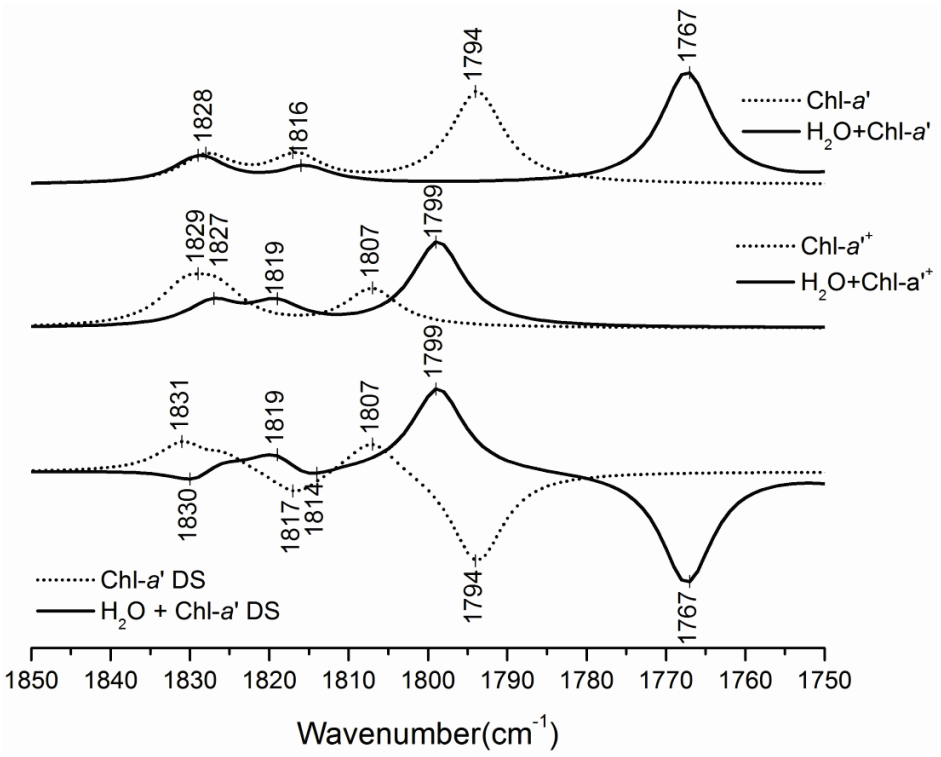

Figure 7.24: Calculated IR Spectra for H_2O+Chl-*a*'/Chl-*a*' (top) and H_2O+Chl-*a*'$^{+}$/Chl-*a*'$^{+}$ (*middle*) in the gas phase. The "cation minus neutral" IR DS are also shown (*bottom*).

Table 7.8: Calculated frequencies and intensities (in parenthesis [in km/mole]) for the different carbonyl modes of H_2O+Chl-*a*/H2O+Chl-*a*', Chl-*a*/*a*', H_2O+Chl-*a*$^{+}$/H2O+Chl-*a*'$^{+}$ and Chl-*a*$^{+}$/*a*'$^{+}$.

Mode	Neutral	Shift Δν(ΔI)	Cation	Shift Δν(ΔI)
ν (17^3 C=O)				
H_2O +Chl-*a*	1829(236)	0(0.4%)	1836(223)	0(5%)
Chl-*a*	1829(235)		1836(213)	
H_2O+Chl-*a*'	1829(194)	1(0%)	1827(167)	1(-26%)
Chl-*a*'	1828(194)		1826(226)	
ν (13^1 and 13^3 C=O) s				
H_2O +Chl-*a*	1813(99)	1(-23%)	1809(56)	-21(-86%)
Chl-*a*	1812(129)		1830(397)	
H_2O+Chl-*a*'	1815(114)	-2(-39%)	1819(153)	-12(-39%)
Chl-*a*'	1817(186)		1831(250)	
ν (13^1 and 13^3 C=O) as				
H_2O +Chl-*a*	1772(919)	-29(28%)	1805(683)	0(218%)
Chl-*a*	1801(719)		1805(215)	
H_2O+Chl-*a*'	1767(786)	-27(21%)	1799(601)	-8(125%)
Chl-*a*'	1794(652)		1807(267)	

The frequency shift induced by including the H_2O H-bond to Chl-*a*/Chl-*a*' for each calculation is shown along with the mode intensity change [in parenthesis (in%)].

The calculated IR spectra in the presence of H_2O H-bond shows that the frequency of the anti-symmetrically coupled 13^1 keto and 13^3 ester C=O vibration of Chl-*a*/Chl-*a*' in the neutral

state is significantly impacted by the presence of the H_2O molecule, while the intensities are less impacted. In the cation state the effect is vice versa, where the frequency of vibration is not much affected but the intensities of the vibration is significantly impacted.

The anti-symmetrically coupled 13^1 keto and 13^3 ester C=O vibration of Chl-*a*/Chl-*a*' in the neutral state decreases by 29/37 cm^{-1} while the intensity increases by 28%/21%. In the cation state the frequency of the modes are not affected by the H-bond while the intensities increases by 218%/125% respectively for Chl-a^+/Chl-a'^+ (Table 7.7).

The neutral state frequency of the symmetrically coupled 13^1 keto 13^3 ester C=O mode of Chl-*a*/Chl-*a*' is not significantly impacted by the H-bond interaction to H_2O, while in the cation state the frequency decreases by 21/12 cm^{-1}. The intensity of the symmetrically coupled 13^1 keto 13^3 ester C=O mode vibration of Chl-*a*/Chl-*a*' decreases in the neutral and cation state upon introduction of H-bond by 23%/39% and 86%/39%, respectively (Table 7.7).

The frequency and intensity of vibration of the 17^3 ester C=O group of Chl-*a*/Chl-*a*' is mostly unaffected by the introduction of the H-bond to H_2O. The only exception being Chl-a'^+, for which the intensity of vibration of the 17^3 ester C=O group decreases by 26% in the presence of H_2O H-bond (Table 7.7).

The gas phase vibrational frequency calculations of Chl-*a*/Chl-*a*' in the presence of a water molecule directly H-bonded to 13^1 keto C=O group shows that the 13^1 keto and 13^3 ester C=O modes still show symmetric and anti-symmetric coupled vibrations. The 17^3 ester group vibration of Chl-*a*/Chl-*a*' is not coupled to the 13^1 keto and 13^3 ester C=O group vibrations in the neutral or cation state. The frequency down-shift of symmetrically and anti-symmetrically coupled 13^1 keto and 13^3 ester C=O modes induced by the water molecule H-bonded to 13^1 keto C=O group of Chl-*a*/Chl-*a*' is similar to the down-shift caused by the H-bond by Thr residue.

7.3.9 Effect of H_2O H-bond and Dielectric Media on the Vibrational Modes of Chl-*a*/Chl-*a*'

The vibrational frequencies of Chl-*a*/Chl-*a*' in the presence of H_2O H-bond was also calculated in CCl_4 and THF to simulate the dielectric properties of PS I protein. The nearest hydrogen atom of water molecule for the geometry optimized structure is at a distance of ~1.90Å (CCl_4) and ~1.89 Å (THF) from the oxygen atom of 13^1 keto C=O group of both Chl-*a* and Chl-*a*' in the neutral state. For the cation state this distance is ~1.95 Å (CCl_4) and ~1.93Å (THF) for both Chl-a^+ and Chl-a'^+.

The calculated IR spectra for the cation and neutral states of Chl-*a*/Chl-*a*' in CCl_4 and THF along with the corresponding cation minus neutral IR DS are shown in Figures 7.25/7.26 and 7.27/7.28, respectively. The solid lines in Figures 7.25/7.26 and 7.27/7.28 show the calculated spectra in the presence of the H-bond provided by the water molecule in CCl_4 and THF. The calculated IR spectra for Chl-*a*/*a*' in solvents in the absence of the H_2O H-bond (dotted line) are also shown for comparison.

The harmonic vibrational mode frequencies and intensities associated with the C=O modes of H_2O+Chl-*a*/H_2O+*a*', H_2O+Chl-a^+/H_2O+Chl-a'^+, Chl-*a*/*a*' and Chl-a^+/a'^+ in CCl_4 and THF are listed in Tables 7.9 and 7.10.

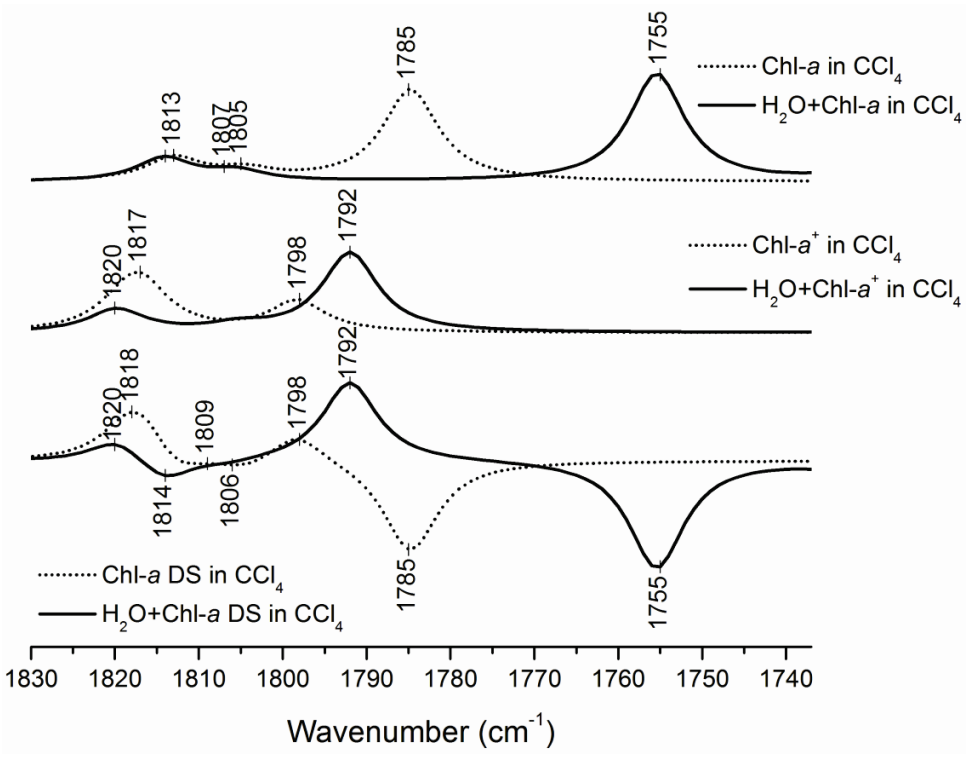

Figure 7.25: Calculated IR Spectra for H_2O+Chl-*a*/Chl-*a* (top) and H_2O+Chl-*a*$^+$/Chl-*a*$^+$ (*middle*) in CCl_4. The "cation minus neutral" IR DS are also shown (*bottom*).

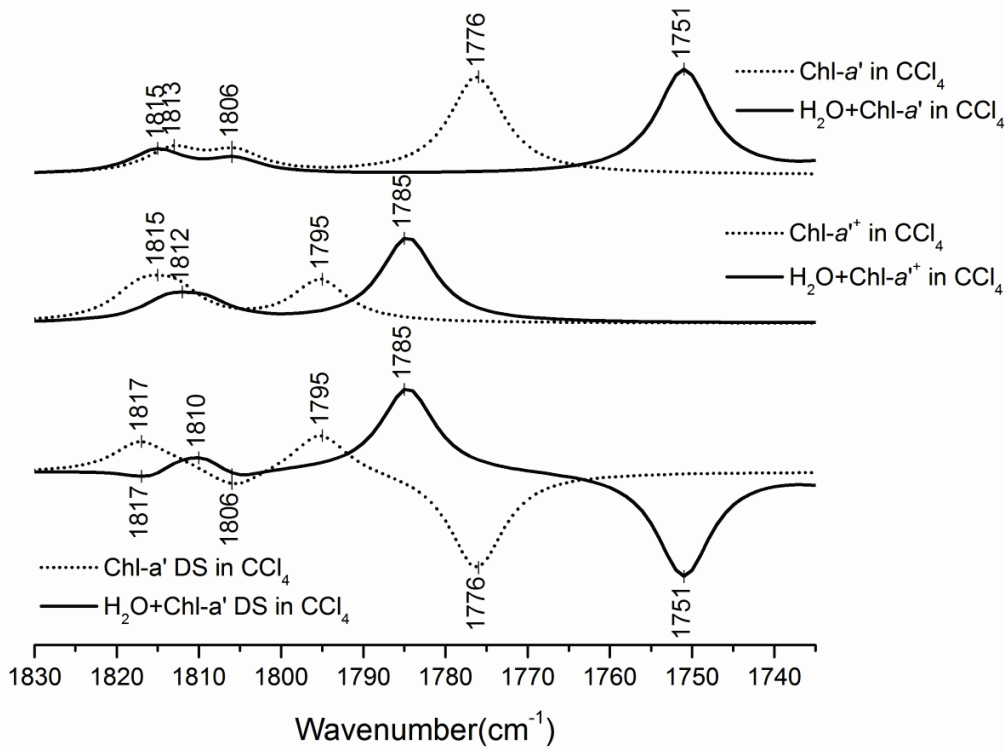

Figure 7.26: Calculated IR Spectra for H_2O+Chl-*a*'/Chl-*a*' (top) and H_2O+Chl-*a*'$^+$/Chl-*a*'$^+$ (*middle*) in CCl_4. The "cation minus neutral" IR DS are also shown (*bottom*).

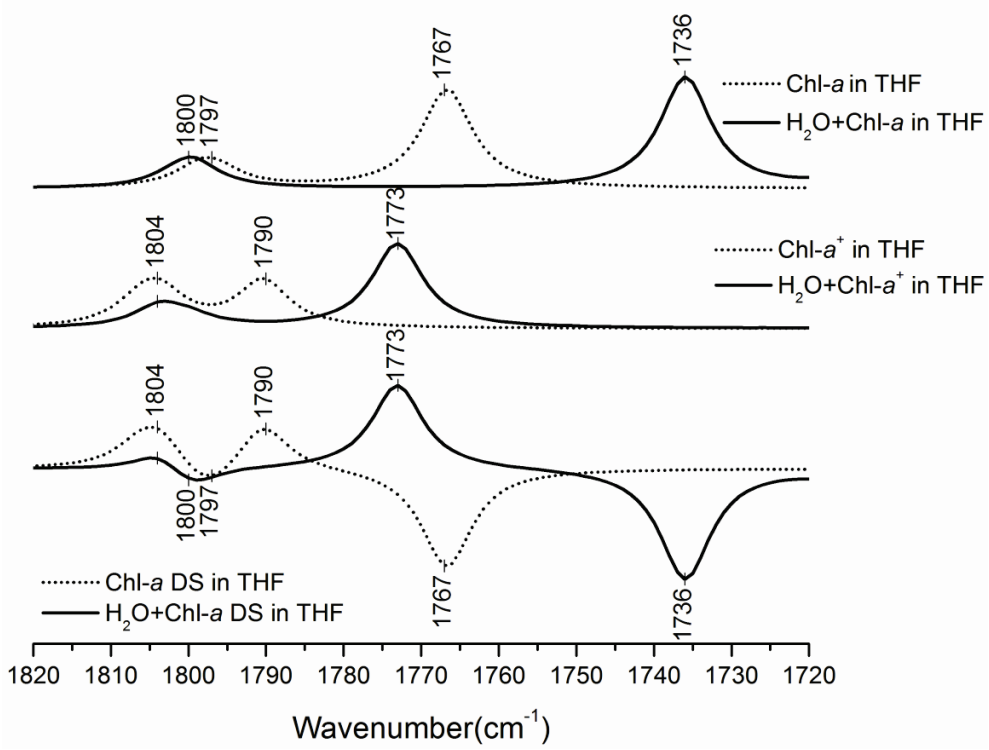

Figure 7.27: Calculated IR Spectra for H_2O+Chl-*a*/Chl-*a* (top) and H_2O+Chl-*a*$^+$/Chl-*a*$^+$ (*middle*) in THF. The "cation minus neutral" IR DS are also shown (*bottom*).

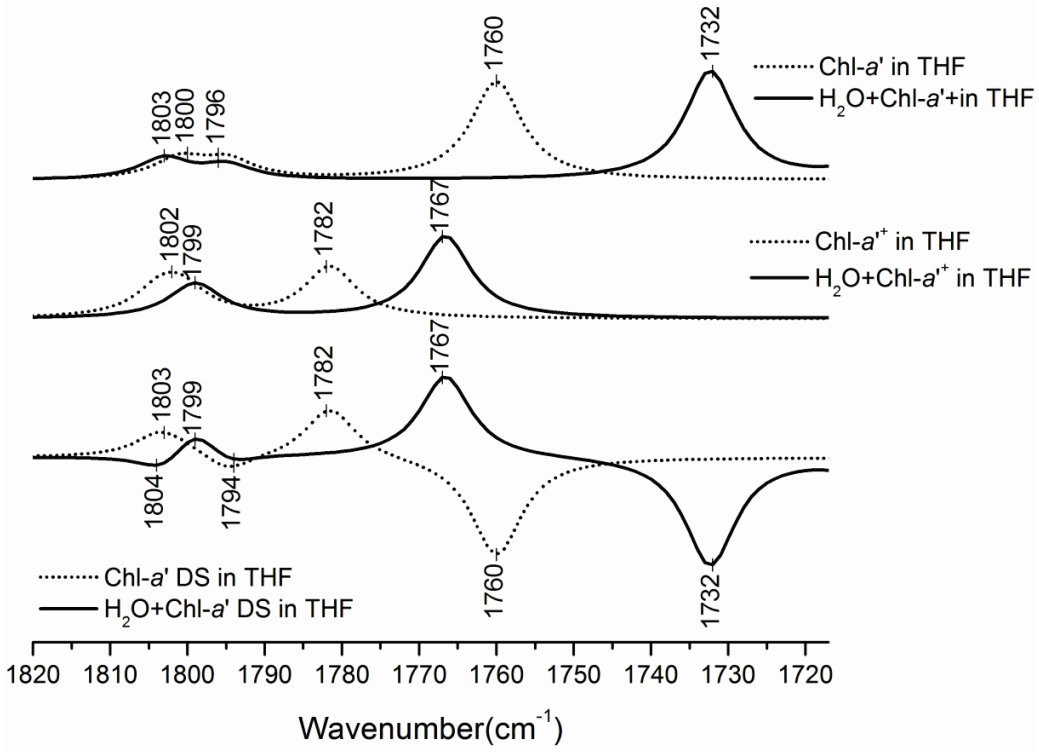

Figure 7.28: Calculated IR Spectra for H_2O+Chl-*a*'/Chl-*a*' (top) and H_2O+Chl-*a*'$^+$/Chl-*a*'$^+$ (*middle*) in THF. The "cation minus neutral" IR DS are also shown (*bottom*).

Table 7.9: Calculated frequencies and intensities (in parenthesis [in km/mole]) for the different carbonyl modes of H_2O+Chl-*a*/*a*', Chl-*a*/*a*', H_2O +Chl-a^+/a'^+ and Chl-a^+/a'^+ in CCl_4.

Mode	Neutral	Shift Δν(ΔI)	Cation	Shift Δν(ΔI)
ν (17^3 C=O)				
H_2O+Chl-*a* in CCl_4	1814(290)	1(1%)	1820(284)	1(31%)
Chl-*a* in CCl_4	1813(287)		1819(217)	
H_2O+Chl-*a*' in CCl_4	1815(253)	2(-0.4%)	1814(216)	1(-31%)
Chl-*a*' in CCl_4	1813(254)		1813(311)	
ν (13^1 and 13^3 C=O) s				
H_2O+Chl-*a* in CCl_4	1806(125)	2(-1%)	1805(81)	-12(-86%)
Chl-*a* in CCl_4	1804(126)		1817(568)	
H_2O+Chl-*a*' in CCl_4	1806(150)	0(-31%)	1809(190)	-8(-41%)
Chl-*a*' in CCl_4	1806(216)		1817(324)	
ν (13^1 and 13^3 C=O) as				
H_2O+Chl-*a* in CCl_4	1755(1341)	-30(17%)	1792(993)	-6(158%)
Chl-*a* in CCl_4	1785(1142)		1798(385)	
H_2O+Chl-*a*' in CCl_4	1751(1118)	-25(7%)	1785(911)	-10(102%)
Chl-*a*' in CCl_4	1776(1047)		1795(451)	

The frequency shift induced by including the H_2O H-bond to Chl-a/Chl-a' for each calculation is shown along with the mode intensity change [in parenthesis (in%)].

Table 7.10: Calculated frequencies and intensities (in parenthesis [in km/mole]) for the different carbonyl modes of H_2O+Chl-*a*/*a*', Chl-*a*/*a*', H_2O+Chl-a^+/a'^+ and Chl-a^+/a'^+ in THF.

Mode	Neutral	Shift Δν(ΔI)	Cation	Shift Δν(ΔI)
ν (17^3 C=O)				
H_2O+Chl-*a* in THF	1802(116)	3(-58%)	1804(342)	0(-34%)
Chl-*a* in THF	1799(276)		1804(520)	
H_2O+Chl-*a*' in THF	1803(334)	2(4%)	1800(252)	-1(-39%)
Chl-*a*' in THF	1801(320)		1801(414)	
ν (13^1 and 13^3 C=O) s				
H_2O+Chl-*a* in THF	1799(425)	3(67%)	1800(155)	-6(-54%)
Chl-*a* in THF	1796(255)		1806(336)	
H_2O+Chl-*a*' in THF	1795(220)	0(-23%)	1798(304)	-6(-19%)
Chl-*a*' in THF	1795(287)		1804(377)	
ν (13^1 and 13^3 C=O) as				
H_2O+Chl-*a* in THF	1736(1836)	-31(12%)	1773(1400)	-17(82%)
Chl-*a* in THF	1767(1637)		1790(771)	
H_2O+Chl-*a*' in THF	1732(1702)	-28(10%)	1767(1290)	-15(61%)
Chl-*a*' in THF	1760(1551)		1782(802)	

The frequency shift induced by including the H_2O H-bond to Chl-*a*/Chl-*a*' for each calculation is shown along with the mode intensity change [in parenthesis (in%)].

The calculated IR spectra of Chl-*a*/Chl-*a*' in solvents in the presence of H_2O H-bond shows that the frequency of the anti-symmetrically coupled mode decreases by 30/25 cm^{-1} for Chl-*a*/Chl-*a*' in CCl_4 while in THF the corresponding decrease in frequency is 31/28 cm^{-1}. The intensity of the anti-symmetrically coupled 13^1 keto and 13^3 ester C=O vibration increases on the

other hand by 17%/7% for Chl-*a*/Chl-*a*' in CCl_4, while in THF the corresponding increase is 12%/10%. For cation states of Chl-*a*/Chl-*a*' in solvents the effect of H-bond interaction to H_2O is similar to the neutral state where the frequency of the vibrations decreases while the intensity increases. The frequency of the anti-symmetrically coupled mode decreases by 6/10 cm^{-1} for Chl-a^+/Chl-a'^+ in CCl_4 while the intensity increases by 158%/102%. In THF, the frequency of the anti-symmetrically coupled modes of Chl-a^+/Chl-a'^+ decreases by 17/15 cm^{-1} while the intensity increases by 82%/61% upon introduction of the H_2O H-bond (Tables 7.9 and 7.10).

The effect of H-bonding interaction to the 13^1 keto C=O group on the frequency symmetrically coupled 13^1 keto and 13^3 ester C=O groups of Chl-*a*/Chl-*a*' is not significant, unlike in the case of the anti-symmetrically coupled modes. The effect of H_2O H-bond on intensities of the vibrational modes on the other hand is significant, and leads to an increase in intensity of the symmetrically coupled 13^1 keto and 13^3 ester C=O group vibrations of Chl-*a*/Chl-*a*'. The frequency of the symmetrically coupled mode decreases by 2-3cm^{-1} for Chl-*a* while the frequency of Chl-*a*' is unaffected in CCl_4 and THF. The intensity of the symmetrically coupled 13^1 keto and 13^3 ester C=O vibration of Chl-*a*/Chl-*a*' decreases by 1/31% in CCl_4. In THF the corresponding decrease in intensity is 67%/23%. In the cation state, the frequency of the symmetrically coupled modes of Chl-a^+/Chl-a'^+ decreases by 12/8 cm^{-1} while the intensity decreases by 86%/41% in CCl_4. In THF the corresponding decrease in frequency and intensity are 6/6cm^{-1} and 54%/19% respectively (Tables 7.9 and 7.10).

The frequency of the 17^3 ester C=O group in CCl_4 and THF is mostly unaffected by the H-bond introduced to 13^1 keto C=O group of Chl-*a*/Chl-*a*'. The intensity of the 17^3 ester C=O group vibration of Chl-*a*/ Chl-*a*' is unaffected in CCl_4 while in THF the intensity of Chl-*a* decreases by 58% and the intensity of Chl-*a*' increases by 4%. For the cation state of Chl-a^+, the

intensity increases by 31% while for Chl-*a*'$^{+}$ the intensity decreases by 31% in CCl_4. In THF the intensity of 17^3 ester C=O group of Chl-*a*$^{+}$/ Chl-*a*'$^{+}$ decrease by 34%/39% (Tables 7.9 and 7.10).

The vibrational frequency calculations of Chl-*a*/Chl-*a*' in solvents in the presence of a water molecule directly H-bonded to 13^1 keto C=O group shows that the 13^1 keto and 13^3 ester C=O modes still show symmetric and anti-symmetric coupled vibrations. The 17^3 ester group vibration of Chl-*a*/Chl-*a*' in CCl_4 is not coupled to the 13^1 keto and 13^3 ester C=O group vibrations in the neutral or cation state. But for the vibrational frequency calculated in THF , especially for the cation states, strong coupling was observed between the 17^3 ester, 13^1 keto and 13^3 ester C=O group vibrations. Also the frequency of both symmetrically and anti-symmetrically coupled C=O group vibrations down-shifted in the presence of the H-bond. The frequency down-shift of symmetrically and anti-symmetrically coupled 13^1 keto and 13^3 ester C=O modes induced by the water molecule H-bonded to 13^1 keto C=O group of Chl-*a*/Chl-*a*' is similar to the down-shift caused by the H-bond by Thr residue.

7.3.10 Calculated Redox Potential of Chl-*a*/Chl-*a*' in the Presence of H_2O H-bond

The ionization potential (IP) of Chl-*a*/Chl-*a*' in the presence of H_2O H-bond was calculated as discussed before. The calculated total energy and the IP's for Chl-*a* and Chl-*a*' are given in Tables 7.14 and 7.15.

The calculated redox potential for Chl-*a*/Chl-*a*' with H_2O or Thr H-bond are almost identical to the calculated value for Chl-*a*/Chl-*a*' in the absence of any H-bond interaction. These results indicate that the H-bonding interaction has little effect in determining the redox potential of chlorophyll pigments.

7.3.11 Effect of Axial Ligand and H-bond Interactions on the Vibrational Modes of Chl-a/a'

The effect of axial ligation and H-bond interactions on the vibrational modes of Chl-*a*/*a*' was further investigated by including the axial ligating histidine residue to the central Mg atom and the hydrogen bonding threonine residue to the 13^1 keto C=O group in the model. The starting geometry for His+Thr+Chl-*a*' were directly obtained from the X-ray crystal structure of PSI [6] by including the axial ligating residue HisA680 and the ThrA743 residue which provides H-bonding interactions to P_A(Chl-*a*'). His+Thr+Chl-*a* initial geometry was obtained by including His B660 residue that provides axial ligand to P_B (Chl-*a*) and by changing TyrB727, which is the homologues residue on *PsaB* protein, to Thr. The histidine residue in both cases was truncated to methyimidazole while the carboxyl and amino end of the threonine residue was truncated using a methyl group. Also the phytyl chain of Chl-*a*/Chl-*a*'is replaced with a methyl group at the 17^4 position.

Figures 7.29 and 7.30 show the geometry optimized structures of His+Thr+Chl-*a*/His+Thr+Chl-*a*' in the neutral and cation states. After geometry optimization the hydroxyl group of the Thr residue is at a distance of 1.94Å from the 13^1 keto C=O oxygen of both His+Thr+Chl-*a*/His+Thr+Chl-*a*' in the neutral state. For the cation state the corresponding distance is 2.03/2.02 Å for His+Thr+Chl-a^+/His+Thr+Chl-a'^+. Also the angle between the 13^1 keto C=O oxygen and the hydroxyl group (O_{chl}-H_{thr}-O_{thr} angle) is ~166/170° for His+Thr+Chl-*a*/His+Thr+Chl-*a*' in the neutral state. In the cation state the corresponding angles are ~160/163°, respectively. After optimization the ligating imidazole nitrogen is ~2.2 Å from the central magnesium atom in the neutral and cation states.

The calculated IR spectra for the cation and neutral states of the models in Figures 7.29 and 7.30, along with the corresponding cation minus neutral IR DS are shown in Figures

7.31/7.32 respectively. The solid lines in Figures 7.31/7.32 show the calculated spectra in the presence of the ligand and H-bond. The calculated IR spectra for Chl-*a*/*a*' model without the ligand and H-bond (dotted line) are also shown for comparison. The harmonic vibrational mode frequencies and intensities associated with the C=O modes of His+Thr+Chl-*a*/His+Thr+Chl-*a*', His+Thr+Chl-a^+/His+Thr+Chl-a'^+, Chl-*a*/*a*' and Chl-a^+/a'^+ are listed in Table 7.11.

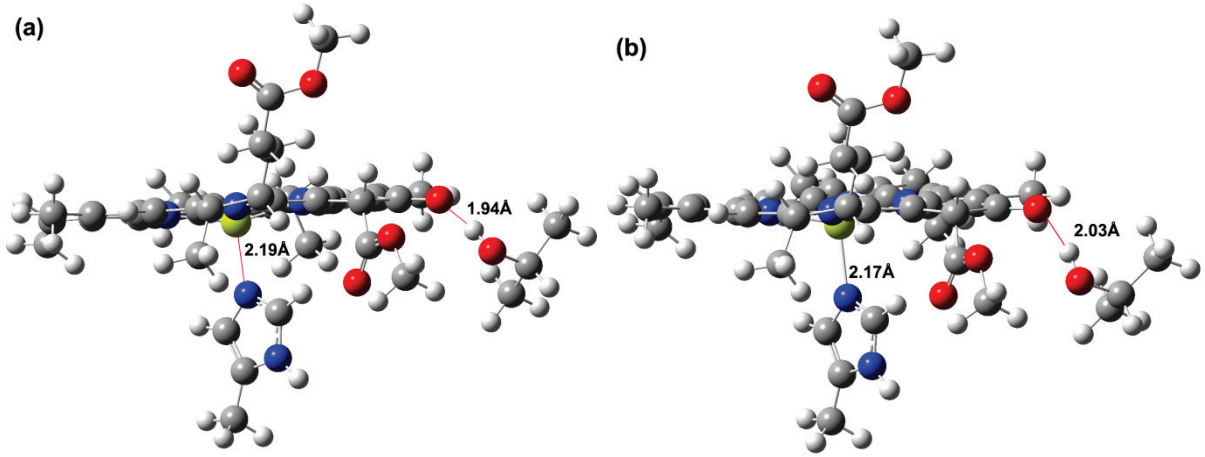

Figure 7.29: Geometry Optimized (energy minimized) molecular structural models of Chl-*a* and Chl-a^+ in the presence of a histidine residue that provides an axial ligand and a threonine residue that provides H-bond to 13^1 keto C=O group (a) neutral and (b) cation states.

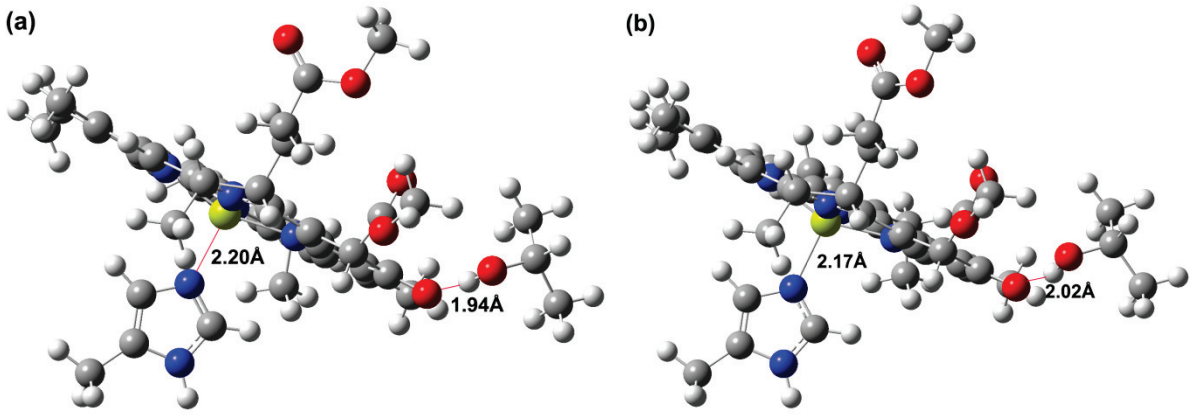

Figure 7.30: Geometry Optimized (energy minimized) molecular structural models of Chl-*a*' and Chl-a'^+ in the presence of a histidine residue that provides an axial ligand and a threonine residue that provides H-bond to 13^1 keto C=O group (a) neutral and (b) cation states.

Table 7.11: Calculated frequencies and intensities (in parenthesis [in km/mole]) for the different carbonyl modes of His+Thr+Chl-*a*/His+Thr+Chl-*a*', Chl-*a*/*a*', His+Thr+Chl-a^+/His+Thr+Chl-a'$^+$and Chl-a^+/a'$^+$.

Mode	Neutral	Shift Δν(ΔI)	Cation	Shift Δν(ΔI)
ν (17^3 C=O)				
His+Thr+Chl-*a*	1828(251)	-1(7%)	1836(241)	0(13%)
Chl-*a*	1829(235)		1836(213)	
His+Thr+Chl-*a*'	1827(203)	-1(5%)	1826(156)	0(-31%)
Chl-*a*'	1828(194)		1826(226)	
ν (13^1 and 13^3 C=O) s				
His+Thr+Chl-*a*	1792(131)	-20(2%)	1797(278)	-33(-30%)
Chl-*a*	1812(129)		1830(397)	
His+Thr+Chl-*a*'	1814(165)	-3(-11%)	1818(213)	-13(-15%)
Chl-a'_{82}	1817(186)		1831(250)	
ν (13^1 and 13^3 C=O) as				
His+Thr+Chl-*a*	1748(1368)	-53(90%)	1785(709)	-20(230%)
Chl-*a*	1801(719)		1805(215)	
His+Thr+Chl-*a*'	1748(1200)	-46(84%)	1787(621)	-20(133%)
Chl-*a*'	1794(652)		1807(267)	

The frequency shift induced by including the ligand and Thr H-bond to Chl-*a*/Chl-*a*' for each calculation is shown along with the mode intensity change [in parenthesis (in%)].

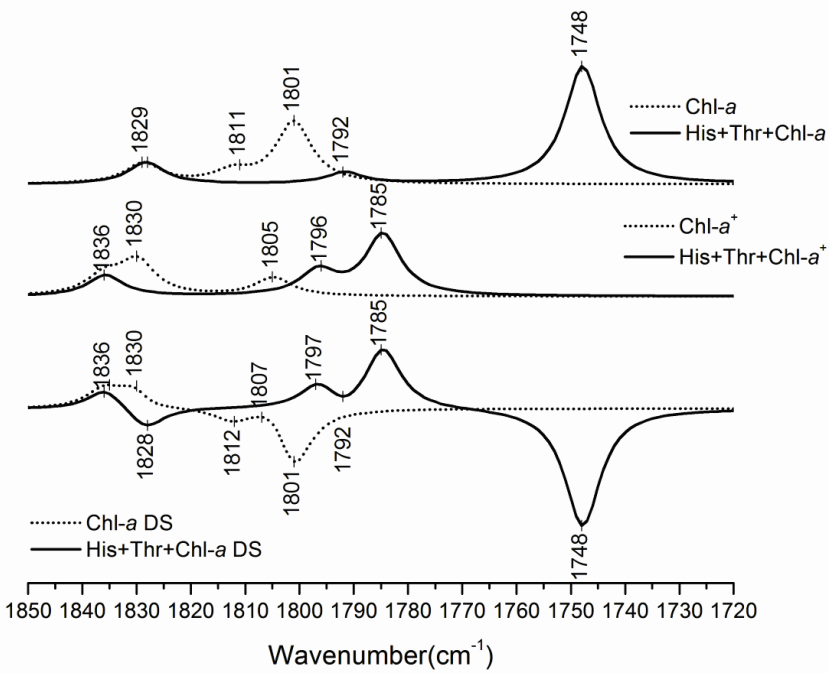

Figure 7.31: Calculated IR Spectra for His+Thr+Chl-*a*/Chl-*a* (top) and His+Thr+Chl-a^+/Chl-a^+ (*middle*) in the gas phase. The "cation minus neutral" IR DS are also shown (*bottom*).

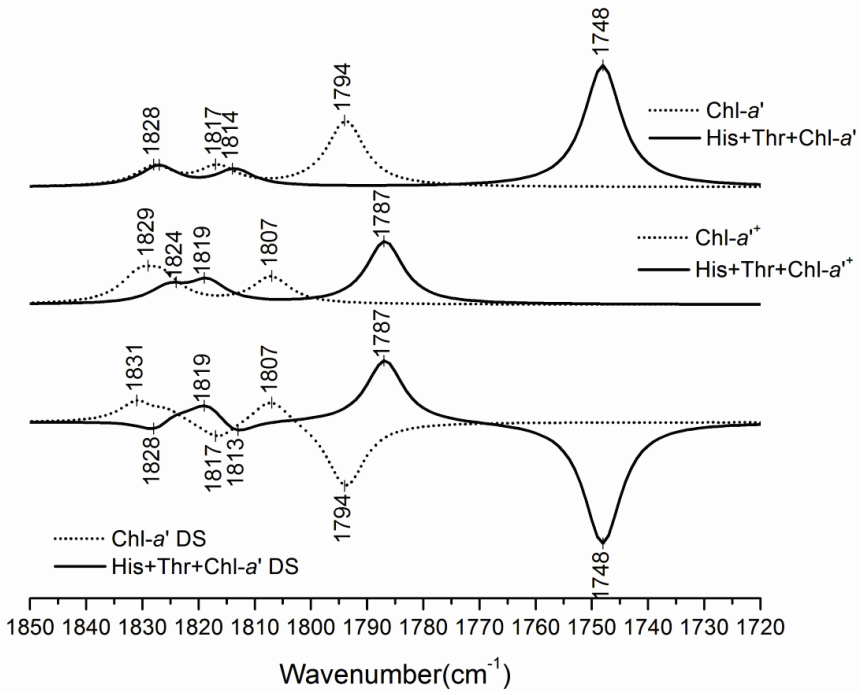

Figure 7.32: Calculated IR Spectra for His+Thr+Chl-*a'*/Chl-*a'* (top) and His+Thr+Chl-*a'*$^{+}$/Chl-*a'*$^{+}$ (*middle*) in the gas phase. The "cation minus neutral" IR DS are also shown (*bottom*).

The calculated IR spectra in the presence of ligand and H-bond shows that the frequency of the anti-symmetrically coupled 13^1 keto and 13^3 ester C=O vibration of Chl-*a*/Chl-*a*' in the neutral and cation state is significantly impacted. The frequency of the anti-symmetrically coupled 13^1 keto and 13^3 ester C=O vibration of Chl-*a*/Chl-*a*' decrease by 53/46cm^{-1} while the intensity increases by 90%/84% in the neutral state. In the cation state the frequency decreases by 20 cm^{-1} for both Chl-*a*$^{+}$ and Chl-*a*'$^{+}$ while in the intensity increases by 230%/133% respectively (Table 7.11).

The frequency and intensity of the symmetrically coupled 13^1 keto 13^3 ester C=O mode of Chl-*a*/Chl-*a*' is not significantly impacted by the presence of the ligand or H-bond. The frequency of the symmetrically coupled 13^1 keto 13^3 ester C=O mode vibration of Chl-*a*/Chl-*a*' decrease by 20/3cm^{-1} while the intensity increases/decreases by 2%/11% in the neutral state. In the cation state the frequency decreases by 33/13 cm^{-1} for Chl-*a*$^{+}$/Chl-*a*'$^{+}$ while in the intensity decreases by 30%/15% respectively (Table 7.11).

The frequency of the 17^3 ester C=O group is unaffected by the presence of the ligand and H-bond while the intensities slightly increases, an exception being the Chl-*a*'$^+$ state where the intensity of the vibration decreases by 31% compared to the model where the ligand and H-bond are absent (Figure 7.11).

The vibrational frequency calculations of Chl-*a*/Chl-*a*' in the presence of axial ligand and H-bond shows that the 13^1 keto and 13^3 ester C=O modes still show symmetric and anti-symmetric coupled vibrations. The 17^3 ester group vibration of Chl-*a*/Chl-*a*' is not coupled to the 13^1 keto and 13^3 ester C=O group vibrations in the neutral or cation state. Axial ligand and H-bond causes the frequency of both symmetrically and anti-symmetrically coupled C=O group vibrations down-shift significantly. Again the downshift in frequency observed for the anti-symmetrically couple mode is significantly higher compared downshift observed for the symmetrically coupled vibration of the 13^1 keto and 13^3 ester C=O group.

7.3.12 Effect of Axial Ligand, H-bond and Dielectric Media on Vibrational Modes of Chl-*a*/Chl-*a*'

The vibrational frequencies of Chl-*a*/Chl-*a*' in the presence of ligand and H-bond was also calculated in CCl_4 and THF to simulate the dielectric properties of PS I protein. After geometry optimization the hydroxyl group of the Thr residue is at a distance of 1.92/1.91Å from the 13^1 keto C=O oxygen of Chl-*a*' in CCl_4/THF in the neutral state. In the cation state the corresponding distance is 1.99/1.96Å, respectively. For Chl-*a* in CCl_4/THF the corresponding distances are 1.92/1.93Å in the neutral state and 2.01/1.99Å in the cation state. The angle between the 13^1 keto C=O oxygen and the hydroxyl group (O_{chl}-H_{thr}-O_{thr} angle) is ~167˚ in both CCl_4 and THF for Chl-*a* in the neutral state, while for Chl-*a*' the corresponding angle is ~170˚/171˚ in CCl_4 /THF. In the cation state the angle between the 13^1 keto C=O oxygen and the

hydroxyl group is ~163˚/168˚ for Chl-*a* and ~167˚/171˚ for Chl-*a*'. After optimization the ligating imidazole nitrogen is ~2.2 Å from the central magnesium atom in the neutral and cation states in both solvents.

The calculated IR spectra for the cation and neutral states of the models in CCl_4 and THF, along with the corresponding cation minus neutral IR DS are shown in Figures 7.33/7.34 and 7.35/7.36, respectively. The solid lines in Figures 7.33/7.34 and 7.35/7.36 show the calculated spectra in the presence of the ligand and H-bond. The calculated IR spectra for Chl-*a*/*a*' model without the ligand and H-bond (dotted line) are also shown for comparison. The harmonic vibrational mode frequencies and intensities associated with the C=O modes of His+Thr+Chl-*a*/His+Thr+Chl-*a*', His+Thr+Chl-a^+/His+Thr+Chl-a'^+, Chl-*a*/*a*' and Chl-a^+/a'^+ are listed in Tables 7.12 and 7.13.

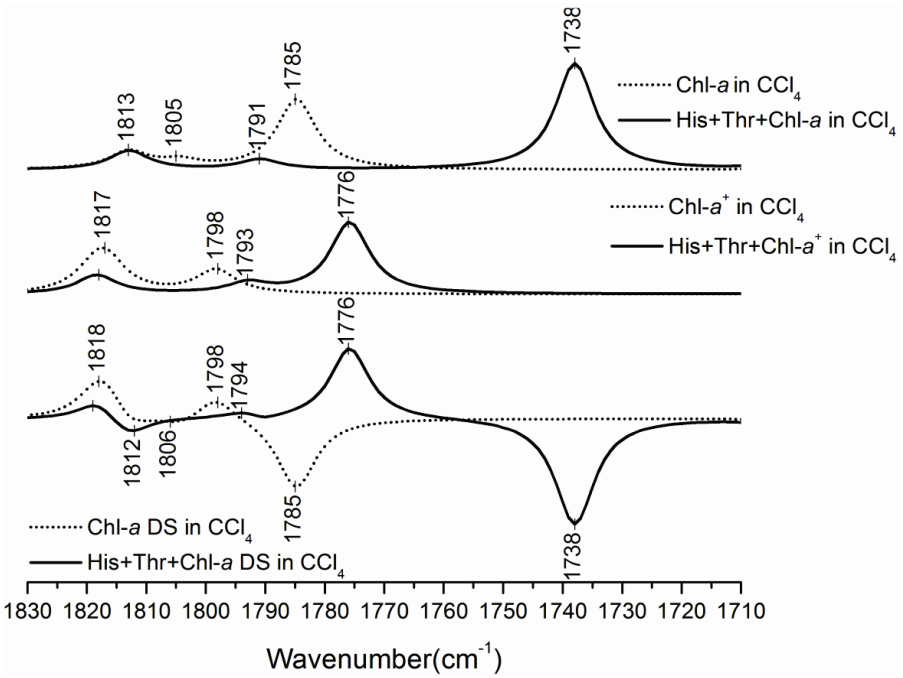

Figure 7.33: Calculated IR Spectra for His+Thr+Chl-*a*/Chl-*a* (top) and His+Thr+Chl-a^+/Chl-a^+ (*middle*) in CCl_4. The "cation minus neutral" IR DS are also shown (*bottom*).

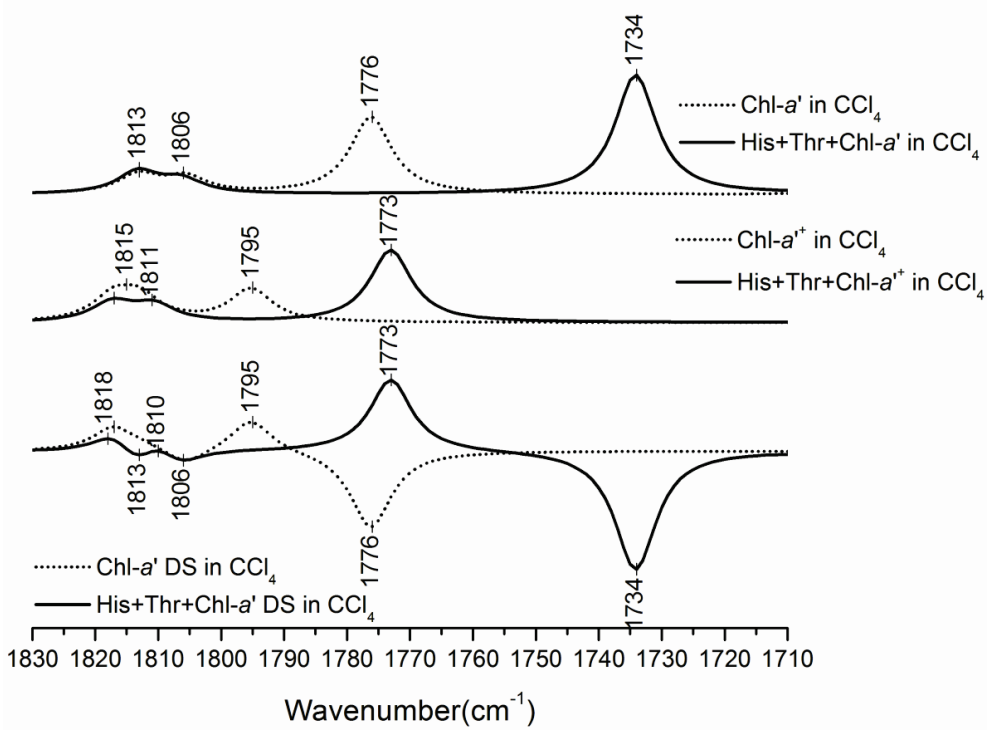

Figure 7.34: Calculated IR Spectra for His+Thr+Chl-*a'*/Chl-*a'* (top) and His+Thr+Chl-*a'*$^{+}$/Chl-*a'*$^{+}$ (*middle*) in CCl_4. The "cation minus neutral" IR DS are also shown (*bottom*).

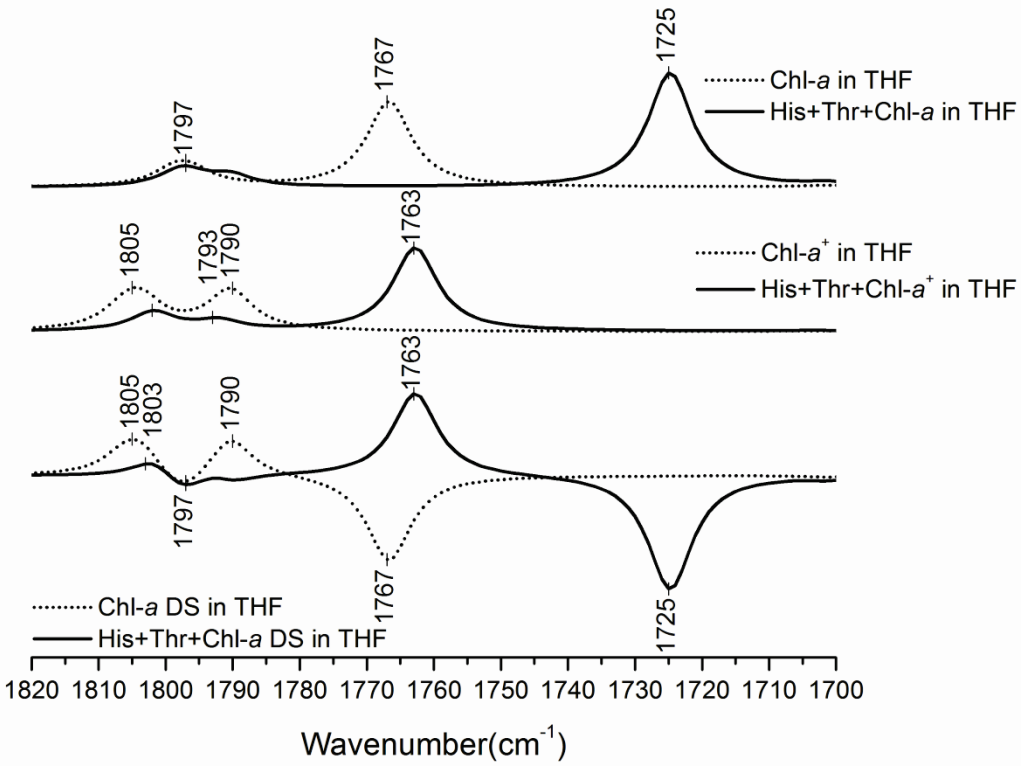

Figure 7.35: Calculated IR Spectra for His+Thr+Chl-*a*/Chl-*a* (top) and His+Thr+Chl-*a*$^{+}$/Chl-*a*$^{+}$ (*middle*) in THF. The "cation minus neutral" IR DS are also shown (*bottom*).

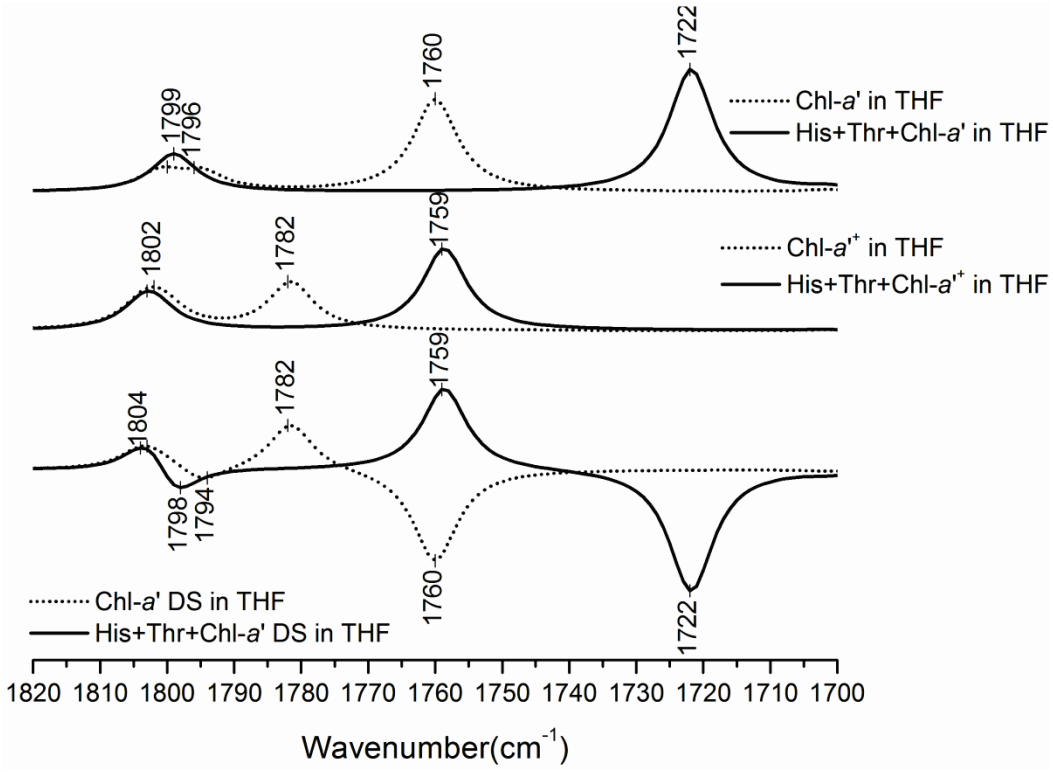

Figure 7.36: Calculated IR Spectra for His+Thr+Chl-*a'*/Chl-*a'* (top) and His+Thr+Chl-*a'*$^{+}$/Chl-*a'*$^{+}$ (*middle*) in THF. The "cation minus neutral" IR DS are also shown (*bottom*).

The calculated IR spectra in solvents in the presence of ligand and H-bond shows that the frequency and intensity of the anti-symmetrically coupled 13^1 keto and 13^3 ester C=O vibration of Chl-*a*/Chl-*a*' is significantly impacted in both neutral and cation state. The frequency of the anti-symmetrically coupled 13^1 keto and 13^3 ester C=O vibration of Chl-*a*/Chl-*a*' decrease by 47/42cm^{-1} while the intensity increases by 52%/54% in CCl_4 in the neutral state. In THF, the frequency of the anti-symmetrically coupled 13^1 keto and 13^3 ester C=O vibration of Chl-*a*/Chl-*a*' decrease by 42/38cm^{-1} while the intensity increases by 34%/32% in the neutral state. In the cation state the frequency decreases by 22 cm^{-1} for both Chl-*a*$^{+}$ and Chl-*a*'$^{+}$ while the intensity increases by 202% and 117% respectively in CCl_4. In THF, for the cation state the frequency of the anti-symmetrically coupled 13^1 keto and 13^3 ester C=O vibration of Chl-*a*/Chl-*a*' decrease by 27/23cm^{-1} while the intensity increases by 106%/71% (Tables 7.12 and 7.13).

Table 7.12: Calculated frequencies and intensities (in parenthesis [in km/mole]) for the different carbonyl modes of His+Thr+Chl-*a*/His+Thr+Chl-*a*', Chl-*a*/*a*', His+Thr+Chl-*a*$^+$/His+Thr+Chl-*a*'$^+$ and Chl-*a*$^+$/*a*'$^+$ in CCl_4.

Mode	Neutral	Shift Δν(ΔI)	Cation	Shift Δν(ΔI)
ν (17^3 C=O)				
His+Thr+Chl-*a* in CCl_4	1813(307)	0(7%)	1818(303)	-1(40%)
Chl-*a* in CCl_4	1813(287)		1819(217)	
His+Thr+Chl-*a*' in CCl_4	1813(304)	0(20%)	1817(263)	4(-15%)
Chl-*a*' in CCl_4	1813(254)		1813(311)	
ν (13^1 and 13^3 C=O) s				
His+Thr+Chl-*a* in CCl_4	1791(160)	-13(27%)	1793(166)	-24(-71%)
Chl-*a* in CCl_4	1804(126)		1817(568)	
His+Thr+Chl-*a*' in CCl_4	1806(186)	0(-14%)	1811(222)	-6(-31%)
Chl-*a*' in CCl_4	1806(216)		1817(324)	
ν (13^1 and 13^3 C=O) as				
His+Thr+Chl-*a* in CCl_4	1738(1733)	-47(52%)	1776(1163)	-22(202%)
Chl-*a* in CCl_4	1785(1142)		1798(385)	
His+Thr+Chl-*a*' in CCl_4	1734(1615)	-42(54%)	1773(980)	-22(117%)
Chl-*a*' in CCl_4	1776(1047)		1795(451)	

The frequency shift induced by including the ligand and Thr H-bond to Chl-*a*/Chl-*a*' for each calculation is shown along with the mode intensity change [in parenthesis (in%)].

The frequency and intensity of the symmetrically coupled 13^1 keto 13^3 ester C=O mode of Chl-*a*/Chl-*a*' in solvents is not significantly impacted by the presence of the ligand or H-bond. In CCl_4, the frequency of the symmetrically coupled 13^1 keto 13^3 ester C=O mode vibration of Chl-*a*/ Chl-*a*$^+$ decrease by 13/24cm^{-1} while the intensity increases/decreases by 27%/71%. In THF, the frequency of the symmetrically coupled 13^1 keto 13^3 ester C=O mode vibration of Chl-*a*/ Chl-*a*$^+$ decrease by 6/14cm^{-1} while the intensity decreases by 17%/45%. For Chl-*a*', in CCl_4, the frequency of symmetrically coupled 13^1 keto 13^3 ester C=O mode is unaffected while the intensity decreases by 14%. For Chl-*a*'$^+$, in CCl_4, the frequency of the symmetrically coupled mode decreases by 6 cm^{-1} accompanied by a decrease in intensity of 31%. In THF, the frequency of the symmetrically coupled 13^1 keto 13^3 ester C=O mode vibration of Chl-*a*'/ Chl-*a*'$^+$ increases/decrease by 3/2cm^{-1} while the intensity decreases by 21%/24% (Tables 7.12 and 7.13).

The frequency of the 17^3 ester C=O group in solvents is unaffected by the presence of the ligand and H-bond while the intensities are modified. In CCl_4 and THF the intensity of the 17^3

ester C=O group of Chl-*a*/ Chl-*a*' increases by 7%/20% and 30%/29% respectively. In the cation state, in CCl_4 the intensity of Chl-a^+ increases by 40% while the intensity of Chl-*a*'$^+$ decreases by 15%. In THF, the intensity of 17^3 ester C=O group mode of Chl-*a*$^+$/ Chl-*a*$^+$' decreases by 31%/5% (Tables 7.12 and 7.13).

Table 7.13: Calculated frequencies and intensities (in parenthesis [in km/mole]) for the different carbonyl modes of His+Thr+Chl-*a*/His+Thr+Chl-*a*', Chl-*a*/*a*', His+Thr+Chl-*a*$^+$/His+Thr+Chl-*a*'$^+$ and Chl-*a*$^+$/*a*'$^+$ in THF.

Mode	Neutral	Shift Δν(ΔI)	Cation	Shift Δν(ΔI)
ν (17^3 C=O)				
His+Thr+Chl-*a* in THF	1797(359)	-2(30%)	1802(360)	-2(-31%)
Chl-*a* in THF	1799(276)		1804(520)	
His+Thr+Chl-*a*' in THF	1799(414)	-2(29%)	1803(392)	2(-5%)
Chl-*a*' in THF	1801(320)		1801(414)	
ν (13^1 and 13^3 C=O) s				
His+Thr+Chl-*a* in THF	1790(212)	-6(-17%)	1792(184)	-14(-45%)
Chl-a_{82} in THF	1796(255)		1806(336)	
His+Thr+Chl-*a*' in THF	1798(227)	3(-21%)	1802(286)	-2(-24%)
Chl-*a*' in THF	1795(287)		1804(377)	
ν (13^1 and 13^3 C=O) as				
His+Thr+Chl-*a* in THF	1725(2189)	-42(34%)	1763(1589)	-27(106%)
Chl-*a* in THF	1767(1637)		1790(771)	
His+Thr+Chl-*a*' in THF	1722(2046)	-38(32%)	1759(1370)	-23(71%)
Chl-*a*' in THF	1760(1551)		1782(802)	

The frequency shift induced by including the ligand and Thr H-bond to Chl-*a*/Chl-*a*' for each calculation is shown along with the mode intensity change [in parenthesis (in%)].

The vibrational frequency calculations of Chl-*a*/Chl-*a*' in solvents in the presence of axial ligand and H-bond shows that the 13^1 keto and 13^3 ester C=O modes show symmetric and anti-symmetric coupled vibrations. The 17^3 ester group vibration of Chl-*a*/Chl-*a*' is not coupled to the 13^1 keto and 13^3 ester C=O group vibrations in the neutral or cation state. Axial ligand and H-bond causes the frequency of both symmetrically and anti-symmetrically coupled C=O group vibrations down-shift significantly.

7.4 Discussion

7.4.1 Effect of Ligand and H-bond on the Vibrational Properties of Chl-*a*/Chl-*a*'

FTIR spectroscopy is a sensitive molecular specific probe and is extensively used to study the electronic and structural properties of P_{700}, the primary electron donor in PS I. (P_{700}^+-

P_{700}) FTIR DS have been obtained under many sets of conditions: from PS I particles from different strains, to particles with site directed mutations near the P_{700} and A_0 Chl's (See Chapters 2, 3 and 4), to specifically isotope labeled PS I particles. The C=O groups of the chlorophylls of P_{700} gives intense bands in the IR region and controversy persists concerning the assignment of these bands in (P_{700}^{+}-P_{700}) FTIR DS [79].The bands in the (P_{700}^{+}-P_{700}) FTIR DS are assigned by comparing with electrochemically generated (Chl-*a*$^{+}$-Chl-*a*) and (pyroChl-*a*$^{+}$-pyroChl-*a*) FTIR DS (PyroChl-*a* is similar to Chl-*a* but lacks a 13^3 ester group). Hence obtaining a precise understanding of vibrational properties of Chl-*a* and Chl-*a*$^{+}$ is the first step in understanding the (P_{700}^{+}-P_{700}) FTIR DS. Density functional theory based vibrational frequency calculations of several Chl-*a*/Chl-*a*' model structures in gas phase and solvents have been successfully undertaken before [79, 80] (See Chapter 5). The calculated (Chl-*a*$^{+}$-Chl-*a*) IR DS in solvents bear a remarkable similarity to the electrochemically generated (Chl-*a*$^{+}$-Chl-*a*) experimental spectra [79] (Chapter 5).Here the vibrational properties of the chlorophyll components of P_{700} were calculated in the presence of the amino acid residues that provide central ligand to the Mg^{2+} and H-bond to the C=O groups. The dielectric effect of the protein environment was simulated in these calculations using Polarizable Continuum Model. Thus the effect these peripheral groups have on the vibrational properties of Chl-*a* and Chl-*a*' have been identified.

The Chl-*a*/Chl-*a*' structural models including the peripheral amino acid residues were fully geometry optimized before calculating the vibrational frequencies. The starting chlorophyll geometries for the calculation were obtained from the crystal structure of P_{700} along with the histidine residue that provides the central ligand. To simulate the effect of H-bond to Chl-*a*' the ThrA743 residue that provides H-bonding network to P_A chlorophyll of P_{700} was included in the

structural model. As the 13^1 keto C=O group of P_B chlorophyll of P_{700} is free from any such interactions, the effect of H-bond on Chl-*a* was investigated by changing the TyrB718 residue to a threonine residue. The energy minimized structures are not significantly different from the crystal structure an exception being the Chl-*a* model with the ligand. The orientation of the imidazole ring relative to the chlorin plane is notably different in the geometry optimized structure, as the ring is rotated ~45° compared to the cryst al structure. This significant change in geometry upon energy minimization indicates that the steric hindrance on the histidine is important in holding the ligand in place in the protein.

The vibrational frequency of Chl-*a*/Chl-*a*' was calculated in the presence of histidine ligand to the central magnesium in the gas phase as well as in solvents with dielectric constants 2.228(CCl_4) and 7.58 (THF). The calculated frequencies were compared to the model without the fifth ligand to the Mg. The calculated results, in gas phase and solvents, shows that the central Mg ligand has little effect on the vibrational frequency modes of the C=O groups of chlorophyll. The effect of the Mg ligand on the vibration frequency modes of Chl-*a*/Chl-*a*' was further investigated by adding a water molecule as ligand (data not shown). The calculated DS of Chl-*a*/Chl-*a*' in the presence of water ligand was almost identical to the calculated DS in the presence of the imidazole ligand which confirm the conclusion that the effect of the ligand on the vibrational frequencies of chlorophyll molecules is none or insignificant.

H-bonding introduced to the 13^1 keto C=O groups of Chl-*a*/Chl-*a*' causes significant down-shift in frequency of vibration of the C=O group. Previously it has been shown that the13^1 keto and 13^3 ester C=O groups of Chl-*a*/Chl-*a*' are coupled pairs that display symmetric and anti-symmetric vibrations. H-bonding interaction to 13^1 keto C=O group causes these symmetrically and anti-symmetrically coupled modes to down-shift. The presence of a threonine

reside in the vicinity of 13^1 keto C=O group leads to a down-shift of ~25-34 $cm^{-1}$for the anti-symmetrically coupled 13^1 keto and 13^3 ester C=O mode of Chl-*a*/Chl-*a*' in the neutral state while in the cation state the effect of H-bonding seems to be weakened, causing a down-shift of ~4-15 cm^{-1}. The calculated vibrational frequencies in the presence of a water molecule H-bonded to the 13^1 keto C=O group of Chl-*a*/Chl-*a*' illustrate a ~25-31 cm^{-1} down-shift of the anti-symmetrically coupled 13^1 keto and 13^3 ester C=O mode in the neutral state and a ~6-17 cm^{-1} down-shift in the cation state. For the symmetrically coupled 13^1 keto and 13^3 ester C=O mode, the frequency down-shift introduced by the H-bond are negligible. The calculations indicate that the effect of H-bond introduced by threonine residue and the water molecule are very similar.

Vibrational frequency was also calculated for Chl-*a*/Chl-*a*' models by including both ligating histidine reside and the threonine residue H-bonded to the 13^1 keto C=O group in the gas phase and in solvents. The presence of histidine ligand and threonine residue in the vicinity of 13^1 keto C=O group leads to a down-shift of ~38-53cm^{-1} for the anti-symmetrically coupled 13^1 keto and 13^3 ester C=O mode of Chl-*a*/Chl-*a*' in the neutral state while in the cation state the down-shift is ~20-27 cm^{-1}. For the symmetrically coupled 13^1 keto and 13^3 ester C=O mode, the frequency down-shift introduced by the H-bond in the presence of the histidine ligand is negligible.

The calculated vibrational frequency down-shifts caused by introducing a H-bond to the 13^1 keto C=O group of Chl-*a*/Chl-*a*' are slightly lower than the experimentally observed shifts in (P_{700}^+-P_{700}) FTIR DS of PS I protein complex where a down-shift of ~60 cm^{-1} is predicted for the 13^1 C=O group of P_A which is involved in a H-bonding network involving ThrA743 residue. This is clearly an indication that the unusually low vibrational absorption of the 13^1 C=O group of P_A mode cannot be explained using the effect of H-bonding interaction introduced by the

ThrA743 residue only. Additional calculations involving all the amino acid residues in the vicinity of 13^1 keto C=O group of P_A might be helpful in further investigating this matter.

7.4.2 Effect of Ligand and H-bond on the Redox Potential of Chl-*a*/Chl-*a*'

The Ionization Potential (IP) for Chl-*a*/Chl-*a*' models were calculated from the difference in the electronic energy between the neutral and cation states as described by Hasegawa et. al. [137].The redox potential (E_{ox}) can be calculated from the IP by subtracting the absolute potential of Standard Hydrogen Electrode (SHE) which has been estimated to be 4.43 eV [137]. The calculated total energies, ionization potential and oxidation energies for Chl-*a*/Chl-*a*' models are listed in Tables 7.14 and 7.15.

The calculated redox potential values for Chl-*a* and Chl-*a*' are almost identical for all the models considered here including the calculations in solvents. This is expected as Chl-*a*' is a structural isomer of Chl-*a*, and the only difference in the structure being the orientation of the 13^2 group.

The calculated E_{ox} values for Chl-*a*/Chl-*a*' models in the presence of the ligand is ~380-400mV lower compared to the models without the ligand. Table 7.14 shows that the calculated E_{ox} values for Chl-*a*/Chl-*a*' in the presence of ligand are 1168/1161mV (gas phase), 636/621mV (CCl_4) and 345/333mV (THF). The calculated values in solvents are significantly lower than the experimentally observed value for Chl-*a*. This decrease in redox potential can be attributed to the strong axial ligand to the Mg provided by the polar histidine aminoacid group. A suggestion could be that the unpaired electron of the histidine ligand stabilizes the charge on Chl-a^+/a'^+ thereby lowering the redox potential. The effect of the ligands on the redox potential of chlorophylls and bacteriochlorophylls has been extensively investigated by Heimdal et

al.[83]and it was shown that the axial ligands decrease the redox potential. The calculated redox potential values for Chl-*a* are in agreement with the results of Heimdal et al.

For the best of our knowledge this is the first study where the effect of H-bond on the redox potential has been investigated. The calculated E_{ox} values for Chl-*a*/Chl-*a*' models in the presence of the H-bond to the 13^1 keto C=O group shows that the redox potential is essentially independent of the nature of interactions to the C=O groups of the chlorophyll molecule. This is a very valid result as it was though that the H-bonding to the P_A chlorophyll was a factor in determining the redox potential of P_{700}.

Table 7.14: Calculated total energies, ionization potential and oxidation energies for Chl-*a*

	E_{elec}(Hartrees)		E_{elec}(eV)		IP(eV)	E_{ox}^{cal}(V)=IP-4.43
	Chl *a*	Chl a^+	Chl *a*	Chl a^+		
Chl-*a*	-2188.908	-2188.689	-59563.26	-59557.28	5.982	1.552
Ligand + Chl-*a*	-2454.480	-2454.274	-66789.84	-66784.24	5.598	1.168
Thr + Chl-*a*	-2383.277	-2383.053	-64852.29	-64846.21	6.079	1.649
His+ Thr + Chl-*a*	-2648.849	-2648.640	-72078.89	-72073.20	5.695	1.265
H_2O + Chl-*a*	-2265.332	-2265.111	-61642.85	-61636.83	6.026	1.596
Chl-*a* in CCl_4	-2188.921	-2188.724	-59563.61	-59558.26	5.353	0.9228
Ligand + Chl-*a* in CCl_4	-2454.492	-2454.306	-66790.16	-66785.10	5.066	0.6361
Thr+Chl-*a* in CCl_4	-2383.290	-2383.090	-64852.64	-64847.22	5.418	0.9879
His+ Thr + Chl-*a* in CCl_4	-2648.860	-2648.672	-72079.20	-72074.06	5.140	0.7104
H_2O + Chl-*a* in CCl_4	-2265.347	-2265.148	-61643.26	-61637.86	5.401	0.9712
Chl-*a* in THF	-2188.935	-2188.753	-59563.98	-59559.02	4.958	0.5282
Ligand + Chl-*a* in THF	-2454.504	-2454.329	-66790.50	-66785.72	4.775	0.3450
Thr+ Chl-*a* in THF	-2383.303	-2383.120	-64853.02	-64848.03	4.992	0.5623
His+ Thr+ Chl-*a* in THF	-2188.908	-2188.689	-59563.26	-59557.28	5.982	1.552
H_2O +Chl-*a* in THF	-2454.480	-2454.274	-66789.84	-66784.24	5.598	1.168

Table 7.15: Calculated total energies, ionization potential and oxidation energies for Chl-a'

	E_{elec}(Hartrees)		E_{elec}(eV)		IP(eV)	E_{ox}^{cal}(V)=IP-4.43
	Chl *a*	Chl a^+	Chl *a*	Chl a^+		
Chl-*a*'	-2188.908	-2188.687	-59563.24	-59557.24	5.995	1.565
Ligand + Chl-*a*'	-2454.474	-2454.269	-66789.67	-66784.08	5.591	1.161
Thr + Chl-*a*'	-2383.276	-2383.052	-64852.27	-64846.19	6.081	1.651
His + Thr + Chl-*a*'	-2648.843	-2648.633	-72078.72	-72073.02	5.701	1.271
H_2O +Chl-*a*'	-2265.331	-2265.109	-61642.84	-61636.79	6.046	1.616
Chl-*a*' in CCl_4	-2188.921	-2188.725	-59563.61	-59558.26	5.358	0.9280
Ligand + Chl-*a*' in CCl_4	-2454.489	-2454.303	-66790.07	-66785.02	5.051	0.6205
Thr + Chl-*a*' in CCl_4	-2383.289	-2383.088	-64852.64	-64847.16	5.475	1.045
His+Thr+Chl-*a*' in CCl_4	-2648.856	-2648.667	-72079.08	-72073.94	5.143	0.7126
H_2O +Chl-*a*' in CCl_4	-2265.347	-2265.149	-61643.27	-61637.86	5.406	0.9764
Chl-*a*' in THF	-2188.936	-2188.754	-59564.01	-59559.06	4.953	0.5226
His + Chl-*a*' in THF	-2454.504	-2454.329	-66790.49	-66785.73	4.763	0.3327
Thr+Chl-*a*' in THF	-2383.301	-2383.121	-64852.94	-64848.05	4.897	0.4674
His+Thr+Chl-*a*' in THF	-2648.871	-2648.693	-72079.47	-72074.65	4.821	0.3914
H_2O + Chl-*a*' THF	-2265.364	-2265.181	-61643.72	-61638.73	4.990	0.5600

7.5 Conclusions

The vibrational frequency of Chl-*a*/Chl-*a*' model structures were calculated in the presence of axial ligand and H-bond. The calculations show that the 13^1 keto and 13^3 ester C=O modes of Chl-*a*/Chl-*a*' are coupled and display symmetric and anti-symmetric coupled vibrations in the presence of the axial ligand and H-bond. Including the axial ligand to the Chl-*a*/Chl*a*' model has no significant effect on the 13^1 keto and 13^3 ester C=O symmetric or anti-symmetric coupled modes. H-bond interactions on the other hand causes a significant down-shift in frequency of the anti-symmetrically coupled modes of 13^1 keto and 13^3 ester C=O groups. The calculated down-shift for the anti-symmetrically coupled mode is comparable to the experimentally observed down-shift for the C=O group of P_A chlorophyll in P_{700} in the presence of H-bond. Redox potential of Chl-*a*/Chl-*a*' models were calculated from the electronic energy of the models. The calculated redox potential values show that the axial ligand reduces the reduction potentials, while H-bond interaction has no effect on determining the redox potential.

CHAPTER 8

CALCULATED PROPERTIES OF P_{700}, A CHLOROPHYLL-*A*'/CHLOROPHYLL-*A* HETERODIMER

8.1 Introduction

Photosystem I (PS I) [6] is a membrane-spanning, protein complex found in plants, algae and cyanobacteria. PS I uses light to drive the formation of reducing products that lead to the reduction of carbon dioxide (taken from the atmosphere) to glucose. In the PS I core, light illumination induces a charge separation between a (hetero) dimeric Chlorophyll-*a*'/*a* (Chl-*a*'/*a*) electron donor called P_{700} and a terminal iron sulfur cluster called F_B. Chl-*a*' is a 13^2 stereoisomer of Chl-*a*. The two pigments of P_{700} are bound to the pseudo C_2 symmetric membrane spanning proteins called *PsaA* and *PsaB*. The pigments of P_{700} bound to *PsaA/PsaB* are called P_A/P_B, respectively. P_A/P_B is the Chl-*a*'/Chl-*a* species, respectively.

The oxidation potential (E_{ox}) of P_{700} plays a significant role in determining the electron transfer kinetics in PS I. E_{ox} of P_{700} is ~440 mV [10], significantly lower than that of monomeric Chl-*a* (~800 mV) or P_{680} (~1200 mV), the homodimeric Chl-*a* species that functions as primary electron donor in PS II.

One of the goals of computational research on photosynthetic reaction centers is to model these extreme redox properties of the dimeric donor cofactors. Here the redox properties of P_{700} were calculated and the results were compared to the calculated redox properties of P_{680}.

The nature of the charge distribution over the pigments in the P_{700}^+ state is unclear. FTIR studies suggest that the charge distribution is 1:1 to 1:2 (P_A:P_B) [63]. These results may disagree with ENDOR studies, which indicate a localized spin distribution over the Chls of P_{700}^+ of 1:6 to

1:9 (P_A:P_B) [66, 72]. To investigate these issues the charge and spin distributions over the pigments in the P_{700}^+ state were also calculated.

In the PS I crystal structure the macrocycles of P_A and P_B are parallel and separated by 3.6 Å. Pyrole rings I and II of P_A and P_B overlap, and the Mg^{2+} ions are separated by 6.3 Å (Figure 8.1). The N_{4A}-Mg_A-Mg_B-N_{4B} dihedral angle is ~57° [6].

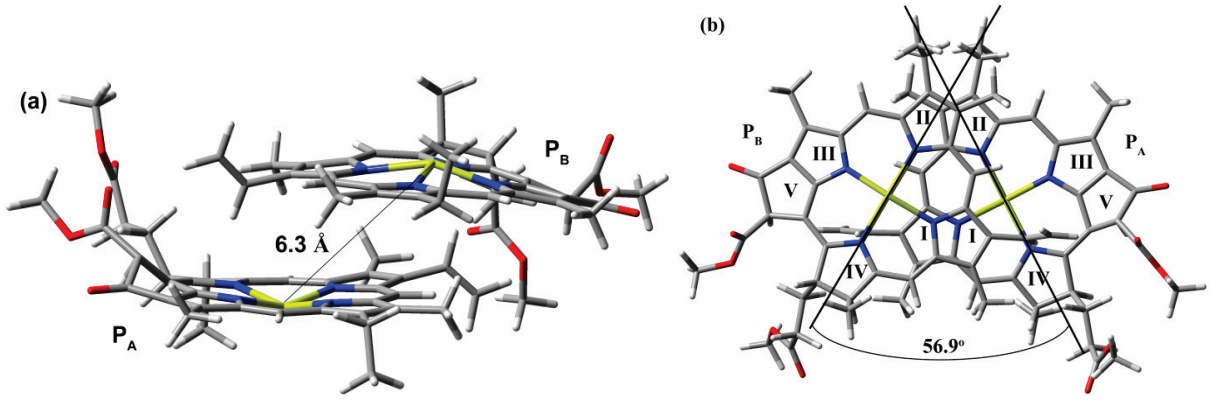

Figure 8.1: (a) Structure of P_{700} showing the Mg-Mg distance (b) The angle between the lines formed by the Mg-N4 bonds on either pigment is 56.9º.

8.2 Materials and Methods

Two different P_{700} models were used in the calculations presented here. For the first model (which is called P_{700}_1JB0), the atomic coordinates of P_{700} from the crystal structure were used [6]. Hydrogen atoms are added and geometry optimized at the B3LYP/6-31G(d) level, keeping all heavy atoms fixed. In the crystal structure, ring V of P_A is bent out of plane of the macrocycle. This is an artifact. Hence the heavy atoms of ring V were allowed to freely optimize along with the hydrogen atoms. The phytyl chain of both Chl's is replaced with a methyl group at the 17^4 position. This P_{700} model contains 164 atoms.

The second model (called P_{700}_opt) also contains 164 atoms and is fully geometry optimized at the B3LYP/6-31G(d) level (Figures 8.2 and 8.3).

Mulliken population analysis implemented within Gaussian 03 [87] was used to calculate the charge and spin distributions over the pigments of P_{700}^{+}. To model solvent effects, the integral equation formalism (IEF) of the polarizable continuum model (PCM) [90-95] was used, as it is implemented in Gaussian 03.

The electronic energy of both model dimers was calculated at B3LYP/6-311+G(d) level, in vacuum and in solvents with dielectric constants of 2.228 (CCl4) and 7.58 (THF) as described previously [137].

8.3 Results and Discussion

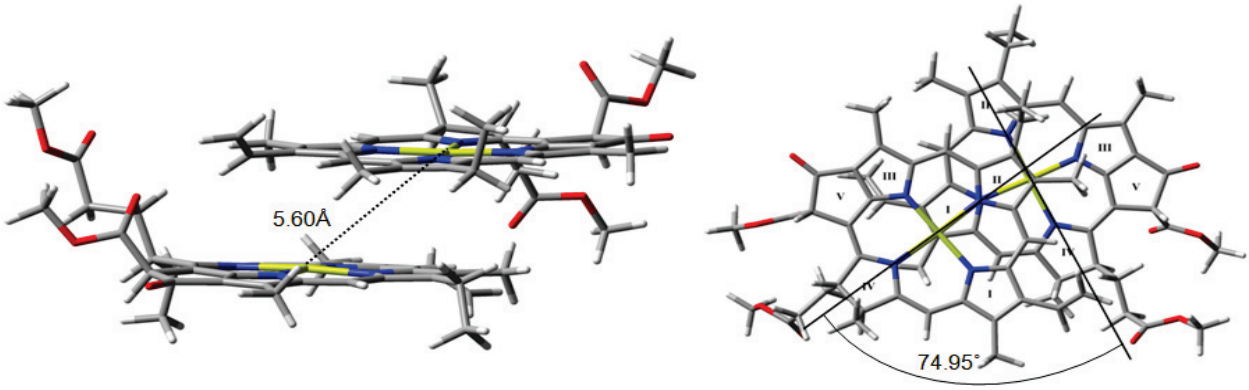

Figure 8.2: Structure of fully geometry optimized P_{700} in the neutral state. The angle between the lines formed by the Mg-N_4 bonds on either pigment is 74.95º for the neutral state.

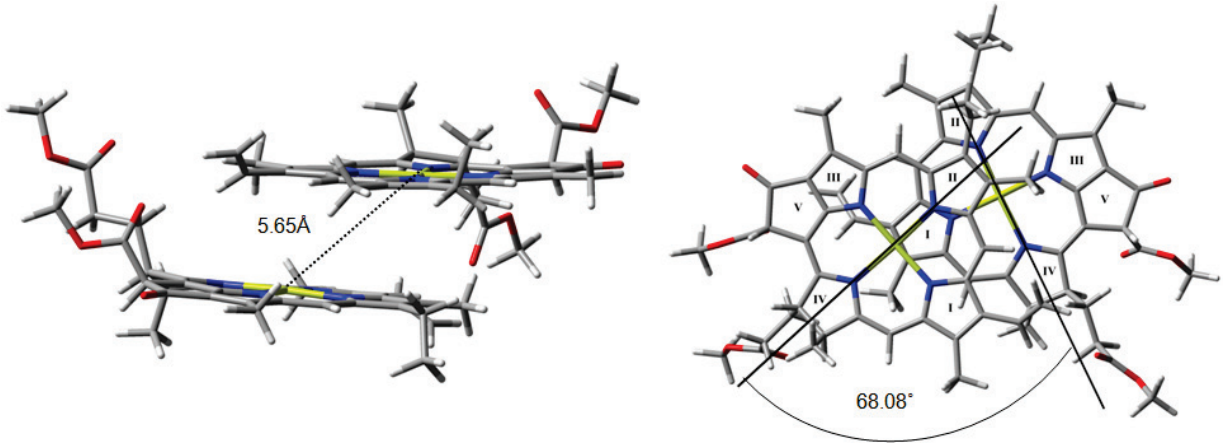

Figure 8.3: Structure of fully geometry optimized P_{700} in the cation state. The angle between the lines formed by the Mg-N_4 bonds on either pigment is 68.08º for the cation state.

For the optimized P_{700} and P_{700}^{+} models the chlorin planes deviate somewhat from parallel, and are separated by ~3.8 Å. The overlap of the pyrole rings of the two pigments are clearly different from the crystal structure. The Mg^{2+} ion separation is 5.60 Å and 5.65 Å and the N_{4A}-Mg_A-Mg_B-N_{4B} dihedral angles are ~75° and 68° for P_{700} and P_{700}^{+}, respectively (Figures 8.2 and 8.3). Optimization causes the inter-planer distance to increase slightly, while the Mg^{2+} ion separation decreases. This decrease could be due to lack of histidine ligands that pull the Mg out of plane of the macrocycle. From comparing the optimized structures in Figures 8.1, 8.2 and 8.3 with the X-ray crystal structure a RMS deviation of 1.24 Å and 1.06 Å was obtained for the neutral and cation states, respectively. Presumably, with the incorporation of protein amino acids into the calculation, the pigments will have less steric freedom, and the optimized structures may more closely resemble the crystal structure.

8.3.1 Calculated Charge/Spin Distribution

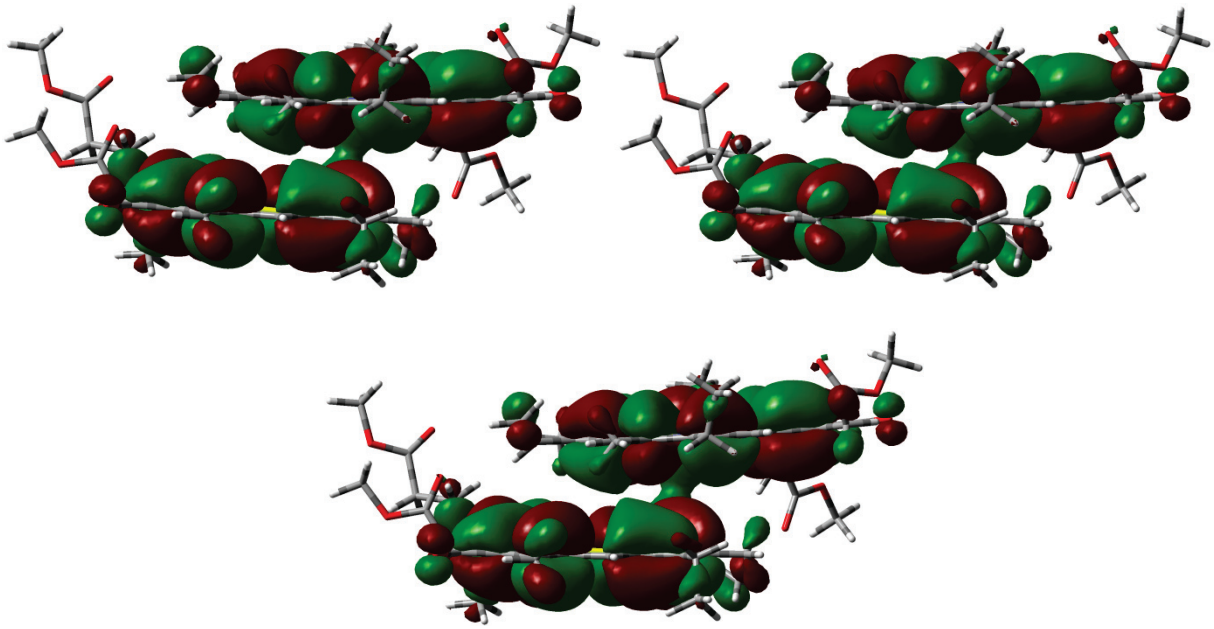

Figure 8.4: The HOMO of P_{700}^{+} obtained from the fully geometry optimized model (*clockwise*) in the gas phase, in CCl_4 and THF. Red color represents positive electron density while green color represents negative electron density. The value of the isosurface is 0.01.

For the P_{700}^{+} structure shown in Figure 8.3 the calculated charge distribution over the two pigments is 1:0.998 in the gas phase. In solvents the calculated charge distribution over P_{700}^{+} is 1:1.03 (CCl_4) and 1:1.09 (THF) (see Table 8.1). These results suggest that the positive charge on P_{700}^{+} is delocalized over the two chlorophyll pigments of P_{700}.

The highest occupied molecular orbitals (HOMO's) of the P_{700}^{+} model in the gas phase and in solvents are shown in Figure 8.4. The spin density distributions in the corresponding models are shown in Figure 8.5. It is clearly evident from Figures 8.4 and 8.5 that the unpaired charge/spin is delocalized over the two chlorophylls of P_{700}.

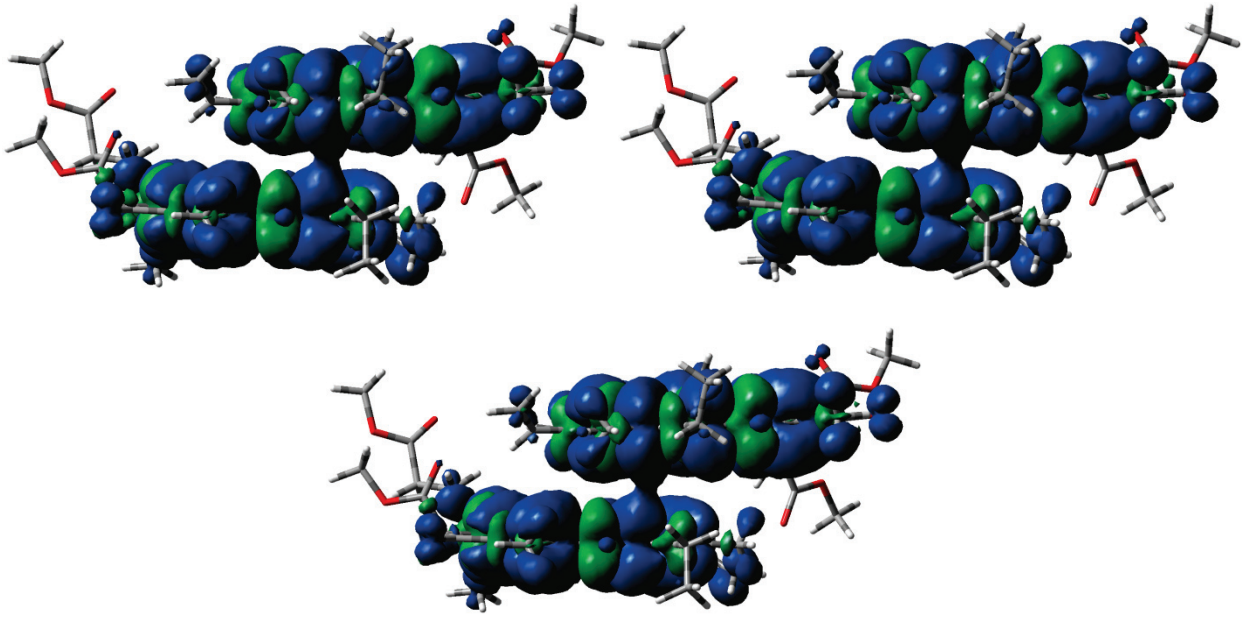

Figure 8.5: Spin density distribution in P_{700}^{+} obtained from the fully geometry optimized model (*clockwise*) in the gas phase, in CCl_4 and THF. Blue color represents positive spin density while green color represents negative spin density. The value of the spin density contour is 0.0001.

For the P_{700} model with only hydrogen atoms optimized, the calculated charge distribution over P_{700}^{+} is 1:1.35 in the gas phase and 1:1.26/1:1.05 in CCl_4/THF respectively. Thus the calculated charge distribution from both models suggests that the charge on P_{700} is delocalized in the cation state. These results are in agreement with FTIR data [63]. The

calculated charge distribution is similar to that obtained by Sun et. al [139], who used a lower level of theory and did not include the 17^3 ester C=O group.

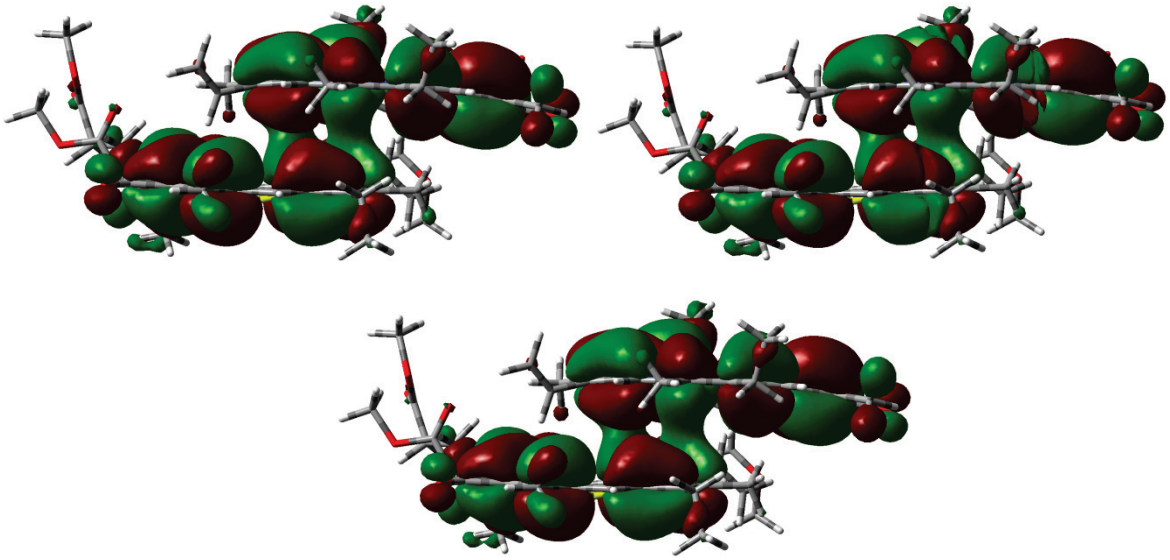

Figure 8.6: The HOMO of P_{700}^+ obtained from the P_{700}_1JB0 model (*clockwise*) in the gas phase, in CCl_4 and THF. Red color represents positive electron density while green color represents negative electron density. The value of the isosurface is 0.01.

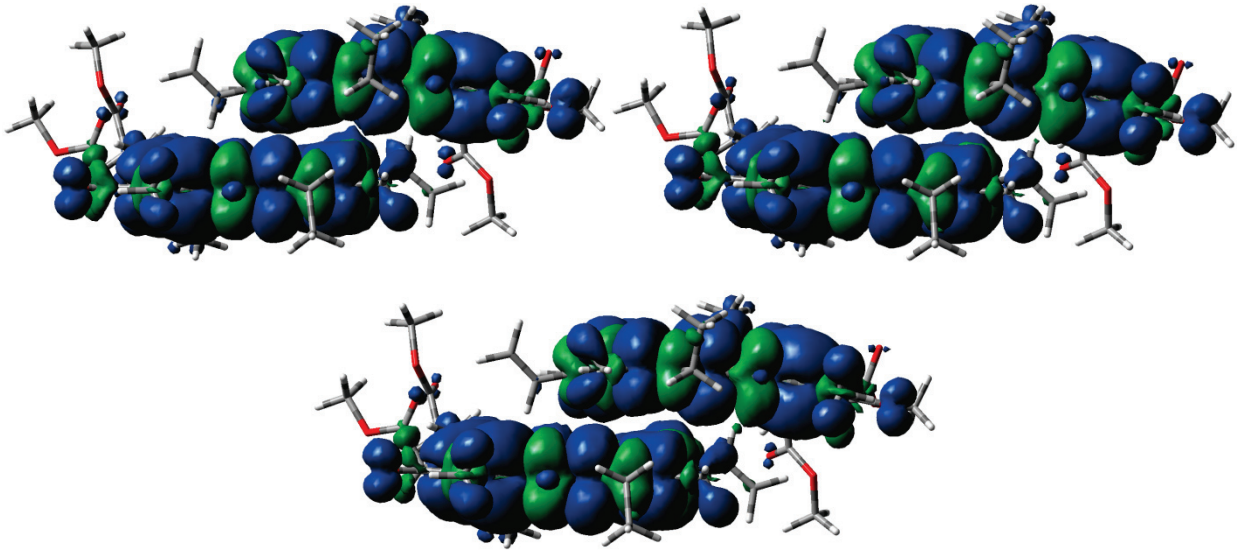

Figure 8.7: Spin density distribution in P_{700}^+ obtained from the P_{700}_1JB0 model (*clockwise*) in the gas phase, in CCl_4 and THF. Blue color represents positive spin density while green color represents negative spin density. The value of the spin density contour is 0.0001.

Table 8.1: Charge and spin distribution for cation state of P_{700}_1JB0 ,P_{700}_opt and P_{680}_2AXT models, obtained from single point energy calculations at the B3LYP/6-311+G(d) level.

	ε = 1	ε=2.228	ε=7.58
Charge (P_A:P_B)			
P_{700}_1JB0	1 : 1.35	1 : 1.26	1 : 1.05
P_{700}_opt	1 : 0.99	1 : 1.03	1 : 1.09
P680_2AXT	1 : 1.63	1 : 1.62	……..
Spin (P_A:P_B)			
P_{700}_1JB0	1 : 1.16	1 : 1.08	1 : 0.89
P_{700}_opt	1 : 1.48	1 : 1.54	1 : 1.65
P680_2AXT	1 : 0.84	1 : 0.85	……..

The charge distribution over P_{680}^+ was also calculated for a P_{680} model with only hydrogen atoms optimized, starting from the crystal structure of PS II [10]. The calculated charge distribution over P_{680}^+ is 1:1.63 (P_{D1}:P_{D2}) and 1:1.62(P_{D1}:P_{D2}) in the gas phase and in CCl_4, respectively. Recently Takahashi et al. calculated a ratio of 1:1.174 (P_{D1}:P_{D2}) for a Chl-*a* dimer that is purported to be representative of P_{680}^+ [140]. In their model of P_{680} the 17^3 ester C=O group of both chlorophylls were replaced with ethyl groups. The calculated results for P_{680}_2AXT and P_{700}_1JB0 are very similar, so are the results obtained by Takahashi et al. This is surprising as it is thought that the charge distribution over the pigments of P_{680} is highly localized [141]. So, for the P_{680} model (and probably the P_{700} model studied here) the calculated charge (and spin) distribution over the pigments may not be a reliable indicator of the appropriateness of the computational approach. Certainly, any calculated results are best considered only within the context of many calculations on various dimeric chlorophyll species that may or may not include a protein environment.

8.3.2 Calculated Redox Potential

The ionization potential (IP) of the Chl-*a*'/*a* dimer can be estimated from the difference in the calculated electronic energies of the neutral and cation states. The ionization potential for

P_{700}_1JB0 and P_{700}_opt and P_{680}_2AXT were calculated in the gas phase and in solvents. The ionization potential for a monomeric Chl-*a* molecule was also calculated. The cofactor E_{ox} (in Volts) was obtained from the calculated ionization potential by subtracting the absolute potential of SHE referenced to vacuum, which has been estimated to be 4.43 eV as described by Hasegawa et. al.[137]. The calculated E_{ox} for P_{700}_1JB0, P_{700}_opt and P_{680}_2AXT models along with that of a monomeric chlorophyll model in the gas phase and in solvents is given in Table 8.2. Also given is the E_{ox} value calculated for a P_{680} model by Takahashi et. al.[140]

Table 8.2: Calculated redox potentials for P_{700}_1JB0, P_{700}_opt and P_{680}_2AXT models, obtained from single point energy calculations at the B3LYP/6-311+G(d) level.

	ε = 1	ε=2.228	ε=7.58
E_{ox} (V)			
P_{700}_1JB0	1.622	1.071	0.705
P_{700}_opt	1.546	1.064	0.767
P680_2AXT	1.620	1.087	……..
Chl-*a*	1.827	1.191	0.797
P_{680}[140]		1.099(ε=2.247)	

For both optimized and unoptimized P_{700}/P_{700}^{+} models, as well as for a monomeric Chl-*a*/Chl-a^{+} model, the calculated E_{ox} for ε = 1.0/2.228/7.58 are listed in Table 8.2. The dielectric constant around the pigments in photosynthetic reaction centers has been estimated to be between 2.2-7.6 [96, 97, 131-134]. Also listed in Table 8.2 is the E_{ox} calculated for the P_{680}_2AXT model and the model studied by Takahashi et al previously [140]. The calculated E_{ox} values are very similar for both the hetero and homodimeric Chl-a models. This is perplexing given the very different E_{ox} that P_{700} and P_{680} are known to operate at. It is also confusing to observe that the calculated E_{ox} values are virtually same for P_{700}_1JB0 and P_{700}_opt. It is a valuable result, however, for diagnosing the appropriateness of the computational methods. Given that the same redox potentials are calculated for Chl-*a* dimer models that are supposedly

representative of systems operating at very different redox potentials, it is probably unwise to relate calculated IP's directly to available experimental data. Especially so when the results are based on isolated calculations without consideration of the protein environment, hence more detailed calculations involving the protein backbone are clearly required.

8.4 Conclusions

The charge and spin distribution in the cation state of P_{700} was obtained using fully geometry optimized as well as un-optimized model of P_{700} starting from the X-ray crystal structure. The calculated charge and spin distribution of P_{700}^{+} in both models is delocalized over both chlorophylls. The charge/spin distribution was also obtained for a P_{680} model for comparison and the calculated results are similar to that of P_{700}. This is surprising as it is thought that the charge distribution over the pigments of P_{680} is highly localized.

The redox potential was calculated for the P_{700} models as well as for the P_{680} model. The calculated redox potential are very similar for both the hetero (P_{700}) and homodimeric (P_{680}) Chl-*a* models. This is perplexing because P_{700} and P_{680} are known to operate at very different redox potentials. These results are valuable, however, for diagnosing the appropriateness of the computational methods.

Given that the same redox potentials are calculated for Chl-*a* dimer models that are supposedly representative of systems operating at very different redox potentials, it is probably unwise to relate calculated IP's directly to available experimental data. More detailed calculations involving the protein environment are clearly required to obtain a detailed understanding of the very different redox properties of P_{700} and P_{680}.

CHAPTER 9

DISSERTATION SUMMARY

Photosystem I (PS I) is a pigment protein complex present in the thylakoid membrane of plants and bacteria that catalyses the light-induced transfer of electrons across the membrane. In PS I the electron transfer process is initiated by light induced oxidation of a hetero-dimeric Chl-*a* / Chl-*a*' (P_B/ P_A) species called P_{700}. The protein interaction to the primary electron donor P_{700} is highly asymmetric, with P_A being involved in a hydrogen bond network with several surrounding amino acid residues and P_B being free of any such interactions.

Low temperature FTIR Difference Spectroscopy was used to study a series of mutants from cyanobacterium *Synechocystis* sp. 6803 where the amino acid residues in the proximity of the C=O groups of the two chlorophylls of P_{700} where specifically changed. On the *PsaA* protein a single mutation of ThrA739 to Phe as well as a set of three mutations were ThrA739 changed to Tyr, SerA603 to Gly, and TyrA599 to Leu were studied. The aim of these mutations were to modify the hydrogen bonding interactions to the C=O groups of P_A by making the environment similar to the C=O modes of P_B, which exhibits no hydrogen bonding interaction with the protein backbone.

The low temperature FTIR Difference spectroscopy measurements of the different *PsaA* mutants indicate that the hydrogen bonding to the C=O groups of P_A have been significantly impacted upon mutations, which is evident from the mutation induced changes of the FTIR DS bands assigned to the 13^1 keto and 13^3 ester C=O groups of P_A

A similar set of mutants where the amino acid residues in the vicinity of P_B were modified, in an attempt to introduce hydrogen bonding interaction to the C=O groups of P_B, were

also studied. On the *PsaB* protein a single mutation of TyrB718 to Thr , a double mutant were GlyB585 was changed to Ser and LeuB581 was changed to Tyr as well as a set of three mutations were TyrB718 changed to Thr, GlyB585 to Ser, and LeuB581 to Tyr were studied.

The low temperature FTIR Difference spectroscopy measurements of the *PsaB* mutants suggests the possibility that the mutations introduces H-bonding interaction to 13^1 keto C=O group of P_B.

DFT based vibrational frequency calculations of Chl-*a* model molecules were undertaken in the presence and absence of H-bond interactions to the 13^1 keto C=O group in order to assist the interpretation of the mutation induced spectral changes in the different *PsaA* and *PsaB* mutants. These calculations show that the ester and keto C=O groups of Chl-*a* molecule shows coupled vibrations. The spectral changes observed over a wide spectral region in these mutants can thus be easily explained by treating the 13^1 keto and 13^3 ester C=O groups as coupled modes.

The FTIR difference spectroscopy data from the different *PsaA* and *PsaB* mutants suggests that the pigment-protein interactions are unique to each pigment and also demonstrate that the strong hydrogen bonding interactions that exist between the 13^1 keto and 13^3 ester carbonyl groups of P_A and three key residues of *PsaA* cannot be duplicated on the *PsaB* side by simply replacing the corresponding amino acid residues by their *PsaA* homologues.

The electron transfer cofactors in PS I arranged along two virtually identical branches extending across the thylakoid membrane from the primary electron donor, P_{700} raises the question whether both branches of cofactors are equally active in PS I. Pigments on the two branches are spectroscopically indistinguishable; hence the focus has been on creating site-

directed mutants where point mutations are made for specific amino acids along the *PsaA* or *PsaB* branch.

The directionality of electron transfer in PS I particles has been investigated using different spectroscopic techniques including, EPR and ultrafast spectroscopy. Ramesh et al. [24, 26], employing optical ultrafast spectroscopy, reported that upon replacement of the Met axial ligand to A_0 on the *PsaA* or *PsaB* protein by His in PS I particles from *C. reinhardtii* equal amount of A_0^- was accumulated in both mutants. Also it was shown that the accumulation of A_0^- is transient and that the reoxidation of A_0^- occurs within 1-2 ns, two orders of magnitude slower than in wild type. These results were taken as in indication that both branches are active in electron transfer in *C. reinhardtii* PS I particles. However, these results were challenged by a low-temperature transient EPR study [142], which indicated that the formation of the $P_{700}^+A_1^-$ radical pair was not affected in the *PsaB* mutant, where as it was significantly diminished in the *PsaA* mutant. The transient EPR measurements at low temperature are only sensitive to those reaction centers undergoing reversible charge separation while the RT ultrafast measurements observe the entire PS I population. Using single flash excitation FTIR DS measurements these two different populations of reaction centers can be observed.

Single flash excitation FTIR DS measurements indicates that mutation of the A_0 ligand on the A branch leads to a decrease in the reversible component of P_{700} while the mutation on the B branch lead to an increase in the reversible component. Hence it can be shown that the conflicting conclusions made from transient EPR and RT ultrafast measurement results were due to the different populations of reaction centers under observation and both measurements in fact show evidence that both branches are active in electron transfer in *C. reinhardtii* PS I particles.

Also, the intensity of the (P_{700}^{+}-P_{700}) FTIR DS for the *PsaA* and *PsaB* branch mutants of A_0 are significantly reduced at RT and low temperature measurements in comparison with the wild type spectra. The change in intensity of the spectra from the mutants was comparable and suggests that both branches are impacted to a similar extent upon mutation in *C .reinhardtii* PS I particles. Hence the FTIR data also provided evidence for bi-directional electron transfer in *C. reinhardtii* PS I particles.

(P_{700}^{+}-P_{700}) FTIR DS has been obtained under many set of conditions: from PS I particles from different species, to particles with site-directed mutations near P_{700} and A_0, to globally and site specifically isotope labeled PS I particles [54, 71, 76, 77]. DFT based vibrational mode frequency calculations were undertaken for several Chl-*a* and Chl-a^{+} model molecular systems in order to assist in the assignment of the difference bands in the (P_{700}^{+}-P_{700}) FTIR DS to vibrations modes of the chlorophyll molecules constituting P_{700} [79, 80]. The calculated (Chl-a^{+}-Chl-*a*) DS in solvents shows remarkable similarity to the experimental (Chl-a^{+}-Chl-*a*) FTIR DS in THF. However, the compositions of the calculated vibrational modes are very different from that suggested from experiment. The calculated data was used to make new suggestions as to the origin of the bands in experimental (Chl-a^{+}-Chl-*a*) FTIR DS.

The effect of solvation on the calculated IR spectra of Chl-*a* has been mostly studied using the PCM method where the solvent is modeled as a dielectric continuum [79, 80]. But PCM method has limitations as they do not model possible axial ligands or hydrogen bonds to Chl-*a* molecule. Hence in order to include the effect of these possible interactions, on the vibrational modes of Chl-*a*, vibrational frequency calculations were performed in the presence of real solvent molecules using the QM/MM method. It has been shown from this study that the

vibrational frequency calculations using QM/MM methods are not better than the gas phase calculations at least at the level of theory under consideration (B3LYP/6-31G(d)/AMBER). Solvent calculations using PCM method gave superior results for vibrational frequencies as well as redox potentials as the calculated results were closer to experimental results.

The effect of axial ligation and H-bonding on the vibrational properties and redox potentials of Chl-*a* was investigated in details using the PCM model. These calculations show that the axial ligands have little or no effect on the frequencies of the calculated IR DS of Chl-*a*. The calculations also shows that the axial ligands decrease the redox potential of Chl-*a* significantly, and could explain the low redox potential of P_{700} in PS I.

Hydrogen bonding to 13^1 keto C=O group of Chl-*a* leads to a significant downshift in the vibrational frequency of the anti-symmetrically coupled 13^1 keto and 13^3 ester C=O modes. The calculations also show that a H-bond introduced to the 13^1 keto C=O group of Chl-*a* leads to a significant decrease in intensity of the symmetrically coupled 13^1 and 13^3 ester C=O modes. The changes in frequency and intensity of the anti-symmetrically and symmetrically coupled modes in the calculated spectra are comparable to the experimentally observed changes in the (P_{700}^{+-} P_{700}) FTIR DS obtained from *PsaB* mutant PS I particles of *S. 6803*. Also the calculations show that the H-bonding to the 13^1 keto C=O group of Chl-*a* has no effect on the redox potential.

DFT methods were also used to calculate the charge, spin and redox properties of two Chl-a/Chl-a' dimer models that are representative of P_{700}, the primary electron donor in photosystem I. In one model that adheres closely the P_{700} structure derived from X-ray crystallography, the calculated charge and spin are evenly distributed between the pigments. Also, a redox potential of ~1.071 V (ε=2.228) was calculated for this model. This is similar to

that found in previous calculations of a Chl-*a* dimer that was suggested to be representative of P_{680} in PS II. P_{700} and P_{680} have very different redox properties, it therefore appears that DFT based calculations on chlorophyll dimers in the absence of the protein environment, may not accurately model their redox properties. In a second model, the chlorophyll-a'/a dimer model was fully geometry optimized. In this case the optimized structure is quite different from that suggested by X-ray crystallography, but the calculated charge and spin properties of this model dimer are similar to that calculated for the un-optimized dimer. This may be a further indication that the protein environment around the pigments strongly modulates the charge, spin and redox properties of chlorophyll dimers.

REFERENCES

1. Gest, H., *History of the word photosynthesis and evolution of its definition.* Photosynthesis Research, 2002. **73**(1-3): p. 7-10.
2. Blankenship, R.E. and H. Hartman, *The origin and evolution of oxygenic photosynthesis.* Trends in Biochemical Sciences, 1998. **23**(3): p. 94-97.
3. Blankenship, R.E., *Origin and Early Evolution of Photosynthesis.* Photosynthesis Research, 1992. **33**(2): p. 91-111.
4. Iverson, T.M., *Evolution and unique bioenergetic mechanisms in oxygenic photosynthesis.* Curr Opin Chem Biol, 2006. **10**(2): p. 91-100.
5. Grotjohann, I. and P. Fromme, *Structure of cyanobacterial Photosystem I.* Photosynthesis Research, 2005. **85**(1): p. 51-72.
6. Jordan, P., et al., *Three-dimensional structure of cyanobacterial photosystem I at 2.5 A resolution.* Nature, 2001. **411**(6840): p. 909-17.
7. Fromme, P., et al., *Structure of photosystems I and II.* Comptes Rendus Chimie, 2006. **9**(2): p. 188-200.
8. Golbeck, G., *Structure and Function of Photosystem I*, in *Annu. Rev. Plant Physiol. Plant Mol. Biol.* 1992. p. 293-324.
9. Golbeck, J.H., *The Structure of Photosystem-I.* Current Opinion in Structural Biology, 1993. **3**(4): p. 508-514.
10. Brettel, K., *Electron transfer and arrangement of the redox cofactors in photosystem I.* Biochimica Et Biophysica Acta-Bioenergetics, 1997. **1318**(3): p. 322-373.
11. Brettel, K. and W. Leibl, *Electron transfer in photosystem I.* Biochimica Et Biophysica Acta-Bioenergetics, 2001. **1507**(1-3): p. 100-114.
12. Chitnis, P.R., *Photosystem I: Function and physiology.* Annual Review of Plant Physiology and Plant Molecular Biology, 2001. **52**: p. 593-626.
13. Cohen, R.O., et al., *Evidence for asymmetric electron transfer in cyanobacterial photosystem I: Analysis of a methionine-to-leucine mutation of the ligand to the primary electron acceptor A(0).* Biochemistry, 2004. **43**(16): p. 4741-4754.
14. Boudreaux, B., et al., *Mutations in Both Sides of the Photosystem I Reaction Center Identify the Phylloquinone Observed by Electron Paramagnetic Resonance Spectroscopy.* J. Biol. Chem., 2001. **276**(40): p. 37299-37306.
15. Hastings, G. and V. Sivakumar, *A Fourier transform infrared absorption difference spectrum associated with the reduction of A(1) in photosystem I: Are both phylloquinones involved in electron transfer?* Biochemistry, 2001. **40**(12): p. 3681-3689.
16. Joliot, P. and A. Joliot, *In vivo analysis of the electron transfer within Photosystem I: Are the two phylloquinones involved?* Biochemistry, 1999. **38**(34): p. 11130-11136.
17. Muhiuddin, I.P., et al., *Evidence from time resolved studies of the P700(.+)/A1(.-) radical pair for photosynthetic electron transfer on both the PsaA and PsaB branches of the photosystem I reaction centre.* FEBS Lett, 2001. **503**(1): p. 56-60.
18. Purton, S., et al., *Site-directed mutagenesis of PsaA residue W693 affects phylloquinone binding and function in the photosystem I reaction center of Chlamydomonas reinhardtii.* Biochemistry, 2001. **40**(7): p. 2167-75.

19. Ali, K., et al., *Bidirectional electron transfer in photosystem I: Replacement of the symmetry-breaking tryptophan close to the PsaB-bound phylloquinone (A(1B))with a glycine residue alters the redox properties of A(1B) and blocks forward electron transfer at cryogenic temperatures.* Biochimica Et Biophysica Acta-Bioenergetics, 2006. **1757**(12): p. 1623-1633.
20. Dashdorj, N., et al., *Asymmetric electron transfer in cyanobacterial photosystem I: Charge separation and secondary electron transfer dynamics of mutations near the primary electron acceptor A(0).* Biophysical Journal, 2005. **88**(2): p. 1238-1249.
21. Luneberg, J., et al., *Spectroscopic Characterization of PS-I Core Complexes from Thermophilic Synechococcus Sp - Identical Reoxidation Kinetics of a(1)(-) before and after Removal of the Iron-Sulfur-Clusters F-a and F-B.* FEBS Lett., 1994. **338**(2): p. 197-202.
22. Xu, W., et al., *Electron Transfer in Cyanobacterial Photosystem I: I. Physiological and Spectroscopic Characterization of Site-directed Mutants in a Putative Electron Transfer Pathway from A_0 through A_1 to F_X.* J. Biol. Chem., 2003. **278**(30): p. 27864-27875.
23. Xu, W., et al., *Electron Transfer in Cyanobacterial Photosystem I: II. Determination of Forward Electron Transfer Rates of Site-Directed Mutants in a Putative Electron Transfer Pathway from A_0 through A_1 to F_x* J. Biol. Chem., 2003. **278**(30): p. 27876-27887.
24. Ramesh, V.M., et al., *Bidirectional electron transfer in photosystem I: accumulation of A0- in A-side or B-side mutants of the axial ligand to chlorophyll A0.* Biochemistry, 2004. **43**(5): p. 1369-75.
25. Guergova-Kuras, M., et al., *Evidence for two active branches for electron transfer in photosystem I.* Proc. Natl. Acad. Sci. U S A, 2001. **98**(8): p. 4437-4442.
26. Ramesh, V.M., et al., *Replacement of the methionine axial ligand to the primary electron acceptor A(0) slows the A(0)(_)(-)reoxidation dynamics in Photosystem I.* Biochimica Et Biophysica Acta-Bioenergetics, 2007. **1767**(2): p. 151-160.
27. Cohen, R.O., *Directionality of Electron Transfer in Cyanobacterial Photosystem I.* PhD Dissertation, 2004.
28. Kass, H., et al., *Orientation and electronic structure of the primary donor radical cation P-700(+center dot) in photosystem I: A single crystals EPR and ENDOR study.* Journal of Physical Chemistry B, 2001. **105**(6): p. 1225-1239.
29. Sivakumar, V., R. Wang, and G. Hastings, *A(1) reduction in intact cyanobacterial photosystem I particles studied by time-resolved step-scan Fourier transform infrared difference spectroscopy and isotope labeling.* Biochemistry, 2005. **44**(6): p. 1880-1893.
30. Agalarov, R. and K. Brettel, *Temperature dependence of biphasic forward electron transfer from the phylloquinone(s) A1 in photosystem I: only the slower phase is activated.* Biochim Biophys Acta, 2003. **1604**(1): p. 7-12.
31. Schlodder, E., et al., *Temperature dependence of forward and reverse electron transfer from A(1)(-), the reduced secondary electron acceptor in photosystem I.* Biochemistry, 1998. **37**(26): p. 9466-9476.
32. Kok, B., *On the reversible absorption change at 705 mu in photosynthetic organisms.* Biochim Biophys Acta, 1956. **22**(2): p. 399-401.

33. Ke, B., *Photosynthesis : photobiochemistry and photobiophysics*, in *Advances in photosynthesis ; v. 10*. 2001, Kluwer Academic Publishers: Dordrecht ; Boston. p. 56-62.
34. Commoner, B., J.J. Heise, and J. Townsend, *Light-Induced Paramagnetism in Chloroplasts.* Proceedings of the National Academy of Sciences of the United States of America, 1956. **42**(10): p. 710-718.
35. Kok, B. and H. Beinert, *The light induced EPR signal of photocatalyst P700. II. Two light effects.* Biochem Biophys Res Commun, 1962. **9**: p. 349-54.
36. Baker, R.A. and E.C. Weaver, *A Correlation of EPR Spins with P_{700} in Spinach Subchloroplast Particles.* Photochemistry and Photobiology, 1973. **18**(3): p. 237-241.
37. Warden, J.T., Jr. and J.R. Bolton, *Simultaneous quantitative comparison of the optical changes at 700 nm (p700) and electron spin resonance signals in system I of green plant photosynthesis.* J Am Chem Soc, 1973. **95**(19): p. 6435-6.
38. Norris, J.R., et al., *Electron Spin Resonance of Chlorophyll and the Origin of Signal I in Photosynthesis.* Proceedings of the National Academy of Sciences of the United States of America, 1971. **68**(3): p. 625-628.
39. Philipson, K.D., V.L. Sato, and K. Sauer, *Exciton interaction in the photosystem I reaction center from spinach chloroplasts. Absorption and circular dichroism difference spectra.* Biochemistry, 1972. **11**(24): p. 4591-4595.
40. Krauss, N., et al., *3-Dimensional Structure of System-I of Photosynthesis at 6 Angstrom Resolution.* Nature, 1993. **361**(6410): p. 326-331.
41. Fromme, P., P. Jordan, and N. Krauß, *Structure of photosystem I.* Biochimica et Biophysica Acta (BBA) - Bioenergetics, 2001. **1507**(1-3): p. 5-31.
42. Fromme, P. and P. Mathis, *Unraveling the Photosystem I reaction center: a history, or the sum of many efforts.* Photosynthesis Research, 2004. **80**(1-3): p. 109-124.
43. Fromme, P., et al., *Structure and function of photosystem I: interaction with its soluble electron carriers and external antenna systems.* Febs Letters, 2003. **555**(1): p. 40-44.
44. Fromme, P., et al., *New Insigths into the structure and function of photosystem I and II.* Febs Journal, 2005. **272**: p. 451-451.
45. Fromme, P., et al., *Structure and function of photosystem I and II.* Biochimica Et Biophysica Acta-Bioenergetics, 2004. **1658**: p. 77-77.
46. Dolphin, D., *The Porphyrins*. 1978, New York: Academic Press.
47. Vernon, L.P. and G.R. Seely, *The chlorophylls*. 1966, New York,: Academic Press. 679.
48. Gibasiewicz, K., et al., *Excitonic Interactions in Wild-Type and Mutant PSI Reaction Centers.* 2003. **85**(4): p. 2547-2559.
49. Fairclough, W.V., et al., *Bidirectional electron transfer in photosystem I: electron transfer on the PsaA side is not essential for phototrophic growth in Chlamydomonas.* Biochimica et Biophysica Acta (BBA) - Bioenergetics, 2003. **1606**(1-3): p. 43-55.
50. McConnell, M.D., *Biochemical and Biophysical Studies of Photoystem I in Chlamydomonas Reinhardtii: Directionality of Electron Transfer and State Transitions.* PhD Dissertation, 2008.
51. Santabarbara, S., et al., *Bidirectional electron transfer in photosystem I: determination of two distances between P700+ and A1- in spin-correlated radical pairs.* Biochemistry, 2005. **44**(6): p. 2119-28.

52. Smith, B.C., *Infrared spectral interpretation : a systematic approach*. 1999, Boca Raton: CRC Press.
53. Sivakumar, V., R. Wang, and G. Hastings, *Photo-Oxidation of P740, the Primary Electron Donor in Photosystem I From Acaryochloris marina.* Biophys. J., 2003. **85**(5): p. 3162-3172.
54. Hastings, G., et al., *Primary donor photo-oxidation in photosystem I: A re-evaluation of (P700(+)-P700) Fourier transform infrared difference spectra.* Biochemistry, 2001. **40**(43): p. 12943-12949.
55. Nabedryk, E., *Light-Induced Fourier Transform Infrared Difference Spectroscopy of the Primary Electron Donor in Photosynthetic Reaction Centers*, in *Infrared spectroscopy of biomolecules. "Light-Induced Fourier Transform Infrared Difference Spectroscopy of the Primary Electron Donor in Photosynthetic Reaction Centers"*, H.H. Mantsch and D. Chapman, Editors. 1996, Wiley-Liss: New York. p. 39-81.
56. Noguchi, T., et al., *Electronic and vibrational structure of the radical cation of P840 in the putative homodimeric reaction center from Chlorobium tepidum as studied by FTIR spectroscopy.* Biochemistry, 1996. **35**(48): p. 15428-35.
57. Breton, J., E. Nabedryk, and W.W. Parson, *A new infrared electronic transition of the oxidized primary electron donor in bacterial reaction centers: a way to assess resonance interactions between the bacteriochlorophylls.* Biochemistry, 1992. **31**(33): p. 7503-10.
58. Nabedryk, E., W. Leibl, and J. Breton, *FTIR spectroscopy of primary donor photooxidation in Photosystem I, Heliobacillus mobilis, and Chlorobium limicola. Comparison with purple bacteria.* Photosynthesis Research, 1996. **48**(1-2): p. 301-308.
59. Noguchi, T., et al., *Fourier transform infrared study on the primary donor P798 of Heliobacterium modesticaldum: Cysteine S-H coupled to P798 and molecular interactions of carbonyl groups.* Biochem., 1997. **36**(40): p. 12329-12336.
60. Binstead, R.A. and N.S. Hush, *Hole localization and spin coupling in .pi.-mono- and .pi.-dications of .mu.-oxoporphyrin dimers. Relevance to structure of oxidized special pair in photosynthetic reaction centers.* J Phys Chem B, 1993. **97**(50): p. 13172-13179.
61. Tavitian, B.A., et al., *Light-induced Fourier transform infrared (FTIR) spectroscopic investigations of primary reactions in photosystem I and photosystem II.* FEBS Letters, 1986. **201**(1): p. 151.
62. Maentele, W., et al., *Fourier Transform Ir Spectroelectrochemistry Of The Bacteriochlorophyll A Anion Radical.* Photochemistry and Photobiology, 1988. **47**(3): p. 451-456.
63. Breton, J., E. Nabedryk, and W. Leibl, *FTIR study of the primary electron donor of photosystem I (P700) revealing delocalization of the charge in P700(+) and localization of the triplet character in (3)P700.* Biochemistry, 1999. **38**(36): p. 11585-92.
64. Nabedryk, E., et al., *Fourier transform infrared difference spectroscopy shows no evidence for an enolization of chlorophyll a upon cation formation either in vitro or during P700 photooxidation.* Biochemistry, 1990. **29**(13): p. 3242-7.
65. Breton, J., *Fourier transform infrared spectroscopy of primary electron donors in type I photosynthetic reaction centers.* Biochim Biophys Acta, 2001. **1507**(1-3): p. 180-93.

66. Krabben, L., et al., *Influence of the axial ligands on the spectral properties of P700 of photosystem I: A study of site-directed mutants.* Biochemistry, 2000. **39**(42): p. 13012-13025.
67. Kim, S.Y., et al., *Determination of chlorophyll and chlorophyll cationic radical infrared modes in the difference FT-IR spectrum of PSI by in situ isotopic labeling.* Biophysical Journal, 2000. **78**(1): p. 134a-134a.
68. Wang, R., et al., *FTIR difference spectroscopy in combination with isotope labeling for identification of the carbonyl modes of P700 and P700+ in photosystem I.* Biophys J, 2004. **86**(2): p. 1061-73.
69. Bender, S.L. and B.A. Barry, *Light-induced dynamics in Photosystem I electron transfer.* Biophys. J., 2008: p. biophysj.108.135418.
70. Kim, S., et al., *A reaction-induced FT-IR study of cyanobacterial photosystem I.* Biochemistry, 2001. **40**(50): p. 15384-15395.
71. Kim, S. and B.A. Barry, *Identification of Carbonyl Modes of P700 and $P700^+$ by in situ Chlorophyll Labeling in Photosystem I.* J. Am. Chem. Soc., 2000. **122**: p. 4980-4981.
72. Webber, A.N. and W. Lubitz, *P700: the primary electron donor of photosystem I.* Biochim Biophys Acta, 2001. **1507**(1-3): p. 61-79.
73. Breton, J., et al., *The two histidine axial ligands of the primary electron donor chlorophylls (P700) in photosystem I are similarly perturbed upon P700+ formation.* Biochemistry, 2002. **41**(37): p. 11200-10.
74. Witt, H., et al., *Hydrogen bonding to P700: Site-directed mutagenesis of threonine A739 of photosystem I in Chlamydomonas reinhardtii.* Biochemistry, 2002. **41**(27): p. 8557-8569.
75. Wang, R., et al., *Mutation induced modulation of hydrogen bonding to P700 studied using FTIR difference spectroscopy.* Biochemistry, 2003. **42**(33): p. 9889-97.
76. Breton, J., P.R. Chitnis, and M. Pantelidou, *Evidence for hydrogen bond formation to the PsaB chlorophyll of P700 in photosystem I mutants of Synechocystis sp. PCC 6803.* Biochemistry, 2005. **44**(14): p. 5402-8.
77. Pantelidou, M., P.R. Chitnis, and J. Breton, *FTIR spectroscopy of Synechocystis 6803 mutants affected on the hydrogen bonds to the carbonyl groups of the PsaA chlorophyll of P700 supports an extensive delocalization of the charge in P700.* Biochemistry, 2004. **43**(26): p. 8380-8390.
78. Li, Y., et al., *Directing electron transfer within Photosystem I by breaking H-bonds in the cofactor branches.* Proc Natl Acad Sci U S A, 2006. **103**(7): p. 2144-9.
79. Parameswaran, S., R. Wang, and G. Hastings, *Calculation of the Vibrational Properties of Chlorophyll a in Solution.* J. Phys. Chem. B, 2008. **112**(44): p. 14056-14062.
80. Wang, R., S. Parameswaran, and G. Hastings, *Density functional theory based calculations of the vibrational properties of chlorophyll-a.* Vibrational Spectroscopy, 2007. **44**(2): p. 357-368.
81. Balaban, T.S., *Are syn-ligated (bacterio)chlorophyll dimers energetic traps in light-harvesting systems?* FEBS Lett, 2003. **545**(2-3): p. 97-102.
82. Balaban, T.S., et al., *Relevance of the diastereotopic ligation of magnesium atoms of chlorophylls in Photosystem I.* Biochim Biophys Acta, 2002. **1556**(2-3): p. 197-207.

83. Heimdal, J., et al., *The role of axial ligands for the structure and function of chlorophylls.* J Biol Inorg Chem, 2007. **12**(1): p. 49-61.
84. Sun, Y., et al., *The effect of axial Mg2+ ligation and peripheral hydrogen bonding on chlorophyll a.* Chemical Physics Letters, 2004. **387**(1-3): p. 12-16.
85. O'Malley, P. and S. Collins, *The Effect of Axial Mg Ligation on the Geometry and Spin Density Distribution of Chlorophyll and Bacteriochlorophyll Cation Free Radical Models: A Density Functional Study.* J. Am. Chem. Soc., 2001. **123**(44): p. 11042-11046.
86. Smith, B.C., *Fundamentals of Fourier Transform Infrared Spectroscopy*. 1996, New York: CRC press.
87. M. J. Frisch, G.W.T., H. B. Schlegel, G. E. Scuseria, , et al., *Gaussian 03, Revision D.01,*. Gaussian, Inc., Wallingford CT, 2004.
88. Wheeler, R.A., *Quinones and Quinoidal Radicals in Photosynthesis. in Theoretical Biochemistry--Processes and Properties of Biological Systems.* Eriksson, L. A.;ed.; Elsevier: Amsterdam, 2001. **9**: p. 655-690.
89. Bandaranayake, K.M.P., et al., *Modeling the A(1) binding site in photosystem - I. Density functional theory for the calculation of "anion-neutral" FTIR difference spectra of phylloquinone.* Vibrational Spectroscopy, 2006. **42**(1): p. 78-87.
90. Cances, E., et al., *Integral Equation Methods for Molecular Scale Calculations in the Liquid Phase.* Mathematical Models & Methods in Applied Sciences, 1999. **9**(1): p. 35.
91. Tomasi, J.C., Roberto ; Mennucci, Benedetta; Cappelli, Chiara;Corni, Stefano *Molecular properties in solution described with a continuum solvation model.* Phys. Chem. Chem. Phys., 2002. **4**: p. 5697 - 5712.
92. Tomasi, J., B. Mennucci, and R. Cammi, *Quantum Mechanical Continuum Solvation Models.* Chem Rev, 2005. **105**(8): p. 2999-3094.
93. Tomasi, J., B. Mennucci, and E. Cances, *The IEF version of the PCM solvation method: an overview of a new method addressed to study molecular solutes at the QM ab initio level.* Journal of Molecular Structure-Theochem, 1999. **464**(1-3): p. 211-226.
94. Mennucci, B. and J. Tomasi, *Continuum solvation models: A new approach to the problem of solute's charge distribution and.* Journal of Chemical Physics, 1997. **106**(12): p. 5151.
95. Cances, E., B. Mennucci, and J. Tomasi, *An new integral equation formalism for the polarizable continuum model: Theoretical background.* Journal of Chemical Physics, 1997. **107**(8): p. 3032.
96. Steffen, M.A., K. Lao, and S.G. Boxer, *Dielectric Asymmetry in the Photosynthetic Reaction Center.* Science, 1994. **264**(5160): p. 810-816.
97. Rabenstein, B., G.M. Ullmann, and E.W. Knapp, *Calculation of protonation patterns in proteins with structural relaxation and molecular ensembles – application to the photosynthetic reaction center.* European Biophysics Journal, 1998. **27**(6): p. 626-637.
98. Golbeck, J.H., *Photosystem I. The Light-Driven Plastocyanin:Ferredoxin Oxidoreductase, Advances in Photosynthesis and Respiration, Volume 24.* Springer,Dordrecht, 2006.
99. Redding, K. and A. Van der Est, *The Directionality of Electron Transfer in Photosystem I, in Photosystem I: The Light-Driven Plastocyanin:Ferredoxin*

Oxidoreductase.,Advances in Photosynthesis and Respiration, Volume 24, J.H Golbeck Editior. Springer,Dordrecht, 2006: p. 413-437.
100. Fromme, P. and I. Grotjohann, *Structural Analysis of Cyanobacterial Photosystem I, in Photosystem I: The Light-Driven Plastocyanin:Ferredoxin Oxidoreductase.,Advances in Photosynthesis and Respiration, Volume 24, J.H Golbeck Editior.* Springer,Dordrecht, 2006: p. 47-69.
101. Breton, J., *FTIR Studies of the Primary Electron Donor, P700.* The Light-Driven Plastocyanin, John H. Golbeck (ed), 2006: p. 271-289.
102. Rigby, S.E.J., et al., *Photoaccumulation of the PsaB phyllosemiquinone in Photosystem I of Chlamydomonas reinhardtii.* Biochimica et Biophysica Acta (BBA) - Bioenergetics, 2002. **1556**(1): p. 13-20.
103. Walker, D., *Energy, plants and man*. 2nd ed ed. 1993, Brighton, East Sussex : Mill Valley, CA: Oxygraphics.
104. Blankenship, R.E., *Molecular Mechanisms of Photosynthesis*. 2002: Blackwell Science Ltd.
105. Akiyama, M.M., H. ; Kise, H.; Watanabe, T.; Miyachi, S.; Kobayashi, M., *Detection of Chlorophyll d' and Pheophytin a in a Chlorophyll d-Dominating Oxygenic Photosynthetic Prokaryote Acaryochloris marina.* Anal Sci, 2001. **17**(1): p. 205-208.
106. Yoshida, E., A. Nakamura, and T. Watanabe, *Reversed-phase HPLC determination of chlorophyll a' and naphthoquinones in photosystem I of red algae: existence of two menaquinone-4 molecules in photosystem I of Cyanidium caldarium.* Anal Sci, 2003. **19**(7): p. 1001-5.
107. Kobayashi, M., *Study of precise pigment composition of photosystem 1-type reaction centers by means of normal-phase HPLC.* Journal of Plant Research, 1996. **109**(2): p. 223-230.
108. Pedretti, A., L. Villa, and G. Vistoli, *VEGA – An open platform to develop chemo-bio-informatics applications, using plug-in architecture and script programming.* Journal of Computer-Aided Molecular Design, 2004. **18**(3): p. 167-173.
109. Maseras, F. and K. Morokuma, *IMOMM: A new integrated ab initio + molecular mechanics geometry optimization scheme of equilibrium structures and transition states.* Journal of Computational Chemistry, 1995. **16**(9): p. 1170-1179.
110. Humbel, S.p., S. Sieber, and K. Morokuma, *The IMOMO method: Integration of different levels of molecular orbital approximations for geometry optimization of large systems: Test for n-butane conformation and SN2 reaction: RCl+Cl.* Journal of Chemical Physics, 1996. **105**(5): p. 1959.
111. Matsubara, T., S. Sieber, and K. Morokuma, *A test of the new "integrated MO + MM" (IMOMM) method for the conformational energy of ethane and n-butane.* International Journal of Quantum Chemistry, 1996. **60**(6): p. 1101-1109.
112. Svensson, M., et al., *ONIOM: A Multilayered Integrated MO + MM Method for Geometry Optimizations and Single Point Energy Predictions. A Test for Diels-Alder Reactions and $Pt(P(t\text{-}Bu)_3)_2 + H_2$ Oxidative Addition.* J Phys Chem B, 1996. **100**(50): p. 19357-19363.
113. Svensson, M., S.p. Humbel, and K. Morokuma, *Energetics using the single point IMOMO (integrated molecular orbital+molecular orbital) calculations: Choices of*

computational levels and model system. Journal of Chemical Physics, 1996. **105**(9): p. 3654.
114. Dapprich, S., et al., *A new ONIOM implementation in Gaussian98. Part I. The calculation of energies, gradients, vibrational frequencies and electric field derivatives.* Journal of Molecular Structure: THEOCHEM, 1999. **461-462**: p. 1-21.
115. Vreven, T. and K. Morokuma, *On the application of the IMOMO (integrated molecular orbital + molecular orbital) method.* Journal of Computational Chemistry, 2000. **21**(16): p. 1419-1432.
116. Vreven, T., et al., *Geometry optimization with QM/MM, ONIOM, and other combined methods. I. Microiterations and constraints.* Journal of Computational Chemistry, 2003. **24**(6): p. 760-769.
117. Hai, L. and D. Truhlar, *QM/MM: what have we learned, where are we, and where do we go from here?* Theoretical Chemistry Accounts: Theory, Computation, & Modeling, 2007. **117**(2): p. 185-199.
118. Bakowies, D. and W. Thiel, *Hybrid Models for Combined Quantum Mechanical and Molecular Mechanical Approaches.* J Phys Chem B, 1996. **100**(25): p. 10580-10594.
119. Hratchian, H.P., et al., *QM:QM electronic embedding using Mulliken atomic charges: energies and analytic gradients in an ONIOM framework.* J Chem Phys, 2008. **128**(3): p. 034107.
120. Vreven, T., et al., *Combining Quantum Mechanics Methods with Molecular Mechanics Methods in ONIOM.* Journal of Chemical Theory and Computation, 2006. **2**(3): p. 815-826.
121. Wang, J., et al., *Development and testing of a general amber force field.* Journal of Computational Chemistry, 2004. **25**(9): p. 1157-1174.
122. Wang, J., et al., *Automatic atom type and bond type perception in molecular mechanical calculations.* Journal of Molecular Graphics and Modelling, 2006. **25**(2): p. 247-260.
123. Ceccarelli, M., P. Procacci, and M. Marchi, *An ab initio force field for the cofactors of bacterial photosynthesis.* Journal of Computational Chemistry, 2003. **24**(2): p. 129-142.
124. Ceccarelli, M.P., Piero; Marchi,Massimo *An ab initio force field for the cofactors of bacterial photosynthesis.* J Comput Chem, 2006. **27**(13): p. 1620.
125. Stanienda, A., *Electrochemical investigations of chlorophylls a and b and of the pheophytins a and b. Z. Phys. Chem.*, 1965. **229**: p. 257-272.
126. Borg, D.C., et al., *The π-Cation Radical of Chlorophyll a.* Proceedings of the National Academy of Sciences of the United States of America, 1970. **67**(2): p. 813-820.
127. Wasielewski, M.R., et al., *Monomeric chlorophyll a enol: Evidence for its possible role as the primary electron donor in photosystem I of plant photosynthesis.* Proceedings of the National Academy of Sciences of the United States of America, 1981. **78**(5): p. 2957-2961.
128. G. R. Seely, *The Energetics of Electron-transfer Reactions of Chlorophyll and other Compounds* Photochemistry and Photobiology, 1978. **27**(5): p. 639-654.
129. Saji, T. and A.J. Bard, *Electrogenerated chemiluminescence. 29. The electrochemistry and chemiluminescence of chlorophyll a in N,N-dimethylformamide solutions.* Journal of the American Chemical Society, 1977. **99**(7): p. 2235-2240.

130. Barboi, N.I. and I.I. Dilung, *Electrometric study of photochemical oxidation of chlorophyll and a series of its derivatives. Biofizika*, 1969. **14**: p. 980-985.
131. Sharp, K.A. and B. Honig, *Electrostatic Interactions in Macromolecules: Theory and Applications.* Annual Review of Biophysics and Biophysical Chemistry, 1990. **19**(1): p. 301-332.
132. Simonson, T. and C.L. Brooks, *Charge Screening and the Dielectric Constant of Proteins: Insights from Molecular Dynamics.* Journal of the American Chemical Society, 1996. **118**(35): p. 8452-8458.
133. L. I. Krishtalik, A.M.K., E. L. Mertz,, *Electrostatics of proteins: Description in terms of two dielectric constants simultaneously.* Proteins: Structure, Function, and Genetics, 1997. **28**(2): p. 174-182.
134. Mertz, E.L. and L.I. Krishtalik, *Low dielectric response in enzyme active site.* Proceedings of the National Academy of Sciences of the United States of America, 2000. **97**(5): p. 2081-2086.
135. Reiss, H. and A. Heller, *The absolute potential of the standard hydrogen electrode: a new estimate.* J Phys Chem B, 1985. **89**(20): p. 4207-4213.
136. Crystal, J. and R.A. Friesner, *Calculation of the Ionization Potentials and Electron Affinities of Bacteriochlorophyll and Bacteriopheophytin via ab Initio Quantum Chemistry.* The Journal of Physical Chemistry A, 2000. **104**(11): p. 2362-2366.
137. Hasegawa, K. and T. Noguchi, *Density Functional Theory Calculations on the Dielectric Constant Dependence of the Oxidation Potential of Chlorophyll: Implication for the High Potential of P680 in Photosystem II.* Biochemistry, 2005. **44**(24): p. 8865-8872.
138. J. Fajer, I.F., M. S. Davis, A.Forman and L. K. Hanson, *Photosynthetis Energy Transduction; Spectral and Redox Characteristics of Chlorophyll Radicals in Vitro and in Vivo.* Electrochemical and Spectrochemical Studies of Biological Redox Components, Americal Chemical Society, Washington D.C. , 1982. **Advances in Chemical Series 201**: p. 489-513.
139. Sun, Y.M., et al., *A DFT study on the electronic character of P700(+).* Journal of Theoretical & Computational Chemistry, 2006. **5**(4): p. 733-741.
140. Takahashi, R., K. Hasegawa, and T. Noguchi, *Effect of Charge Distribution over a Chlorophyll Dimer on the Redox Potential of P680 in Photosystem II As Studied by Density Functional Theory Calculations.* Biochemistry, 2008. **47**(24): p. 6289-6291.
141. Diner, B.A., et al., *Site-Directed Mutations at D1-His198 and D2-His197 of Photosystem II in Synechocystis PCC 6803: Sites of Primary Charge Separation and Cation and Triplet Stabilization&#x2020.* Biochemistry, 2001. **40**(31): p. 9265-9281.
142. McConnell, M.D., et al., *Directionality of electron transport through Photosystem I of Chlamydomonas reinhardtii probed by transient electron paramagnetic resonance.In 13th International Congress of Photosynthesis, Program and Abstracts, August 29–September 3. Humana Press, Montreal,Canada. P2A–18.* 2004.